Cilia-dependent signaling pathways controlling adipose tissue plasticity

Dissertation zur
Erlangung des Doktorgrades (Dr. rer. nat.)
der Mathematisch-Naturwissenschaftlichen Fakultät der
Rheinischen Friedrich-Wilhelms-Universität Bonn

vorgelegt von

Nora Louise Winnerling

aus Bergisch Gladbach

Bonn, 2022

Angefertigt mit Genehmigung der Mathematisch-Naturwissenschaftlichen
Fakultät der Rheinischen Friedrich-Wilhelms-Universität Bonn

Erstgutachterin (Betreuerin):   Prof. Dr. Dagmar Wachten

Zweitgutachterin: Prof. Dr. Irmgard Förster

Fachnahes Mitglied: Prof. Dr. Elvira Mass

Fachfremdes Mitglied: Prof. Dr. Ute Nöthlings

Tag der Promotion: 01.04.2022

Erscheinungsjahr: 2022

Declaration

Parts of this thesis have already been published or submitted for publication:

<u>Paper</u>:

K. Sieckmann*, **N. Winnerling***, M. Huebecker, P. Leyendecker, D. Ribeiro, T. Gnad, A. Pfeifer, D. Wachten, and J.N. Hansen. J.N. 2022. AdipoQ-a simple, open-source software to quantify adipocyte morphology and function in tissues and in vitro. *Mol Biol Cell.* 33:br22.

<u>Poster</u>:

Matschat N., Beckert V., Mass E., Wachten D.
Cilia-dependent effects on adipose tissue differentiation and their implications for obesity in Bardet-Biedl syndrome. "Cluster Science Days 2018" of the Immunosensation excellence cluster, 05.-06.11.2018, Biomedizinisches Zentrum (BMZ), University Hospital, Bonn, Germany

Matschat N., Beckert V., Mass E., Wachten D.
Cilia-dependent regulatory pathways in adipose tissue differentiation and their influence on obesity in Bardet-Biedl Syndrome. Annual meeting 2019" of the Bonner Forum Biomedizin (BFB), 14.-15.02.2019, Sportschule Hennef, Hennef, Germany

Matschat N., Beckert V., Mass E., Wachten D.
Cilia-dependent signaling pathways controlling adipose tissue plasticity. "Cluster Science Days 2019" of the Immunosensation excellence cluster, 04.-05.11.2020, Biomedizinisches Zentrum (BMZ), University Hospital, Bonn, Germany

Matschat N., Mass E., Wachten D.
Cilia-dependent signaling pathways controlling adipose tissue plasticity. Annual meeting 2019" of the Bonner Forum Biomedizin (BFB), 27.-28.02.2020, Sportschule Hennef, Hennef, Germany

Matschat N., Mass E., Wachten D.
Cilia-dependent signaling pathways controlling adipose tissue plasticity. "Cluster Science Days 2020" of the Immunosensation excellence cluster, 09.-10.11.2020, Biomedizinisches Zentrum (BMZ), University Hospital, Bonn, Germany

Winnerling N., Hansen J.N., Sieckmann K., Makdissi N., Mass E., Wachten D.
Cilia-dependent signaling pathways controlling adipose tissue plasticity. "Cluster Science Days 2021" of the Immunosensation excellence cluster, 09.-10.11.2021, Biomedizinisches Zentrum (BMZ), University Hospital, Bonn, Germany

Table of contents

Inhaltsverzeichnis

List of figures

IV

List of tables

List of abbreviations

°C	Degree Celsius
Å	Ångström
AC	Adenylyl cyclase
Ac. α-TUB	Acetylated α-tubulin
Adcy3	Adenyly cyclase type 3
AgRP	Agouti-related protein
ALMS	Alström syndrome
ANOVA	Analysis of variance
Aq. soln.	Aqueous solution
ARL13B	ADP-ribosylation factor-like protein 13B
AT	Adipose tissue
AUC	Area under the curve
BAT	Brown adipose tissue
BBS	Bardet-Biedl-Syndrome
BMP	Bone morphogenic proteins
BrdU	Bromdesoxyuridin
BSA	Bovine serum albumin
C/EBP	CCAAT-enhancer-binding protein
CaCl$_2$	Calcium chloride
caesar	Center of Advanced European Studies and Research

cAMP	Cylic adenosine monophosphate
CCL	CC-chemokine ligand
CD	Control diet
CDx	Cluster of differentiation x
CEP	centrosomal protein
CO_2	Carbon dioxide
CT	ChemiBLOCKER in PBS + 0.5% TritonX-100
Cy3	Cyanine Dye 3
DAPI	4′,6-diamidin-2-phenylindol
ddH_2O	Double-destilled water
dH2O	Destilled water
DHA	Docosahexaenoic acid
DIO	Diet-induced obesity
dk	Donkey (Equus asinus)
DMEM	Dulbecco's Modified Eagle's Medium
DMSO	Dimethylsulfoxide
DNA	Deoxyribonucleic acid
dNTPs	Deoxynucleoside tripshophates
DPP4	Dipeptidyl peptidase 4
DREADD	G protein-coupled designer receptors, exclusively activated by designer drug
EDTA	2,2′,2″,2‴-(Ethane-1,2-diyldinitrilo)tetraacetic acid
EGFP	Enhanced green fluorescent protein
EMP	Erythro-myeloid progenitors
EPAC	Exchange protein activated by cAMP
et al.	Et alii
EtOH	Ethanol
F12	Ham's F-12 Nutrient Mixture
FABP4	Fatty-acid binding protein 4
FACS	Fluorescent-activated cell sorting
FCS	Fetal calf serum
FFAR4	Free fatty acid receptor 4
FMO	Fluorescence minus one
g	Gram
G0/G1	Resting phase of the cell cycle
GFP	Green fluorescent protein
GLI	Glioma-associated transcription factors
GLI-A	Activator form of glioma-associated transcription factors
GLI-R	Repressor form of glioma-associated transcription factors
GLUT4	Glucose transporter type 4
GM	Growth medium

GPCR	G protein-coupled receptor
GPR161	G protein-coupled receptor 161
gt	Goat
GTP	Guanosine-5'-triphosphate
GTT	Glucose tolerance test
gWAT	Gonadal white AT
$G\alpha_i$	Inhibitory G protein alpha subunit
$G\alpha_s$	Stimulatory G protein alpha subunit
h	Hour(s)
H2O	
HCl	Hydrochloric acid
HE	Hematoxylin and eosin
HET	House for Experimental Therapie
HFD	High fat diet
Hh	Hedgehog
HOMA	Homeostatic model assessment
HSC	hematopoietic stem cell
i.p.	Intraperitoneal
iBAT	interscapular brown AT
IBMX	3-Isobutyl-1-methylxanthine
ICAM1	Intercellular adhesion molecule 1
ICC	Immunocytochemistry
IFT	Intraflagellar transport
IGF 1	Insulin-like growth factor 1
IL	Interleukin
IR	Insulin resistance
ITT	Insulin tolerance test
iWAT	Inguinal white AT
JBTS	Joubert syndrome
KLF4	Krüppel-like factor 4
KO	Knockout
L	Liter
LANUV	Landesamt für Natur, Umwelt und Verbraucherschutz
M	Molar
m	Milli
MACS	Magnetic-activated cell sorting
MCHII	Major histocompatibility complex II
MCHR1	Melanin-concentrating hormone receptor 1
MCP-1	Monocyte chemoattractant protein-1
MEF	Mouse embryonic fibroblasts

MEM	Minimum Essential Medium
mG	Membrane green fluorescent protein
min	Minute(s)
MKS	Meckel Gruber syndrome
mol	Mole
ms	Mouse (Mus musculus)
MSC	Mesenchymal stem cell
mT	Membrane tdTomato
mTOR	mechanistic target of rapamycin
MΦ	Macrophage
n	Nano
NaCl	Sodium chloride
NAFL	Nonalcoholic fatty liver
NAFLD	Nonalcoholic fatty liver disease
NASH	Nonalcoholic steatohepatitis
NPHP	nephronophthisis
NPY2R	Neuropeptide Y receptor Y2
ON	Overnight
P	Purmorphamine
p-CREB	phosphorylated cAMP response-element binding-protein
P1-3	Precursor subpopulation 1-3
P4-17	Postnatal day 4-17
PBS	Phosphate buffered saline
PBS-T	PBS-Tween
PCR	Polyermase chain reaction
pCREB	Phosphorylated cAMP response-element binding-protein
PDE	Phosphodiesterase
PDGFRα	Platelet-derived growth factor α
Pen Strep	Penicillin Streptomycin
PFA	Paraformaldehyde
pH	p[H+]
PH domain	Pleckstrin homology domain
PI(4,5)P$_2$	Phosphatidylinositol 4,5-biphosphate
PIP	Phosphatidylinositol phosphate
PKA	Protein kinase A
PKA-C	PKA catalytic subunit
PKA-RIα	PKA regulatory subunit type I α
PKD	polycystic kidney disease
PLL	Poly-L-lysine
POMC	Pro-opiomelanocortin

PPARγ	Peroxisome proliferator-activated receptor γ
PTCH1	12-transmembrane receptor Patched1
Ptch1	Patched 1
PVH	Paraventricular hypothalamus
R26	Rosa26 locus
rb	Rabbit
rcf	Relative centrifugal force
rec	Recombinant
RNA	Ribonucleic acid
rpm	Round per minute
rpWAT	Retroperitoneal white AT
RT	Room temperature
rt	Rat (Rattus norvegicus)
RTK	Receptor tyrosine kinase
s	Second(s)
S.D.	Standard deviation
SAG	Smoothened agonist
SCA1	Stem cell antigen 1
SDS	Sodium dodecyl sulfate
siRNA	Small interfering RNA
SMO	Smoothened
SSTR3	Somatostatin receptor 3
SVF	Stromal vascular fraction
T2D	Diabetes mellitus type 2
TA	Annealing temperature
tE	Elongation time
TE	Tris-EDTA
tg	Transgene
TGF β	Transforming growth factor β
TIM4	T-cell immunoglobulin and mucin domain-containing protein 4
TNFα	Tumor necrosis factor α
TPR	Tetratricopeptide
TZ	Transition Zone
U	Unit
UMAP	uniform manifold approximation and projection
V	Volt
V	Volume
VAP1	Vascular adhesion protein 1
w/v	Weight per volume
WAT	White adipose tissue

Wnt	Wingless Int-1
WT	Wild type
x g	x times gravitational force (9.81 m/sec2)
Δ	Delta (difference between analyzed condtion and control)
µ	Micro

Abstract

Primary cilia serve as cellular antennae that detect extracellular signals and transduce this information into an intracellular response. Dysfunction of primary cilia leads to a range of severe diseases, i.e., the Bardet-Biedl-Syndrome (BBS). BBS patients and knockout (KO) mouse models display obesity as a cardinal feature. It is known that loss of BBS protein function alters the ciliary protein repertoire, which in turn disrupts ciliary function. Obesity in BBS is primarily caused by primary cilia dysfunction in hypothalamic neurons, leading to hyperphagia. However, data from obese *Bbs*-KO mice revealed paradoxical higher insulin sensitivity and glucose tolerance compared to control obese mice, which has been attributed to enhanced differentiation of pre-adipocytes. The ability of pre-adipocytes to undergo adipogenesis is crucial to maintain white adipose tissue (WAT) homeostasis during obesity by shifting the expansion towards hyperplasia. Interestingly, adipogenesis has been shown to be cilia-dependent. Thus, ciliary dysfunction on pre-adipocytes might contribute to the obesity phenotype in BBS.

To elucidate the role of primary cilia in WAT, I analyzed the obesity phenotype of different ciliopathy mouse models and investigated pre-adipocyte function and fate. Conditional ablation of cilia attenuated WAT development *in vivo*, while conditional loss of adenylyl cyclase 3 (AC3) in pre-adipocytes and global loss of BBS8 resulted in severe obesity. In contrast, loss of BBS6 only showed an effect challenged with high fat diet (HFD). This highlights the crucial role of primary cilia for WAT plasticity and indicates distinct functions of different BBS proteins. My results demonstrate that $Bbs8^{-/-}$ mice prior to obesity development showed impaired glucose handling, which, however, did not aggravate further during obesity development and was even improved in comparison to diet-induced obesity. Surprisingly, this was not associated with an increase in adipogenesis. In contrast, $Bbs6^{-/-}$ and conditional AC3-KO mouse models, both, displayed severe glucose intolerance. Additionally, I revealed specific changes in the fate of pre-adipocytes in $Bbs8^{-/-}$ cells already before the onset of obesity, indicating that BBS proteins fulfill specific functions in controlling WAT homeostasis.

To further analyze the underlying molecular causes and functional consequences, I established a sorting strategy to isolate different pre-adipocyte subpopulations to perform transcriptomic and functional analyses and, thereby, unravel the molecular consequence of loss of BBS proteins.

Zusammenfassung

Primäre Zilien dienen als zelluläre Antenne, welche extrazelluläre Signale detektieren und eine zelluläre Reaktion hervorrufen. Dysfunktionale primäre Zilien rufen eine Reihe an schwerwiegenden Erkrankungen hervor, wie das Bardet Biel Syndrome (BBS). Ein Hauptmerkmal in Patienten sowie in entsprechenden Knockout (KO)-Mausmodellen ist Übergewicht. Es ist bekannt, dass der Verlust von BBS-Proteinen die Proteinlokalisierung im primären Zilium verändert, was dessen Funktion stört und zur Erkrankung führt. Übergewicht wurde bisher primär auf ziliären Funktionsverlust auf Neuronen im Hypothalamus zurückgeführt. Jedoch weisen übergewichtige *Bbs*-KO-Mäuse im Vergleich zu übergewichtigen Kontrollmäusen überraschend hohe Insulinsensitivität und Glukosetoleranz auf. Dies wurde auf vermehrte Differenzierung von Präadipozyten zurückgeführt. Die Fähigkeit von Präadipozyten sich zu reifen Adipozyten zu differenzieren ist zentral, um die Homöostase des weißen Fettgewebes während der Gewichtszunahme zu erhalten. Dies wird durch eine vermehrte hyperplasische Gewebsexpansion gewährleistet. Interessanterweise wurde gezeigt, dass Zilien die Adipogenese regulieren. Daher ist anzunehmen, dass dysfunktionale Zilien auf Präadipozyten zum Übergewichtsphänotypen im BBS beitragen.

Um die Rolle der primären Zilien im weißen Fettgewebe aufzuklären, habe ich den Übergewichtsphänotypen verschiedener Ziliopathie-Maus-Modelle analysiert und die Funktion von Präadipozyten untersucht. Ein spezifischer Verlust des Ziliums auf Präadipozyten führte zu reduzierter Fettgewebsentwicklung *in vivo*, während der Verlust von Adenylatcyclase 3 (AC3) in Präadipozyten und der globale Verlust von BBS8 in schwerem Übergewicht mündeten. Im Gegensatz dazu zeigte sich ein Effekt durch den Verlust von BBS6 erst unter einer fettreichen Diät (HFD). Dies hebt die zentrale Rolle der primären Zilien für die Plastizität des Fettgewebes hervor und deutet auf unterscheidbare Funktionen von verschiedenen BBS Proteinen hin. Meine Ergebnisse demonstrieren, dass Bbs8$^{-/-}$-Mäuse zwar bereits vor der Gewichtszunahme eine Beeinträchtigung der Glukosetoleranz aufweisen, sich diese jedoch nicht im Laufe der Gewichtszunahme verschlechtert und im Endeffekt im Vergleich zu Diät-induziertem Übergewicht sogar verbessert ist. Erstaunlicherweise war dies nicht mit erhöhter Adipogenese verbunden. Im Gegensatz dazu entwickelten Bbs6$^{-/-}$-Mäuse und der Präadipozyten-spezifische AC3-KO eine schwerwiegend gestörte Glukosetoleranz. Zusätzlich konnte ich spezifische Änderungen in der Eigenschaft der Präadipozyten in Bbs8$^{-/-}$-Mäusen feststellen, welche bereits vor der Entwicklung von Übergewicht auftraten. Dies zeigt, dass BBS-Proteine wichtige Funktionen erfüllen, um die Fettgewebshomöostase zu regulieren.

Um die molekularen Ursachen und funktionellen Konsequenzen detaillierter zu analysieren, habe ich eine Methode etabliert, um die verschiedenen Subpopulationen von Präadipozyten im Gewebe zu isolieren und voneinander zu trennen. Damit können Transkriptionsanalysen und funktionelle Experimente durchgeführt werden, welche es ermöglichen die molekularen Auswirkungen des Verlusts einzelner BBS-Proteine aufzuklären.

1. Introduction

1.1 Primary cilia

Cilia are small membrane protrusions that project from the cell surface (Goetz and Anderson, 2010; Malicki and Johnson, 2017; Silverman and Leroux, 2009). Cilia in eucaryotes can be classified into immotile/primary cilia and motile cilia. Motile cilia convey cell movement, e.g., as sperm flagellum, or generate fluid flow by collectively beating in wave-like patterns (Elgeti and Gompper, 2013; Gilpin *et al.*, 2020; Mitchison and Valente, 2017). In contrast, primary cilia are non-motile, solitary, and present on almost all mammalian cells (Flood and Totland, 1977; Sorokin, 1962). Although primary cilia were first described in 1889 and named "primary cilia" in 1968, they were largely ignored by cell biologists and regarded as an evolutionary vestige (Sorokin, 1962; Zimmermann, 1898). Only after the discovery of the intraflagellar transport (IFT) machinery (Kozminski *et al.*, 1993) and its association with severe disease development upon IFT88 ablation and, in turn, cilia formation (Pazour *et al.*, 2000), primary cilia were recognized as important subcellular compartments. By now, primary cilia are known to function as a cellular antenna that perceives extracellular stimuli from the environment and locally transduce them into an intracellular response (Garcia *et al.*, 2018; Nachury and Mick, 2019; Nauli *et al.*, 2003; Wachten and Mick, 2021).

1.1.1 Structure

The primary cilium is surrounded by the ciliary membrane and consists of the axoneme, the transition zone, and the basal body at the ciliary base (Fisch and Dupuis-Williams, 2011). Primary cilia form at the apical surface of most polarized vertebrate cells during the resting phase (G0/G1) (Quarmby and Parker, 2005) by forming the microtubule-based axoneme, which originates from the basal body. The axoneme consists of nine microtubule doublets, each containing one A- and one B-tubule (Ishikawa, 2017; Satir and Christensen, 2007). During cilia formation, the mother centriole is recruited to the membrane. The distal appendages mediate centriole-membrane docking, transforming the mother centriole into the basal body. During this process, the distal appendages mature into transition fibers, defining the border between the plasma and ciliary membrane (Anderson, 1972). The ciliary membrane is continuous with the plasma membrane. However, the lipid and protein composition is unique and tightly regulated to fulfill tissue and cell-specific cilia functions (Garcia *et al.*, 2018; Rohatgi and Snell, 2010). The unique ciliary protein and lipid identity is maintained: i) the IFT machinery, ii) a diffusion barrier, and iii) gatekeeper complexes at the ciliary base (Figure 1). The IFT machinery is required for targeted, bidirectional trafficking of ciliary proteins. Anterograde transport towards the ciliary tip acts along B-tubules driven by the motor protein kinesin, whereas retrograde transport towards the ciliary base acts along A-tubules driven by the motor protein dynein (Nakayama and Katoh, 2018; Rosenbaum and Witman, 2002; Stepanek and Pigino, 2016). To ensure ciliary compartmentalization, the transition zone (TZ) serves as a gate, preventing the free diffusion of proteins between cell body and cilium (Reiter *et al.*, 2012) and is formed above the transition fibers, where Y-shaped linker connect the

microtubules to the ciliary membrane (Gilula and Satir, 1972). Multiple conserved protein complexes, including complexes of nephronophthisis (NPHP), centrosomal protein of 290 kDa (CEP290, also known as BBS14), and the Meckel Gruber syndrome (MKS) proteins occupy distinct domains within the TZ and cooperate to ensure TZ formation and function (Garcia *et al.*, 2018; Gonçalves and Pelletier, 2017; Williams *et al.*, 2011). These proteins can also interact with components of the IFT or gatekeeper complexes at the ciliary base to efficiently deliver cargo in and out of the cilium. Gatekeeper complexes are required for selective transport of proteins and act as an adapter to load cargo to the IFT machinery for ciliary trafficking. Proteins of the TUBBY family control ciliary protein import, while the BBSome complex controls β-arrestin 2-mediated ciliary export (Lechtreck *et al.*, 2009; Mukhopadhyay *et al.*, 2010; Nachury and Mick, 2019; Sun *et al.*, 2012; Ye *et al.*, 2018). It is still under debate whether the BBSome also plays a role in the ciliary import of certain proteins.
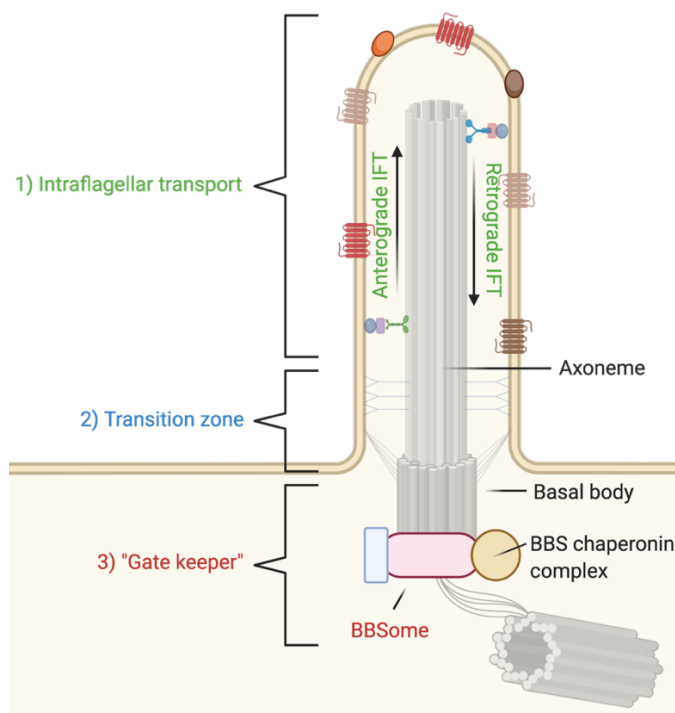
Figure 1: The unique ciliary protein composition is maintained by distinct regulatory mechanisms. To ensure and maintain the tissue- and cell-specific ciliary protein composition, the import and export is actively regulated and restricted. Transport in and out of the cilium is dependent on the intraflagellar transport (IFT) machinery, while free and lateral diffusion is restricted by the transition zone (TZ). Additionally, the gatekeeper complex, BBSome, sorts cargo at the ciliary base by serving as an adapter to load cargo to the IFT trains and enable proteins to cross the TZ.

1.1.2 BBSome

The BBSome is a conserved octameric protein complex (BBS1, BBS2, BBS4, BBS5, BBS7, BBS8, BBS9, and BBIP10 (BBS18)), serving as a gatekeeper at the ciliary base that controls the ciliary localization of especially of GPCRs (Lechtreck *et al.*, 2009; Nachury *et al.*, 2007; Nachury and Mick, 2019). To fulfill its gatekeeper function, several other proteins are important for BBSome assembly and function. The BBS chaperonin complex proteins (BBS6, BBS10, and BBS12) share sequence homology to the CCT/TRiC family group II chaperonins and mediate BBSome assembly with the help of six additional CCT proteins (Seo *et al.*, 2010; Zhang *et al.*, 2012b). The small Arf-like GTPase Arl6 (also known as BBS3), which is localized to the ciliary membrane and the basal body, is required to recruit the BBSome to the ciliary base (Jin *et al.*,

2010). The BBSome/Arl6 complex can then shuffle to the ciliary tip, where Arl6 interacts with IFT27 (also known as BBS19) (Aldahmesh *et al.*, 2014). IFT27 is a Rab-like GTPase, associated with IFT25 to interact with the IFT-B complex, which binds Arl6^{GDP} (Liew *et al.*, 2014; Wang *et al.*, 2009a). Export of BBSome and its cargo is dependent on IFT27 interaction. Thus, multiple proteins act together to ensure ciliary protein transport. Mutations in BBSome components disrupt its transport function and alter the ciliary protein localization, i.e., some proteins are absent from cilia (e.g., SSTR3, MCHR1, and NPY2R (Berbari *et al.*, 2008; Loktev and Jackson, 2013)), while others accumulate (e.g., SMO, PTCH1, phospholipase D, or dopamine D1 receptor (Lechtreck *et al.*, 2013; Zhang *et al.*, 2013; Zhang *et al.*, 2012a)). Although the loss of ciliary protein localization upon BBSome dysfunction indicates a role in ciliary protein import, growing evidence suggests that the BBSome mainly acts as an adapter for ciliary export of signaling proteins, e.g., activated GPCRs (Nachury and Mick, 2019; Ye *et al.*, 2018). The molecular mechanism underlying the specific recognition of activated GPCRs for ciliary export has been recently identified: Activated GPCRs are tagged for export by ubiquitination in a β-arrestin 2-dependent manner. Ubiquitination then acts as export signal and leads to the ciliary removal mediated by the BBSome (Shinde *et al.*, 2020). The BBSome, therefore, fulfills an important role to ensure proper function of the cilium.

1.1.3 Function

Primary cilia constitute a signaling hub that fulfills sensory functions by detecting and transmitting extracellular cues to regulate diverse cellular processes during development and tissue homeostasis. Specific receptors and their downstream effector molecules are enriched in primary cilia, providing the molecular basis to act as cellular antennae that performs chemosensation, thermosensation, and mechanosensation (Nachury and Mick, 2019; Nauli *et al.*, 2003; Wachten and Mick, 2021). Different signaling pathways have been reported in primary cilia, including receptor tyrosine kinase (RTK), G-protein coupled receptor (GPCR), Hedgehog (Hh), Wingless Int-1 (Wnt), Notch, transforming growth factor-β (TGF-β), and mechanistic target of rapamycin (mTOR) signaling (Ezratty *et al.*, 2011; Gigante and Caspary, 2020; Lancaster *et al.*, 2011; Malicki and Johnson, 2017; Satir *et al.*, 2010; Wachten and Mick, 2021; Wheway *et al.*, 2018). Additionally, primary cilia can secrete ectosomes from the ciliary membrane, indicating its role not solely as signal receivers, but also as transmitters (Wang and Barr, 2018).

Primary cilia are essential for embryonic development (Goetz and Anderson, 2010). Loss of cilia formation during embryonal development leads to severe developmental defects, including incorrect left-right asymmetry (situs-inversus), cardiac loop inversion, and neural tube closure defects (Marszalek *et al.*, 1999; Murcia *et al.*, 2000; Yanardag and Pugacheva, 2021). However, primary cilia also play an important role in the postnatal and adult state, orchestrating tissue-specific functions to maintain tissue homeostasis and function (Satir *et al.*, 2010; Yanardag and Pugacheva, 2021) Of note, nearly all stem cells so far have primary cilia, indicating its importance to regulate differentiation into multiple cell types and maintain tissue homeostasis (Liau *et al.*,

2020; Lyu and Zhou, 2017; Singh *et al.*, 2016; Vestergaard *et al.*, 2016; Yanardag and Pugacheva, 2021). Only their presence on hematopoietic stem cells (HSCs) is still under debate.

Primary cilia dysfunction leads to severe diseases commonly termed ciliopathies (Hildebrandt *et al.*, 2011; Reiter and Leroux, 2017; Waters and Beales, 2011). So far, over 180 genes and at least 35 diseases have been connected to defects or loss of primary cilia, which affect a variety of organs (Gerdes *et al.*, 2009; Mitchison and Valente, 2017; Reiter and Leroux, 2017; Waters and Beales, 2011). These diseases include polycystic kidney disease (PKD), red-cone dystrophy, Meckel-Gruber syndrome (MKS), Joubert syndrome (JBTS), Senior–Løken syndrome, Alström syndrome (ALMS), and the Bardet–Biedl syndrome (BBS), which all present with overlapping phenotypes (Gerdes *et al.*, 2009; Waters and Beales, 2011; Wheway and Mitchison, 2019). Eight of the BBS-associated genes encode for proteins that form the BBSome (Nachury *et al.*, 2007), the gatekeeper complex involved in ciliary protein trafficking, three form the BBS chaperonin complex necessary for correct BBSome assembly (Seo *et al.*, 2010; Zhang *et al.*, 2012b), and others localize to the basal body or the retrograde IFT.

1.2 Bardet-Biedl syndrome

BBS is a rare, autosomal recessive ciliopathy with its prevalence ranging from 1:160,000 in Switzerland to a higher prevalence of 1:13,500-1:17,500 in isolated minorities, e.g., Kuwaiti Bedouins or Newfoundland (Farag and Teebi, 1989; Klein and Ammann, 1969; Parfrey *et al.*, 2002). So far, at least 25 causative genes have been identified, including *BBS1-BBS21*, *NPHP1*, *FBN3,* and *CEP19,* (Forsythe *et al.*, 2018; Lindstrand *et al.*, 2014; Wang *et al.*, 2017; Yıldız Bölükbaşı *et al.*, 2018), which can genetically confirm approximately 75% of individuals with BBS (Stoetzel *et al.*, 2007) and all encode for proteins associated with primary cilia (Figure 2). Mutations in BBS-associated genes do not affect ciliogenesis or ciliary structure per se, but rather alter the ciliary protein composition due to BBSome-related disruption of the transport system (Eguether *et al.*, 2014; Lechtreck *et al.*, 2009; Mick *et al.*, 2015). This results in a pleiotropic phenotype and the severity of symptoms greatly vary depending on mutation type, affected gene, and other individual factors. Therefore, the diagnosis of BBS is based on clinical signs and symptoms, classified into primary and secondary characteristics based on their prevalence. Primary features are: Retinal red-cone dystrophy (>90%), obesity (72-95%), polydactyly (58-73%), hypogonadism (74-96%), renal defects (46-95%) and mental retardation/cognitive impairment (41-87%) (Beales *et al.*, 1999; Feuillan *et al.*, 2011; Imhoff *et al.*, 2011; Moore *et al.*, 2005; Mujahid *et al.*, 2018; Ramirez *et al.*, 2004). Some secondary signs include developmental delays, dental anomalies, ataxia, anosmia, endocrinopathies, or congenital heart disease (Beales *et al.*, 1999). To be diagnosed with BBS, patients must show four primary- or three primary- with at least two secondary characteristics (Beales *et al.*, 1999). While some phenotypes such as polydactyly are present at birth, others like obesity or retinal degeneration develop postnatally. Thus, BBS patients are diagnosed on average at an age of nine years (Beales *et al.*, 1999).

Additionally, almost half of the BBS patients present with diabetes mellitus type II (T2D) with a median age of onset of 43 years (Moore *et al.*, 2005). In contrast, another obesity-associated ciliopathy, the Alström syndrome (ALMS), already develops T2D at 16 years (Marshall *et al.*, 2005; Marshall *et al.*, 2011) although obesity development is rather similar. More detailed comparison of metabolic parameters, such as triglycerides levels, HOMA-IR (a clinical parameter to assess insulin resistance), and the presence of metabolic syndrome (defined as a combination of multiple metabolic features) indicated high variations in BBS patients dependent on the genetic cause of the disease (Feuillan *et al.*, 2011; Mujahid *et al.*, 2018). The two most prevalent affected genes in these studies, *BBS1* and *BBS10*, showed opposing metabolic characteristics: *BBS10* patients showed higher triglyceride levels, insulin resistance, and up to 75 % were categorized with metabolic syndrome, whereas only 27 % of the *BBS1* patients displayed a metabolic syndrome (Feuillan *et al.*, 2011; Mujahid *et al.*, 2018). Another clinical parameter of BBS is hyperleptinemia, which has been shown to be present in *BBS1* and to a higher degree in *BBS10* patients compared to control obese patients (Feuillan *et al.*, 2011).

BBS proteins control leptin receptor trafficking and signaling in the hypothalamus (Seo *et al.*, 2009). In turn, impaired leptin signaling dysregulates the satiety feeling and food intake, leading to hyperphagia (Feuillan *et al.*, 2011). Therefore, ciliary dysfunction in satiety feeling regulating neurons in the hypothalamus has been proposed to drive the obesity phenotype in BBS. Different BBS mouse models recapitulate BBS phenotypes like obesity, increased leptin levels, and hyperphagia (Marion *et al.*, 2012; Rahmouni *et al.*, 2008). Intriguingly, pair-fed Bbs2$^{-/-}$ and Bbs4$^{-/-}$ mice still displayed increased WAT masses compared to WT control mice, indicating that ciliary dysfunction not only controls food intake but also regulates adipose tissue (AT) plasticity, contributing to obesity development (Rahmouni *et al.*, 2008).
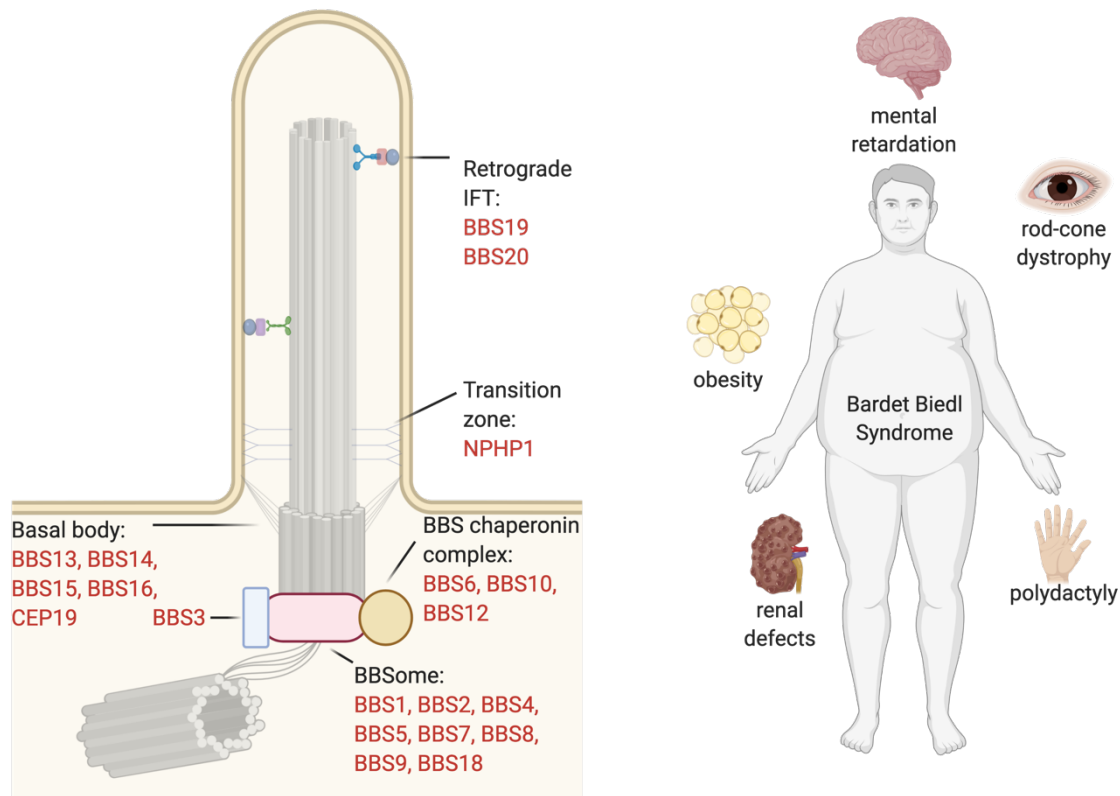
Figure 2: Ciliary localization of BBS-associated proteins and BBS symptoms. (A) The ciliary localization of proteins encoded by the 25 different causative BBS genes. For BBS17 and FBN3, the subcellular localization is ill-defined. **(B)** The main affected organs and symptoms of BBS.

1.3 White adipose tissue

Generally, obesity is a consequence of an imbalance in energy homeostasis, i.e., between energy uptake and energy expenditure as seen for hyperphagia (Hill *et al.*, 2012; Rosen and Spiegelman, 2006). The white adipose tissue (WAT) stores surplus energy in form of neutral lipids and serves as a critical regulator of systemic energy homeostasis (Marcelin and Chua, 2010). WAT is a dynamic and plastic tissue, which rapidly reacts to changes in the environment to maintain systemic energy balance, e.g., it increases its storing capacity in response to increased caloric levels, leading to tissue expansion. In mice, it has been demonstrated that one week of high-fat diet (HFD) feeding was sufficient to double the mass of gonadal WAT (Kleemann *et al.*, 2010). In contrast, prolonged fasting periods led to a severe reduction in WAT mass until being almost totally consumed after 72 h (Tang *et al.*, 2017).

Besides its function in energy storage and release, WAT is now recognized as a major endocrine organ, which signals via cytokines, lipids, matrix proteins, growth factors, and hormones. The adipocyte-secreted factors are collectively called "adipokines" and communicate locally and systemically with different cell types and organ systems e.g., brain, liver, muscle, heart, pancreas, thymus, and spleen to regulate food intake, energy expenditure, and other metabolic processes (Booth *et al.*, 2016; Coelho *et al.*, 2013). The most prominent adipokine, leptin, is essential to regulate appetite and satiety, energy expenditure, and glucose metabolism (Amitani *et al.*, 2013; Martínez-Uña *et al.*, 2020; Park and Ahima, 2015) and correlates with WAT mass. As described

above, leptin controls neuronal functions in the hypothalamus to regulate food intake (Park and Ahima, 2015), but it also acts on other organs, preventing toxic lipid accumulation, increasing fatty acid oxidation, and decreasing lipogenesis (Martínez-Uña *et al.*, 2020). Hence, WAT exerts its energy homeostatic function by intensive crosstalk with other organ systems.

1.3.1 Metabolic syndrome

Excessive WAT accumulation causes lipotoxicity due to ectopic steatosis, associated with increased co-morbidities and mortality (Caputo *et al.*, 2017; Vegiopoulos *et al.*, 2017; WHO, 2021). This highlights the crucial role of WAT for whole body metabolic health. During obesity, the oxygen consumption of adipocytes increases, leading to local hypoxia (Lee *et al.*, 2014), which triggers a higher rate of cell death (Giordano *et al.*, 2013; Kuroda and Sakaue, 2017) and free fatty-acid release. Subsequently, an inflammatory cascade gets activated, accompanied by an infiltration of immune cells (Lee and Olefsky, 2021; Vegiopoulos *et al.*, 2017; Weisberg *et al.*, 2003). These changes result in AT dysfunction and in the development of a chronic, low-grade inflammation, called metaflammation (Christ *et al.*, 2019; Hosogai *et al.*, 2007; Hotamisligil, 2006; Saltiel and Olefsky, 2017). This inflammatory state is characterized by elevated levels of pro-inflammatory cytokines and chemokines (Christ *et al.*, 2019), such as transforming growth factor β (TGFβ), tumor necrosis factor α (TNFα) (Hotamisligil *et al.*, 1993), interleukin 6 (IL-6) (Cottam *et al.*, 2004), and monocyte chemoattractant protein-1 (MCP-1) (Kanda *et al.*, 2006).

Metaflammation has now been considered as a major driving force for a complex metabolic disorder called "metabolic syndrome". Metabolic syndrome refers to a combination of interrelated factors, which together significantly increase the risks for cardiovascular disease. Multiple, generally accepted definitions exist and all of them rely on the presence of at least three of the following criteria: obesity, hyperglycemia, high blood triglycerides levels, increased high-density lipoprotein cholesterol levels, and hyperinsulinemia/insulin resistance. The definitions differ in the cut-offs and combinations of necessary and additional criteria (Eckel *et al.*, 2005; Huang, 2009). In this context, it has been shown that the different WAT depots play distinct role in the development of the disease: Greater visceral adiposity has a higher impact on the development of metabolic syndrome than increased subcutaneous adiposity (Berry *et al.*, 2013; Item and Konrad, 2012; Karpe and Pinnick, 2015; Vishvanath and Gupta, 2019). The expression of pro-inflammatory cytokines e.g., IL-6, IL-8, and MCP-1, is generally higher in visceral AT, while leptin expression is higher in subcutaneous AT (Caputo *et al.*, 2017; Fain *et al.*, 2004; Lee and Fried, 2010; Lee *et al.*, 2013). Thus, WAT-depot intrinsic factors correlate with the observed differences in the metabolic phenotype. However, the most important factor that controls the metabolic outcome and, in turn, the severity of the metabolic syndrome is the mechanisms underlying WAT expansion (Ghaben and Scherer, 2019).

1.3.2 WAT expansion

WAT either expands by increasing the volume of stored fat in existing adipocytes (hypertrophy) or by recruitment of new adipocytes (hyperplasia) (Haczeyni *et al.*, 2018). The relative contribution of these two measures critically determines the metabolic health (Ghaben and Scherer, 2019; Vishvanath and Gupta, 2019; Ye *et al.*, 2021). Metabolic disorders have been associated with adipocyte hypertrophy (Arner *et al.*, 2010; Kanda *et al.*, 2006; Vegiopoulos *et al.*, 2017; Virtue and Vidal-Puig, 2010; Ye *et al.*, 2021), whereas hyperplasia has been associated with a healthy metabolic state (Arner *et al.*, 2010; Ghaben and Scherer, 2019; Gray and Vidal-Puig, 2007; Hoffstedt *et al.*, 2010; Miyazaki *et al.*, 2002; Ye *et al.*, 2021). Promoting adipogenesis and, thereby, hyperplasia, by thiazolidinedione, a class of anti-diabetic drugs, ameliorate insulin resistance and protect from obesity-related metabolic disorders (Hallakou *et al.*, 1997; Miyazaki *et al.*, 2002; Okuno *et al.*, 1998; Shao *et al.*, 2018). Based on such reports, the "limited expandability hypothesis" has been proposed, stating that the inability of WAT to adequately expand to meet the increased demand for energy storage results in AT dysfunction, leading to the development of metabolic syndrome (Gray and Vidal-Puig, 2007; Vidal-Puig, 2013; Virtue and Vidal-Puig, 2010). In this hypothesis, any given individual has a defined limit of AT storage capacity influenced by genetic factors. Once this limit is exceeded, lipids will be deposited ectopically and cause toxic effects. In mice, it has been reported that gWAT expansion in HFD fed mice reached a plateau after about 15 wks of HFD treatment (Gealekman *et al.*, 2014). While hypertrophy is a general feature of HFD-induced AT remodeling, hyperplasia upon HFD feeding was observed in a mouse strain-dependent manner, indicating the role of genetic factors (Jo *et al.*, 2009). However, the molecular factors contributing to different AT storage capacities are largely unknown. Interestingly, Bbs12$^{-/-}$ mice displayed increased adipogenesis, leading to obesity, but the inflammatory and metabolic parameters were "healthier" compared to age-matched diet-induced obesity mice (Marion *et al.*, 2012). Hence, ciliary dysfunction by BBS might increase adipogenesis and AT expandability, leading to a different AT morphology and consequently metabolic outcome.

1.3.3 Adipogenesis

The balance between hypertrophy and hyperplasia is determined by the precursor cell pool, comprised of mesenchymal stem cells (MSCs) and committed pre-adipocytes, which replenish mature adipocytes (Figure 3A). MSCs and pre-adipocytes are both ciliated, whereas mature adipocytes and immune cells are not ciliated (Hilgendorf, 2021; Marion *et al.*, 2009). Therefore, ciliated MSCs and pre-adipocytes might be the cell type that is affected by BBS, determining the AT phenotype (Marion *et al.*, 2009). These ciliated precursor cells reside in the stromal vascular fraction (SVF) of WAT, exhibit the potential to undergo differentiation to mature adipocytes, and thereby contribute to WAT remodeling and tissue homeostasis. Adipogenesis is a multistep process, consisting of *i)* the commitment of MSCs to the adipocyte lineage, *ii)* mitotic clonal expansion, and *iii)* terminal differentiation into mature adipocytes (Ahmad *et al.*, 2020). Terminal differentiation is tightly regulated and triggered by several transcription

factors, including CCAAT-enhancer-binding protein α/β/δ (C/EBPα/β/δ) and the peroxisome proliferator-activated receptor γ (PPARγ) (Cao *et al.*, 1991; Farmer, 2006; Siersbæk and Mandrup, 2011). These two key transcription factors C/EBPα and PPARγ bilaterally induce their expression. Both have been shown to be required for WAT formation: PPARγ is the master regulator as is restores WAT development even in the absence of C/EBPα, while the converse does not rescue WAT formation (Rosen *et al.*, 2002). Different signaling cascades and transcription factors are linked together in a temporally controlled signaling network that eventually leads to the expression of the key transcription regulators C/EBPα and PPARγ (Cao *et al.*, 1991; Siersbæk and Mandrup, 2011) (Figure 3B). In the first wave, C/EBPβ and C/EBPδ get activated and then act in concert to stimulate PPARγ transcription by direct binding to the promotor region. Later during differentiation, C/EBPβ and C/EBPδ are replaced by C/EBPα (Cao *et al.*, 1991; Salma *et al.*, 2004; Siersbæk and Mandrup, 2011). Additionally, many other factors influence the activation of C/EBPβ and C/EBPδ during early differentiation (Siersbæk and Mandrup, 2011) (Cristancho and Lazar, 2011; Farmer, 2006). Importantly, activated phosphorylated cAMP response element-binding protein (p-CREB), activation of glucocorticoid receptor, and KOX20 induce the expression of C/EBPβ (Cao *et al.*, 1991; Chen *et al.*, 2005; Farmer, 2006; Siersbæk and Mandrup, 2011; Zhang *et al.*, 2004), while the sterol regulatory element-binding protein 1 (SREBP-1) (Kim and Spiegelman, 1996), the liver X receptor (Ross *et al.*, 2002), and the krüppel-like factors (Mori *et al.*, 2005; Rosen and Spiegelman, 2006) modulate the key regulators during the second wave. Once C/EBPα and PPARγ expression is activated, their positive feed-back-loop inevitably causes terminal differentiation by induction of adipocyte-specific genes, including those encoding for fatty-acid binding protein 4 (FABP4), Perilipin, glucose transporter type 4 (GLUT4), lipoprotein lipase, and fatty acid synthase (Lefterova *et al.*, 2008; Moseti *et al.*, 2016; Tontonoz and Spiegelman, 2008). *In vitro*, different pharmacological substances act in combination to induce adipogenesis (Ding *et al.*, 2003; Zebisch *et al.*, 2012) (Figure 3B). The most potent and widely used induction cocktail includes *i)* thiazolidinedione, such as rosiglitazone, which directly activate the master regulator PPARγ (Lehmann *et al.*, 1995; Tontonoz and Spiegelman, 2008; Zebisch *et al.*, 2012), *ii)* 3-isobutyl-1-methylxanthine (IBMX), which stimulates adipogenesis indirectly by inhibiting phosphodiesterases, thereby increasing cAMP levels and activating C/EBPβ via CREB, and *iii)* insulin and glucocorticoids, such as dexamethasone, which also activate C/EBPβ (Ding *et al.*, 2003; Siersbæk and Mandrup, 2011; Zebisch *et al.*, 2012).

Adipogenesis is regulated by many more factors and signaling pathways, such as bone morphogenetic proteins (Huang *et al.*, 2009), interleukin 17 (IL17) (Zúñiga *et al.*, 2010), transforming growth factor β (TGFβ) (Merrick *et al.*, 2019), insulin-like growth factor 1 (IGF-1) (Zhu *et al.*, 2009), Wingless-Int1 (WNT) (Christodoulides *et al.*, 2009), and Hedgehog (Hh) (Cousin *et al.*, 2007; Kopinke *et al.*, 2021; Suh *et al.*, 2006) signaling pathways. Strikingly, receptors of these pathways are localized to the primary cilium in pre-adipocytes (Marion *et al.*, 2009; Vestergaard *et al.*, 2016). A prime example is the free fatty-acid receptor 4 (FFAR4 or GPR120): FFAR4 activation by its natural ligand

omega-3 fatty acid docosahexaenoic acid (DHA) increased ciliary cAMP levels, triggering a signaling cascade, which resulted in exchange protein directly activated by cAMP (EPAC)-dependent chromatin remodeling and promoted adipogenesis (Hilgendorf *et al.*, 2019). This highlights the important role of primary cilia in adipogenesis. Also, ciliary cAMP signaling seems to be a central part of the regulation of adipogenesis. Besides various GPCRs, the adenylyl cyclase AC3 localize to primary cilia and is widely used as a ciliary marker (Antal *et al.*, 2017; Berbari *et al.*, 2007; Bishop *et al.*, 2007), and has also been associated with obesity (Grarup *et al.*, 2018; Saeed *et al.*, 2018). Hence, primary cilia on pre-adipocytes are essential for healthy WAT remodeling and cAMP signaling might have an important function in converting extracellular signals into a pro-adipogenic response.
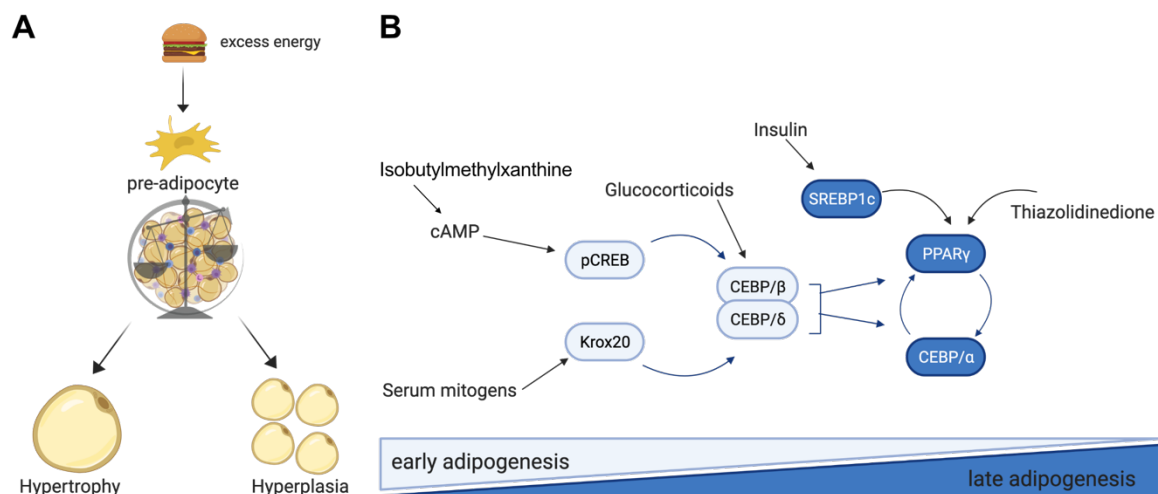
Figure 3: The balance between WAT expansion via hypertrophy or hyperplasia depends on pre-adipocytes undergoing adipogenesis. (A) WAT expansion occurs either through hypertrophy or hyperplasia (or both) and is dependent on pre-adipocyte recruitment. **(B)** Adipogenesis is a tightly orchestrated process, resulting in the terminal differentiation of pre-adipocytes into mature adipocytes. Physiological extracellular and pharmacological factors can induce the underlying intracellular cascade of different transcription factors leading to the activation of the key transcription factor PPARγ.

1.3.4 Subpopulations

Rising interest in adipocyte precursor cells has led to extensive single-cell transcriptomic analysis, providing new insights into their molecular and functional diversity (Burl *et al.*, 2018; Cho *et al.*, 2019; Ferrero *et al.*, 2020; Hepler *et al.*, 2018; Merrick *et al.*, 2019; Nahmgoong *et al.*, 2022; Sárvári *et al.*, 2021; Schwalie *et al.*, 2018). Although a final, consistent definition of pre-adipocytes is still lacking, some markers have repeatedly been found in pre-adipocyte populations: Pdgfrα/β⁺, SCA1⁺, CD29⁺, CD34⁺, CD24⁺, CD31⁻, CD45⁻, Ter119⁻, CD11b⁻, and LY6C⁻ (Bilal *et al.*, 2021; Burl *et al.*, 2018; Cho *et al.*, 2019; Ferrero *et al.*, 2020; Hepler *et al.*, 2018; Merrick *et al.*, 2019; Nahmgoong *et al.*, 2022; Sárvári *et al.*, 2021; Schwalie *et al.*, 2018; Steenhuis *et al.*, 2008; Vishvanath *et al.*, 2016). The high-resolution power of single-cell transcriptomics has also revealed the existence of at least three subpopulations, covering the full range from early stem cell-like precursor to AT lineage-committed pre-adipocyte (Burl *et al.*, 2018; Cho *et al.*, 2019; Ferrero *et al.,* 2020; Hepler *et al.*, 2018; Merrick *et al.*, 2019; Sárvári *et al.*, 2021; Schwalie *et al.*, 2018). These subpopulations

differ by specific gene expression profiles and functional properties. The stem cell-like subpopulation ("P1") is the most distinct subpopulation, characterized by the expression of CD55 (also known as complement decay-accelerating factor) and CD26 (also known as dipeptidyl peptidase 4 (DPP4)), and the lack of CD54 (also known as intercellular adhesion molecule 1 (ICAM1)), vascular adhesion protein 1 (VAP1) (also known as amine oxidase copper containing 3), and CD142 (also known as tissue factor, encoded by the gene *F3*) (Ferrero *et al.*, 2020; Merrick *et al.*, 2019; Schwalie *et al.*, 2018). Its stem cell-like character is highlighted by its multipotency, giving rise to osteoblasts or adipocytes dependent on the stimulus (Merrick *et al.*, 2019). The other two subpopulations represent committed pre-adipocytes ("P2") and regulatory pre-adipocytes ("P3"), which were shown to be more closely related with respect to their gene expression pattern (Ferrero *et al.*, 2020; Merrick *et al.*, 2019; Sárvári *et al.*, 2021; Schwalie *et al.*, 2018). Both populations lack the expression of P1 marker CD55 and CD26, but instead, express CD54 and VAP1. Additionally, P3 expresses CD142 (Ferrero *et al.*, 2020; Merrick *et al.*, 2019; Schwalie *et al.*, 2018). Higher expression levels of adipocyte-related genes, such as *Pparγ*, *Fabp4*, *Lpl*, and *Plin2* underline the committed signature of P2 (Burl *et al.*, 2018; Merrick *et al.*, 2019; Sárvári *et al.*, 2021; Schwalie *et al.*, 2018). The regulatory function of P3 is supported by its paracrine inhibitory effect on the adipogenesis of the other two subpopulations (Schwalie *et al.*, 2018). A hierarchy between those subpopulations was proposed based on *in silico* pseudo-temporal trajectory analysis (Merrick *et al.*, 2019; Nahmgoong *et al.*, 2022). This was then validated by transplant experiments with fluorescence-based cell tracing, revealing the unidirectional conversion from P1 to P2 and P3 and interconvertible P2 and P3 (Merrick *et al.*, 2019) (Figure 4).

Functionally, P2 displayed highly adipogenic potential even when only stimulated with insulin, whereas P1 barely differentiated with insulin but fully differentiated upon stimulation with a full induction cocktail (Merrick *et al.*, 2019). The adipogenic potential of P3 is still controversial as P3 was first reported to display reduced adipogenic potential (Schwalie *et al.*, 2018), but this was not supported by another report showing they were fully adipogenic (Merrick *et al.*, 2019). Nevertheless, the transcriptomic signature is different. So overall, the reported adipogenic potential of the different subpopulations is in line with their commitment to the adipocyte lineage. Additionally, the proliferation capability reduces with increasing commitment, whereby P1 represents the most highly proliferative subpopulation (Cho *et al.*, 2019). Another identified difference between those subpopulations was the responsiveness to anti-adipogenic TGFβ signaling: Treatment with TGFβ inhibited the adipogenic potential of P1 but had no effect on the other two subpopulations (Merrick *et al.*, 2019). Collectively, first functional experiments match their categorization based on the transcriptomic signatures and underline their different functions within the whole tissue (Figure 4). How the interplay and balance between those different subpopulations regulates physiological WAT expansion is still unknown. Even less is known about the role of primary cilia in controlling the function of the different subpopulations. Ciliary dysfunction might impair the identity, fate, or function and thereby contribute to WAT pathology in BBS.
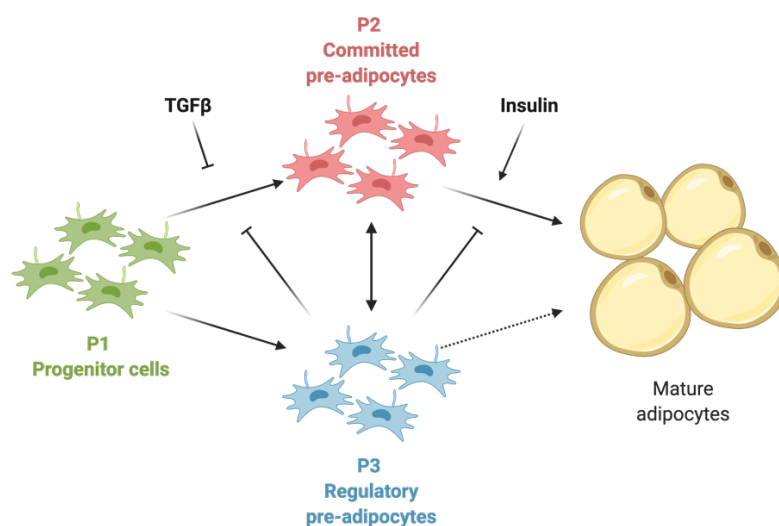
Figure 4: Proposed model of pre-adipocyte subpopulations and lineage hierarchy. Schematic model of pre-adipocyte subpopulations and their lineage hierarchy. Multiple papers defined three different pre-adipocyte subsets based on gene expression profiles. Trajectory analysis revealed lineage hierarchy (Merrick *et al.*, 2019), while functional assays indicated a paracrine inhibitory function of P3 (Schwalie *et al.*, 2018), an inhibitory effect of TGFβ signaling on P1, and a pro-adipogenic effect of insulin on P2 (Merrick *et al.*, 2019).

1.4   Hypothesis and aim of the thesis

I hypothesize that primary cilia are key regulators of adipogenesis. In turn, primary cilia dysfunction in pre-adipocytes alters AT plasticity during chronic overnutrition in BBS, determining the metabolic outcome of obesity. I aimed to: 1) analyze and compare the *in vivo* AT, metabolic, and immune cell phenotype of different ciliopathy mouse models, 2) establish markers and staining protocols to identify pre-*adipocytes in vitro* and *in vivo*, 3) investigate how primary cilia regulate adipogenesis and what are the underlying signaling pathways, and 4) study whether cell fate and function of pre-adipocyte subpopulations are cilia-dependent.

2. Materials and methods

2.1   Chemicals

Chemicals in *pro analysis* quality, kits, and other reagents were purchased from AppliChem (Darmstadt), BioRad (Munich), Eppendorf (Hamburg), Fresenius Kabi (Bad Homburg vor der Höhe), Invitrogen (Karlsruhe), Merck (Darmstadt), Miltenyi Biotec (Bergisch Gladbach, Germany), Phoenix pharmaceuticals (Burlingame, USA), Promega (Madison, USA), Quiagen (Hilden), Roth (Karlsruhe), Sigma (Steinheim), and Thermo Fisher Scientific (Waltham, USA). Oligonucleotides were generated and ordered from Eurofins MWG Operon (Ebersberg). Primary and secondary antibodies were purchased Abcam (Cambridge, UK) Alomone (Jerusalem, Israel), BD Biosciences (Franklin Lakes, USA), BD Pharmingen Inc (San Diego, USA), Biolegend (San Diego, USA), BioRad (Hercules, USA), Cell Signaling (Massachusetts, USA), Dianova (Hamburg), Fabgennix (Frisco, USA), Invitrogen (Waltham, USA), Life Technologies (Carlsbad, USA), Merck (Burlington, USA), Neuromics (Edina, USA), Phoenix pharmaceuticals (Burlingame, USA), Proteintech (Manchester, UK), R&D Systems (Minneapolis, USA), Santa Cruz Biotechnology (Dallas, USA), Sigma-Aldrich (St. Louis, USA), SinoBiological (Beijing, China), Thermo Fisher Scientific (Waltham, USA).

All buffers and solutions were prepared using double-distilled water (ddH2O). Autoclaving for sterilization was performed at 121°C for 20 min, if necessary. Sterile-filtering of buffers was achieved using 0.45 µm or 0.22 µm pore filter membranes (Millipore) in a vacuum filtration.

Phosphate buffered saline (PBS) was prepared in a 10-fold stock with 1.3 M NaCl, 70 mM Na_2HPO_4, 30 mM NaH_2PO_4, and adjusted to pH 7.4 at RT using 1 M NaOH. For usage, the 10-fold PBS stock was diluted to a 1-fold concentration in H_2O. Sterile PBS that was used for cell culture was purchased from Gibco (DPBS).

2.2   Antibodies

Table 1: List of primary antibodies.

Antigen	Antibody	Species	Dilution	Company	Cat. number
AC3 (9E2)	Anti-AC3	Rat	1:200	n.a.	n.a.
ARL13B	Anti-ARL13B	Mouse	1:500	Abcam	ab136648
ARL13B	Anti-ARL13B	Rabbit	1:150	Proteintech	17711-1-AP
C/EBPβ	Anti-C/EBPβ	Mouse	1:500	Santa Cruz	sc-7962
PECAM-1	Anti-PECAM-1	Rat	1:200	BD Pharmigen	553370
F4/80	Anti-F4/80	Rat	1:500	BioRad	MCA497GA
FABP4	Anti-FABP4	Goat	1:400	R&D Systems	AF1443
Perilipin	Anti-Perilipin	Goat	1:400	Abcam	Ab61682
FFAR4	Anti-FFAR4	Rabbit	1:100	Thermofisher	PA5-50973
FFAR4	Anti-FFAR4	Mouse	1:100	Santa Cruz	sc-390752
ac. α-TUB	Anti-ac. α-TUB	Mouse	1:500	Sigma Aldrich	T6793
VAP1	Anti-VAP1	Rat	1:100	Abcam	ab81673
KI67	Anti-KI67	Rat	1:500	Invitrogen	14-5698-82
SCA1	Anti-SCA1				

Table 2: List of secondary antibodies.

Antibody	Antigen	Species	Dilution	Supplier	Cat. number
dk anti ms Cy3	mouse IgG	donkey	1:500	Dianova	715-165-151
gt anti ms A488	mouse IgG	goat	1:400	Life Technologies	A11029
dk anti ms A647	mouse IgG	donkey	1:500	Invitrogen	A31571
dk anti rb A647	rabbit IgG	donkey	1:500	Dianova	711-605-152
dk anti rb Cy3	rabbit IgG	donkey	1:250	Dianova	711-165-152
gt anti rb A488	rabbit IgG	goat	1:500	Life Technologies	A11034
dk anti rt Cy3	mouse IgG	donkey	1:250	Dianova	712-165-153
dk anti rt A488	mouse IgG	donkey	1:500	Dianova	712-545-153
dk anti rt A647	mouse IgG	donkey	1:150	Dianova	712-605-153
dk anti gt Cy3	mouse IgG	donkey	1:1000	Dianova	705-165-147
dk anti gt A647	mouse IgG	donkey	1:75	Life Technologies	A21447

Table 3: List of antibodies for flow cytometry and FACS.

For flow cytometry and FACS			
Antibody	**Fluorophore**	**Producer**	**Cat. number**

Streptavidin	BV785	Biolegend	405249
CD31	Biotin	Biolegend	102503
CD45	Biotin	Biolegend	103103
TER119	Biotin	Biolegend	116203
CD55	APC	Biolegend	122513
CD29	PerCP-efluor710	eBioscience (Thermo)	46-0291
CD142	PE (conjugated via kit)	SinoBiological	50413-R001
VAP1	DyLight 488 (conjugated via kit)	abcam	ab81673
CD26 (DPP-4)	PE/Cy7	Biolegend	137809
CD54	APC-Fire 750	Biolegend	116125
SCA1	BV510	Biolegend	108129
Hoechst 33258		Thermo Fisher	H1398
CD34 (excluded for	BV421	Biolegend	119321

Table 4: List of antibodies used for MACS.

For MACS			
Antibody	**Fluorophore**	**Producer**	**Cat. number**
CD31	Biotin	Biolegend	102503
CD45	Biotin	Biolegend	103103
TER119	Biotin	Biolegend	116203
CD55	Biotin (conjugated with kit)	Biolegend	122513
CD54	Biotin	Biolegend	116103
CD26 (DPP-4)	Biotin (conjugated with kit)	Biolegend	137809
VAP1	Biotin (conjugated via kit)	abcam	ab81673

Fluorophore conjugation followed the manufacturer's instructions. In case of anti-VAP1 antibody the concentration of the antibody was too low, so it was concentrated prior to conjugation via centrifugal filter (Amicon® Ultra).

Conjugation kits: Lightning-Link® for Biotin (abcam, ab201796), Lightning-Link® Rapid for DyLigt488 (Novus Biologicals, 322-0005) and LYNX Rapid Conjugation Kit for PE (BioRad, LNK021RPE).

2.3 Mice

2.3.1 Licenses

All experiments were performed in agreement with the German law of animal protection and local institutional animal care committees (Landesamt für Natur, Umwelt und Verbraucherschutz, LANUV; Az 84-02.04.2014.A194). Mice were kept in individually ventilated cages in the mouse facility of the Center of Advanced European Studies and Research (caesar) and of the university hospital Bonn (House for Experimental Therapie (*HET*)). Animals were given water and complete- or very high-fat content (LARD) diet (ssniff Spezialdiäten) *ad libitum*. Mice were raised under a normal circadian light/dark cycle of each 12 h and animals were given water and complete- or very high-fat content (LARD) diet (ssniff Spezialdiäten) ad libitum (LANUV

Az 81-02.04.2019.A170). To compare ciliopathy- and diet-induced obesity, a cohort of single-housed mice at 11 weeks (wks) of age were switched to HFD for 7.5 wks, while another was kept on CD. Mice were sacrificed using cervical dislocation or transcardial perfusion after anaesthesia with isofluorane (Baxter) or ketamine (Medistar) and xylazine (Ceva), respectively. The breeding and maintenance of Bbs8-, Bbs6 knock out and Pdgfra-Cre IFT20-flox mouse lines were approved by LANUV Az 81-02.04.2019.A428.

2.3.2 Mouse lines

2.3.2.1 Bbs8 knockout mice

Bbs8 knockout mice were generated in the lab of Prof. Rendall R. Reed and kindly provided by jun. Prof. Helen May Simera (Johannes-Gutenberg-Universität, Mainz). The knockout lacks the start codon and the first two exons of the *Bbs8* gene (Tadenev *et al.*, 2011).

2.3.2.2 Bbs6 knockout mice

Bbs6 knockout mice were created in the lab of Prof. Phil Beales and kindly provided by jun. Prof. Helen May Simera (Johannes-Gutenberg-Universität, Mainz). The knockout lacks exon 3 in the Bbs6/Mkks gene (Ross *et al.*, 2005).

2.3.2.3 Pdgfra-Cre

C57BL/6-Tg(Pdgfra-cre)1Clc/J (Pdgfra-Cre, Stock No.: 013148) mice were purchased from the Jackson Laboratory. The cre recombinase is expressed under the control of the *Pdgfra* promotor, which can be used to breed conditional knock-out mouse lines.

2.3.2.4 Pdgfra-Cre AC3-E4-flox

AC-E4-flox mice were generated in the lab of Prof. Daniel R. Storm (mice were kindly provided by Prof. Daniel R. Storm, University of Washington, USA). By crossing male Pdgfra-Cre$^{cre/+}$ mice with female AC3-E-flox$^{flox/flox}$ mice, exon 4 of *Adcy3,* which is flanked by loxP sites, is excised, leading to a conditional deletion of AC3 in *Pdgfra*-expressing cells.

2.3.2.5 Pdgfra-Cre IFT20-flox

B6.129S7(129S4)-*Ift20$^{tm1.1Gjp}$*/J (IFT20-flox, Stock No.: 012565) mice were purchased from the Jackson Laboratory. By crossing male Pdgfra-Cre$^{cre/+}$ with female IFT20-flox$^{flox/flox}$ mice, exon 2-3 of *IFT20,* which is flanked by loxP sites, is excised, leading to a conditional deletion of IFT20 in *Pdgfra*-expressing cells.

2.3.2.6 Pdgfra-Cre R26-tdTomato/ R26-mT/mG

Gt(ROSA)26Sor$^{tm14(CAG-tdTomato)Hze}$ (R26-tdTomato; Stock No.: 007908) and *Gt(ROSA)26Sor$^{tm4(ACTB-tdTomato,-EGFP)Luo}$*/J (R26-mT/mG, StockNo.: 007576) mice were purchased from the Jackson Laboratory. Pdgfra-Cre$^{cre/+}$ male mice were crossed with female R26-tdTomato$^{tg/tg}$ mice. Cre recombination deletes the STOP cassette, leading to tdTomato expression in *Pdgfra*-expressing cells. By crossing male Pdgfra-Cre$^{cre/+}$

mice with female R26-mT/mG$^{tg/tg}$ mice, the cell membrane-localized tdTomato (mT), which is flanked by loxP sites, is excised, leading to a switch in fluorescence, by expression of a cell membrane-localized EGFP (mG) in *Pdgfra*-expressing cells.

2.3.2.7 Csfr1-Cre IFT20-flox

B6.129S7(129S4)-*Ift20*$^{tm1.1Gjp}$/J (IFT20-flox, Stock No.: 012565) and FVB-Tg(Csf1r-icre)1Jwp/J (Csfr1-Cre, Stock No.: 021024) mice were purchased from the Jackson Laboratory. By crossing male Csfr1-Cre$^{cre/+}$ with female IFT20-flox$^{flox/flox}$ mice, exon 2-3 of *IFT20,* which is flanked by loxP sites, is excised, leading to a conditional deletion of IFT20 in *Csfr1*-expressing cells.

2.3.3 Isolation and genotyping of genomic DNA from mouse tails

For genotyping, genomic deoxyribonucleic acid (DNA) was isolated from tail tips or ear clips of mice according to the following protocol: The tissue was incubated overnight at 56°C in 450 µL tail lysis buffer (Table 5) and 50 µL proteinase K (10 mg/mL, Biolab Innovative Research Technologies). Following, the dissociated tissue was pelleted for 5 min with 20,000 g at room temperature (RT). The DNA-containing supernatant was transferred into a new 1.5 mL reaction tube and mixed with 500 µL isopropanol by gentle inversion. Subsequently, the DNA was pelleted for 30 min with 20,000 g at 4°C. Afterwards, the supernatant was aspirated and the DNA pellet washed with 70% Ethanol and centrifugation for 10 min with 20,000 g at 4°C. Following aspiration of the supernatant, the pellet was dried at 37°C and resuspended in 50-100 µL Tis-EDTA (TE,Table 6) buffer.

For genotyping polymerase chain reaction (PCR) the master mix was prepared (Table 7) and the required annealing temperature and elongation time was set according to the used primer pairs (Table 8).

Table 5: Lysis buffer.

Lysis buffer in H$_2$O (pH adjusted to pH 8 at RT)
100 mM EDTA (Sigma Aldrich)
10 mM Tris/HCl (Carl Roth)
0.5 % Sodium dodecyl sulfate (SDS) (Carl Roth)

Table 6: TE buffer.

TE buffer in H$_2$O (pH adjusted to pH 8 at RT)
100 mM EDTA
10 mM Tris/HCl

Table 7: Mastermix for PCR reaction.

DreamTaq™ master mix (Thermo Scientific)	PCR mix
300 µL DreamTaq™ 10x buffer	1 µL DNA
32 µL DreamTaq™ Polymerase (5 U/µL)	1 µL of each primer (10 mM)
50 µL 100 µM dNTPs	8.3 µL DreamTaq™ master mix
868 µL H$_2$O	add to 20 µL H$_2$O

Table 8: List of PCR primer and required cycler settings.

Mouse line	PCR	Primer#	Sequence (5' to 3')	T_A (°C)	t_E (sec)
AC3-E4-flox	AC3-E4 wt	C3697	ACCCTTTGAGGCCAGGGGCAA	56	40
		C3698	CTGCGGTGAGAGCCTGGCACA		
Bbs6	Bbs6	C3503	TACAGAGGCACCTGGCTACC	62	40
		C3504	TCCTGTGGCATTATGGGTCT		
		C3505	AAATGGCGTTACTTAAGCTAGCTTGC		
Bbs8	Bbs8 wt	C3689	CCGGCAGAACAAACTGTATTGGT	57	40
		C3690	TGCTGGCATTTAATGAGGAAGCGTC		
	Bbs8 rec	C3691	CCTGGCGGAGGGAATAAAAAG	57	40
		C3692	CGTCCTTGAAGAAGATGGTGCG		
		C0099	GTGAAACAGCATTGCTGTCACTT		
Cre	Cre	C0098, C4468	GCGGTCTGGCAGTAAAAACTATC GAGATATCTTTAACCCTGATC	54	60
IFT20-flox	Ift20-flox	C3860	ACTCAGTATGCAGCCCAGGT	58	50
		C3861	GCTAGATGCTGGGCGTAAAG		
		C4468	GAGATATCTTTAACCCTGATC		
Pdgfra-Cre	Pdgfra-Cre	C4468, WAC0129	GAGATATCTTTAACCCTGATC TTTATGTTTGGCTTTTGTCATTTG	54	60
R26-tdTomato	R26-tomato int	C2458	GGCGAGGGCCGCCCC	58	45
		C2459	TTCAGGGCCTGGTGGATC		
	R26-tomato rec	C2158	GGCATTAAAGCAGCGTATCC	62	40
		C2159	CTGTTCCTGTACGGCATGG		
	R26-tomato wt	C2156	AAGGGAGCTGCAGTGGAGTA	60	40
		C2157	CCGAAAATCTGTGGGAAGTC		
R26-mT/mG	R26mT_mG	C4426	GTTATGTAACGCGGAACTCCA	60	30
		C4427	CAGGACAACGCCCACACA		
		C4428	CTTCCCTCGTGATCTGCAAC		

Int:internal, rec: recombinant, wt: wild-type

To determine the genotype based on the PCR products, DNA fragments were separated according to their size using DNA agarose gel electrophoresis and visualized under UV light via intercalating ethidium bromide. The gel (2% (v/w) agarose (GENAXXON bioscience) in 1x TAE buffer (50 mM EDTA, 1 M Tris/acetate, pH adjusted to 7.5) was dissolved by heating in a microwave, before adding ethidium bromide (AppliChem) to reach a final concentration of 1 µg/mL. After mixing the gel was poured into a gel chamber with inserted comb (Biometra). As a size standard 6 µL of GeneRuler 1 kb DNA ladder (Thermo Fisher Scientific) was loaded per lane. 1 x TAE buffer was used as running buffer. The electrophoresis was performed at 120 V for 20 min. After electrophoresis, the DNA fragments were visualized with UV light using an Agarose Gel Documentation (Vilber Lourmat).

2.3.4 Isolation of tissues

2.3.4.1 Dissection of mice

Usually, mice were anesthetized using isofluorane (Baxter). After cervical dislocation, mice were dissected to harvest different organs, like AT, liver, and blood for serum. Tissues were either subjected to further processing, like cell isolation, paraffin

embedding, and cryopreservation, or snap-frozen in liquid nitrogen and kept at - 80°C for long-term storage.

2.3.4.2   Perfusion of mice
To analyze immune cells in the AT, circulating immune cells in the blood had to be washed out of the tissue. For those experiments mice were anesthetized by intraperitoneal injection of 200 mg/kg body weight ketamine (Medistar) and 50 mg/kg body weight xylazine (Ceva). A thoracotomy of the anesthetized animal was performed and the left ventricle was cut carefully to insert a perfusion round tip gavage to the ascending aorta. Next, the right atrium was incised and the circulatory system was washed with a phosphate-buffered saline solution using a syringe, coupled by a tube to the round tip gavage until de-staining of the liver indicated that the blood was washed out. This procedure was performed by trained colleagues (Dr. Christina Klausen and Dr. Mylene Hübecker).

2.3.4.3   Cryopreservation in sucrose gradient
After dissection, the liver was fixed overnight at 4°C in 4% paraformaldehyde (PFA, Alfa Aesar) in PBS and then washed three times with PBS. For cryopreservation the liver was incubated in 10 % sucrose (in PBS, Carl Roth) for 1 h at room temperature on a shaker, followed by incubation in 30 % sucrose (in PBS) overnight at 4°C. Afterward, the liver was snap-frozen on dry ice with or without embedding in Tissue Tek (Sacura) and was kept at -80°C for long-term storage.

2.3.4.4   Cryo-sectioning of murine liver
Frozen liver samples were sliced into 16 µm sections using the cryostat (Thermo Scientific™ HM 355S Automatic Microtome Package) and mounted on Surgipath® X-tra® Microscope Slides (Leica Biosystems). This was done by the histology facility at university hospital Bonn. Sections were stored at -20°C for long-term storage.

2.3.4.5   Paraffin embedding
WAT was fixed for 24 h in 4% PFA at 4°C, before being further processed using the automated Epredia™ Excelsior™ AS Tissue Processor (Thermo Fisher Scientific™ Inc.). First, tissues were dehydrated by six incubation steps in increasing ethanol (EtOH) concentrations (70-100% at 30°C for 1 h each, UKB Pharmacy). This was followed by three steps in a clearing agent, xylene (30°C for 1 h each, AppliChem), to remove the ethanol, before incubating three times in molten paraffin wax (62°C for 80 min each, Labomedic), which infiltrates the sample and replaces the xylene. Infiltrated tissues were then casted into molds together with liquid paraffin (65°C) and cooled to form a solid paraffin block with embedded tissue (Leica EG1150 H Paraffin Embedding Station and Leica EG1150 C Cold Plate). Paraffin-embedded WAT was sliced into 5 µm sections using a Thermo Scientific™ HM 355S Automatic Microtome and mounted on Surgipath® X-tra® Microscope Slides (Leica Biosystems). To represent the whole tissue, three different tissue depths were sliced and collected.

Several 20 µm cutting steps were performed between each tissue depth. Sections were stored at room temperature.

Previously, samples were manually processed for embedding in which each step was performed for 60 min on a shaker: six incubation steps in increasing EtOH concentrations (70-100%), two steps in xylene, and two incubation steps in molten paraffin wax (Paraplast Plus, Carl Roth).

2.4   Histochemical staining

2.4.1 Hematoxylin and eosin staining

This histological staining is a combination of two dyes, hematoxylin and eosin (HE). Hematoxylin is a basic dye staining basophilic structures, primarily those containing nucleic acids like nuclei, in blue-purple, while eosin is an acidic dye staining cytoplasm and extracellular matrix in pink.

WAT sections were stained for histological analysis with Mayer′s hemalum solution (Sigma Aldrich, 1.09249) and Eosin Y solution (1% in water, Roth) using the Leica ST5020 Multistainer combined with Leica CV5030 Fully Automated Glass Coverslipper. Deparaffinization of paraffin-embedded WAT slices was performed by two heating steps (60°C for 6 min each) to melt the wax and three subsequent steps in xylene (AppliChem; 1 min each), before incubation in a graded alcohol series (100%-70% ethanol; 80 sec each) to rehydrate the tissue sections and ending with a final rinsing step in sterile distilled water (dH$_2$O) (80 sec). Next, tissue slices were stained with Mayer′s hemalum solution (3 min), before washing in running tap water (5 min). To counterstain with eosin, slides were immersed in eosin (25 sec) and then rinsed in dH2O (80 sec), before incubation on a graded alcohol series (70%-100% ethanol; 80 sec each) to dehydrate the tissue. After two final steps in xylene (60 sec each), stained slides were mounted with CV Mount (Leica Biosystems). This staining was conducted by the histology facility at University Hospital Bonn.

Liver cryosections and previous WAT paraffin sections were stained manually. Deparaffinization of paraffin-embedded WAT slices was achieved by a heating step at 60°C to melt the wax and two subsequent steps in xylene (Roth; 1 min each), before continuing with incubation in a graded alcohol series (100%-70% ethanol; 2 min each) to rehydrate the tissue sections. Liver cryosections skip these first steps and directly start with the rehydration steps. Staining with Mayer′s hemalum solution (Sigma Aldrich, MHS16) was performed for 5 min, before washing in running tap water for another 5 min. To counterstain with Eosin Y solution (Sigma Aldrich), slides were dipped 12x in eosin and then 10x in 50% EtOH, before incubation on a graded alcohol series (70%-100% ethanol; 2 min each) to dehydrate tissue again. After two final steps in xylene (1 min each) stained slides were mounted in Entellan (Merck).

Stained sections were stored at RT until imaging with either the Zeiss Axio Scan.Z1 Slide Scanner at the Microscopy Core Facility of the Medical Faculty at the University of Bonn or the Nikon Eclipse Ti microscope.

For WAT the whole tissue slice was imaged and analyzed via a custom ImageJ PlugIn AdipoQ from Jan Niklas Hansen to determine the size of each adipocyte. AdipoQ

analyzsis constitutes a two-step workflow consisting of the two ImageJ plugins AdipoQ Preparator and AdipoQ Analyzer. The AdipoQ Preparator segments the image into fore- and background and creating a mask. The AdipoQ Analyzer quantifies the produced mask and outputs various parameters: the number of individual objects (i.e., adipocytes) and the size of each object. The output files from the AdipoQ Analyzer can be readily read-in into excel or R for further post-hoc analysis (Sieckmann *et al.*, 2022). All events smaller than 350 µm^2 were considered to be too small to represent adipocytes, as described previously (Parlee *et al.*, 2014). After filtering all objects smaller than 350 µm^2 out, the average cell size and a cell size distribution could be determined. For the cell size distribution cells were sorted into different size ranges and the frequency of cells in each size range was calculated.

2.5   Isolation of stromal vascular fraction from WAT

Stromal vascular fraction (SVF) cells were harvested from murine WAT. Therefore, WAT was dissected immediately after sacrificing the mice and transferred into 2 mL ice-cold WAT buffer (PBS + 0.5% BSA) per mice. To prepare tissues for enzymatic digestion they were minced into small pieces (approx. 2 mm) and transferred into a 50 mL tube. To flush all the minced pieces the plate was washed with 1 mL WAT buffer per mice. Enzyme solution was prepared freshly each time (Table 9) and transferred to each tube containing the minced tissue in a 1:1 ratio. Incubate tissue for tissue digestion in a shaker (170 rpm, 30 min, 37°C). The digestion was stopped through adding of 6 mL cold WAT buffer, followed by pipetting the solution up and down for several times. Then, fat-enzyme solution was filtered by flowing it over a cell strainer (100 µm diameter, Corning) into a new 50 mL tube. After centrifugation (500 g, 10 min, 4°C), three phases form, with floating adipocytes on top, an intermediate phase and the pellet containing the stromal vascular fraction. Supernatant was discarded. The pellet contains the SVF. Further processing depended on the experiment.

Table 9: Enzyme solution for isolation of SVF.

Enzyme solution per mouse	Collagenase II (200 mg/mL in PBS) (Life Technologies)	PBS with 0.5% BSA (heat shock fraction) (Sigma-Aldrich) (WAT buffer)	Ca$_2$Cl (1 M)
3 mL	30 µL	2.955 mL	15 µL

2.6   Flow cytometry

Pre-adipocyte and macrophages subpopulations within the WAT were analyzed by flow cytometry using BD FACSymphony™ A5 Cell Analyzer. SVF was isolated as described earlier. For flow cytometry experiments the pellet after SVF isolation was resuspended in 50 µL FcBlock (10 min, 1:100 anti-msCD16/32 Biolegend)+2% rat serum (BioRad) in FACS buffer (PBS+0.5% BSA+2mmol/L EDTA)), before FACS buffer was added to the desired volume. The cell count was determined by diluting the cell solution 1:50 in FACS buffer, before mixing 10 µL of the cell solution 1:2 with Trypan Blue Solution (0.4%, Gibco/Life technologies) and counting cells using a Neubauer counting chamber (LO - Laboroptik Ltd).

Then, 50 µL cell suspension with 100 µL FACS buffer was plated into 96 well plate, before spinning cells down by centrifugation (500 rcf, 10 min, 4°C). Then, the plate was flipped with speed, put on paper, and turned back up. Cells were resuspended in 20 µL antibody mix (Table 3) and incubated for 30 min on ice. Then 100 µL FACS buffer was added, before spinning cells down by centrifugation (500 rcf, 10 min, 4°C). Plate flipping and antibody incubation was repeated using 100 µL second antibody mixture. After this 100 µL of FACS buffer was again added, plate was centrifugated (500 rcf, 10 min, 4°C), plate was flipped with speed, and the cells were resuspended in 100 µL FACS buffer. For flow cytometry measurements the sample was filtered with a cell strainer (70 µm diameter) right before acquisition. For addition of a live-dead stain 100 µL Hoechst 1:5000 in FACS buffer was added to the sample. If needed, cell suspension was further diluted with FACS buffer. Generally, the whole cell suspension was measured. The set-up of the machine, filter and laser settings was done by AG Mass.

2.7 Cell sorting

2.7.1 Fluorescence-Activated Cell Sorting

Pre-adipocyte subpopulations within the WAT were analyzed and sorted by FACS using BD FACS Aria Fusion. SVF was isolated as described earlier. The pellet after SVF isolation was resuspended in resuspended in erythrocyte lysis buffer (1 mL, 2 min), followed by stopping the lysis with 9 mL FACS buffer, and centrifugation (500 rcf, 10 min, 4°C) to pellet the cells down again. Then, cells were resuspended in 50 µL FcBlock (10 min), before FACS buffer (PBS+0.5% BSA+2 mmol/L EDTA) was added to the desired volume. The cell count was determined by diluting the cell solution 1:50 in FACS buffer, before mixing 10 µL of the cell solution 1:2 with Trypan Blue Solution (0.4%) and counting cells using a Neubauer counting chamber. For the antibody mix, CD34 was skipped. Otherwise, this follows the protocol for flow cytometry (2.6Flow cytometry)

The set-up of the machine, filter and laser settings was done by the Flow cytometry Core Facility of the Medical Faculty at the University of Bonn. Cells were either sorted in 1 mL medium for further cultivation of the sorted populations or in 1 mL Trizol for subsequent bulk ribonucleic acid (RNA) sequencing.

2.7.2 Magnetic-Activated Cell Sorting

Pre-adipocyte subpopulations within the WAT were analyzed and sorted by magnetic-activated cell sorting (MACS) using Streptavidin MicroBeads (Miltenyi Biotec). SVF was isolated as described earlier, but with an erythrocyte lysis step (1 mL, 2 min), followed by stopping the lysis with 9 mL FACS buffer, and centrifugation (500 rcf, 10 min, 4°C) to pellet the cells down again. Then, cells were resuspended in 2 mL

MACS buffer (=FACS buffer), followed by filtration into a new falcon through a cell strainer (40 µm diameter).

MACS procedure was done by a series of two separations based on different steps of biotin-labeled antibody stainings (Table 4: List of antibodies used for MACS.). First, depletion of lineage^{+} cells (CD31, CD45, and TER119) and secondly, a positive selection of P1 (CD55 and CD26) or P2 (VAP1 and CD54) cells. Procedure followed the manufacturer's instructions using MACS column (MS) and the magnetic QuadroMACS™ Separator (Miltenyi Biotec). All antibody incubation steps were performed for 30 min on ice and the optional step with anti-biotin-fluorochrome was skipped. The cell fractions of interest were centrifugates (500 rcf, 10 min, 4°C) and the cells were resuspended in medium and plated for further cultivation.

2.8 Cell culture

2.8.1 Maintenance of primary cells

To transfer isolated SVF into cell culture, the SVF cell pellet was resuspended in erythrocyte lysis buffer (1 mL, 2 min, Biolegend). Lysis was stopped by addition of 9 mL WAT buffer, followed by a filtration into a new falcon through a cell strainer (40 µm diameter). After a final centrifugation step (500 rcf, 10 min, 4°C) the pellet was resuspended in 2 mL growth medium (GM) (Table 10). The cell count was determined by diluting 10 µL of the cell solution 1:2 with Trypan Blue Solution (0.4%) and counting cells using a Neubauer counting chamber. Cells were then pre-cultured on 60 mm plates, with the aim of getting rid of dying cells, which did not survive the isolation process to later ensure a more even seeding of SVF cells.

Cells were incubated at 37°C with 5% CO_2 in GM for 24 h, before washing cell debris and dead cells with GM. Half of the medium was changed every two days and cells were grown up to max 80% confluency, before seeding for an experiment.

Table 10: Cultivation medium for SVF.

Adipocyte culture medium	DMEM/Ham's F-12 (1:1) (1x) + GlutaMAX™-I	10% Fetal Bovine Serum (FCS) (BIOCHROM)	1% Pen/Strep (Gibco)
Growth medium	Adipocyte culture medium	33 µM Biotin (Sigma Aldrich)	17 µM D-Pantothenic acid (D-PA) (Sigma Aldrich)

DMEM: Dulbecco's Modified Eagle's Medium (Gibco/Life Technologies); FCS: fetal calf serum; Pen Strep: Penicillin Streptomycin

For subsequent experiments, cells were seeded at a high cell density of $1.32*10^5$ cells/cm^2 to ensure direct confluency in 24 h. To this end, cells were washed with PBS, before inducing detachment by incubation with Trypsin-EDTA (0.05%, Gibco/Life Technologies) for 5 min. The digestion was stopped with at least 3x volume of GM. After cell count determination, cells were further diluted with GM to the desired cell density for subsequent seeding.

2.8.2 Induction of adipogenesis

For adipogenesis analysis, the SVF was seeded onto CellCarrier Ultra 96-well plates (PerkinElmer). The following day adipogenesis was induced by exchanging the medium with an induction cocktail. Full induction cocktail contained 5 µg/mL insulin (Sigma), 1 µM Dexamethasone (Sigma-Aldrich), 100 µM 3-isobutyl-1-methylxanthine (IBMX; Sigma-Aldrich), and 1 µM rosiglitazone (Sigma-Aldrich). In contrast, the concentrations of supplements were lower in the reduced induction cocktail, which contained 0.4 µg/mL insulin, 0.1 µM Dexamethasone, 20 µM IBMX, and rosiglitazone was omitted completely. To activate the FFAR4 pro-adipogenic signaling pathway the reduced induction cocktail was supplemented either with 100 mM docosahexaenoic (DHA) (Sigma), as the natural ligand, or with 100 mM TUG891 (Tocris), as a pharmacological agonist. After 3 days of induction, media was exchanged by aspirating approx. 3/4 of the volume, and adding freshly prepared maintenance medium containing 1 µg/mL insulin. Maintenance medium was changed every other day. Additionally, as a negative control, undifferentiated cells were kept, which were cultured only in GM. After a total of 7 days of culturing, cells were fixed with 4% paraformaldehyde (PFA, 16% w/v aq. Soln., methanol free, Alfa Aesa) for 10 min and subsequently washed thrice with PBS. Then, the fixed cells were stained with 4',6-Diamidin-2-phenylindol (DAPI, 1:10,000, Life Technologies) and 0.5 µg/mL LD540 in PBS for 15 min. Cells were washed thrice with PBS. The CellDiscoverer7 (Zeiss) was used for automated image acquisition at 10x magnification. Of every well, four images were taken, each in a z-stack. Analysis of images was performed with ImageJ using the PlugIn AdipoQ Preparator and AdipoQ Analyzer (Sieckmann *et al.*, 2022)(in revision). Briefly, the color channels (DAPI and LD540) were splitted to determine a custom threshold for the analysis. A custom threshold was necessary, because of autofluorescence of the lipids occurring in the DAPI channel and due to a problem with the available threshold algorithms, when analyzing an image without positive signal, as in the undifferentiated controls. Here, the algorithms will adjust the threshold per image based on the highest signal to be able to detect something. This led to very different thresholds between conditions and to falsely positive signals in the undifferentiated cells. To overcome this limitation, LD540 threshold was calculated based on the average intensity of the undifferentiated wells and the standard deviation (SD). Threshold was set as mean intensity ± 1-5 SD after checking back on images with positive signals. For DAPI a similar approach was selected, but the mean intensity was not calculated for the full images, but only for areas with background signal induced by lipid droplets. Therefore, images with strong differentiation were used. The calculated threshold could then be set during AdipoQ analysis to detect positive signal and the total area of the positive signal above the threshold was quantified. The level of adipogenesis, expressed as the adipogenic index, was assessed by dividing the total LD540 area by the total DAPI area.

For oil-red-o quantification and analysis of the inhibitory effect of Hedgehog (Hh) signaling, SVF was seeded on Greiner 24 well instead and stayed confluent for 2 days before inducing adipogenesis with the full induction cocktail (see above). Hh signaling was activated by 2 µM purmorphamine (P) (Tocris), as a pharmacological agonist of

SMO. Adipogenesis was maintained by 1 µM rosiglitazone instead of 1 µg/mL insulin for another 7 days. Then, cells were fixed with 10% PFA (16% w/v ag. Soln., methanol free, Alfa Aesa) for 1 h and subsequently washed thrice with PBS. Before staining, fixed cells were washed twice with ddH$_2$O, once for 5 min with 60% isopropanol and then with 1-(2,5-dimethyl-4-(2,5-dimethylphenyl) phenyldiazenyl) azonapthalen-2-ol (Oil-Red-O) for 20 min. The working solution was freshly prepared from the stock solution (5 mg/mL in 2-propanol (isopropanol)) by diluting 37.5 mL of the stock solution with 50 mL ddH$_2$O, letting it stand for 1 h, before filtering the working solution just before the staining to avoid any precipitates. Wells were completely filled. After the staining, wells were washed 2-5x with H$_2$O. These steps had to be done with care and without ever completely emptying the wells, as floating staining precipitates otherwise touch and stick to the cells. Overfilling the wells with H$_2$O helped flushing these precipitates off. To reduce unspecific staining wells were additionally washed thrice with 60% isopropanol for 5 min. Residual staining could then be quantified by eluting the dye in a minimal volume of 250 µL isopropanol on a shaker (10 min). The absorbance could then be measured by photometric analysis. To this end, 200 µL of the eluate was transferred to a 96-well plate and the absorbance was measured at 570 nm (FLUOstar® Omega).

2.8.3 *Ex vivo* cultivation of explants

To follow postnatal adipose tissue development, pre-gWAT of male mice on P4 was dissected and separated from the testis, epididymis, and vas deferens. To allow attachment of the tissue sample to the surface of the well, the explants were placed in the middle of the well of a 24-well plate in a low volume of cultivation medium (150-200 µL) (Table 11) for at least 24 h. Subsequently, medium was added to get a total volume of approximately 1 mL and explants were cultivated for 14 days in total (Cox *et al.*, 2021). A medium change (exchange ¾ of the medium) was done on day 7/8. After 14 days of cultivation, explants were fixed in 10% PFA for 1 h and washed thrice with PBS in preparation for Oil Red O staining.

Table 11: Cultivation medium for explants.

Explant culture medium	Gibco™ RPMI 1640 Medium, no phenol red	10% FCS	1% Pen/Strep

2.9 Immunocytochemistry

Immunocytochemistry (ICC) was conducted using a combination of different primary (Table 1) and secondary antibodies (Table 2). For convenience, cells were grown on coverslips (12 mm, VWR) pre-coated with poly-L-lysine (PLL, Sigma Aldrich) to allow adhesion of the cells. PLL coating was performed under sterile condition by incubating the coverslips in 0.1 mg/mL PLL for at least 30 min at room temperature (RT). After cultivation, the cells were washed once with PBS and fixed for 10 min with 4% PFA (16% w/v aq. soln., methanol free, Alfa Aesar) in PBS at RT. After three washing steps with PBS, the cells were blocked for 30 min at RT with CT blocking solution (CT, Chemieblocker (Merck Millipore) 1:20 in PBS + 0.5% Triton-X100 (Sigma-Aldrich)).

Thereafter, cells were incubated for 1 h at RT with primary antibodies diluted in CT. After the incubation time, cells were washed thrice with PBS and incubated again for 1 h at RT in the dark with fluorophore-conjugated secondary antibodies diluted in CT with DAPI (1:10,000, Life Technologies). Afterward, cells were washed thrice with PBS, and coverslips were mounted with Aqua-Poly/Mount (Polysciences, Inc.) for imaging. At least 12 after mounting, fluorescence images were acquired with Olympus FV1000, Nikon eclipse Ti, Leica SP5, or Leica SP8 with Lightning confocal laser scanning microscope, using the 60x/63x objectives if not otherwise noted. For imaging of cilia, confocal z-stacks (step size 0.5 µm, 60x objective) were performed. Images are shown as maximal projection, if not otherwise noted.

For stimulation with smoothened agonist (SAG) (Sigma Aldrich) cells were treated with 1 µM SAG for 48 h before fixation.

2.10 Whole mount staining

Small dissected tissue sample were washed with PBS and then fixated with 1% PFA in PBS for 30 min at RT. Then, sample was washed thrice with PBS, followed by 3x incubation in PBS + 1% TritonX-100 for 10 min each. Tissue was blocked for 1 h in PBS + 10% FCS + 1% TritonX-100 (blocking buffer), before incubation with primary antibodies (Table 1) in the blocking buffer overnight (ON) (4°C, shaking). Afterwards, tissues were washed intensively, first, in PBS + 10% FCS + 1% TritonX-100 (3x, 20 min each) and secondly, in PBS + 1% TritonX-100 (3x, 10 min each). Secondary antibodies (Table 2) with DAPI (1:10.000) in blocking buffer were incubate with the tissue for 5 h, before washing with PBS + 1% TritonX-100 (3x, 5 min each) and lastly with PBS. Stained tissues were mounted with Aqua-Poly/Mount. If necessary due to the 3D size of the tissue slides with depressions were used (Marienfeld Superior™ 1320202).

2.11 Assessment of the metabolic state of mice

2.11.1 Glucose tolerance test

Glucose tolerance test (GTT) is a method to detect the ability of the body to utilize glucose in circulation. It is a diagnostic aid in the diagnosis of diabetes mellitus, insulin resistance, and other glucose handling affecting diseases. To assess the effect of diet- or genotype-induced obesity on glucose handling, mice were subjected twice to a GTT, once at a pre-obese timepoint (approximately 9-10 wks of age) and once at an obese timepoint (approximately 17-19 wks of age). To measure glucose handling, mice were fasted for 6 hours before an intraperitoneal (i.p.) injection of glucose with sterile 50% glucose solution (2 g/kg body weight, Fresenius Kabi), and blood glucose levels were measured with a blood glucose meter (OneTouch Verio Flex®) and tests trips (OneTouch® Verio) over several time points (0, 15, 30, 60, and 90 min). The repeated blood samples were taken from an incision of the tail. To determine and reduce stress-related fluctuations a control injection with 0.9% NaCl (Fresenius Kabi) was performed first and exactly as the GTT, but additionally, mice had to be fixated to perform the incision of the tails. During GTT the fixation of the mice was foregone to reduce stress,

as the incision wound of the tail could be carefully reopened even after 3 days in between procedures.

Control injections indicate a slight tendency towards a rise in blood glucose levels, possibly due to stress. Some mice failed to respond to GTT, possibly due to stress or misplaced injections into unwanted areas, such as the intestine, leading to a delay in glucose levels entering the blood. This affects the outcome of the GTT and confuses the interpretation of the results. Therefore, I applied a threshold to distinguish between responding and non-responding mice. I selected the control condition (WT mice on CD) to calculate a threshold as 20% of the highest blood glucose level at the important determining timepoints 15 and 30 min after injection. Since, this threshold was dependent on the responsiveness of the control animals, low animal numbers might decrease the change of having at least one nicely responding animal for a decent threshold.

2.11.2 Insulin tolerance tests

Insulin tolerance test (ITT) is a method to determine the whole-body sensitivity of insulin. It is a standard test to assess the insulin resistance status. To assess the effect of diet- or genotype-induced obesity on insulin resistance, mice were subjected twice to ITT, as previously described for GTT (Punkt), but with i.p. injection of human insulin (0,75 U/kg body weight, Sigma) diluted in 0.9% NaCl (Fresenius Kabi).

Some mice failed to respond to ITT, mostly due to stress or misplaced injections into unwanted areas, such as the intestine, leading to a delay in glucose levels entering the blood. This affects the outcome of the ITT and confuses the interpretation of the results. Therefore, I applied a threshold to distinguish between responding and non-responding mice. I selected the control condition (WT mice on CD) to calculate a threshold as 20% of the strongest drop in blood glucose level at the important determining timepoints 15 and 30 min after injection. Since, this threshold was dependent on the responsiveness of the control animals, low animal numbers might decrease the change of having at least one nicely responding animal for a decent threshold.

2.12 Measuring weight gain and food intake

To assess weight gain and food intake before and during obesity development, mice were single housed and a given amount of food (10-12 g/d) was provided during food intake measurements. For one week at the beginning (age 8-9 wks) and later six wks during obesity development (age 11-17 wks), food intake and mouse weight were measured daily at the same time (9-10 am).

2.13 Software applications

2.13.1 Software

Table 12: List of utilized software.

Software	Version
Affinity Designer	Version 1.10.4
Biorender	Biorender.com
EndNote X9	Version X9.3.3
Fiji/ImageJ	Version 2.3.0/1.53f
FlowJo for MacOS	Version 10.6.2
GraphPad Prism 9 for MacOS	Version 9.3.0
Microsoft® Excel for Mac	Version 16.58
Microsoft® Powerpoint for Mac	Version 16.58
Microsoft® Word for Mac	Version 16.58
QuPath for MacOS	Version 0.2.3
RStudio for MacOS	Version 1.2.5042

2.13.2 PlugINs

Table 13: List of utilized ImageJ PlugIns.

ImageJ PlugIn	Author	Comment
AdipoQ Analyzer	HansenJN (Sieckmann *et al.*, 2022)(in revision)	Available on: https://github.com
AdipoQ Preparator	HansenJN (Sieckmann *et al.*, 2022)(in revision)	Available on: https://github.com
CiliaQ	HansenJN (Hansen *et al.*, 2021)	Available on: https://github.com
CiliaQ_Preparator	HansenJN (Hansen *et al.*, 2021)	Available on: https://github.com
ExtractSharpestPlane	HansenJN	Available on: https://github.com

Table 14: List of utilized FlowJo PlugIns.

FlowJo PlugIn	Author (Algorithm/PlugIn)	Comment
CytoNorm	Sofie Van Gassen/Ian Taylor, Matt Swindle	Version 1.2.3
DownSample	Richard Halpert	Version 3.3

2.13.3 R-scripts

Custom-made R scripts for the analysis of adipogenesis (from Katharina Sieckmann) and AT histology after ImageJ based image analysis

Custom-made R script for the analysis and visualization of flow cytometry data kindly provided by the group of Elvira Mass.

2.14 Statistics

Statistics were performed using GraphPad Prism 9. Data represent mean values with standard deviation (± S.D.) from independent experiments (n numbers are indicated) if not stated otherwise. Statistical significances and performed tests are depicted in the respective figures and legends.

3. Results

3.1   Mouse lines

My hypothesis is that ciliary signaling in pre-adipocytes is important for white adipose tissue (WAT) function and homeostasis and that, in turn, primary cilia dysfunction disturbs WAT development and function. To test this hypothesis, I used two global *Bbs*-knockout (KO) mouse models: Bbs8$^{-/-}$ (Tadenev *et al.*, 2011) and Bbs6$^{-/-}$ (Ross *et al.*, 2005) mice. BBS is caused by ciliary dysfunction and one mayor phenotype is obesity. Interestingly, the WAT phenotype in obese *Bbs12$^{-/-}$* mice has been shown to be averse to other obesity mouse model, such as the leptin-deficient *ob/ob* mice (Marion *et al.*, 2012). Bbs8 is a core BBSome component (Nachury *et al.*, 2007), whereas Bbs6, like Bbs12, localizes to the chaperonin complex (Seo *et al.*, 2010). I decided to use both Bbs6 and Bbs8 knockout mice, aiming to unravel whether these two different proteins, and thereby different BBS components, fulfill different roles in regulating primary cilia function.

BBS alters the ciliary protein localization, especially the localization of G-protein coupled receptors (GPCRs), which couple to G_{ai} oder G_{as} and, thereby, signal via adenylyl cyclase (AC) and 3', 5'-cyclic adenosine monophosphate (cAMP) signaling (Hilgendorf *et al.*, 2016; Wachten and Mick, 2021). Thus, BBS is supposed to alter ciliary cAMP signaling. Interestingly, loss-of-function mutations in the *Adcy3* gene, encoding for AC3 have been shown to cause monogenic severe obesity in humans and mice (Grarup *et al.*, 2018; Saeed *et al.*, 2018). Additionally, AC3 is highly enriched in primary cilia of neurons throughout the brain (Berbari *et al.*, 2007; Bishop *et al.*, 2007) and has also been detected in other ciliated cell types, i.e., in cilia of cells derived from the mesenchymal stem cell lineage (Antal *et al.*, 2017), which also include adipocyte progenitors. To examine whether AC3-dependent cAMP signaling plays a role in ciliated pre-adipocytes, I analyzed the ciliary AC3 localization using immunocytochemistry by co-staining either with anti-ADP ribosylation factor like GTPase 13b (ARL13B) or anti-acetylated α-tubulin (ac. α-TUB) antibody, which both label primary cilia (Caspary *et al.*, 2007; LeDizet and Piperno, 1991). To this end, I first used pre-mature gWAT isolated from mice at postnatal day 4 (P4), as this predominantly contains pre-adipocytes, and stained for cilia and AC3. Cells in WAT precursor tissue displayed primary cilia, which were AC3$^+$ (Figure 5A). Of note, this staining protocol did not allow to distinguish between different ciliated cell types in the precursor WAT. Thus, I isolated the stromal vascular fraction (SVF) from WAT and co-stained the cells with a C/EBPβ antibody, a marker for pre-adipocytes (Chapter 3.9.2) and revealed that C/EBPβ$^+$ cells within the SVF displayed almost exclusive AC3 localization in primary cilia (Figure 5B).
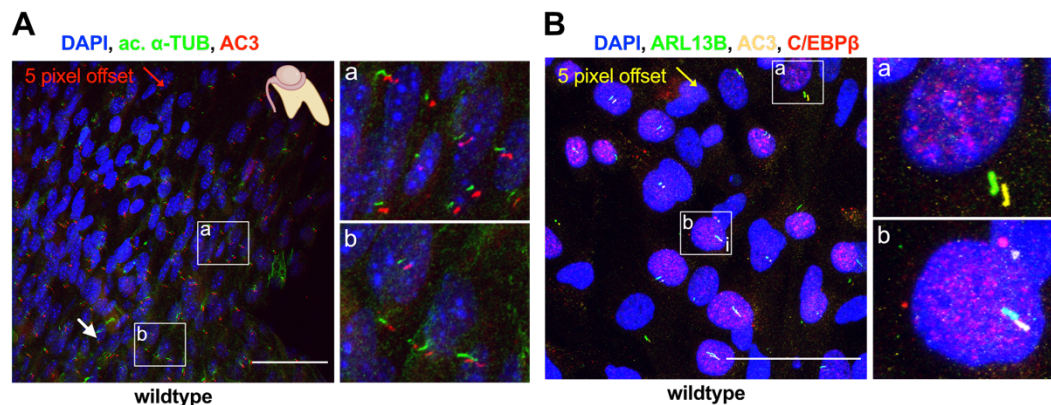
Figure 5: AC3 is localized to primary cilia in pre-adipocytes. (A) WAT precursor tissue contains ciliated cells, which contain AC3 in the cilium. Representative images of gWAT precursor tissue isolated at postnatal day 4 (P4), stained with DAPI (blue, DNA) as well as with an anti-acetylated α-tubulin (green, cilia) and an anti-AC3 (red) antibody. White squares (a, b) indicate zoomed in areas shown on the right. The red channel has been shifted by 5 pixels. Scale bar: 50 µm. **(B)** Representative images of AC3 localization in primary cilia of pre-adipocytes. The stromal vascular fraction (SVF) has been isolated from 15 weeks old wild-type mice and stained with DAPI (blue, DNA) as well as with an anti-ARL13B (green, cilia), an anti-C/EBPβ (red, pre-adipocytes), and an anti-AC3 (yellow) antibody. White squares (a, b) indicate zoomed in areas shown on the right. Yellow channel was pixel shifted by 5 pixels. Scale bar: 50 µm.

Based on these results, I decided to generate conditional AC3 knockout mice, lacking AC3 in adipocyte progenitors to unravel the role of ciliary cAMP signaling in regulating primary cilia function and its contribution to the BBS obesity phenotype. Additionally, I also aimed to investigate the role of primary cilia per se in controlling pre-adipocyte function and generated another conditional knockout mouse line lacking cilia.

3.1.1 Generation of cre-driven conditional knock-out mouse lines

A cre-recombinase expressed under a cell-type-specific promotor can be used to induce excision of the gene-of-interest flanked by loxP sites (Nagy, 2000; Sauer, 1987). To target pre-adipocytes, I used a mouse line that expresses the cre-recombinase under the platelet-derived growth factor receptor α (*Pdgfra*) promotor. First, I tested whether this approach indeed targets pre-adipocytes. To this end, I used two reporter mice, the R26-tdTomato (Madisen *et al.*, 2010) and the R26-mT/mG mouse line (Muzumdar *et al.*, 2007). In these reporter mice, the expression cassette was inserted into the *Gt(ROSA)26Sor* locus on chromosome 6 (R26) to provide constitutive and ubiquitous gene expression (Madisen *et al.*, 2010). When crossing R26-tdTomato mice with heterozygous Pdgfra-cre (Pdgfra^cre/+) mice, the cell type-specific cre-recombinase deletes the stop cassette (Figure 6A) and promotes the expression of the gene encoding for tdTomato in *Pdgfra* expressing cells. I isolated the stromal vascular fraction (SVF) containing ciliated pre-adipocytes from gonadal white adipose tissue (gWAT) of Pdgfra^cre/+ R26-tdTomato^tg/+ and Pdgfra^+/+ R26-tdTomato^tg/+ (control) mice and compared reporter gene expression. The SVF from Pdgfra^cre/+ R26-tdTomato^tg/+ mice showed tdTomato staining in the majority of cells, most of them also being ciliated (Figure 6B), demonstrating that cells of the SVF have been successfully targeted. But not all cells in the SVF are pre-adipocytes and reliable pre-adipocytes markers are so far lacking (Berry *et al.*, 2015; Cawthorn *et al.*, 2012). To ensure that I

target pre-adipocytes, which differentiate into mature adipocytes, I also analyzed WAT from Pdgfra$^{cre/+}$ R26-mT/mG$^{tg/+}$ mice. In Pdgfra$^{cre/+}$ R26-mT/mG$^{tg/+}$ mice, the cell type-specific cre-recombinase deletes the membrane-targeted tandem dimer Tomato (mT) expression cassette (Figure 6C), thereby, promoting production of membrane-localized EGFP (mG). Hence, targeted cells are labeled by mG, while non-targeted cells are labeled by mT. In comparison to control mice (Pdgfra$^{+/+}$ R26-mT/mG$^{tg/+}$), the WAT from Pdgfra$^{cre/+}$ R26-mT/mG$^{tg/+}$ mice showed mG fluorescence in mature adipocytes (Figure 6D). Mature adipocytes can be identified by the presence of a big lipid droplet, which pushes the nucleus and all the cytoplasm to the edge of the cell. Thus, I confirmed that targeted cells differentiate into mature adipocytes. Other cell types, intercalated between the mature adipocytes, produced mT (Figure 6D), demonstrating that Pdgfra$^{cre/+}$ mice allow to target pre-adipocytes, in line with previous reports (Berry and Rodeheffer, 2013; Krueger *et al.*, 2014).
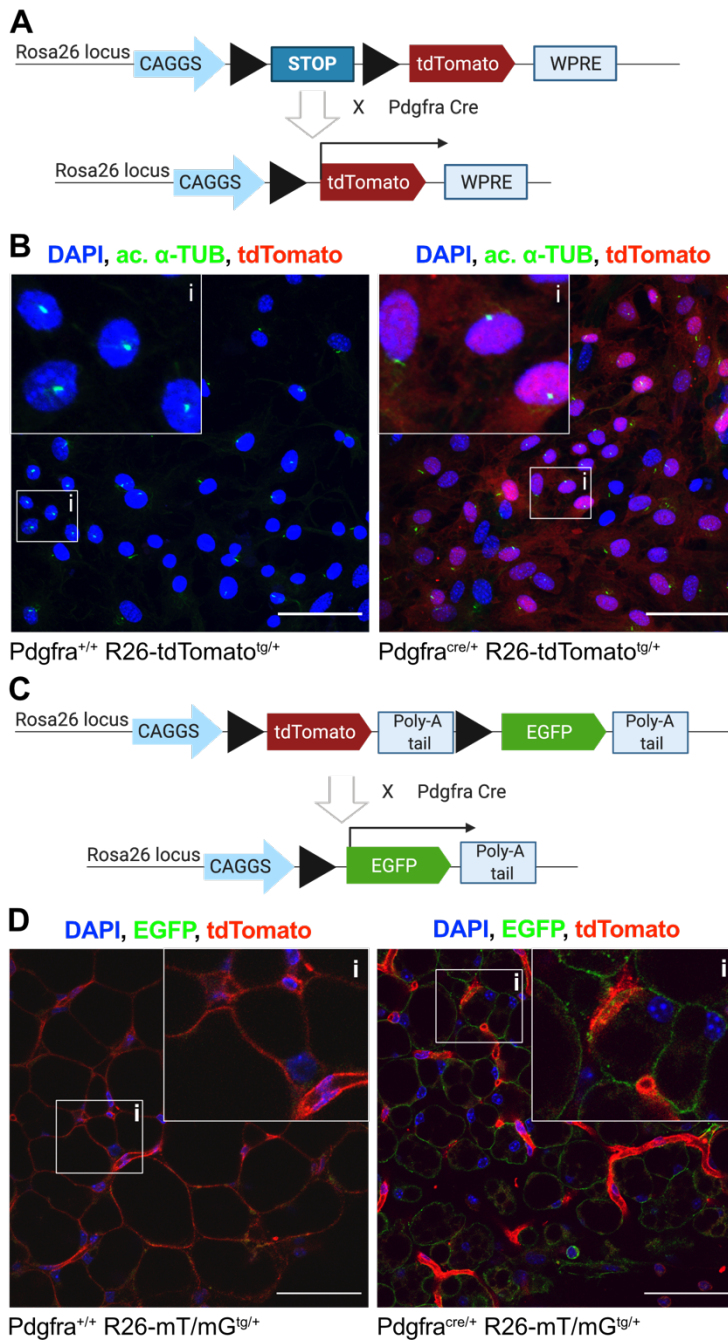
Figure 6: Verification of targeting approach in cre-recombinase-driven, conditional knockout in *Pdgfra* expressing cells. (A) Schematic representation of the tdTomato-reporter system, expressing dtTomato in *Pdgfra* expressing cells. **(B)** Adipose tissue-derived stromal vascular fraction expressing tdTomato (red) stained with DAPI (blue, DNA) and an anti-acetylated α-tubulin (ac. α-TUB) antibody (green) to label primary cilia. **(C)** Schematic representation of Pdgfra$^{cre/+}$ R26-mT/mG switch reporter system, expressing membrane-localized tdTomato (mT), which switches to a membrane-localized EGFP (mG) in *Pdgfra* expressing cells. **(D)** Adipose tissue (AT) from Pdgfra$^{cre/+}$ R26-mT/mG$^{tg/+}$ mouse shows successful targeting of adipocytes (green) and non-targeted cells (red). Scale bars: 50 µm.

After validation of my targeting approach, I generated two different conditional knock-out mouse lines by either knocking out *Ift20* (Figure 7A) or *Adcy3* (Figure 6A) in pre-adipocytes. To this end, IFT20-flox$^{flox/flox}$ (Ift20$^{f/f}$) or AC3-E4-flox$^{flox/flox}$ (Ac3$^{f/f}$) mice were crossed with Pdgfra$^{cre/+}$ mice.

Ift20 encodes for a protein essential for ciliary assembly, and its loss abolishes primary cilia formation (Jonassen *et al.*, 2008). I performed immunochemistry staining of SVF isolated from Pdgfra$^{cre/+}$ Ift20$^{f/f}$ and Pdgfra$^{+/+}$ Ift20$^{f/f}$ mice to verify cilia loss in pre-adipocytes using two different ciliary marker antibodies. In Pdgfra$^{+/+}$ Ift20$^{f/f}$ cells, both antibodies co-stained primary cilia, as evident by a 5-pixel offset of the ARL13B channel (Figure 7B). In contrast, no labeled primary cilia were observed in Pdgfra$^{cre/+}$ Ift20$^{f/f}$ cells. Ac. α-TUB is also found in the cytoskeleton in the body, as observed in the

Pdgfra^{cre/+} Ift20^{f/f} cells, demonstrating that the antibody staining was successful and cilia were not present (Figure 7B). I quantified primary cilia loss by counting the number of cilia and normalizing it to the number of cells, indicated by 4',6- diamidino-2-phenylindole, dihydrochloride (DAPI)-positive nuclei: 67 % of the cells were ciliated in Pdgfra$^{+/+}$ Ift20$^{f/f}$ cells, whereas, only 2 % of the cells were ciliated in Pdgfra$^{cre/+}$ Ift20$^{f/f}$ cells (Figure 7C).
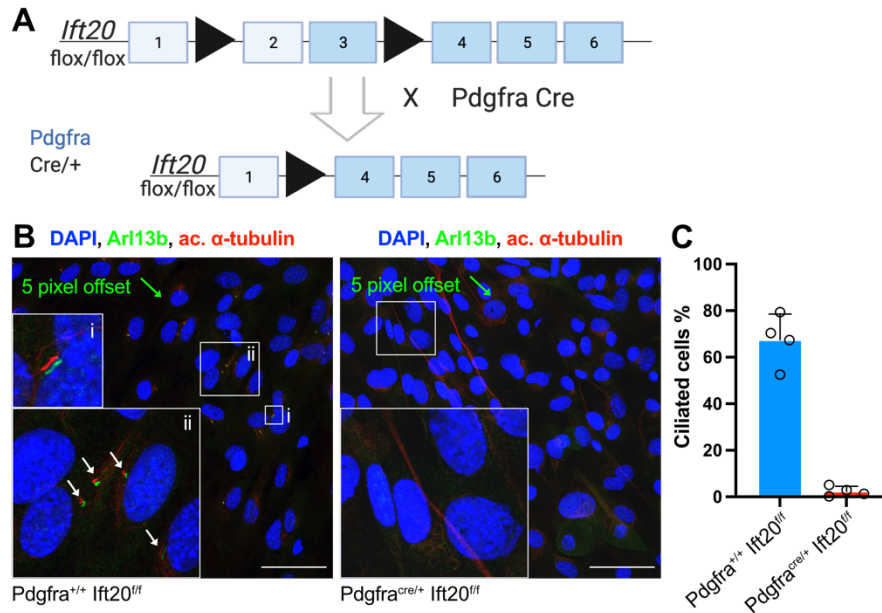
Figure 7: Verification of *Ift20* deletion in cre-recombinase driven, conditional knockout mouse line, causing cilia ablation. (A) Schematic representation of *Ift20* deletion in Pdgfra expressing cells, resulting in adipose tissue precursor cells lacking primary cilia. **(B)** Immuno-chemistry staining of AT-SVF with DAPI (blue, DNA) and with anti-ARL13B (green) and anti-ac. α -TUB antibody (red) to label primary cilia. Green channel is pixel-shifted by 5 pixels. Scale bars: 50 μm. **(C)** Quantification of ciliated cells based on the counted number of cilia per total count of nuclei. Data are shown as mean ± S.D. and with individual data points, n = 4.

A global knockout of AC3, encoded by *Adcy3,* has been shown to cause hyperphagia, resulting in obesity (Wang *et al.*, 2009b), linking AC3 and ciliary cAMP signaling defects to obesity. I generated a conditional knockout mouse line lacking AC3 in *Pdgfra*-expressing cells (Figure 8A) to separate the effect of AC3 loss in neurons, resulting in hyperphagia and, in turn, obesity (Cao *et al.*, 2016; Wang *et al.*, 2009b) from the role of AC3 in pre-adipocytes. I labeled cells from the SVF, isolated from Pdgfra$^{cre/+}$ Ac3$^{f/f}$ and Pdgfra$^{+/+}$ Ac3$^{f/f}$ mice, with an anti-AC3 antibody to first verify loss of AC3 in primary cilia of pre-adipocytes. In Pdgfra$^{+/+}$ Ac3$^{f/f}$ cells, AC3 localized to primary cilia (Figure 8B), whereas in Pdgfra$^{cre/+}$ Ac3$^{f/f}$ cells, AC3 was absent from primary cilia (Figure 8C). I quantified the ciliary localization of AC3 using the ImageJ plugin CiliaQ (Hansen *et al.*, 2021). In this analysis, cilia were reconstructed using the ciliary marker and signal intensity of AC3 was determined within the cilia. The results showed that AC3 intensity in Pdgfra$^{+/+}$ Ac3$^{f/f}$ cells was significantly higher compared to Pdgfra$^{cre/+}$ Ac3$^{f/f}$ cells (Figure 8D).

In summary, I could verify both conditional knock-out mouse lines.
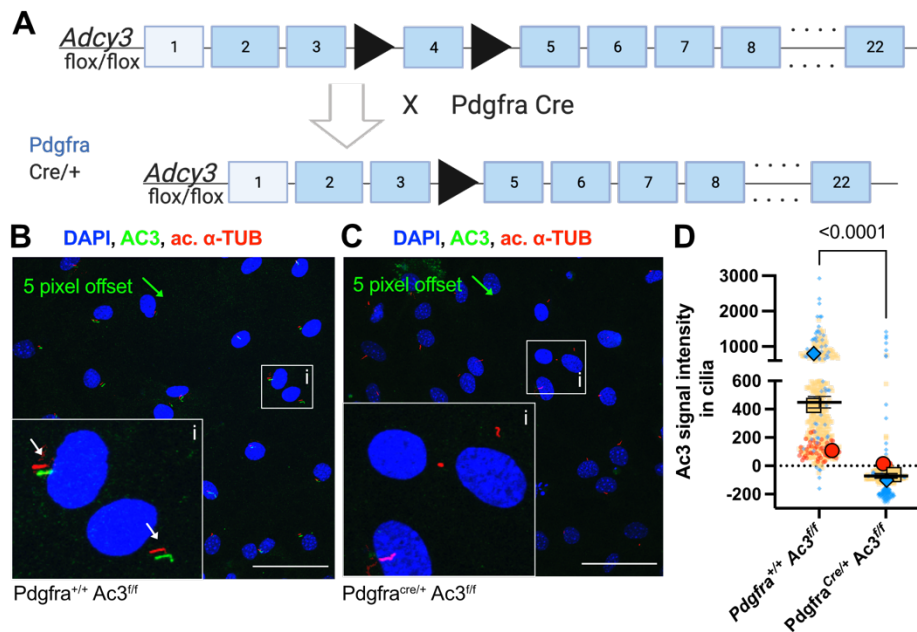
Figure 8: Verification of *Adcy3* deletion in Pdgfra-Ac3, a cre-recombinase driven, conditional knockout mouse line. (A) Schematic representation of *Adcy3* deletion in Pdgfra expressing cells, resulting in adipose tissue precursor cells lacking Ac3. **(B)** AC3 localization in primary cilia of pre-adipocytes. Immunochemistry staining of AT-derived SVF with DAPI (blue, DNA), with anti-AC3 (green), and with anti-acetylated α -tubulin antibody (red) to label primary cilia. Green channel is pixel-shifted by 5 pixels. **(C)** Verification of AC3 KO in primary cilia of pre-adipocytes. AT-derived SVF from Pdgfra[cre/+] Ac3[f/f] stained with DAPI (blue, DNA), with anti-acetylated α -tubulin (red) to label primary cilia and with anti-AC3 antibody(green). Green channel is pixel-shifted by 5 pixels. Scale bars: 50 µm. **(D)** Quantification of background-corrected Ac3 fluorescence intensity in cilia of cells from the SVF of Pdgfra-Ac3 mice using CiliaQ an ImageJ plugin. Cilia are reconstructed in the cilia channel (red) by a Flood-Filler algorithm detecting objects above an automated intensity threshold (Hansen). For background correction, the background intensity threshold is subtracted from AC3 cilia signal intensities. The background intensity threshold is calculated as the mean of 10% highest intensity voxels of background and is set as baseline for unspecific signals, represented as dotted line. Data are shown as mean ± 95 % confidence interval (CI) and with colored individual values and means representing different n-number, p-values were calculated by Mann-Whitney test, n = 3, including at least 27 cilia per experiment.

3.2 Obesity development in ciliopathy models

Then, I first studied the impact of primary cilia dysfunction on WAT remodeling and pathology *in vivo* by analyzing obesity development. As obesity is a major hallmark of BBS, I used the two global *Bbs*-KO mouse models and the conditional Pdgfra-Ac3 mouse line (Chapter 3.1.1). Of note, I will discuss the phenotype of the Pdgfra-Ift20 mouse line in more detail later (Chapter 3.11). With my analyses, I aimed to determine the onset as well as the severity of obesity.

3.2.1 Body and adipose tissue weight gain during aging

First, body weight was measured every two weeks (wks) until the age of 30 wks to decide which timepoints to analyze in more detail for obesity characterization.
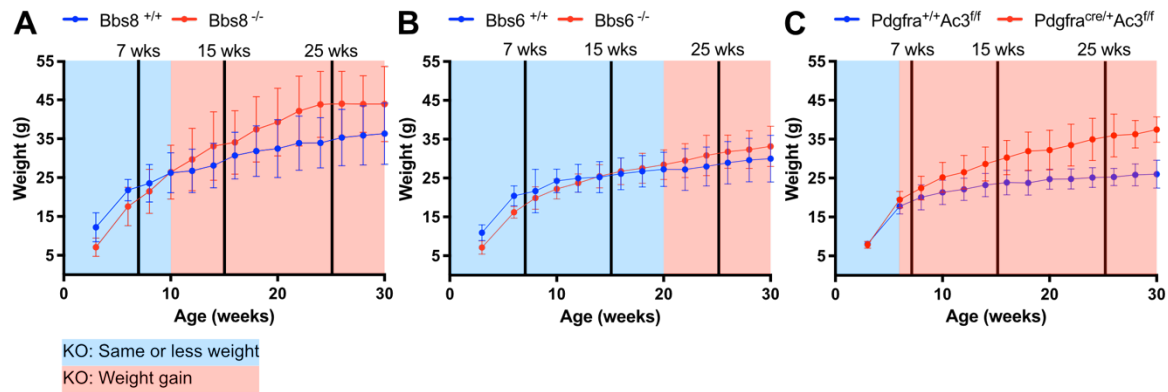
Figure 9: Body weight curves during aging in different ciliopathy models reveal distinct obesity development. (A-C) Body weight was measured every two weeks until the age of 30 wks in Bbs8 **(A)**, Bbs6 **(B)**, and Pdgfra-Ac3 **(C)** mice. Three timepoints were selected for detailed analysis. Data are shown as mean ± S.D., n ≥ 9.

Bbs-KO mice displayed a reduced body weight until the age of 10 wks compared to WT littermates, indicating a runted phenotype in the early, postnatal phase (Figure 9). Additionally, comparison of the body weight indicated differences in onset of obesity: while Bbs8$^{-/-}$ and Pdgfra$^{cre/+}$ Ac3$^{f/f}$ mice started to weigh more than their WT littermates at 10 or 6 wks of age, respectively, Bbs6$^{-/-}$ mice became obese at 20 wks (Figure 9). Also, the relative difference in body weight to control mice was less pronounced in Bbs6$^{-/-}$ than in Bbs8$^{-/-}$ or Pdgfra$^{cre/+}$ Ac3$^{f/f}$ animals (Figure 9), already indicating different roles for Bbs6 and Bbs8 in controlling primary cilia function and, thereby, obesity development. In summary, Pdgfra$^{cre/+}$ Ac3$^{f/f}$ mice resemble the Bbs8$^{-/-}$ phenotype, whereas the weight gain Bbs6$^{-/-}$ is less severe.

To cover different time points during obesity development for a detailed evaluation, I chose the following timepoints: 7 wks as an early pre-obese timepoint for all mouse lines, 15 wks as a weight gaining phase (obese) at least in Bbs8 and Pdgfra-Ac3 mouse lines, and 25 wks as a late obese timepoint, which would also reflect an obese time point in Bbs6$^{-/-}$ mice. In addition, I decided to examine one even later timepoint of 40 ± 10 wks in Bbs6$^{-/-}$ mice only, as obesity seems to develop much later.

First, I determined the body weight and the weight of different AT depots at the defined time points. The following AT depots were examined: subcutaneous inguinal WAT (iWAT), visceral gonadal- and retroperitoneal WAT (rp- and gWAT), and interscapular brown AT (iBAT) (Bagchi and MacDougald, 2019) (Figure 10). I investigated these different AT depots because they are known to play different roles during obesity: expansion of subcutaneous WAT is associated with a metabolically healthier state, whereas, visceral WAT expansion is associated with the development of metabolic syndrome (Berry *et al.*, 2013; Item and Konrad, 2012; Karpe and Pinnick, 2015; Vishvanath and Gupta, 2019).
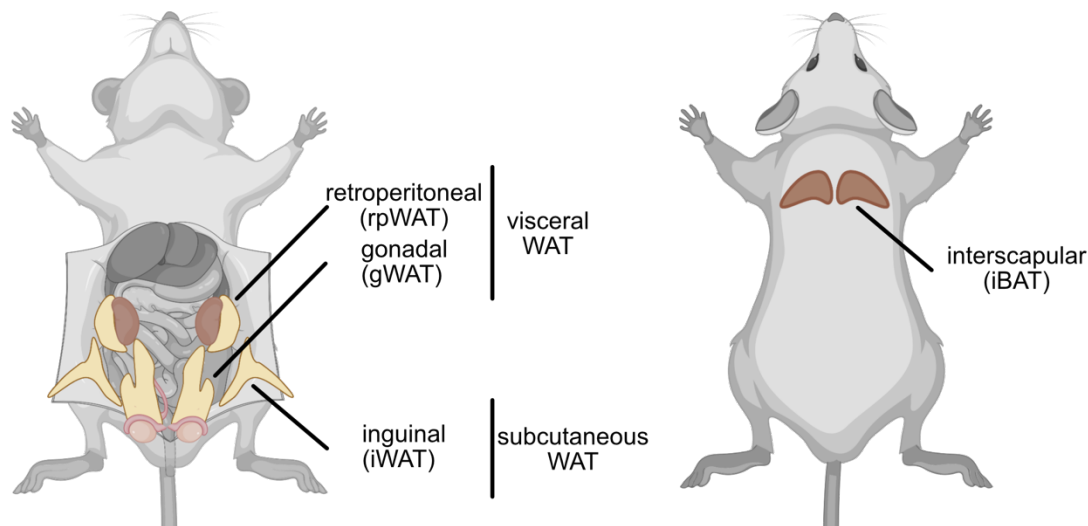
Figure 10: Location of different analyzed AT depots in the mice. Left: Ventral view on the localization of analyzed visceral and subcutaneous WAT depots. Right: Dorsal view on the localization of the analyzed BAT.

As I aimed to quantify body weight and AT mass gain compared to WT, I normalized the data to the average body weight of WT mice on CD for each time point and set it to 100%. For the analysis of AT mass, I calculated the delta of the AT mass of KO mice compared to the average AT mass of WT mice on CD for each time point. As gender-dependent differences in body weight and weight gain have been reported (Bergmann *et al.*, 1995; Chang *et al.*, 2018; Hong *et al.*, 2009; Palmer and Clegg, 2015), I also evaluated gender-specific differences and observed that male mice showed an increased body weight compared to female mice (Figure 11). To correct for this general gender-dependent baseline difference, I performed the normalizations for female and male animals separately.
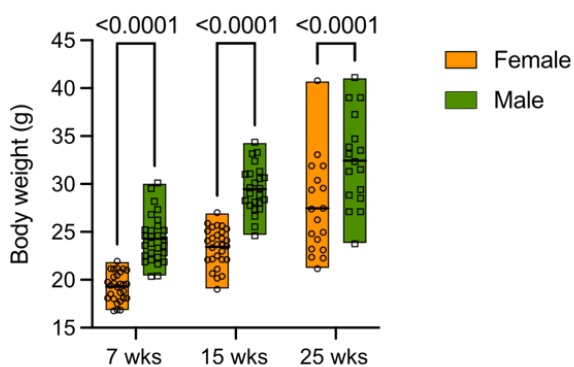
Figure 11: Male mice display consistently higher body weight compared to female mice. Body weight data of wildtype mice at different ages were combined regardless of mouse line to compare female with male animals. Bodyweight of male mice was significantly higher than female body weight. Data are shown as mean ± S.D. and with individual data points, p-values were calculated by Šídák's multiple comparisons test, n ≥ 17.

To check for differences in weight gain susceptibility of the KO mice, I investigated whether gender influenced weight gain in any examined parameter over the different timepoints in the KO mice. To this end, I performed a Two-way ANOVA, testing the effect of gender and age by comparison of female and male mice at the different timepoints (7, 15, and 25 wks as well as 40 wks for Bbs6). As I have already shown age dependent obesity development (Figure 9), I did not include the p-values for the age effect, but only the p-values for the gender effect. My results revealed AT depot-

dependent gender effects in different mouse lines (Table 15). In turn, whenever a gender effect was detected, I examined female and male mice separately.

Table 15: AT depot dependent effects of gender were revealed by Two-way ANOVA. Testing was performed for the parameters gender and age fitting a main effect only model. Listed p-values have been calculated for the gender effect on body weight and AT weight gain.

Mouse line	Body	gWAT	iWAT	rpWAT	iBAT
Bbs8	0.1078	**0.0051**	0.0354	0.3138	0.3589
Bbs6	0.6205	**0.0040**	0.1297	0.1513	0.1155
Pdgfra-Ac3	**0.0045**	**0.0004**	**0.0149**	0.3168	0.8951

Next, I compared weight gain between WT and KO at the different timepoints to investigate obesity development. Body weight of Bbs8$^{-/-}$ mice was significantly higher compared to Bbs8$^{+/+}$ mice at 15 wks of age and older (Figure 12A,B). This was accompanied by a significant weight gain in all analyzed AT depots (Figure 12C-F). I investigated gWAT and iWAT for each gender separately, as a gender effect had been detected in these AT depots. Indeed, the increase in gWAT in female Bbs8$^{-/-}$ mice reached higher average values than in male Bbs8$^{-/-}$ mice (Figure 12C). A similar effect was visible for iWAT, although the increase in male iWAT mass failed to reach significance at both younger timepoints (Figure 12D). As Bbs8$^{-/-}$ mice became obese in both genders, I combined them in the analyses, demonstrating that the gWAT and iWAT mass was increased (Figure 12C,D). Surprisingly, despite a lean body weight at the age of 7 wks, AT mass in the different depots was already significantly increased (Figure 12C-E). Taken together, Bbs8$^{-/-}$ at a young and lean state exhibit already increased AT mass, indicating a predisposition to obesity, which develops further during aging. These results show that loss of Bbs8 triggers a severe and fast increase in AT mass, which affects all AT depots.
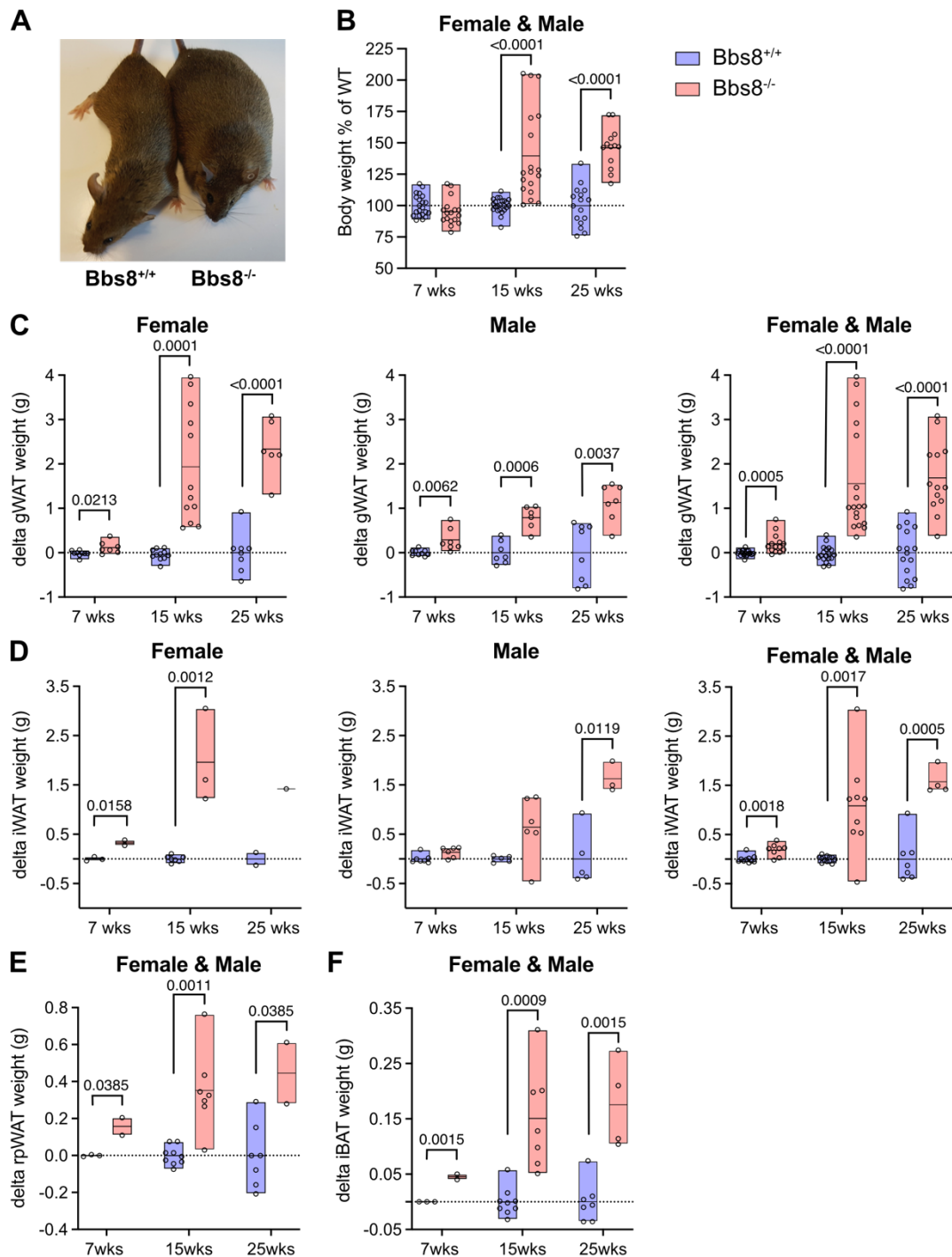
Figure 12: Bodyweight and adipose tissue (AT) mass gain in different AT depots in Bbs8 mice.
(A) Exemplary image of age-matched obese Bbs8$^{-/-}$ mice vs. lean Bbs8$^{+/+}$. **(B)** Bodyweight increase in Bbs8$^{-/-}$ compared to Bbs8$^{+/+}$ at 7, 15, and 25 ± 2 weeks of age. Dotted line represents the mean of Bbs8$^{+/+}$ set to 100 %. **(C-F)** AT mass increase in Bbs8$^{-/-}$ compared to Bbs8$^{+/+}$ at 7, 15, and 25 ± 2 weeks of age was calculated by subtraction of the mean AT mass of Bbs8$^{+/+}$ (delta) in gWAT **(C)**, iWAT **(D)**, rpWAT **(E)**, and iBAT **(F)**. Data are shown as mean ± S.D. and with individual data points, p-values were calculated by Holm-Šídák's multiple comparisons, n ≥ 2.

The body weight of Bbs6$^{-/-}$ mice was only significantly higher at the latest timepoint of 40 wks (Figure 13A,B). This is in line with previous reports showing that the body weight of Bbs6$^{-/-}$ mice increased after 28 wks of age (Fath *et al.*, 2005). But even at this late timepoint, not all mice exhibited an obese phenotype, indicating that Bbs6$^{-/-}$

are less prone to develop obesity and that there is no full penetrance of the phenotype (Figure 13B). Body weight gain at 40 wks coincided with increased AT mass in all depots, except for gWAT in male Bbs6$^{-/-}$ mice, representing a gender difference. Weight differences only occurring at this late stage hint towards an effect, which is not primary caused by loss of Bbs6, but might reflect other unrelated effects of aging in this mouse line. In summary, while Bbs8$^{-/-}$ developed severe obesity already at 15 wks of age, Bbs6$^{-/-}$ remained lean, demonstrating different roles of BBSome and BBS chaperonin complex for obesity.
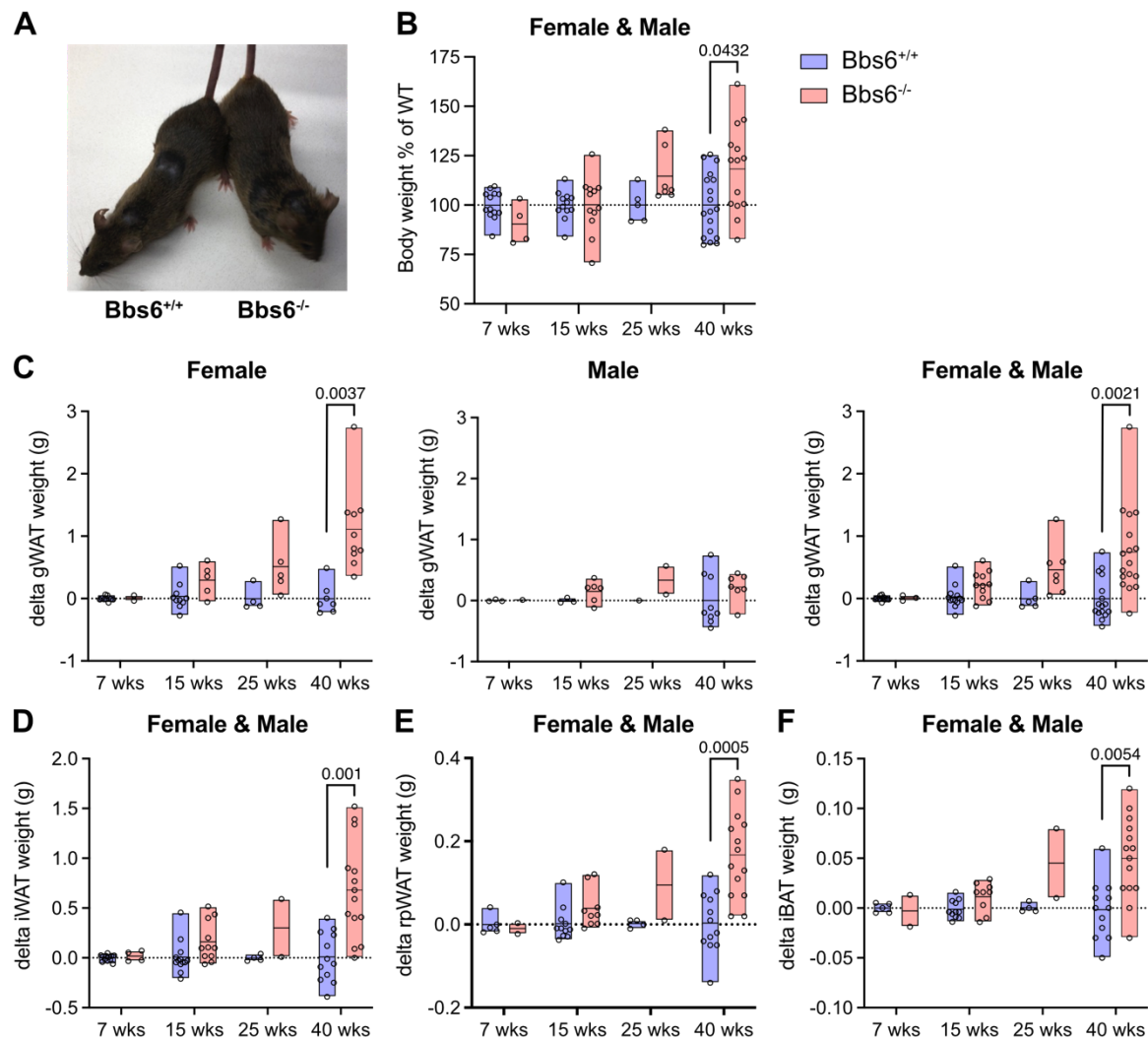
Figure 13: Bodyweight and adipose tissue (AT) mass gain in different AT depots in Bbs6 mice. **(A)** Exemplary image of age-matched Bbs6$^{-/-}$ mice vs. Bbs6$^{+/+}$. **(B)** Bodyweight increase in Bbs6$^{-/-}$ compared to Bbs6$^{+/+}$ at 7, 15, 25 ± 4, and 40 ± 10 weeks of age. Dotted line represents the mean of Bbs6$^{+/+}$ normalized to 100%. **(C-F)** AT mass increase in Bbs6$^{-/-}$ compared to Bbs6$^{+/+}$ at 7, 15, 25 ± 4, and 40 ± 10 weeks of age was calculated by subtraction of the mean AT mass of Bbs6$^{+/+}$ (delta) in gWAT **(C)**, iWAT **(D)**, rpWAT **(E)**, and iBAT **(F)**. Data are shown as mean ± S.D. and with individual data points, p-values were calculated by by Holm-Šídák's multiple comparisons, n ≥ 2.

In the Pdgfra-Ac3 mouse line, I investigated body weight, gWAT, and iWAT for each gender separately as Pdgfra-Ac3 presented a pronounced gender bias (Table 15). Although both female and male Pdgfra$^{cre/+}$ Ac3$^{f/f}$ mice became obese (Figure 14A), the increase in body weight as well as gWAT and iWAT weight was much higher in female

compared to male Pdgfra$^{cre/+}$ Ac3$^{f/f}$ mice (Figure 14B-D). However, as the tendency was the same for both, I combined females and males for overall analyses, demonstrating a significant increase in body weight and AT mass compared to control mice, which started at 7 wks and increased dramatically during aging.

In summary, my detailed analysis underlined that the loss of cAMP synthesis by AC3 in pre-adipocyte resembles the phenotype of Bbs8$^{-/-}$ mice: Both mouse lines developed severe obesity with an early onset. These results suggest that a change in ciliary cAMP signaling might underlie the disease pathology in Bbs8$^{-/-}$, but not in Bbs6$^{-/-}$ mice.
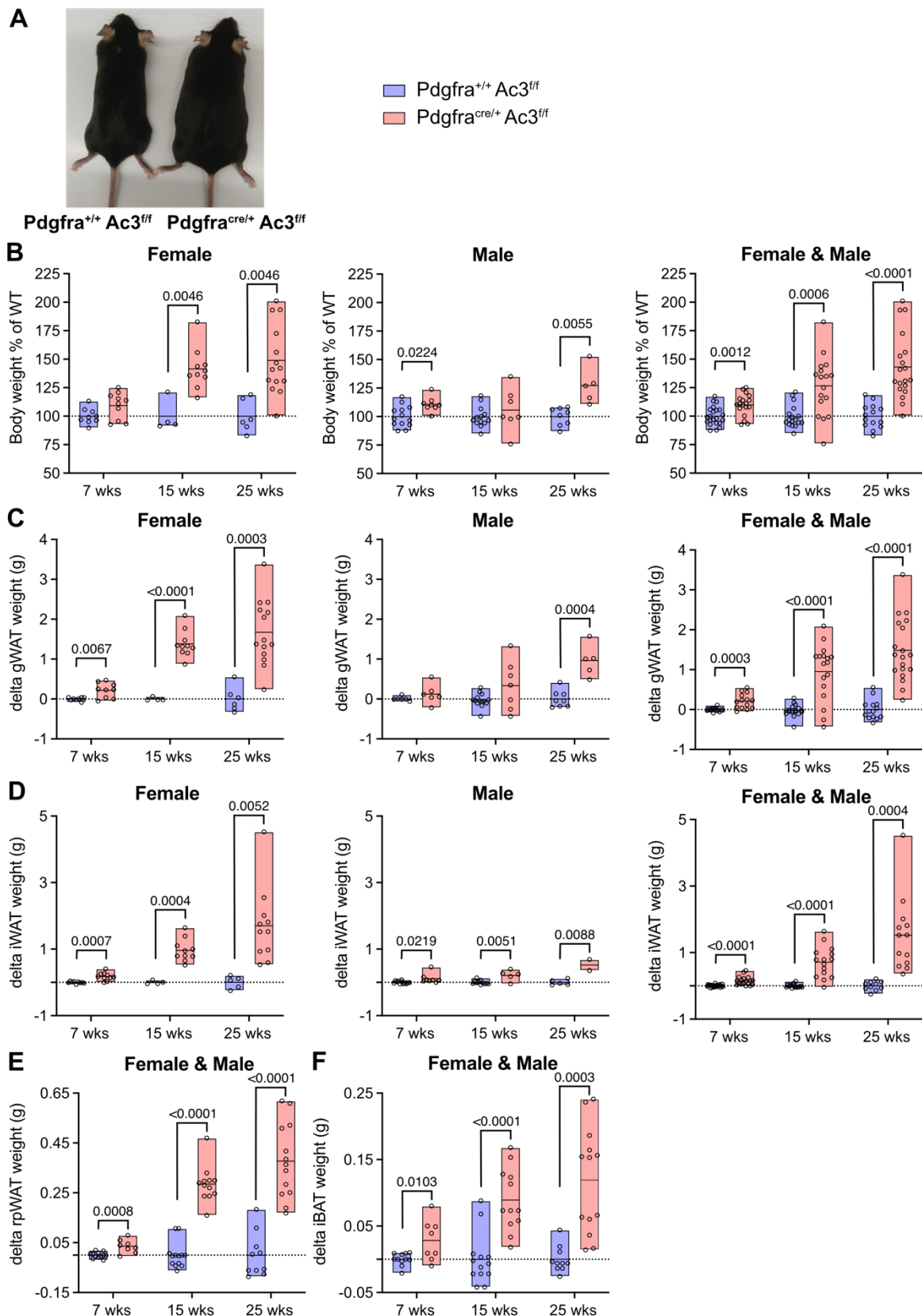
Figure 14: Bodyweight and adipose tissue (AT) mass gain in different AT depots in Pdgfra-Ac3 mice. (A) Exemplary image of age-matched obese Pdgfra$^{cre/+}$ Ac3$^{f/f}$ vs lean Pdgfra$^{+/+}$ Ac3$^{f/f}$. **(B)** Bodyweight increase in Pdgfra$^{cre/+}$ Ac3$^{f/f}$ compared to Pdgfra$^{+/+}$ Ac3$^{f/f}$ at 7, 15, and 25 ± 2 weeks of age. Dotted line represents the mean of Pdgfra$^{+/+}$ Ac3$^{f/f}$ normalized to 100%. **(C-F)** AT mass increase in Pdgfra$^{cre/+}$ Ac3$^{f/f}$ compared to Pdgfra$^{+/+}$ Ac3$^{f/f}$ at 7, 15, and 25 ± 2 weeks of age was calculated by subtraction of the mean AT mass of Pdgfra$^{+/+}$ Ac3$^{f/f}$ (delta) in gWAT **(C)**, iWAT **(D)**, rpWAT **(E)**, and iBAT

(F). Data are shown as mean ± S.D. and with individual data points, p-values were calculated by Holm-Šídák's multiple comparisons, n ≥ 2.

3.2.2 Body and adipose tissue weight gain during *High-fat diet* challenge

Obesity can have different consequences for whole body health and it has been shown that obesity induced by primary cilia dysfunction can be beneficial compared to diet-induced obesity (DIO) (Marion *et al.*, 2012). Therefore, I analyzed genotype- and diet-induced obesity (DIO) development by comparing pre-obese and obese timepoints to delineate the contribution of ciliary dysfunction to AT development and obesity-related metabolic changes.
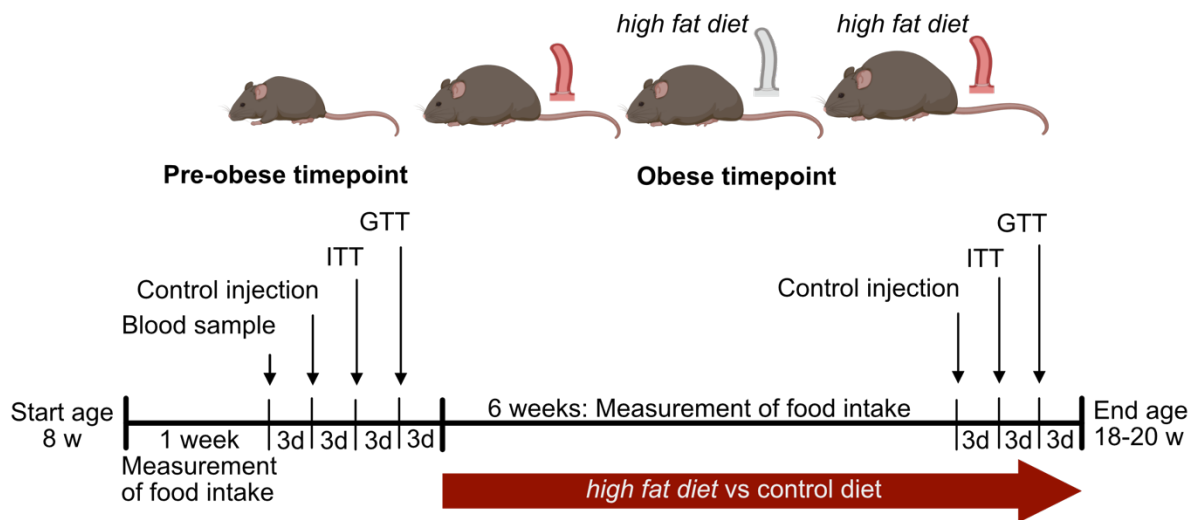
Figure 15: Experimental set-up to study obesity development and metabolic changes at pre- and obese timepoints. The experiment starts at the age of 8-weeks when mice are lean. Over 10-12 weeks, mice develop diet- or knockout-(KO) induced obesity. Mice were single-housed for the duration of the experiment to monitor food intake and the metabolic state was assessed via insulin- (ITT) and glucose tolerance test (GTT) before and after obesity.

I designed an experimental set-up that covered pre-obese and obese timepoints in different mouse models (Figure 15). To compare obesity development in ciliopathy models to diet-induced obesity, one cohort of mice was fed a high-fat diet (HFD), starting at approximately 11 wks (time point when genotype-dependent obesity starts to develop). Mice stayed on HFD until the end of the experiment (approximately 7.5 wks) and I monitored food intake and weight gain by daily measurements during the first 6 weeks of HFD feeding. The metabolic state of mice was assessed by insulin- and glucose tolerance tests before and after diet-induced obesity (Figure 15).

First, I investigated whether gender had an effect on weight gain upon HFD feeding. To this end, I performed a Two-way ANOVA testing the effect of gender and genotype in female versus male mice on HFD. As effects of genotype on obesity development were shown before (Figure 9), I did not include the p-values for the genotype effect, but only the p-values for the gender effect. This revealed gender-dependent differences in all parameters for Bbs6, and in body and gWAT weight for Bbs8 mice (Table 16). Of note, this analysis was not performed for Pdgfra-Ac3 mice due to a lack of female animals. Based on this result, I examined female and male mice separately whenever a gender effect was detected.

Table 16: Mouse line dependent gender-specific effects were revealed by Two-way ANOVA. Testing was performed for the parameters gender and genotype fitting a main effect only model. Listed p-values have been calculated for the gender effect on body weight and AT weight gain.

Mouse line	Body	gWAT	iWAT	rpWAT	iBAT
Bbs8	**0.0536**	**0.0148**	0.9510	0.5299	0.7939
Bbs6	**<0.0001**	**0.0016**	**0.0003**	**0.0071**	**0.0001**
Pdgfra-Ac3	NA	NA	NA	NA	NA

First, I investigated whether DIO weight gain mimics the phenotype of ciliopathy models. Indeed, DIO mirrored Bbs8$^{-/-}$ mice on CD with respect to body weight and WAT depot mass (despite iBAT) (Figure 16A-E). In contrast, DIO mirrored Pdgfra$^{cre/+}$ Ac3$^{f/f}$ only in respect to body weight, but surprisingly not in respect to WAT depot masses, which were all significantly higher in DIO mice (Figure 18A-E). Therefore, Pdgfra$^{cre/+}$ Ac3$^{f/f}$ ameliorates AT gain compared to DIO. As Bbs6$^{-/-}$ did not gain weight on CD, I examined the effect of HFD feeding on Bbs6$^{-/-}$ and Bbs6$^{+/+}$ mice. The first striking observation was a prominent sexual dimorphism in Bbs6$^{+/+}$ mice: Male Bbs6$^{+/+}$ mice significantly gained weight upon HFD feeding, whereas female mice remained lean (Figure 17A-E). Of note, phenotypic sexual dimorphisms in response to DIO have been previously reported (Bruder-Nascimento *et al.*, 2017; Vaanholt *et al.*, 2008). In contrast, Bbs6$^{-/-}$ mice significantly gained weight upon HFD feeding in both genders. In summary, male mice on HFD showed a similar weight gain in Bbs6$^{+/+}$ and Bbs6$^{-/-}$ (only significantly different in iWAT) (Figure 17C), whereas female mice on HFD gained weight in Bbs6$^{-/-}$ but not in Bbs6$^{+/+}$ mice. My results demonstrate that a HFD challenge in Bbs6$^{-/-}$ mice resulted in obesity compared to control mice, indicating that otherwise lean Bbs6$^{-/-}$ mice are prone to obesity development. Therefore, my three ciliopathy mouse models display an obesity phenotype but within a spectrum of severity.

In the other two ciliopathy mouse models (Bbs8 and Pdgfra-Ac3), HFD challenge of KO mice aggravated weight gain significantly compared to CD and HFD-fed WT mice. The gender bias in Bbs8 body weight and gWAT was due to a higher weight gain in female Bbs8$^{-/-}$ mice on HFD compared to male mice. Nevertheless, Bbs8$^{-/-}$ mice on HFD became heavily obese in both genders. Therefore, in my subsequent analyses, I combined both genders.
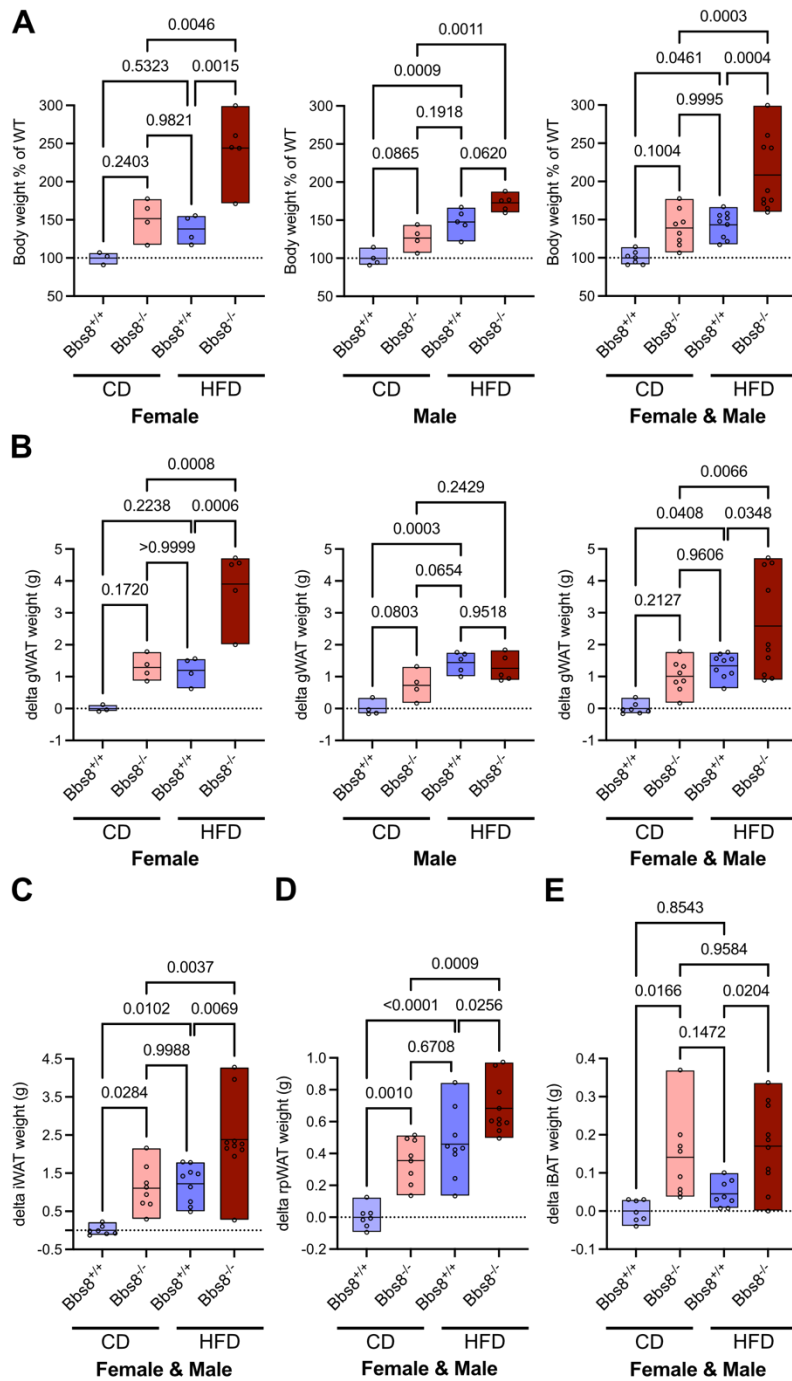
Figure 16: Body- and AT depot weights of Bbs8 mouse lines at obese timepoints. Increase in body- and different AT depot weights (iWAT, gWAT, rpWAT, and iBAT) isolated from single-housed Bbs8 mice after 7-8 weeks HFD vs CD feeding. In accordance to detected effects of gender body- and gWAT gain were shown for female and male mice separately and combined. **(A-E)** Comparison of bodyweight percentage of Bbs8^{+/+} mice on CD (separated by sex: females, males, combined) **(A)**, gWAT gain (separated by sex: females, males, combined) **(B)**, iWAT gain **(C)**, rpWAT gain **(D)**, and iBAT gain **(E)** mice. Data are shown as mean ± Max/Min and with individual data points, p-values were calculated by Šídák's multiple comparisons, n ≥ 7.
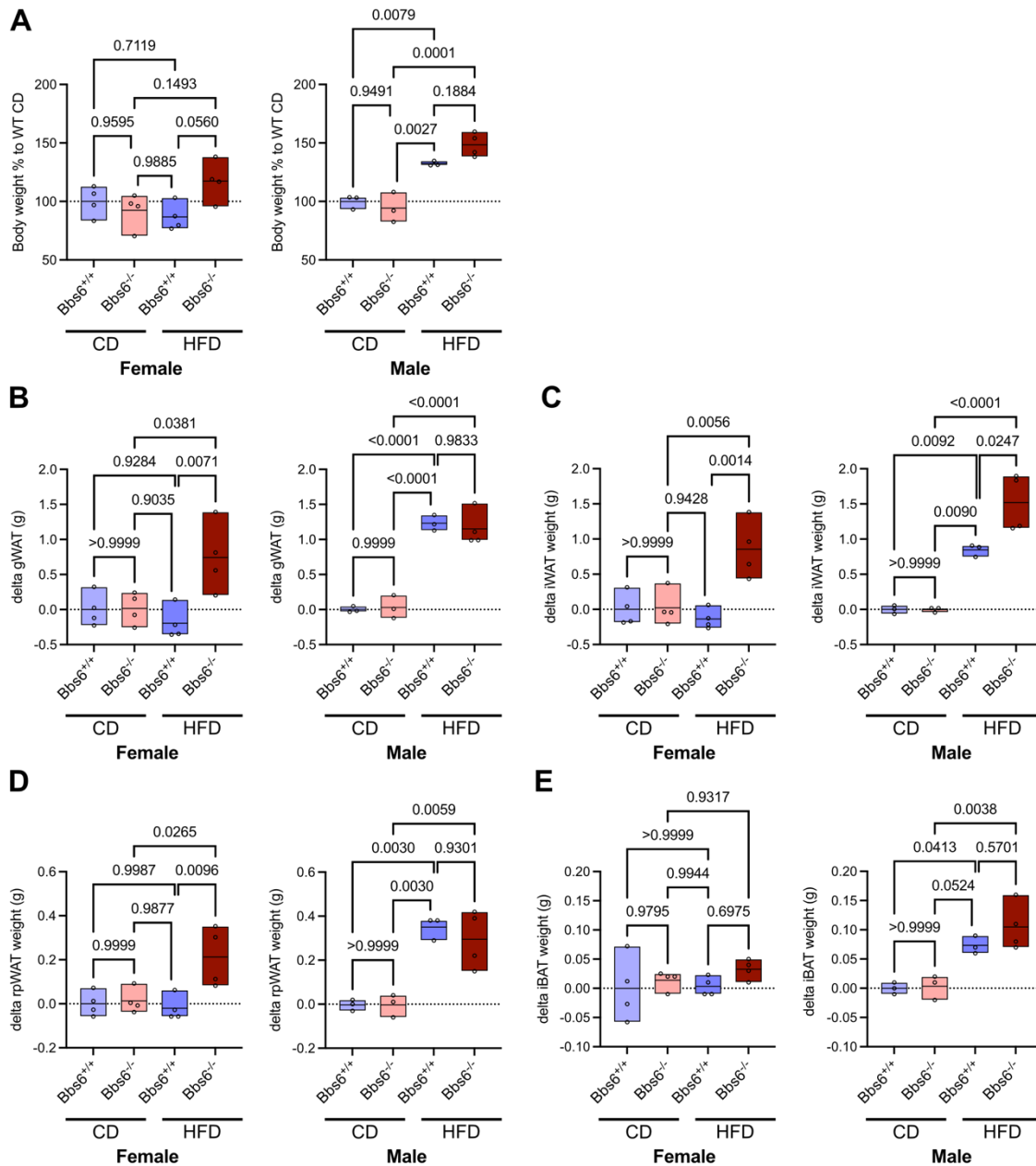
Figure 17: Body- and AT depot weights of Bbs6 mouse lines at obese timepoints. Increase in body- and different AT depot weights (iWAT, gWAT, rpWAT, and iBAT) isolated from single-housed Bbs6 mice after 7-8 weeks HFD vs CD feeding. In accordance to detected effects of gender body-, gWAT- and iWAT gain were shown for female and male mice separately. (A-E) Comparison of bodyweight percentage of Bbs6$^{+/+}$ mice on CD (separated by sex: females, males) **(A)**, gWAT gain (separated by sex: females, males) **(B)**, iWAT gain (separated by sex: females, males) **(C)**, rpWAT gain **(D)**, and iBAT gain **(E)** mice. Data are shown as mean ± Max/Min and with individual data points, p-values were calculated by Šídák's multiple com-parisons, n ≥ 3 per gender.
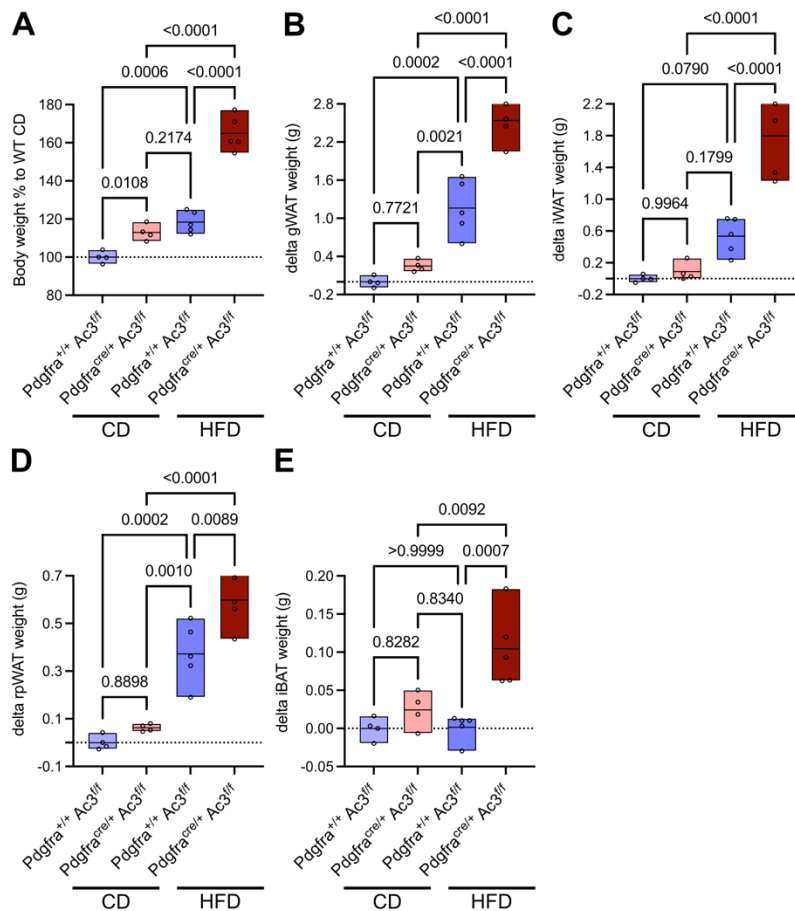
Figure 18: Body- and AT depot weights of Pdgfra-Ac3 mouse lines at obese timepoints. Increase in body- and different AT depot weights (iWAT, gWAT, rpWAT, and iBAT) isolated from single-housed Pdgfra-Ac3 mice after 7-8 weeks HFD vs CD feeding. **(A-E)** Comparison of bodyweight percentage of Pdgfra$^{+/+}$ Ac3$^{f/f}$ mice on CD **(A)**, gWAT gain **(B)**, iWAT gain **(C)**, rpWAT gain **(D)**, and iBAT gain **(E)** mice. Data are shown as mean ± Max/Min and with individual data points, p-values were calculated by Šídák's multiple com-parisons, n ≥ 4.

In summary, DIO mirrored obesity in Bbs8$^{-/-}$ mice on CD, but only to some extent in Pdgfra$^{cre/+}$ Ac3$^{f/f}$ and Bbs6$^{-/-}$ mice. Bbs8$^{-/-}$ and Pdgfra$^{cre/+}$ Ac3$^{f/f}$ mice developed obesity on CD, characterized by increased AT mass and body weight from 15 wks onwards, while Bbs6$^{-/-}$ mice stayed rather lean unless challenged with HFD.

3.3 Food intake

Next, I aimed to determine the underlying mechanisms for obesity development and unravel the contribution of primary cilia dysfunction. Obesity is a result of an imbalance in energy homeostasis, i.e., between energy uptake and energy expenditure (Hill *et al.*, 2012; Rosen and Spiegelman, 2006). I measured the food intake to monitor excess energy uptake, as ciliary dysfunction in hypothalamic neurons is known to impair the satiety feeling and regulation of food intake, leading to hyperphagia in BBS patients and mouse models (Yang *et al.*, 2021). Strikingly, global AC3 knockout mice also display hyperphagia due to neuronal dysfunction (Wang *et al.*, 2009b). By deleting AC3 only in *Pdgfra*-expressing cells, I aimed to prevent neuronal dysfunction and, in turn, hyperphagia to investigate the contribution of ciliary dysfunction in pre-adipocytes to obesity development. As the Bbs6 mouse line had shown sexual dimorphism in response to HFD, I investigated whether they also displayed gender differences in food intake (Table 17). However, I did not observe any gender bias and, therefore, combined data from female and male mice in the following analysis.

Table 17: Two-way ANOVA detected no effect of gender on food intake in Bbs6 mice. Testing was performed for the parameters gender and genotype in preOB timepoint or conditions of obesity induction (diet, genotype, or diet and genotype) in OB timepoint fitting a main effect only model. Listed p-values have been calculated for the gender effect on food intake at preOB and OB timepoints.

Mouse line	Pre-obese timepoint	Obese timepoint
Bbs6	0.5193	0.1917

I first measured food intake at the pre-obese timepoint during the first week of the experiment. Surprisingly, none of the mouse models did show hyperphagia (Figure 19A-C). Food intake in the first few days was rather decreased in the respective KO mice, although they caught up with the corresponding WT controls at the end of the week (Figure 19A-C). This difference in food intake was most pronounced in Bbs8$^{-/-}$ mice, whereas for Bbs6$^{-/-}$ and Pdgfra$^{cre/+}$ Ac3$^{f/f}$ mice, the values did not reach significance in a multiple t-test (Figure 19A-C). My previous results demonstrated that both *Bbs*-KOs displayed a runted phenotype after birth, being much smaller and weaker than their WT littermates (Figure 9). Thus, this initial reduction in food intake could still be a result of this phenotype. In contrast, Pdgfra$^{cre/+}$ Ac3$^{f/f}$ mice were not runted after birth and indistinguishable from their control littermates. In turn, they also showed a less pronounced initial difference in food intake.
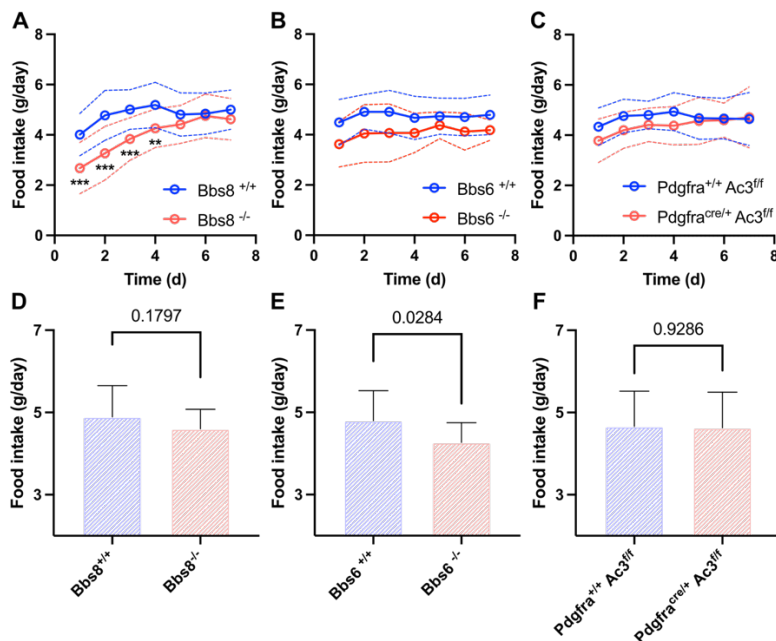
Figure 19: Food intake of different mouse lines during pre-obese timepoint. Mice aged 8 weeks were monitored for food intake for one week. **(A-C)** Daily food intake during first experimental week in Bbs8 **(A)**, Bbs6 **(B)**, and Pdgfra-Ac3 **(C)** mice. Data are shown as mean ± S.D. as dotted lines, p-values were calculated by multiple Student's t-test. **(D-F)** Average daily food intake for days 5-7 of food intake measurement in Bbs8 **(D)**, Bbs6 **(E)**, and Pdgfra-Ac3 **(F)** mice. Data shown as mean ± S.D., p-values were calculated by un-paired Student's t-test, n ≥ 9.

However, also the experimental set-up could have an impact on food intake as mice had to be moved to a different holding room for the experiments, which could have caused stress to the animals at the beginning of the experiment. It has been shown that stress leads to a dramatic drop in food intake, especially during the first five days (Jeong *et al.*, 2013). Thus, KOs might be more prone to stress related changes in food intake than WTs, especially in the Bbs8 mouse line. Based on these results, I decided to calculate the average food intake only for the last days (day 5-7), when stress-related effects should not play a role anymore. Based on this comparison, food intake

in Bbs6^{-/-} mice was reduced whereas the other two mouse lines did not show a significant difference (Figure 19D-F). In summary, no hyperphagia was observed at the early, pre-obese timepoint.

Figure 20: Food intake of different mouse lines during high fat diet (HFD) vs control diet (CD) challenge. Mice aged 11 weeks were monitored for food intake for six weeks. **(A-C)** Daily food intake during HFD and CD feeding of Bbs8 **(A)**, Bbs6 **(B)**, and Pdgfra-Ac3 **(C)**. Data are shown as mean. **(D-F)** Average daily food intake during the last monitored week in Bbs8 **(D)**, Bbs6 **(E)**, and Pdgfra-Ac3 **(F)**. **(G-I)** Corresponding average daily gross-energy uptake was calculated based on energy content and average food intake of Bbs8 **(G)**, Bbs6 **(H)**, and Pdgfra-Ac3 **(I)**. Data are shown as mean ± S.D., p-values were calculated by Holm-Šídák's multiple comparisons, n ≥ 4.

Next, I investigated food intake during obesity development (age 11-17 wks). While food intake was not different between Bbs6^{-/-} and control mice, Bbs8^{-/-} and Pdgfra^{cre/+} Ac3^{f/f} mice on CD exhibited hyperphagia compared to the respective control mice (Figure 20A-C). Hyperphagia was already evident during the first week, indicating that hyperphagia develops first and, in turn, drives obesity. For Bbs8^{-/-} mice, this is in line

with previous reports of hyperphagia (Rahmouni *et al.*, 2008), whereas for Bbs6^{-/-} mice, this finding contradicts a previous report, detecting hyperphagia at 16 wks of age (Fath *et al.*, 2005). As my measurements covered age 11-17 wks, I might have missed the onset of hyperphagia, although there is no indication of increased food intake at the end of my measurements. As Bbs6^{-/-} mice do not show hyperphagia, this also explains why they failed to develop obesity on CD. My results demonstrate that Bbs6 and Bbs8 play different roles in controlling primary cilia function. Furthermore, as Pdgfra[cre/+] Ac3[f/f] present with hyperphagia, it seems rather difficult to separate the effects of hyperphagia induced by neuronal ciliary defects from ciliary defects in pre-adipocytes. While tamoxifen inducible Pdgfra-creER[TM] mouse line has been shown to be rather AT-specific in adult mice (Hilgendorf *et al.*, 2019), this could be much broader during embryonic development, affecting other cell-types, e.g., feeding-regulating neurons in the hypothalamus. To test this hypothesis, my colleague Dr. C. Klausen stained brain slices of Pdgfra[cre/+] R26-tdTomato[tg/+] mice with an antibody against NeuN, a neuronal marker (Gusel'nikova and Korzhevskiy, 2015), and agouti-related protein (AgRP), a marker for a specific subset of neurons located at the arcuate nucleus, which regulate foot intake (Abdalla, 2017). Her results revealed that tdTomato^{+} cells colocalized with NeuN[+] and AgRP^{+} neurons, indicating that *Pdgfra* is not only expressed in pre-adipocytes and their precursors, i.e., mesenchymal stem cells, but also in neurons and their precursors, rendering it rather difficult to distinguish between primary cilia dysfunction in neurons and pre-adipocytes (Figure 21). However, hyperphagia was less pronounced in this model compared to Bbs8^{-/-} mice. Although, I cannot rule out that this is simply a difference in mouse strain, this might indicate that some contributing cells are not targeted and therefore functional.
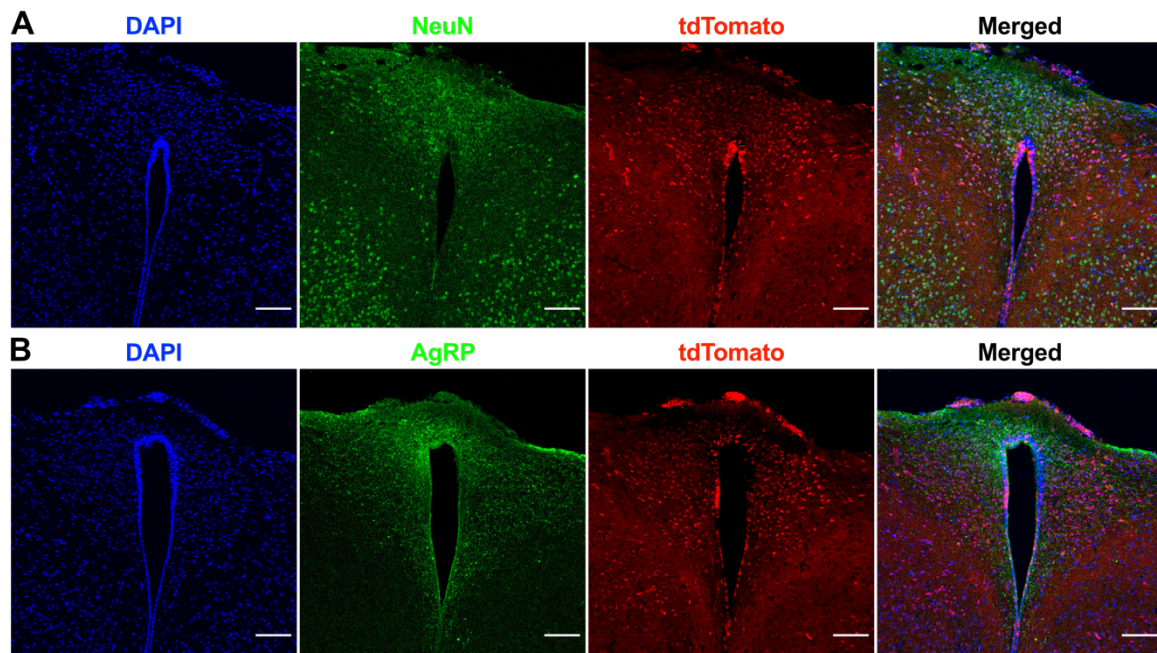
Figure 21: Neurons in the food regulating arcuate nucleus targeted by cre-recombinase-driven, conditional knockout in *Pdgfra* expressing cells. Brain slices of Pdgfra$^{cre/+}$ R26-tdTomato$^{tg/+}$ mice were stained with DAPI (blue), an antibody against neuronal marker (green). Pdgfra expressing cells also express the reporter dtTomato (red). **(A-B)** The reporter dtTomato is present in the arcuate nucleus and colocalizes with general neuronal marker NeuN **(A)** and subpopulations-specific AgRP marker **(B)**. Scale bars: 100 µm.

Next, I investigated the effect of HFD feeding on food intake. Surprisingly, all mice (WT and KO) reduced their food intake upon HFD feeding, but hyperphagia was maintained in Bbs8$^{-/-}$ and Pdgfra$^{cre/+}$ Ac3$^{f/f}$ mice compared to the respective control mice (Figure 20). When challenged with HFD, even Bbs6$^{-/-}$ were eating slightly more, which resulted in an increased WAT mass (Chapter 3.2.2,Figure 17), indicating that upon dietary challenge, differences in feeding behavior can even be observed in this mouse model. When comparing different diets, food intake can be misleading as diets have different energy densities. Therefore, I calculated the total energy uptake based on food intake and energy density of the respective diet for comparison. I hypothesized that WT mice are able to maintain homeostatic energy uptake by reducing their food intake upon switching to HFD whereas KO mice are not able to react accordingly and, thereby, increase their excess energy uptake. In line with my hypothesis, WT mice showed no difference in energy uptake irrespective of the diet, but strikingly, this was also observed for Bbs8$^{-/-}$ and Pdgfra$^{cre/+}$ Ac3$^{f/f}$ mice. These results indicate that not all food regulating mechanisms are disrupted in these ciliopathy models, as the ability to react to changes in energy density of the food is still functional, but the basal level of energy, which is considered "homeostatic", is increased. Still, hyperphagia contributes to obesity development in all my ciliopathy models.

3.4 Metabolic changes during obesity

To investigate the systemic consequences of obesity, I examined the metabolic state of the mice before and after obesity development and compared those parameters between ciliopathy- and diet-induced obesity. To this end, I performed glucose- and

insulin tolerance test (GTT / ITT) by intraperitoneal injection of glucose or insulin, respectively (Andrikopoulos *et al.*, 2008; Benedé-Ubieto *et al.*, 2020). Glucose or insulin was injected (glucose: 2 mg/kg, insulin: 0.75 U/kg body weight of the mouse) to induce high blood glucose or insulin levels after a 6 h fasting period, which is important to provide a stable baseline and to determine fasting glucose levels as another important measure to evaluate the metabolic state. Following injections, blood glucose levels were measured over time to *i)* determine the rate of glucose clearance from the blood and *ii)* to reveal if the administration of insulin leads to a reduction in blood glucose levels (Figure 22). High blood glucose levels are sensed by the pancreatic β cells in the islets of Langerhans, which consequently increases the secretion of the endocrine peptide hormone insulin. Insulin acts on cells throughout the body to orchestrate an anabolic response to high glucose levels, especially in muscle cells, liver, and WAT (Wilcox, 2005) (Figure 22A). Insulin facilitates glucose uptake via translocation of glucose transporters, mainly GLUT4, to the plasma membrane (Holman *et al.*, 1990; Klip and Pâquet, 1990) and stimulates glycogen synthesis (Dent *et al.*, 1990; Shulman *et al.*, 1990), while inhibiting its breakdown (Dent *et al.*, 1990) to store glucose in the liver. Additionally, insulin stimulates fat formation and storage by increasing lipogenesis and inhibiting lipolysis (Assimacopoulos-Jeannet *et al.*, 1995; Kahn and Flier, 2000; Kersten, 2001). Overall, insulin acts to promote a rapid uptake and usage of glucose (Wilcox, 2005). Two main factors that impair glucose tolerance are incorrect insulin secretion in response to high glucose levels and insensitivity of the cells to insulin action (Khan *et al.*, 2019; Rother, 2007). To distinguish between the two, ITTs were performed. Injection of insulin skips the pancreatic response to high glucose levels and directly tests the insulin action to reduce blood glucose levels (Figure 22B). Thus, the GTT allows to measure the physiological response to high glucose levels and ITT allows to shed light on the underlying mechanism.

During GTT in lean WT mice, blood glucose levels increased until 15 min and dropped back to basal levels within 75 min (Figure 22D). During ITT in lean WT mice, blood glucose levels directly dropped after insulin injection until at least 30 min after injection, before slowly increasing again towards homeostatic basal levels (Figure 22D). As a control, I injected a saline solution, which did not substantially affect glucose levels (Figure 22D).
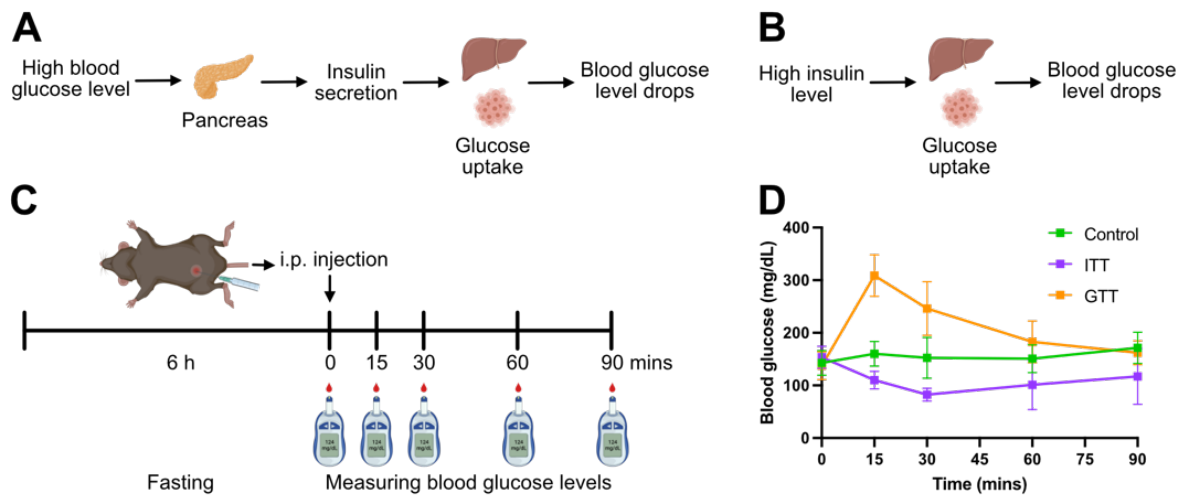
Figure 22: Glucose- and insulin tolerance test to determine metabolic state. (A) Principle of homeostatic glucose handling as base for glucose tolerance test (GTT). High blood glucose level trigger insulin release, which stimulates glucose uptake by the liver and other cells and results in a blood glucose level drop. **(B)** Principle of homeostatic insulin action as base for insulin tolerance test (ITT). High insulin levels act on liver and cells to take up glucose resulting in a blood glucose level drop. **(C)** Time course for Control/GTT/ITT experiments. After a 6 h fasting period basal glucose levels were measured before intra-peritoneal injection of either 0.9% NaCl (Control), 2 mg/kg glucose (GTT) or 0.75 U/kg insulin (ITT). Blood glucose levels were then monitored by repeated measurements (15, 30, 60, and 90 mins after injection). **(D)** Exemplary blood glucose levels during Control, GTT, and ITT performed on single-housed, 9-week old wildtype mice.

To compare the results, I calculated the area under the curve (AUC) for the respective measurements. The starting value was set as baseline and total AUC was calculated for positive peaks (GTT) when blood glucose levels increased and for negative peaks (ITT) when blood glucose levels decreased (Virtue and Vidal-Puig, 2021) (Figure 23).
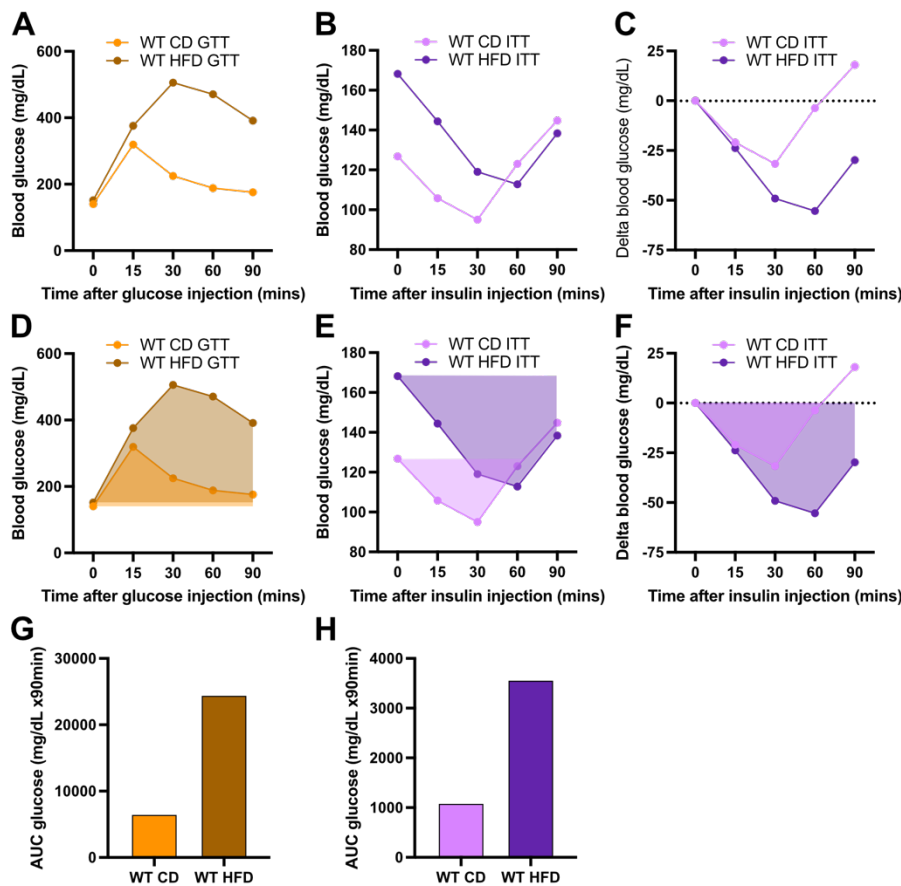
Figure 23: Area under the curve (AUC) as quantitative value to compare results from Glucose- and insulin tolerance test.
After a 6 h fasting period basal glucose levels were measured before intra-peritoneal injection of either 0.9% NaCl (Control), 2 mg/kg glucose (GTT) or 0.75 U/kg insulin (ITT). Blood glucose levels were then monitored by repeated measurements (15, 30, 60, and 90 mins after injection). Wildtype mice at the age of 11 weeks were fed either CD or HFD for 7-8 weeks. **(A-C)** Exemplary blood glucose curves of 18-19 wks old wildtype mice on CD (light color) or HFD (dark color) during GTT **(A)**, ITT **(B)** or ITT normalized to baseline by calculation of the delta value between starting and subsequent blood glucose levels **(C)**. **(D-F)** Visualization of the AUC for the respective curves during GTT **(D)**, ITT **(E)** or ITT normalized to baseline by calculation of the delta value between starting and subsequent blood glucose levels **(F)**. Normalization of ITT curves makes them visually more easily comparable. **(G-H)** Quantitative comparison of AUC of positive peaks or negative peaks in GTT **(G)** or ITT **(H)**, respectively.

Since the Bbs6$^{+/+}$ mice had shown strong sexual dimorphism in response to HFD, which on the one hand led to an obese and on the other hand to a lean phenotype, I investigated whether they displayed gender differences for the metabolic parameters (Table 18). To this end, I tested the AUC calculated for GTT and ITT as well as for fasting blood glucose levels from HFD-fed Bbs6$^{+/+}$ mice comparing female and male. Indeed, I observed a gender bias but only in the AUC for GTT. Thus, GTT results of females and males will be analyzed separately.

Table 18: Gender differences were detected for AUC (GTT), but not AUC (ITT) nor fasting blood glucose levels in HFD-fed Bbs6$^{+/+}$ mice. Testing was performed by unpaired Student's t-test for fasting blood glucose levels and by unpaired t-test with Welch's Correction for AUCs. Listed p-values have been calculated for the gender effect on different metabolic parameters in HFD-fed Bbs6$^{+/+}$ mice.

Mouse line	Fasting glucose	AUC (GTT)	AUC (ITT)
Bbs6	0.2099	**0.0327**	0.1879

I first compared WT and KO mice at the pre-obese timepoint to exclude primary effects on metabolism before obesity development. After a 6 h fasting period, blood glucose levels were higher in pre-obese Bbs8$^{-/-}$ and Pdgfra$^{cre/+}$ Ac3$^{f/f}$ mice compared to their respective WT littermates, indicating a primary metabolic defect even before onset of obesity (Figure 24A, C). In contrast, Bbs6$^{-/-}$ mice displayed no significant difference in fasting blood glucose levels compared to their controls, indicating a normal metabolic state (Figure 24B).
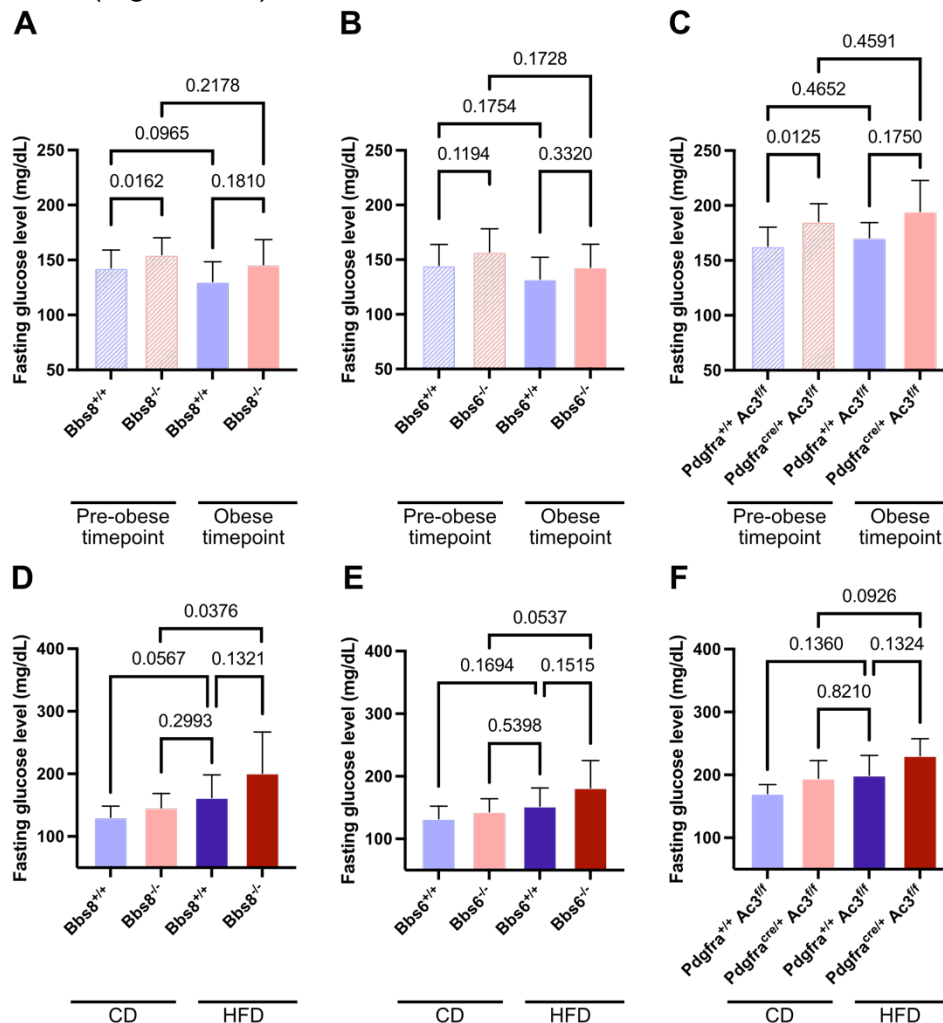
Figure 24: Fasting glucose levels of different mouse lines prior and after obesity development. Blood glucose levels measured after a 6 h fasting period. **(A-C)** Comparison of pOb and Ob timepoint of single-housed Bbs8 **(A)**, Bbs6 **(B)**, and Pdgfra-Ac3 **(C)** on CD (control diet). **(D-F)** Comparison of single-housed Bbs8 **(D)**, Bbs6 **(E)**, and Pdgfra-Ac3 **(F)** mice after 6-7 weeks of HFD or CD feeding. Data are shown as mean ± S.D., p-values were calculated by unpaired Student's t-test, n ≥ 4.

Next, I examined this in more detail via GTTs and ITTs. *Bbs*-KO mice already displayed defects in glucose handling at the pre-obese timepoint compared to the respective WT controls (Figure 25A,C,D,F). An impairment of glucose handling preceding the onset of obesity has also been described for Bbs4$^{-/-}$ mice and attributed to perturbation of insulin release by ciliated pancreatic β-cells (Gerdes *et al.*, 2014), which might also account for the defects observed in Bbs6$^{-/-}$ and Bbs8$^{-/-}$ mice. In contrast, Pdgfra$^{cre/+}$ Ac3$^{f/f}$ mice did not show a difference in glucose handling prior to obesity

compared to control mice (Figure 25A,E). Thus, this mouse line excludes this pancreatic phenotype, which is surprising as *Pdgfra* has been shown to be expressed in β-cells (Chen *et al.*, 2011). Therefore, possible defects in insulin secretion by β-cells in *Bbs*-KO mice might be independent of AC3 signaling. This, however, has to be confirmed in future studies using conditional knockout mice. ITTs revealed a normal reaction to insulin in all KO mice (Figure 26A-F), indicating that glucose impairment in *Bbs*-KO mice is a result of a disturbed insulin secretion and not of insulin insensitivity, in line with the effect described for Bbs4$^{-/-}$ mice (Gerdes *et al.*, 2014).

To reveal whether the metabolic state is further altered during obesity development, I determined fasting glucose level at the obese state (Figure 24D-F). At this stage, both HFD-fed mice and KO mice on CD of all lines showed a tendency towards increased glucose levels. The trend towards hyperglycemia in these mice did not always reach significance due to high variance and low animal numbers.
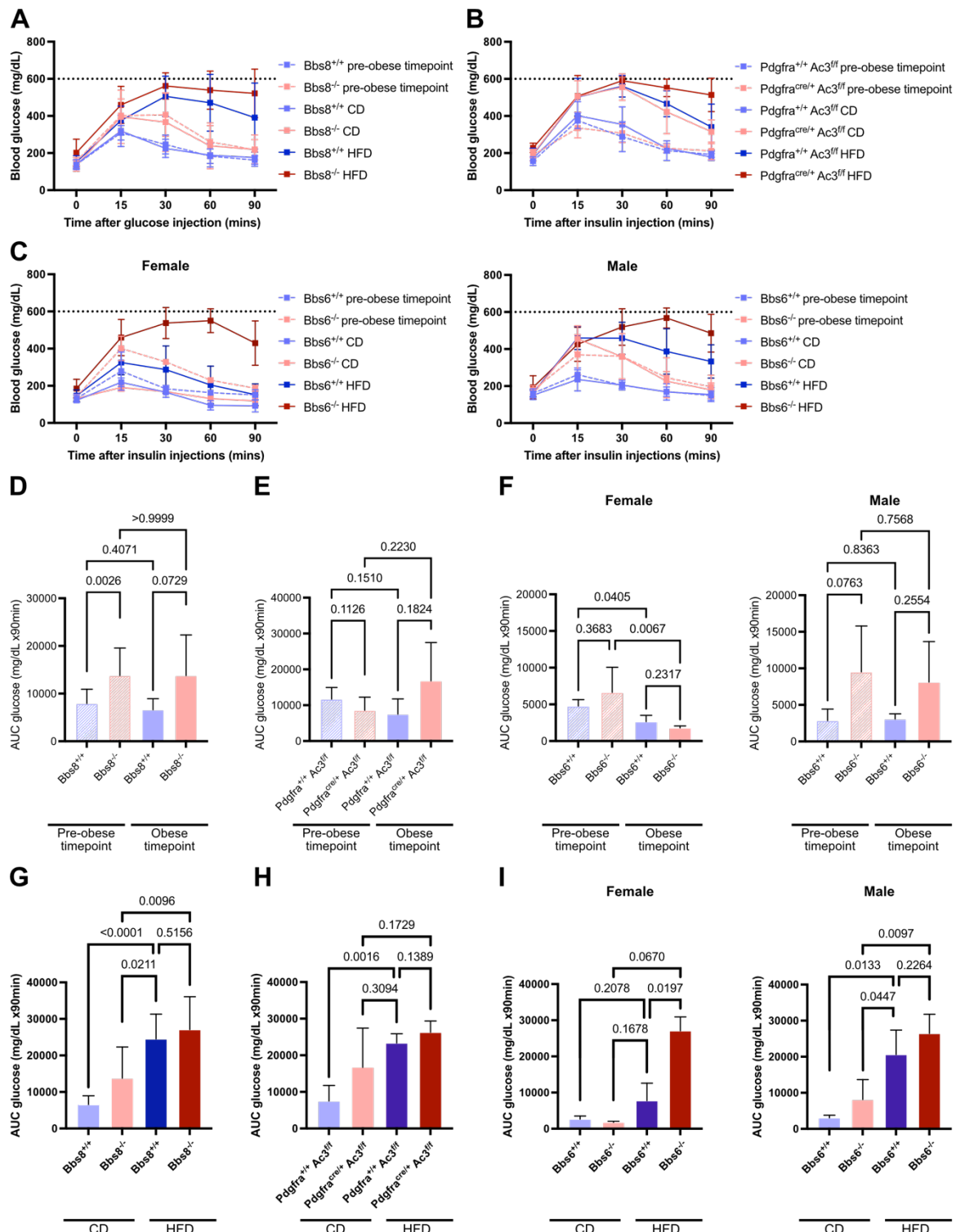
Figure 25: GTT results of different mouse lines at pre-obese and obese timepoints. The experiment starts at the age of 8-weeks, at which point mice are lean. Over 10-12 weeks, mice develop diet- or KO-induced obesity. The metabolic state was measured before and after 7-8 weeks HFD vs CD feeding. **(A-C)** For GTT mice were fasted for 6 h before an intraperitoneal glucose injection with 2 mg/kg bodyweight. Blood glucose levels during GTT in Bbs8 **(A)**, Pdgfra-Ac3 **(B)**, and female and male Bbs6 **(C)**. Dotted line represents the technical detection limit. Data are shown as mean ± S.D., n ≥ 2. **(D-I)** Blood glucose levels during GTT were quantified by calculation of corresponding AUC. AUC is calculated as positive peak area above starting value. (D-F) Comparison of pOb and Ob timepoint of single-housed Bbs8 **(D)**, Pdgfra-Ac3 **(E)**, and female and male Bbs6 **(F)** on CD. **(G-I)** Comparison of single-housed Bbs8 **(G)**, Pdgfra-Ac3 **(H)**, and female and male Bbs6 **(I)** mice after 7-8 weeks of HFD or CD feeding. Data are shown as mean ± S.D., p-values were calculated by unpaired t-test with Welch's Correction, n ≥ 2.

As glucose tolerance is associated with obesity due to increased free fatty acids levels, leading to insulin resistance (Fryk *et al.*, 2021; Hauke *et al.*, 2018)and, thereby, impaired glucose utilization(Khan *et al.*, 2019), I expected higher blood glucose levels throughout the GTT in obese KO mice on CD compared to the pre-obese timepoint. Surprisingly, this was not the case for $Bbs8^{-/-}$ mice: Although $Bbs8^{-/-}$ mice were heavily obese, their GTT did not aggravate with obesity, but rather remained on the pre-diabetic level already observed at the pre-obese state (Figure 25A,D). Glucose handling was even improved in comparison to diet-induced obese $Bbs8^{+/+}$ mice with equivalent obesity development (Figure 25A,G). So, while weight gain in $Bbs8^{-/-}$ on CD was mimicked by DIO in $Bbs8^{+/+}$ mice, obesity-dependent metabolic defects were less severe in the $Bbs8^{-/-}$ on CD compared to diet-induced obese $Bbs8^{+/+}$ mice. This phenotype of improved glucose handling in genotype-induced obesity versus DIO was not observed in the other mouse models that display ciliary dysfunction.

Obese $Pdgfra^{cre/+}$ $Ac3^{f/f}$ mice on CD showed the same high level of glucose tolerance impairment as diet-induced obese control mice (Figure 25B,E,H), despite reduced WAT masses. Thus, although $Pdgfra^{cre/+}$ $Ac3^{f/f}$ mice displayed a similar phenotype as $Bbs8^{-/-}$ mice with respect to weight gain and food intake, glucose handling in $Pdgfra^{cre/+}$ $Ac3^{f/f}$ and $Bbs8^{-/-}$ mice was different.

Due to the strong sexual dimorphism of $Bbs6^{+/+}$ mice in response to HFD (Table 18), I analyzed GTT results of female and male mice separately. Because $Bbs6^{-/-}$ mice do not get obese unless challenged with HFD, I would expect no difference in glucose handling for early and late timepoints in CD-fed $Bbs6^{-/-}$ mice. Indeed, male $Bbs6^{-/-}$ mice displayed the same mild impairment in glucose handling at both timepoints, but surprisingly female $Bbs6^{-/-}$ mice did not show increased blood glucose levels in contrast to the pre-obese timepoint (Figure 25C,F). These conflicting results might be a consequence of female Bbs6 mice being mainly part of the first cohorts of my experiment when I was less experienced and a control injection was not yet included, which might have affected the results of the GTT. This might also affect 2 out of 3 female HFD-fed $Bbs6^{+/+}$. Therefore, GTT results from female Bbs6 mice should be regarded with care and will be dismissed for further conclusions.

To investigate whether the metabolic state is further altered during obesity development, I compared male $Bbs6^{-/-}$ and $Bbs6^{+/+}$ mice on HFD, which displayed a similar weight gain. $Bbs6^{-/-}$ mice on HFD were clearly diabetic, similar to male $Bbs6^{+/+}$ mice (Figure 25C,I)and to KO mice on HFD of the Bbs8 and Pdgfra-Ac3 mouse lines. Here, blood glucose levels even reached the technical detection limit of the GTT, whereby I can only speculate that GTT impairment is even worse than in DIO mice (Figure 25A,B,G,H).

To investigate the underlying pathological change in metabolic homeostasis, I performed the ITT. Strikingly, none of the obese mice displayed insulin resistance (Figure 26), contradicting well established correlations between insulin resistance and obesity (Kahn and Flier, 2000; Martyn *et al.*, 2008; Varghese *et al.*, 2020). Insulin resistance is a secondary effect of obesity and progresses over time. In my experimental set-up, obesity developed over 7-8 wks, which might not be sufficient to

induce detectable insulin resistance. Indeed, Varghese *et al* showed a significant increase in insulin resistance from 12 weeks of HFD feeding onwards (Varghese *et al.*, 2020). Therefore, insulin resistance might not yet have been fully developed. Alternative approaches for future studies would be to measure insulin levels during GTT and after fasting. Hyperinsulinemia during fasting indicates the presence of increased insulin secretion as a counteraction to developing insulin resistance, and insulin levels during GTT allow to determine disturbed insulin secretion upon glucose load. One should also keep in mind that insulin is the most prominent player but other hormones, such as glucagon, somatostatin, might also play a role (Chen *et al.*, 2021b; Kellard *et al.*, 2020; Wagner *et al.*, 2017).
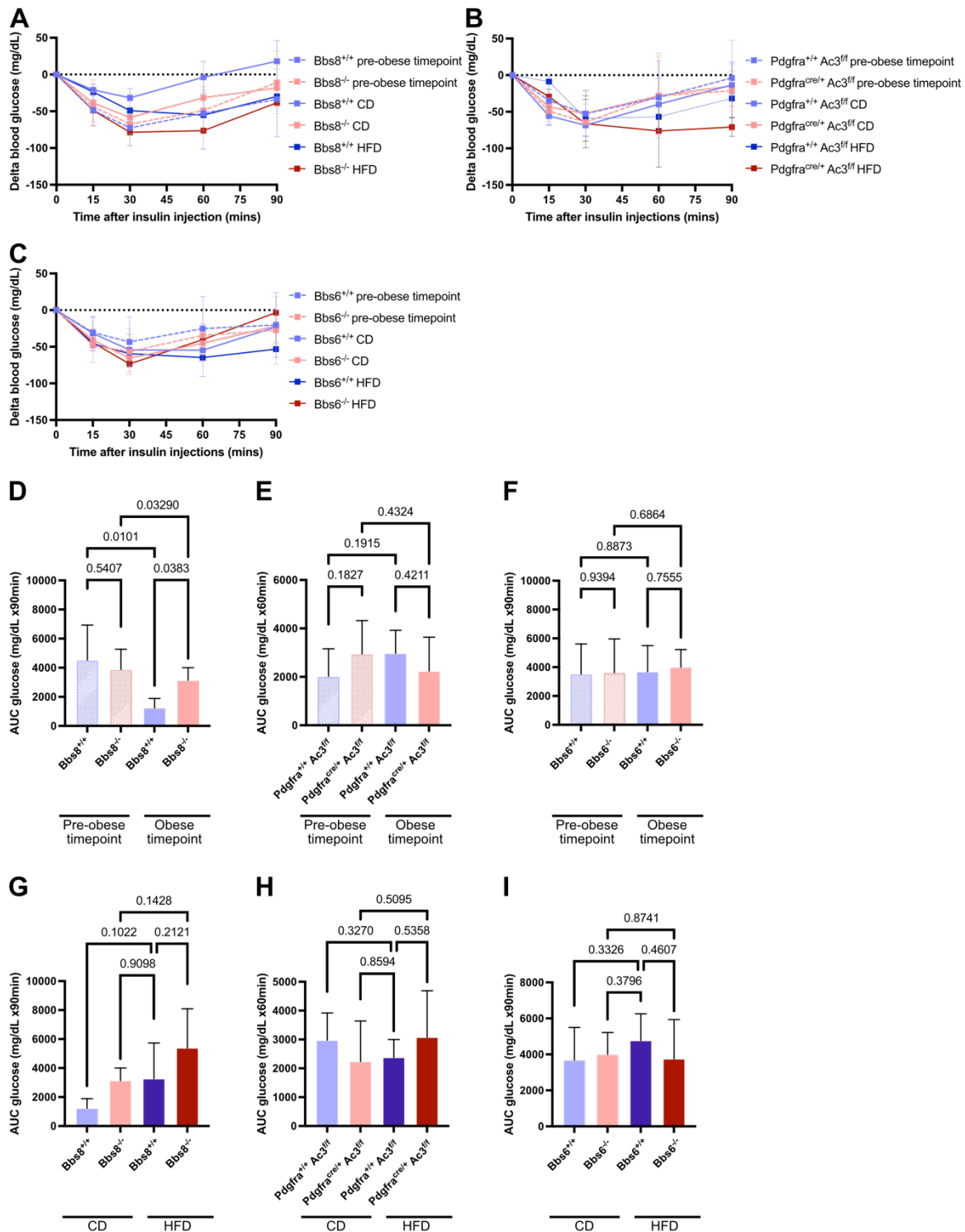
Figure 26: ITT results of different mouse lines at pre-obese and obese timepoints. The experiment starts at the age of 8-weeks, at which point mice are lean. Over 10-12 weeks, mice develop diet- or KO-induced obesity. The metabolic state was measured before and after 7-8 weeks HFD vs CD feeding. **(A-C)** For ITT mice were fasted for 6 h before an intraperitoneal insulin injection with 0.75 U/kg bodyweight. Blood glucose levels during ITT in Bbs8 **(A)**, Pdgfra-Ac3 **(B)**, and Bbs6 **(C)**. Dotted line represents the baseline defined as starting blood glucose levels set to 0. Data are shown as mean ± S.D., n ≥ 2. **(D-I)** Blood glucose levels during ITT were quantified by calculation of corresponding AUC. AUC is calculated as negative peak area below starting value. (D-F) Comparison of pOb and Ob timepoint of single-housed Bbs8 **(D)**, Pdgfra-Ac3 **(E)**, and Bbs6 **(F)** on CD. **(G-I)** Comparison of single-housed Bbs8 **(G)**, Pdgfra-Ac3 **(H)**, and female and male Bbs6 **(I)** mice after 7-8 weeks of HFD or CD feeding. Data are shown as mean ± S.D., p-values were calculated by unpaired t-test with Welch's Correction, n ≥ 2.

In summary, my results show that both *Bbs*-models displayed mild impairment in glucose handling before the onset of obesity. This pre-obese phenotype was not observed in the Pdgfra-Ac3 mouse line. Hence, *Bbs6*- and *Bbs8*-induced ciliary dysfunction results in a primary defect in blood glucose homeostasis, contributing to the disease complexity. Interestingly, loss of *Bbs8* seems to confer protection from severe metabolic deterioration in comparison to DIO mice. In contrast, Pdgfra$^{cre/+}$ Ac3$^{f/f}$ mice displayed equally impaired glucose tolerance despite lower levels of adiposity than DIO mice, indicating an aggravating effect of AC3 ablation. Lastly, my results indicate that obese HFD-fed Bbs6$^{-/-}$ mice experience a diabetic state similar to obese HFD-fed Bbs6$^{+/+}$ mice.

3.5 Lipid toxicity affects the liver secondary to obesity development

Severe obesity leads to the ectopic accumulation of lipids, which is associated with metabolic complications. It is thought that ectopic lipid accumulation starts when WAT expansion reaches its expansion limit and lipids can no longer be stored safely in WAT (Virtue and Vidal-Puig, 2010). Consequently, other organs, such as the liver, can secondarily be affected by obesity. Ectopic lipid accumulation in the liver can lead to nonalcoholic fatty liver disease (NAFLD), which can further by separated into simple nonalcoholic fatty liver (NAFL), also known as hepatic steatosis, and nonalcoholic steatohepatitis (NASH). NAFL is mainly characterized by macrovesicular steatosis in at least > 5 % of hepatocytes, whereas NASH can be distinguished from NAFL by the additional presence of hepatocellular injury in the form of hepatocyte ballooning, inflammation, or fibrosis. NASH can even further progress and lead to hepatic cirrhosis (Bedossa *et al.*, 2012; Cotter and Rinella, 2020). The most common primary causes of NAFLD are obesity, type II diabetes, insulin resistance, and dyslipidemia (Angulo, 2007).

To assess the secondary effects of ciliopathy- versus diet-induced obesity, I examined the liver of the different mouse models using hematoxylin/eosin (HE) staining and histological analysis. Whereas neither CD-fed KO mice nor the HFD-fed WT mice displayed signs of liver steatosis in any of the mouse models, KO mice on HFD covered the full spectrum from none and mild to severe liver steatosis (Figure 27A,C,E). This high interindividual variation was also reflected in the liver weights (Figure 27B,D,F). Thus, liver weight seemed to correlate with the development of liver steatosis. However, I could not detect NAFLD in HFD-fed WT mice, although several studies have shown that HFD feeding leads to NAFLD (Nakamura and Terauchi, 2013; VanSaun *et al.*, 2009). Also here, the time course of 7-8 wks of HFD feeding might not be sufficient to induce hepatic steatosis. VanSaun *et al* addressed this question by examining the development of NAFLD in mice covering a period of 1, 3, 7, 9, 14, and 20 months on HFD. After 3 months of HFD-feeding, liver displayed steatosis, which increased in severity over time until reaching clinical features of NASH by month 9 (VanSaun *et al.*, 2009). Thus, my chosen period (7-8 wks) of HFD feeding in WT mice is simply too short to induce liver steatosis, which also applies to the obese KO mice on CD.
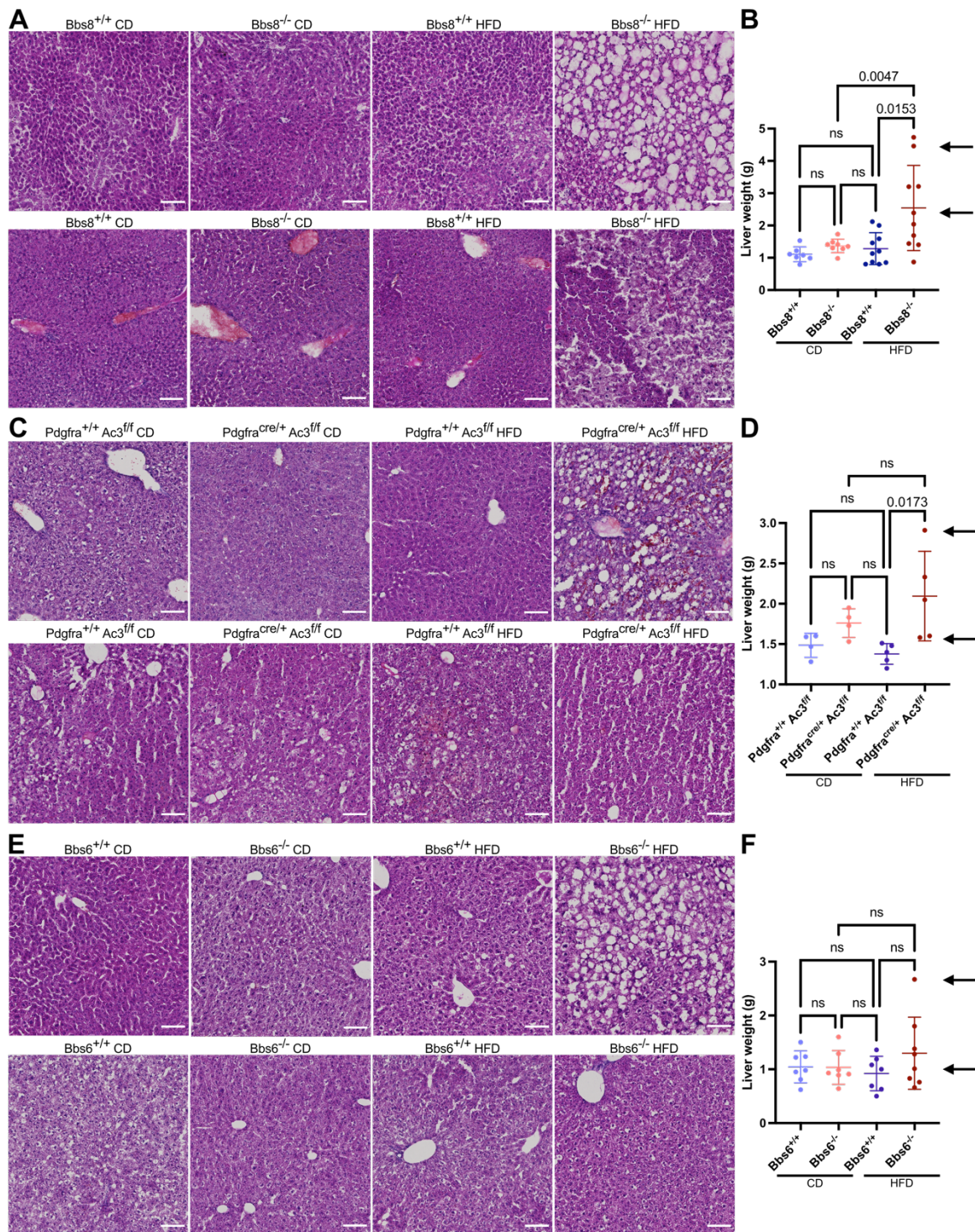
Figure 27: Development of liver steatosis in the different mouse models. Liver was isolated from mice after 7-8 weeks HFD vs CD feeding, fixed with 4 % PFA, and cryopreserved with sucrose before freezing. Cryo-sections were stained with hematoxylin and eosin (HE). **(A)** Exemplary images from Bbs8 mice on HFD or CD. Scale bar: 100 μm. **(B)** Liver weight in Bbs8 mice on HFD or CD. **(C-D)** Equivalent representation for Pdgfra-Ac3 mice on HFD or CD. **(E-F)** Equivalent representation for Bbs6 mice on HFD or CD. Data are shown as mean ± S.D. and with individual data points, p-values were calculated by Šídák's multiple comparisons test, n ≥ 7 (Bbs8), n ≥ 4 (Pdgfra-Ac3), n ≥ 7 (Bbs6). Black arrows indicate data points corresponding to the histological images of HFD-fed KO mice. The higher liver weight always corresponds to the histological image with the highest liver damage.

I then wondered whether the obese KO mice without an additional HFD challenge would develop NAFLD at a later time point. Therefore, I chose the Bbs8 mouse model

to check for NAFLD development during aging. While at age 15 wks, NAFLD was not yet present although mice were already obese, at 24 wks of age, Bbs8$^{-/-}$ mice displayed NAFLD with varying degrees (Figure 28). Since, weight gain in Bbs8$^{-/-}$ starts at 11 wks of age, 15 wks and 24 wks represent 1 and 3 months of obesity induction, respectively. So, the development of NAFLD in Bbs8$^{-/-}$ mice mimics the reported timepoint in HFD-induced NAFLD. Still, I wondered whether the observed ameliorated glucose handling in CD-fed Bbs8$^{-/-}$ compared to HFD-fed Bbs8$^{+/+}$ mice might also protect from NAFLD either by reducing the severity or prolonging the period until onset. This question can only be addressed in future by a time course exceeding the current time frame of the HFD feeding.
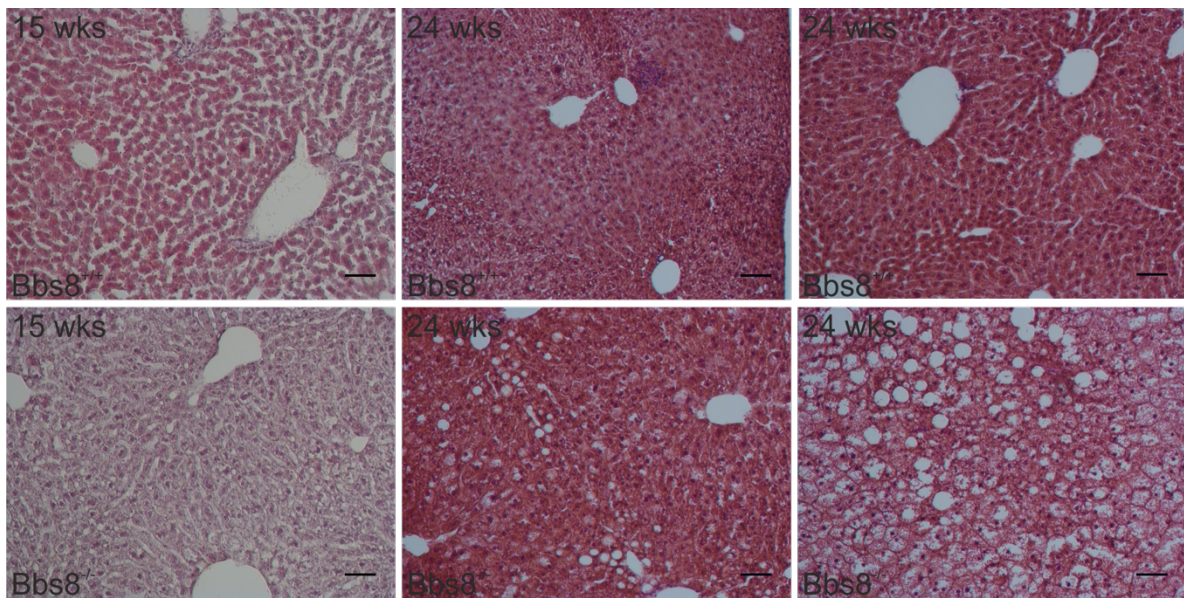
Figure 28: Liver histology shows the development of liver steatosis in Bbs8$^{-/-}$ mice at the age of 24 weeks. Liver isolated from 15 and 24 wks old mice was fixed with 4 % PFA and cryopreserved with sucrose before freezing. Cryo-sections of the liver were stained with hematoxylin and eosin (HE). Macro- and microvesicular steatosis was visible at an age of 24 wks, while at 15 wks, there were no signs of liver steatosis yet. Scale bar: 100µm Objective: 10x.

In summary, these results indicate that NAFLD, develops secondary to obesity and only at a later time point of obesity development. Increased liver weight, which is an indicator for NAFLD, and NAFLD severity was significantly increased in Bbs8$^{-/-}$ and Pdgfra$^{cre/+}$ Ac3$^{f/f}$ on HFD, although some mice continued to display normal liver weight and no NAFLD. HFD-fed Bbs6$^{-/-}$ display the same tendency, but did not reach significance. This is in line with increased adiposity and severe impairment of glucose tolerance in HFD-fed KO mice.

3.6 Adipocyte cell size distribution changes during obesity

The way of WAT expansion critically determines the pathological outcome. In a state of energy surplus, WAT increases its storages capacity in two ways: Adipocytes increase the amount of stored lipids and, thereby, their size, which is termed hypertrophy, or by recruitment of new adipocytes from resident pre-adipocytes to increase the number of adipocytes in the WAT, which is termed hyperplasia (Ghaben

and Scherer, 2019; Haczeyni *et al.*, 2018). Hyperplasia is linked to a metabolically healthy (Arner *et al.*, 2010; Ghaben and Scherer, 2019; Gray and Vidal-Puig, 2007) and hypertrophy to a metabolically non-healthy state of obesity (Vegiopoulos *et al.*, 2017; Virtue and Vidal-Puig, 2010; Ye *et al.*, 2021). I aimed to investigate whether my observed distinct metabolic states could be a result of different WAT expansion. Since gWAT, as part of the visceral WAT, has the biggest impact on metabolism (Berry *et al.*, 2013; Item and Konrad, 2012; Karpe and Pinnick, 2015; Vishvanath and Gupta, 2019), I focused my analysis on this WAT depot using paraffin sections stained with HE (Berry *et al.*, 2014), and analyzed adipocyte size by AdipoQ (Sieckmann *et al.*, 2022)(in revision).

Since the Bbs6$^{+/+}$ mice had shown strong sexual dimorphism in response to HFD, I analyzed whether this was also reflected in WAT morphology. Indeed, I observed a significant difference in the average adipocyte cell size between female and male HFD-fed Bbs6$^{+/+}$ mice (Table 19). Results from the morphology analysis of females and males will thereby be analyzed separately.

Table 19: Average size of adipocytes differed between females and male HFD-fed Bbs6$^{+/+}$ mice. Testing was performed by unpaired Student's t-test.

Condition	Average adipocyte size (µm^2)
Bbs6$^{+/+}$ HFD	0.0054

Young Pdgfra$^{cre/+}$ Ac3$^{f/f}$ mice (7 wks) showed no difference in adipocyte size distribution or in average cell size (Figure 30A,B,E), although AT mass was already increased at this age. This indicates that AT expansion at this early stage is mainly driven by hyperplasia. In contrast, Bbs8$^{-/-}$ mice at 7 wks also showed an increased AT mass, but displayed a shift towards bigger cell sizes, resulting in a significant increase in adipocyte size (Figure 29A,B,E). This increase in cell size matched the average cell size of Bbs8$^{+/+}$ at 15 wks (Figure 29E). With increasing age, both Bbs8$^{-/-}$ and Pdgfra$^{cre/+}$ Ac3$^{f/f}$ mice became more obese on CD (Chapter 3.2.1,Figure 12Figure 13Figure 14), which was also evident in a significantly higher adipocyte size and a strong shift in adipocyte size distribution towards bigger cell sizes (Figure 29Figure 30A,B,E). The latter was also observed for Bbs8$^{+/+}$ mice, albeit less pronounced (Figure 29A,B,E), indicating that adipocyte hypertrophy is also occurring during aging. This age-effect was not detected in the other mouse lines. Therefore, the Bbs8 mouse line might generally be more prone to hypertrophic growth. Since Bbs6$^{-/-}$ mice only gained weight at late age timepoints, I analyzed only AT at the age of 50 wks: Bbs6$^{-/-}$ mice displayed a slight shift in adipocyte size distribution, resulting in a significant increase in cell size (Figure 31A-C). In summary, all mice that became obese expanded WAT by hypertrophy.

To determine if the degree of hypertrophy is altered by ciliary dysfunction, I investigated the WAT morphology between diet- and ciliopathy-induced obesity. First, I compared obese Bbs8$^{-/-}$ mice on CD with DIO Bbs8$^{+/+}$ mice (which reached a similar

body weight): In line with the equal total gWAT mass, DIO in Bbs8$^{+/+}$ mice mimicked the adipocyte size phenotype of Bbs8$^{-/-}$ mice on CD, while HFD in Bbs8$^{-/-}$ mice led to most severe adiposity, accompanied by a further increase in cell size (Figure 29C,D,F). Thus, WAT expanded by hypertrophy, demonstrating that obesity in Bbs8 mice shifts WAT expansion towards hypertrophy independent of the trigger for obesity development and independent of the genotype. Nevertheless, I cannot completely rule out that a slight change in the balance between hyperplasia and hypertrophy exists, but is not detectable with this approach. These results also indicate that the protection from glucose intolerance in CD-fed Bbs8$^{-/-}$ mice is not a result of a healthy WAT expansion as proposed for hyperplasia-driven AT expansion in Bbs12$^{-/-}$ (Marion *et al.*, 2012). Bbs12 is part of the BBS chaperonin-complex, while Bbs8 is part of the BBSome. Therefore, these two complexes might play different roles in regulating AT homeostasis.

Figure 29: Analysis of adipose tissue morphology reveal hypertrophic adipocytes in diet- and Bbs8$^{-/-}$-induced obesity. Paraffin sections of gWAT from mice at different ages (7,15, and 25 wks) and after 7-8 weeks of HFD or CD feeding were stained with hematoxylin and eosin (HE). Adipocyte sizes were determined by image-based analysis with AdipoQ (Sieckmann *et al.*, 2022)(in revision). The average adipocyte size and the frequency of grouped size ranges were calculated. **(A)** Representative images from female Bbs8 mice aged 7, 15, and 25 wks. Due to a week staining, images were converted to black and white images and contrast was enhanced. Scale bar: 100 μm. **(B)** Adipocyte size distribution

in Bbs8 mice during aging. **(C)** Representative images from male Bbs8 mice on HFD or CD. Scale bar: 100 μm. **(D)** Adipocyte size distribution of Bbs8 mice on HFD or CD. **(E)** Average size of adipocytes of Bbs8 mice during aging. **(F)** Average size of adipocytes of Bbs8 mice on HFD or CD. Data are shown as mean ± S.D. and with individual data points, n ≥ 6.

Comparing different causes of obesity in Pdgfra-Ac3 mice displayed a significant increase in adipocyte size in all three obese conditions (Pdgfra$^{cre/+}$ Ac3$^{f/f}$ CD and HFD, Pdgfra$^{+/+}$ Ac3$^{f/f}$ HFD) (Figure 30C,D,E), but in varying degrees in line with variations in total gWAT mass (Chapter 3.2.2,Figure 18). As gWAT mass was not comparable between CD-fed Pdgfra$^{cre/+}$ Ac3$^{f/f}$ and HFD-fed Pdgfra$^{+/+}$ Ac3$^{f/f}$, it is not clear whether any morphological differences are based on alteration in AT expansion or are just a consequence of the degree of AT mass expansion, which will increasingly divert from the homeostatic expansion. I will investigate this possibility in more detail later. Nevertheless, adipocyte size and its distribution showed obesity-dependent expansion dominated by hypertrophy similar to Bbs8.

Figure 30: Analysis of adipose tissue morphology reveal hypertrophic adipocytes in diet- and Pdgfra^{cre/+} Ac3^{f/f}-induced obesity. Paraffin sections of gWAT from mice at different ages (7,15, and 25 wks) and after 7-8 weeks of HFD or CD feeding were stained with hematoxylin and eosin (HE). Adipocyte sizes were determined by image-based analysis with AdipoQ (Sieckmann *et al.*, 2022)(in revision). The average adipocyte size and the frequency of grouped size ranges were calculated. **(A)** Representative images from female Pdgfra-Ac3 mice aged 7, 15, and 25 wks. Due to a week staining,

images were converted to black and white images and contrast was enhanced. Scale bar: 100 µm. **(B)** Adipocyte size distribution in Pdgfra-Ac3 mice during aging. **(C)** Representative images from male Pdgfra-Ac3 mice on HFD or CD. Scale bar: 100 µm. **(D)** Adipocyte size distribution of Pdgfra-Ac3 mice on HFD or CD. **(E)** Average size of adipocytes of Pdgfra-Ac3 mice during aging. **(F)** Average size of adipocytes of Pdgfra-Ac3 mice on HFD or CD. Data are shown as mean ± S.D. and with individual data points, n ≥ 4.

As Bbs6 is part of the BBS chaperonin-complex, I investigated whether hyperplasia predominates in Bbs6$^{-/-}$ similar to Bbs12$^{-/-}$ (Marion *et al.*, 2012). This would lower the hypertrophic degree in Bbs6$^{-/-}$ mice compared to weight-matched control mice. For the analysis of obesity in Bbs6$^{-/-}$, I focused on HFD-fed mice, as only then obesity was induced. The analysis of the effect of HFD feeding in female Bbs6$^{-/-}$ mice surprisingly revealed no significant change in adipocyte size (Figure 31D,E,G), although females Bbs6$^{-/-}$ on HFD had significantly more gWAT mass, demonstrating that these mice maintained AT homeostasis by expanding via hyperplasia. In male mice, HFD feeding resulted in hypertrophy, indicated by increased adipocyte size (Figure 31D,F,H), whereas WAT in female Bbs6$^{-/-}$ maintained the balance of hyperplasia and hypertrophy as in Bbs6$^{+/+}$ mice on CD. Interestingly, male Bbs6$^{-/-}$ on HFD demonstrated a tendency towards smaller cell sizes (Figure 31H), also observable by the increased frequency in the smaller cell size ranges (350-2000 µm^2) (Figure 31F) compared to Bbs6$^{+/+}$ mice on HFD, although this did not reach significance due to low animal numbers. Nevertheless, this might indicate that hyperplasia is also increased in male Bbs6$^{-/-}$ mice. Therefore, I conclude that Bbs8$^{-/-}$ and Bbs6$^{-/-}$ show opposing effects in the way of AT expansion. While Pdgfra$^{cre/+}$ Ac3$^{f/f}$ and Bbs8$^{-/-}$ mice expanded mainly by hypertrophy, Bbs6$^{-/-}$ mice displayed a tendency towards increased hyperplasia, but this did not result in an ameliorated glucose handling compared to DIO. This finding highlights distinct roles of BBSome and BBS chaperonin complex for WAT remodeling.
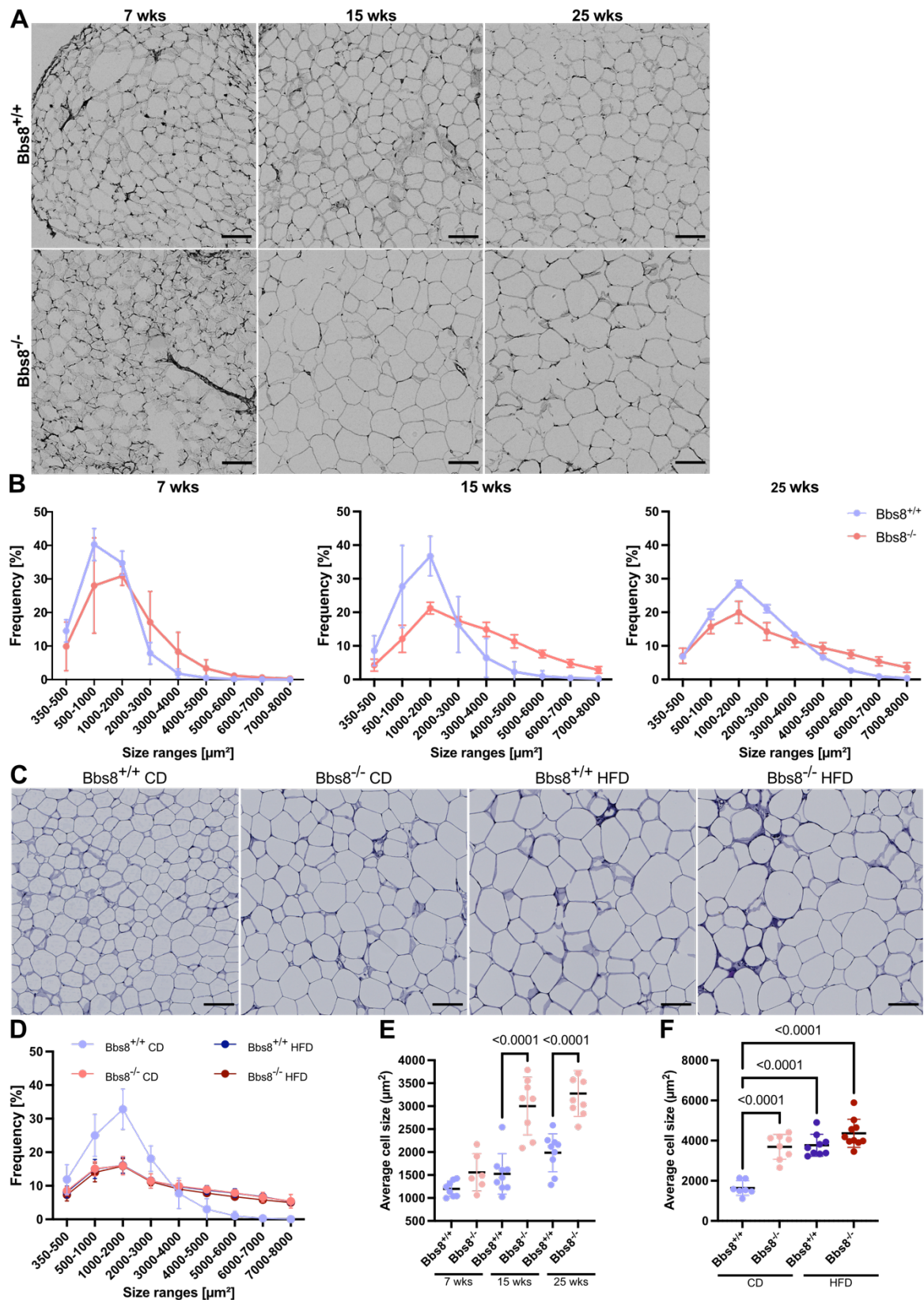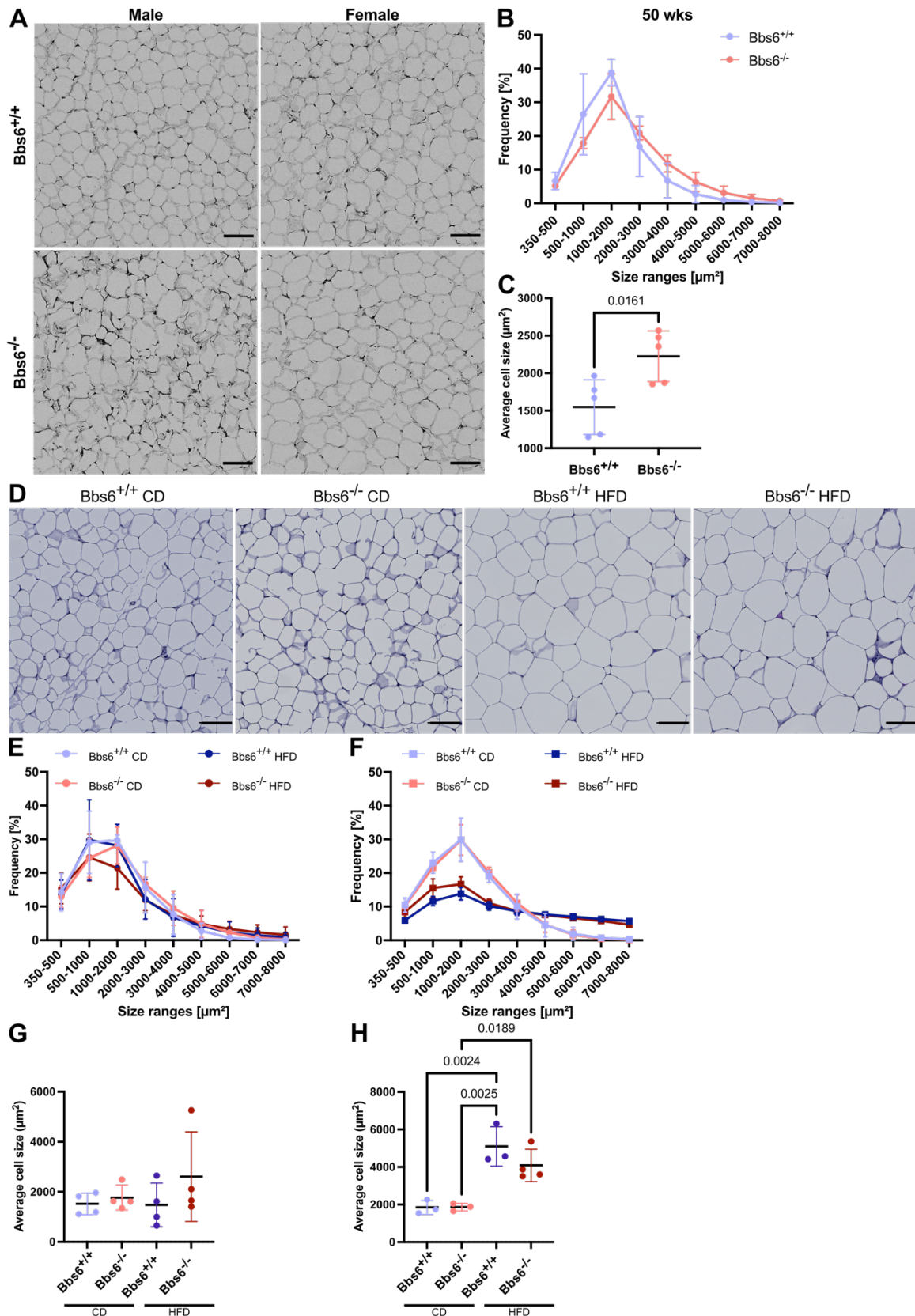
Figure 31: Analysis of adipose tissue morphology reveal hypertrophic adipocytes in diet- and Bbs6^{-/-}-induced obesity. Paraffin sections of gWAT from Bbs6 mice at 50 wks of and after 7-8 weeks of HFD or CD feeding were stained with hematoxylin and eosin (HE). Adipocyte sizes were determined by image-based analysis with AdipoQ (Sieckmann *et al.*, 2022)(in revision). The average adipocyte size and the frequency of grouped size ranges were calculated. **(A)** Representative images from 50 wks old

Bbs6 mice. Due to a week staining, images were converted to black and white images and contrast was enhanced. Scale bar: 100 µm. **(B)** Adipocyte size distribution in 50 wks old Bbs6 mice. **(C)** Average size of adipocytes of 50 wks old Bbs6 mice. **(D)** Representative images from male Bbs6 mice on HFD or CD. Scale bar: 100 µm. **(E)** Adipocyte size distribution of female Bbs6 mice on HFD or CD. **(E)** Adipocyte size distribution of male Bbs6 mice on HFD or CD. **(G)** Average size of adipocytes of female Bbs6 mice on HFD or CD. **(H)** Average size of adipocytes of male Bbs6 mice on HFD or CD. Data are shown as mean ± S.D. and with individual data points, n ≥ 4.

Obesity in CD-fed Bbs8$^{-/-}$ and Pdgfra$^{cre/+}$ Ac3$^{f/f}$ mice led to opposing effects on glucose tolerance. Therefore, I compared the adipocyte cell size and gWAT weight from Bbs8$^{-/-}$ and Pdgfra$^{cre/+}$ Ac3$^{f/f}$ mice on CD. Average cell size and gWAT weight of Bbs8$^{-/-}$ mice were significantly increased compared to Pdgfra$^{cre/+}$ Ac3$^{f/f}$ mice (Figure 32A,B). Since both parameters would indicate an increased risk for metabolic complications in Bbs8$^{-/-}$ compared to Pdgfra$^{cre/+}$ Ac3$^{f/f}$ mice, it is even more surprising that metabolic glucose handling did not reflect this.
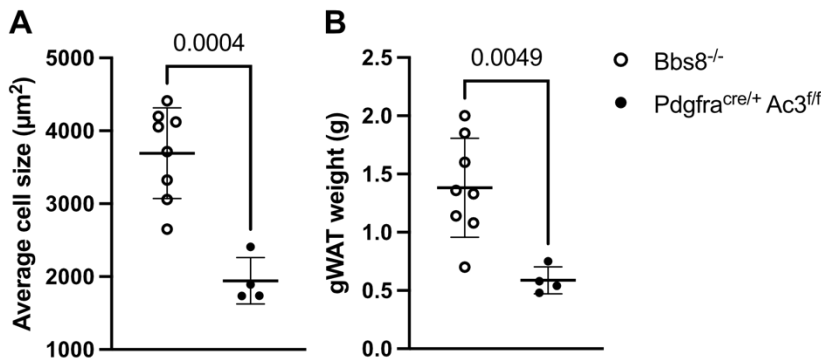
Figure 32: Average cell size and total gWAT mass is increased in CD-fed Bbs8$^{-/-}$ compared to Pdgfra$^{cre/+}$ Ac3$^{f/f}$. Total gWAT was isolated, paraffin embedded, and paraffin sections were stained with hematoxylin and eosin (HE). Adipocyte sizes were determined by image-based analysis with AdipoQ (Sieckmann *et al.*, 2022)(in revision). **(A)** Average cell size of Bbs8$^{-/-}$ compared to Pdgfra$^{cre/+}$ Ac3$^{f/f}$. **(B)** Total gWAT mass of Bbs8$^{-/-}$ compared to Pdgfra$^{cre/+}$ Ac3$^{f/f}$. Data are shown as mean ± S.D. and with individual data points, n ≥ 4.

Adipocyte size can clearly identify hypertrophy, but hypertrophy and hyperplasia contribute together to WAT expansion. Differences in the balance between those two expansion ways is only possible to detect if groups display the same total WAT, as for Bbs8$^{-/-}$ and Bbs8$^{+/+}$ mice on CD and HFD, respectively. Such comparable groups were not present in Pdgfra-Ac3 and in female Bbs6 mice, where the WAT weight was different. Therefore, I analyzed the correlation of WAT morphology to total WAT mass as an additional assessment of a ciliopathy-dependent change in WAT expansion way. Such a relationship has been investigated previously, with some reports suggesting a linear- (Parlee *et al.*, 2014) and others a more complex relationship (Arner *et al.*, 2010; Jo *et al.*, 2009; Spalding *et al.*, 2008). To this end, I combined all data per mouse line, including all analyzed ages and diets. Adipocyte volume was calculated based on the average adipocyte size, assuming a spherical form, and plotted against the total gWAT mass. Since only the Bbs8 mouse line seemed to reach the limit of maximal adipocyte volume, I simply excluded the values reaching this limitation in Bbs8 mice and used linear regression to compare expansion between WT and KO mice.

I compared the slope of the linear regression between WT and KO mice to reveal differences in the way of expansion: a steep slope indicates hypertrophy and a gentle slope indicates hyperplasia (Parlee *et al.*, 2014). The slope of the linear regression was not significantly different between WT and KO mice in Bbs8 and Pdgfra-Ac3 (Figure 33A,B), but differed significantly (p=0.05) in Bbs6 mouse line (Figure 33C). The slope of Bbs6$^{+/+}$ is steeper (more hypertrophy) than the slope for Bbs6$^{-/-}$ mice (more hyperplasia). This supports my previous conclusion that hyperplasia is increased in Bbs6$^{-/-}$ mice. Pdgfra-Ac3 displayed the least variation, indicated by high R^2 values. Also, the regression lines between the genotypes are perfectly overlapping. This clearly answers a previously open question that the morphological differences observed between CD-fed Pdgfra$^{cre/+}$ Ac3$^{f/f}$ and HFD-fed Pdgfra$^{+/+}$ Ac3$^{f/f}$ are a consequence of the varying degree of total AT mass, which will increasingly divert from the homeostatic expansion way. A similar trend was also observed in the Bbs8 mouse line, but the x-y interceptions between the regression lines were different, probably due to a high spread of values indicated by low R^2 values. Of note, I excluded all Bbs8 mice values corresponding to gWAT masses exceeding 3 g, as these did not follow a linear relationship. Surprisingly, the few gWAT masses above 3 g in Pdgfra-Ac3 mouse line still continue to follow linear correlation, indicating either mouse line-specific limits of maximal cell volume a genotype-specific effect, resulting in different cell size limitations.
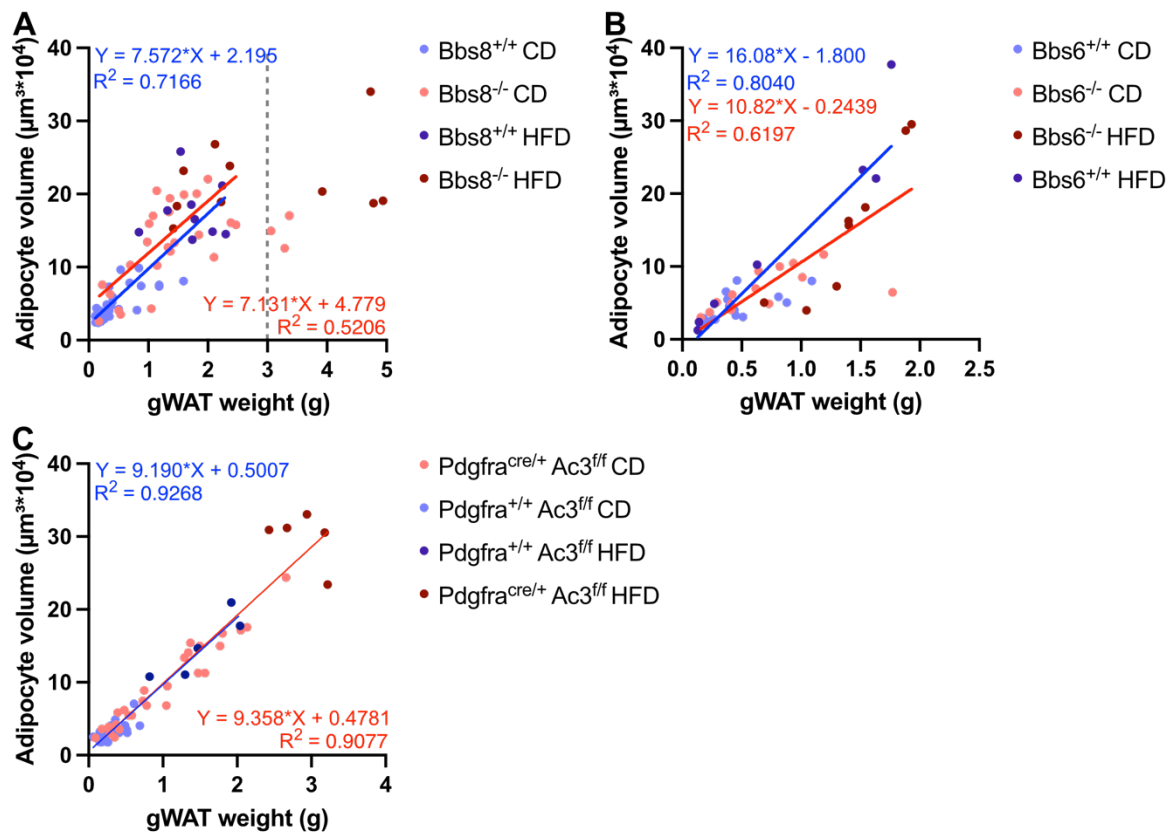
Figure 33: The linear relationship between average adipocyte volume and total gWAT mass from WT and KO mice. Average adipocyte volume was calculated by assuming a spherical form based on the average cell size determined by the histological analysis. **(A-C)** Data points and linear regression line of WT and KO mice of Bbs8 **(A)**, Bbs6 **(B)**, and Pdgfra-Ac3 **(C)**. A steeper or gentler slope for KO-mice compared to WT-mice indicate an increase in hypertrophy or hyperplasia, respectively. So, Bbs6$^{-/-}$ mice expands with increased contribution of hyperplasia, while KO mice in Bbs8 and Pdgfra-Ac3. Data points are color-coded by genotype and diet. Linear regression formula and R^2 values of WT (blue) and KO (red). Dotted line in **(A)** represents limit for excluded values not following linear correlation.

In summary, WAT expansion during obesity is mainly driven by hypertrophy in all mice, but the balance is slightly shifted towards hyperplasia in Bbs6$^{-/-}$ mice, in line with reported hyperplasia-driven WAT expansion in Bbs12$^{-/-}$ mice (Marion *et al.*, 2012). BBS6 and BBS12 are both components of the BBS chaperonin complex, while BBS8 is part of the BBSome. Bbs8$^{-/-}$ mice did not show signs of increased hyperplasia, indicating a BBS chaperonin complex-specific effect on WAT expansion. Bbs8$^{-/-}$ and Pdgfra$^{cre/+}$ Ac3$^{f/f}$ mice displayed a clearly hypertrophic WAT expansion, which increased with total gWAT mass. Although obesity was already further advanced in CD-fed Bbs8$^{-/-}$ compared to Pdgfra$^{cre/+}$ Ac3$^{f/f}$ mice, metabolic glucose impairment was worse in Pdgfra$^{cre/+}$ Ac3$^{f/f}$ mice. Thus, ciliary dysfunction in Bbs8$^{-/-}$ might alter the fate of adipocytes, resulting in a metabolically healthy state despite obesity and hypertrophy. In contrast, ciliary dysfunction in Pdgfra$^{cre/+}$ Ac3$^{f/f}$ might alter the fate of adipocytes, resulting in a metabolically unhealthy state even at a mild obesity state (Chapter 3.2.2,Figure 18).

Analysis of adipocyte size is well suited to detect hypertrophy, but since WAT expansion is a combination of hypertrophy and hyperplasia and hypertrophic expansion worsens with increasing WAT mass and time, hyperplasia might be harder

to detect, especially if not all parameters are the same between groups, e.g., variations in WAT mass. In future experiments, the balance between hyperplasia and hypertrophy could be further elucidated by administration of bromdesoxyuridin (BrdU) over a defined time period. BrdU will be incorporated into the newly synthesized DNA during replication, enabling tracing of new cells and, thereby, hyperplasia via immunohistochemistry.

3.7 Immunophenotype in WAT

Adipocyte hypertrophy and metabolic dysfunction during obesity have been causally linked with the development of inflammation within the AT. Here, macrophages (MΦs) are the immune cell population, which predominantly contributes to the inflammatory phenotype: they are the most abundant immune cell type accumulating during obesity and secrete most of the inflammatory cytokines (Chen *et al.*, 2021a; Félix *et al.*, 2021; Lee and Olefsky, 2021; Weisberg *et al.*, 2003). Therefore, I investigated the WAT immune cell phenotype focusing on MΦs. MΦs in the WAT are of different origin and fulfil distinct functions: Tissue-resident MΦs are derived from multipotent erythro-myeloid progenitors (EMP) formed in the yolk sac during embryogenesis and are thought to maintain tissue homeostasis (Gomez Perdiguero *et al.*, 2015; Wu and Hirschi, 2020), whereas MΦs derived from hematopoietic stem cells (HSC) are mainly recruited from circulating monocytes in a CC-chemokine ligand 2 (CCL2)-dependent manner during obesity (Weisberg *et al.*, 2006). Of these HSC-derived MΦ, inflammatory CDIIc$^+$ cells (δ-MΦ) were reportedly nearly undetectable in young lean mice, but strongly increased during obesity. The δ-MΦ population show high lipid metabolism compared to the other subpopulations (Chen *et al.*, 2021a), which might be a response to lipid leakage from damaged or apoptotic adipocytes in hypertrophic WAT.

The analysis of MΦ subpopulations in WAT was performed by flow cytometry in cooperation with the group of Elvira Mass. To gate for total MΦs, we used the following combination of markers: Lin$^-$ (Lin = Ly6G$^+$/SilecF$^+$/CD3$^+$/CD19$^+$/NKp46$^+$, excluding other immune cell types, such as granulocytes, eosinophils, natural killer cells, B- and T-cells), CD45$^+$, F4/80$^+$, and CDIIb$^+$. Then, the F4/80$^+$ CDIIb$^+$ gate was separated into four different MΦ subpopulations (Figure 34). Two of them represent resident MΦs defined as T-cell immunoglobulin and mucin domain-containing protein 4$^+$ (TIM4) (Cox *et al.*, 2021; Gomez Perdiguero *et al.*, 2015) and cDIIc$^-$ cells that can be separated based on the major histocompatibility complex II (MCHII) marker: TIM4$^+$/CDIIc$^-$/MCHII$^-$ ("α") and TIM4$^+$/CDIIc$^-$/MCHII$^+$ ("β"). The other two subpopulations represent HSC-derived MΦs defined as TIM4$^-$ cells. These can be further separated based on the presence of the markers CDIIc and MCHII: TIM4$^-$/CDIIc$^-$/MCHII$^+$ ("γ") and TIM4$^-$/CDIIc$^+$/MCHII$^+$ ("δ").
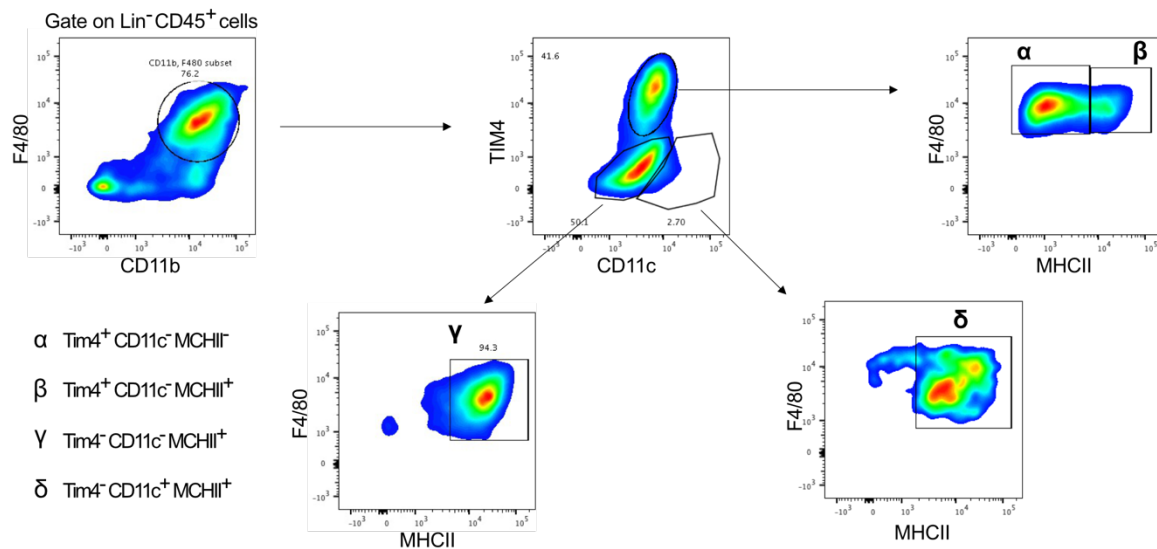
Figure 34: Gating strategy to separate the macrophage subpopulations α, β, γ, and δ. SVF from murine gWAT was isolated, stained with fluorescent antibodies, and analyzed via flow cytometry. Final gating strategy for separation into α, β, γ, and δ subpopulations of pre-gated single, live, and Lin⁻ CD45⁺ cells. The markers F4/80 and CD11b select all macrophages (MΦ), while TIM4, CD11c, and MHCII allow to distinguish between the different subpopulations as indicated. Black arrows highlight the gate that was used to further differentiate in the next gate. Gating strategy was established in cooperation with the Mass group.

There are different ways to compare flow cytometry data: 1) Frequency of a certain superordinate group e.g., CD45⁺ cells, 2) cells per WAT depot (number cells in total tissue), or 3) cell density (number cells per g tissue) (Bapat *et al.*, 2019; Chen *et al.*, 2021a) (Félix *et al.*, 2021; Lumeng *et al.*, 2008). The drawback of method 1 is that CD45⁺, HSC-derived MΦs are known to infiltrate WAT during obesity, whereby total CD45⁺ cells will be increased and subsequently the frequency of subpopulations that remain unchanged will apparently decrease. Method 2 takes the whole WAT depot into account. Mice with increased WAT mass will most likely also contain different cell numbers. Since there are huge variations in WAT mass between individuals and to an even larger extent between lean and obese mice, this value is difficult to compare. The only advantage of this value is that it can give insight whether a certain subpopulations cell number remains stable independent of WAT expansion. Method 3 offers a comparable value, which is normalized to a defined tissue volume. Since WAT mass dramatically increases in obese mice, we decided to use method 3 and calculated the density of MΦs in WAT based on the cell number per g of tissue for a meaningful comparison.

First, I investigated the effect of ciliary dysfunction on macrophage subpopulation in the WAT at different timepoints in Bbs8 mice. Bbs8⁻/⁻ mice at 12 wks of age showed not yet any significant differences in the density of MΦ subpopulations, but at 25 wks Bbs8⁻/⁻ mice display a significant increase in the HSC-derived γ and δ MΦ subpopulations and a decrease in the resident β MΦ subpopulation compared to control mice (Figure 35A,B). Since MΦ populations in Bbs8⁻/⁻ mice were only significantly different at a late timepoint, I only analyzed this later timepoint in the other two mouse models. Bbs6⁻/⁻ mice displayed no significant difference in any subpopulation (Figure 35C) and Pdgfra^cre/+ Ac3^f/f mice showed only a significant

change in the β population, which was decreased compared to control mice (Figure 35D). The γ population displayed a tendency towards an increase, but significance was not reached due to high variances. Significant changes were only detected in Bbs8^{-/-} and Pdgfra[cre/+] Ac3[f/f] mice at 25 wks with established obesity, whereas the MΦ subpopulations in lean 25 wks old Bbs6^{-/-} and 12 wks old Bbs8^{-/-} mice remained unchanged compared to the respective control mice. Thus, the observed changes in subpopulation might reflect obesity-related changes independent of the genotype.
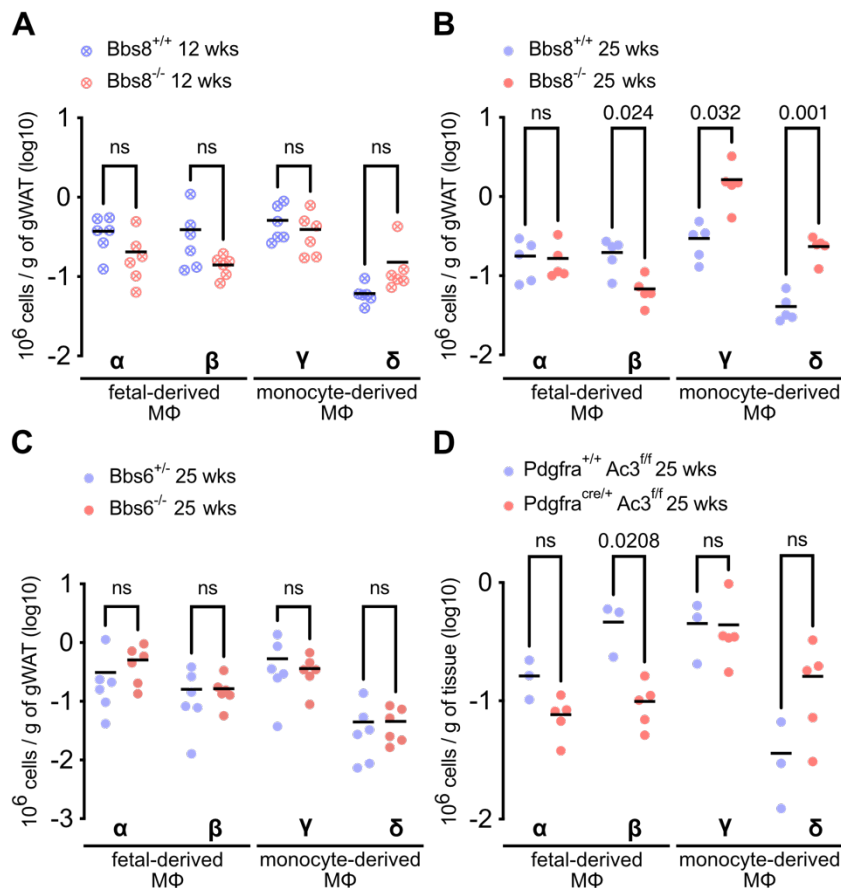
Figure 35: Density of fetal- and monocyte-derived macrophage subpopulations is changed in WAT of obese ciliopathy models. SVF from murine gWAT was isolated from mice to analyze macrophage (MΦ) subpopulations by flow cytometry. Lin^{-} CD45^{+} F4/80^{+} CDIIb^{+} cells mark MΦs, which can be further separated into four subpopulations by TIM4, CDIIc, and MCHII. Results were calculated as number of cells per g of gWAT tissue, based on cell counting and the frequency of live cell gate. **(A)** Number of MΦ subpopulations in 12 wks old Bbs8 mice. **(B-D)** Number of MΦ subpopulations in 25 wks old Bbs8 **(B)**, Bbs6 **(C)**, and Pdgfra-Ac3 mice **(D)**. Data are shown as mean with individual data points, n ≥ 3; p-values were calculated by Šídák's multiple comparisons test. Experiments were performed in cooperation with Vera Beckert (Bbs8 & Bbs6) and Nikola Makdissi (Pdgfra-Ac3) from the Mass lab. Lin: Ly6G, SilecF, CD3, CD19, and NKp46.

Next, I compared MΦ subpopulations isolated from gWAT and iWAT in ciliopathy- and diet-induced obesity. I detected significant changes in MΦ subpopulations in Bbs8 mice: HSC-derived MΦs (γ & δ) were significantly increased in gWAT and iWAT of highly obese Bbs8^{-/-} mice on HFD (Figure 36A,B). This is in line with previous reports describing that HSC-derived MΦs are massively infiltrating WAT during DIO (Chen *et al.*, 2021a; Félix *et al.*, 2021; Weisberg *et al.*, 2003). In contrast, obesity in Bbs8^{-/-} mice

on CD or Bbs8$^{+/+}$ mice on HFD did not induce this infiltration. Bbs8$^{-/-}$ mice on CD were 18-20 wks old, but previous experiments after 25 wks of age showed elevated density of γ and δ MΦs (Figure 35B). These results recapitulate that inflammatory recruitment of HSC-derived MΦs is a secondary effect of obesity, which develops over time and increases with severity of obesity. Thus, similar to the development of NAFLD, my chosen period (7-8 wks) for obesity development is too short to induce infiltration by HSC-derived MΦs exceeding normal tissue density. Since total WAT mass increased, in turn the total number of HSC-derived MΦs has increase in DIO and Bbs8$^{-/-}$ mice to maintain the tissue density. Comparison of weight-matched wildtype and Bbs12$^{-/-}$ mice both under HFD feeding, revealed a beneficial effect of BBS on WAT inflammation (Marion *et al.*, 2012). Hence, although inflammation definitely occurs with increasing severity and time of obesity in Bbs8$^{-/-}$ mice, the degree of inflammation might be reduced compared to equally obese Bbs8$^{+/+}$ mice at later stages. So far, the comparable degree of obesity in Bbs8$^{-/-}$ mice on CD and Bbs8$^{+/+}$ mice on HFD was not sufficient to induce γ or δ MΦs infiltration above normal tissue density, with HSC-derived MΦs numbers increasing equally with WAT tissue expansion. So, I cannot draw the conclusion that loss of BBS8 has a beneficial effect on WAT inflammation, until I compared more severely affected later timepoints during obesity.

Fetal-derived MΦs (α & β) were significantly decreased in gWAT and iWAT of genotype- and diet-induced obesity mice compared to lean Bbs8$^{+/+}$ mice on CD (Figure 36A,B). Only the β subpopulation isolated from iWAT did not reach significance, although a similar trend was present (Figure 36B). Obese Bbs8$^{-/-}$ mice on CD and Bbs8$^{+/+}$ mice on HFD with similar body weight displayed an equally reduced density of the α and β subpopulations (Figure 36A,B). Therefore, obesity seems to be the driver of the observed reduction in these MΦ subpopulations. Little is known about the role of resident MΦs during obesity, as most literature focusses on monocyte-derived MΦs or does not discriminate between the different ontogeny. It has been suggested that resident MΦs do not respond to HFD with increased proliferation or apoptosis, but maintain their total cell number (Félix *et al.*, 2021). In turn, an increase in total WAT mass would lead in a reduced density of tissue-resident MΦs, as I observed in my obese mouse models (Figure 36A,B). To verify this finding, I also calculated the number of cells per total tissue (method 2). This normalization revealed depot-dependent differences. There was no significant difference between fetal-derived MΦ numbers per total gWAT. However, in iWAT, a significant increase in the α and β subpopulations in massively obese Bbs8$^{-/-}$ mice on HFD was observed, whereas obese Bbs8$^{-/-}$ mice on CD and Bbs8$^{+/+}$ mice on HFD showed only a tendency towards increased α MΦ numbers compared to lean control mice, but this did not reach significance (Figure 37). The β subpopulation showed a trend towards higher cell numbers in Bbs8$^{-/-}$ compared to Bbs8$^{+/+}$ mice on both diets (Figure 37). These findings hint towards depot-dependent differences: Resident MΦs proliferate in response to a higher energy intake in iWAT, but not in gWAT, which might contribute to the distinct associated metabolic outcomes. Specific ablation of resident MΦs via conditional KO has been shown to result in reduced WAT mass. It was also shown that resident MΦs stimulate hypertrophic adipocyte expansion via production of PDGFcc and

consequently loss of resident MΦs resulted in an impairment in adipocytes lipid uptake (Cox *et al.*, 2021). Thus, resident MΦs critically regulate WAT expansion, highlighting their key role in WAT remodeling. The tendency of increased numbers of the β MΦs in Bbs8$^{-/-}$ mice is the only indication of a possibly protective effect of the genotype, which could contribute to the improved metabolic outcome, as observed by the maintenance of pre-obese glucose tolerance levels upon obesity development (Chapter 3.4). However, the degree of AT hypertrophy was not altered in Bbs8$^{-/-}$ compared to control mice (Chapter 3.6). Since, there was no change in hypertrophy, the increased β MΦs in Bbs8$^{-/-}$ mice might not affect lipid uptake, but might fulfill a different role. Based on this observation, I hypothesize that α and β MΦs have distinct roles, affecting WAT expansion and metabolism, respectively. Further investigation is needed to delineate functional roles of α and β subpopulations. Inducible depletion of resident MΦ followed by a reconstitution of either α or β MΦ *in vivo* or *ex vivo* will shed light on their specific roles.

In the other two ciliopathy models, Bbs6 and Pdgfra-Ac3, I detected no significant difference in any MΦ subpopulation (Figure 36C-F). Since Bbs6$^{-/-}$ mice remained lean, it is not surprising that obesity related-changes are not present (Figure 36C,D). While Pdgfra-Ac3 displayed similar weight trends than Bbs8 mice, the absolute weight gain of Pdgfra$^{cre/+}$ Ac3$^{f/f}$ mice on HFD reached about half of the weight gain of Bbs8$^{-/-}$ mice on HFD (Chapter 3.2.2,Figure 16Figure 18). Hence, they also did not reach sufficiently high obesity levels to induce γ or δ MΦ infiltration (Figure 36E,F).

In summary, severity of and the time frame for obesity development was not sufficient to induce HSC-derived MΦs infiltration indicative for inflammation, except in the most obese Bbs8$^{-/-}$ mice on HFD and Bbs8$^{-/-}$ mice at a late age of 25 wks. Generally, Bbs8$^{-/-}$ mice developed inflammation over time with increasing obesity as previously described for obese WT mice. Therefore, loss of BBS8 does not protect from development of WAT inflammation. Whether the severity of tissue inflammation is reduced in Bbs8$^{-/-}$ mice could not be addressed due to a lack of weight-matched control in an inflammatory obesity range. To examine the effect of ciliary dysfunction on WAT inflammation, the timeframe for obesity development to induce inflammation, γ and δ MΦs infiltration, and NAFLD needs to be increased in future experiments. Then, cytokine levels in collected blood and WAT tissue samples could be used additionally to examine the inflammatory state of the mice. Preliminary data from gWAT supernatant displayed an increase in monocyte chemoattractant protein 1 (MCP-1, also known as CCL2) in obese HFD-fed ciliopathy models, except Bbs8$^{-/-}$ mice which retained a similar MCP-1 level compared to mice on CD and Bbs8$^{+/+}$ mice on HFD. Hence, modulation of inflammation in Bbs8$^{-/-}$ mice remains a possibility that needs to be explored further. The reduction in resident MΦs density is a consequence of WAT expansion: Resident MΦs maintained their absolute cell numbers in gWAT and slightly increased them with obesity in iWAT, which was, however, not sufficient to completely compensate for overall reduction in density. The resident β MΦ population displayed an additional, genotype-dependent increase in Bbs8$^{-/-}$ mice. Also, obese Bbs8$^{+/+}$ mice showed a tendency towards an increase in β MΦs without reaching significance. If this increase in resident β MΦ numbers in iWAT is responsible for a reduction in metabolic

complication upon iWAT expansion, the genotype-dependent increase in β MΦ numbers might represent an indication for a protective effect of BBS8 loss.
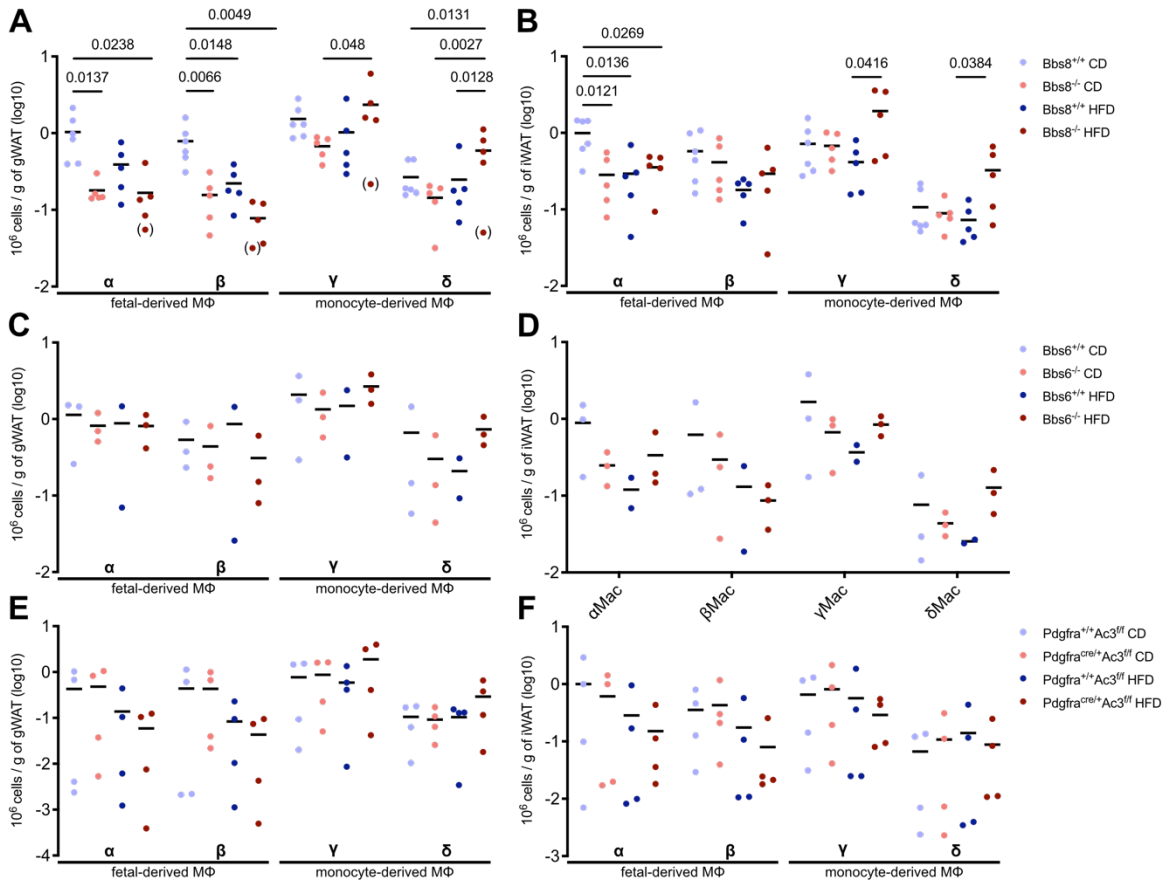
Figure 36: Density of fetal- and monocyte-derived macrophage subpopulations in WAT of ciliopathy- and diet-induced obesity. SVF from murine gWAT and iWAT was isolated from mice after 7-8 weeks of HFD or CD feeding to analyze macrophage (MΦ) subpopulations by flow cytometry. Lin⁻ CD45⁺ F4/80⁺ CDIIb⁺ cells mark MΦ, which can be further separated into four subpopulations by TIM4, CDIIc, and MCHII. Results were calculated as number of cells per g of WAT tissue based on cell counting and the frequency of live cell gate. **(A-B)** Number of MΦ subpopulations in gWAT **(A)** and iWAT **(B)** of Bbs8 mice. **(C-D)** Number of MΦ subpopulations in gWAT **(C)** and iWAT **(D)** of Bbs6 mice. **(E-F)** Number of MΦ subpopulations in gWAT **(E)** and iWAT **(F)** of Pdgfra-Ac3 mice. Data are shown as mean with individual data points, n ≥ 5 (Bbs8), n ≥ 2 (Bbs6), n = 4 (Pdgfra-Ac3); p-values were calculated by Šídák's multiple comparisons test for each subpopulation, ( ) indicate data points from the leanest animal (15 g leaner; body weight) excluded for p-value calculations. Experiments were performed in cooperation with Nikola Makdissi from the Mass lab. Lin: Ly6G, SilecF, CD3, CD19, and NKp46.
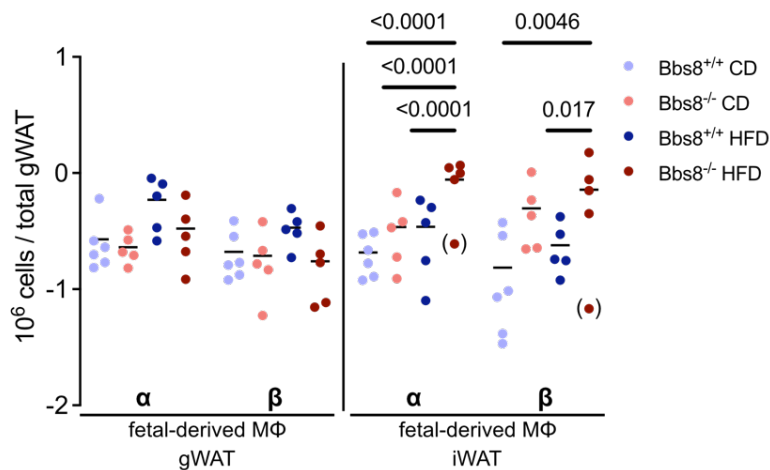
Figure 37: Number of fetal-derived macrophages in total WAT of Bbs8 mice reveal depot-dependent differences. SVF from murine g- and iWAT was isolated from mice after 7-8 weeks of HFD or CD feeding to analyze macrophage (MΦ) subpopulations by flow cytometry. Fetal-derived MΦs are Lin⁻ CD45⁺ F4/80⁺ CDIIb⁺ TIM4⁺, which can be further separated by CDIIc and MCHII. Results were calculated as number cells per total WAT tissue based on cell counting, frequency of live cell gate, and total g WAT. Data are shown as mean with individual data points, n ≥ 5; p-values were calculated by Šídák's multiple comparisons test for each subpopulation, ( ) indicate data points from one outlier animal excluded for p-value calculations (outlier identified in α MΦ by ROUT testing Q = 10%). Experiments were performed in cooperation by Elvira Mass with Nikola Makdissi.

3.8 Characterization of pre-adipocyte localization in whole tissue

The metabolic state of the highly complex and dynamic WAT is tightly coupled to WAT remodeling influenced by immune cells and pre-adipocytes. WAT has to adapt to changes in energy availability to maintain whole body energy homeostasis and function. Pre-adipocytes serve as a progenitor pool to replenish the tissue with new adipocytes, and play an important role in WAT expansion and remodeling to prevent pathological obesity (Vishvanath *et al.*, 2016). Several studies have looked into the localization of these pre-adipocytes in the AT and have come to different conclusions. It has been suggested that pre-adipocytes reside along blood vessels (Baer and Geiger, 2012; Cai *et al.*, 2011; Crisan *et al.*, 2008; Hilgendorf *et al.*, 2019), while others localized them in the reticular interstitium and intercalated between mature adipocytes (Merrick *et al.*, 2019). To analyze the complex network and interaction of pre-adipocytes with other cells within the AT, I aimed to localize pre-adipocytes in their progenitor niche by whole mount staining using fluorescent antibody labeling (Klymkowsky and Hanken, 1991). I focused on gWAT as it develops postnatally during the first 14 days (Figure 38) and until postnatal day 4 (P4), it is translucent and lacks mature adipocytes (Han *et al.*, 2011). At P5, the tissue starts to differentiate and is fully maturated after 14 days. This offers the unique opportunity to investigate pre-adipocyte localization during different developmental stages (Figure 38).
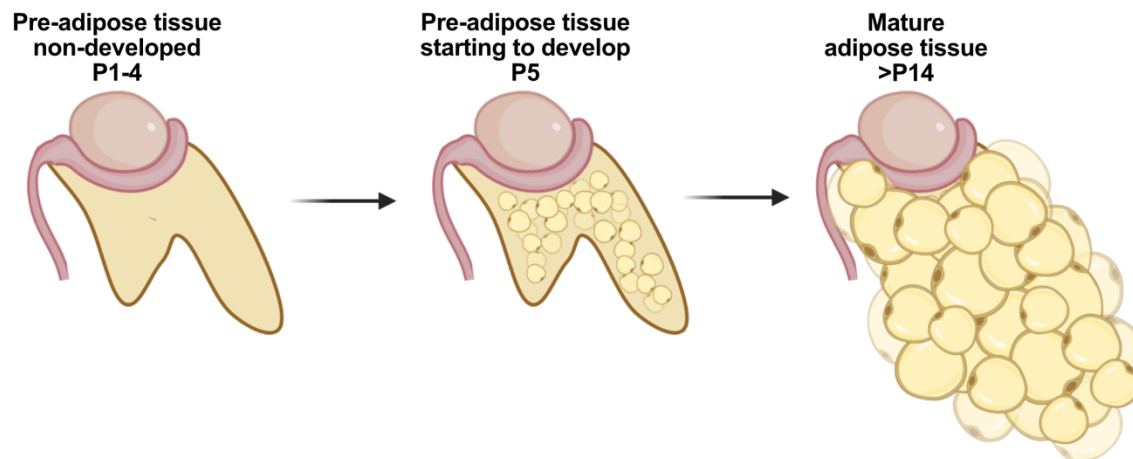
Figure 38: Different timepoints of gonadal WAT development used for whole mount staining. Mice are born with a translucent gWAT precursor tissue, which develops into mature adipose tissue over 14 days *in vivo* (Han). Until post-natal day four (P4), tissue lacks lipid-filled adipocytes and mature adipocytes start to emerge at day five (P5).

3.8.1   Whole mount staining of pre-AT on postnatal day 4

First, I stained non-developed pre-AT at P4 and hypothesized that pre-adipocytes in P4 pre-AT are just about to differentiate. During adipogenesis, cells first proliferate before they differentiate and start incorporating lipids. Therefore, I labeled proliferating cells within the pre-AT using an antibody against KI-67, which is present in the nucleus of proliferating cells (Gerdes *et al.*, 1984; Scholzen and Gerdes, 2000). This staining revealed KI-67+ nuclei throughout the pre-AT (Figure 39A).

Next, I stained with an anti-ARL13B and anti-F4/80 antibody to label primary cilia and macrophages, respectively (Figure 39B). To unequivocally identify primary cilia on pre-adipocytes, additional markers to distinguish between pre-adipocytes and other ciliated cell types are still needed. Macrophages were also present in an astonishing high density, equally distributed throughout the tissue. These might be tissue-resident macrophages, which maintain tissue homeostasis (Gomez Perdiguero *et al.*, 2015; Wu and Hirschi, 2020). F4/80 is a general macrophages marker, but additional staining with specific markers for resident or monocyte-derived macrophages would enable to distinguish these subpopulations. Ciliated cells are also in close proximity to these macrophages. Therefore, interactions between pre-adipocytes and macrophages might play a role, but needs further investigation.

After I established the staining of cilia, I additionally stained cilia in combination with anti-PECAM-1 antibody to visualize the vasculature (Figure 39C): The pre-AT was well-vascularized, which is in line with previous reports demonstrating that angiogenesis precedes adipogenesis (Han *et al.*, 2011). One proposed progenitor niche resides along blood vessels (Baer and Geiger, 2012; Hilgendorf *et al.*, 2019). Hence, I analyzed the proximity of a vessel in more detail.
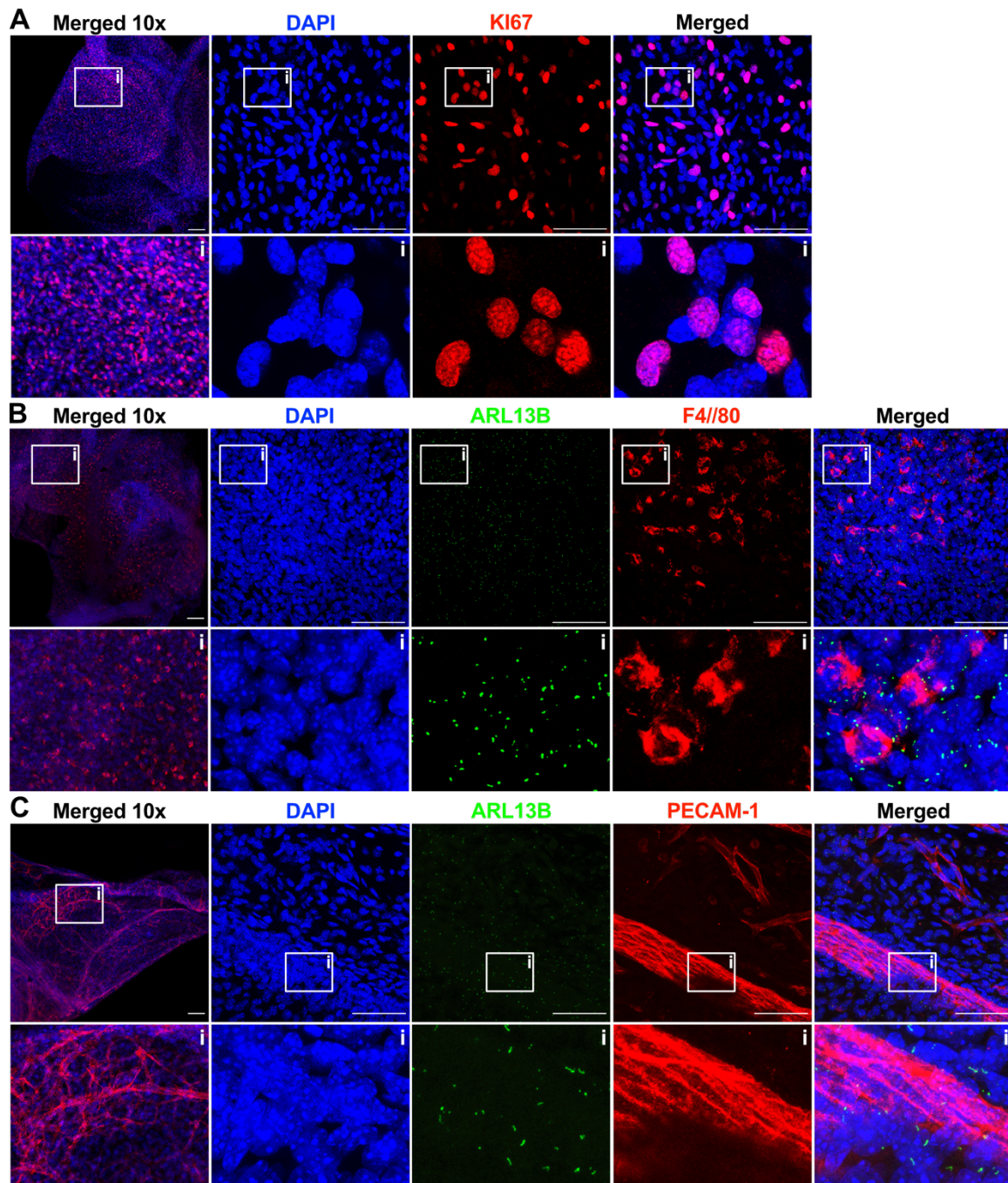
Figure 39: Establishing markers for staining murine, gonadal pre-adipose tissue. Precursor gWAT tissue was isolated at P4 from wildtype mice and fixed with 1% PFA for 30 mins before staining with DAPI (blue, DNA) and different antibodies. An overview image was acquired with 10x objective (left) and detailed images with 63x objective (right). **(A)** Proliferating cells were stained with anti-KI67 antibody (red). **(B-C)** Primary cilia were stained with an anti-ARL13B antibody (**B-C**, green), while the anti-F4/80 and anti-PECAM-1 antibodies marked macrophages (**B**, red) and endothelial cells (**C**, red), respectively. Squares indicate the zoomed in area shown below. Scale bars: 50 μm, except for 10x objective images 100 μm.

I selected a prominent vessel and selected an area for a detailed analysis (Figure 40A). All my images represent a maximal projection of a multi-stack image (Chapter 2.9,2.10). To circumvent the concomitant loss of spatial information, I decided to perform a 3D reconstruction of the selected area using an ImageJ plugin (3D viewer). The 3D reconstruction revealed that the vessel is surrounded by many ciliated

cells (Figure 40B). This result strongly suggest that these cells are pre-adipocytes and blood vessels are indeed progenitor niches, but to clarify an additional marker for pre-adipocytes should be included in future stainings.
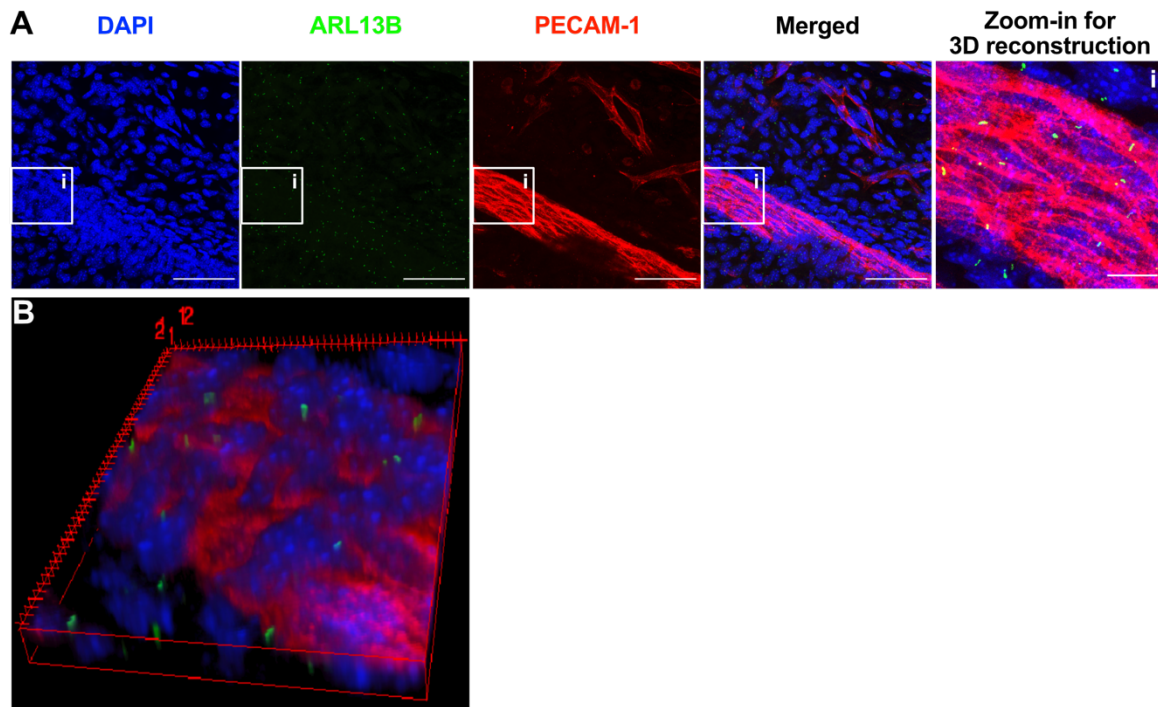
Figure 40: Vessels in murine, gonadal pre-adipose tissue are surrounded by ciliated cells. Precursor gWAT tissue was isolated at P4 from wildtype mice and fixed with 1% PFA for 30 mins before staining with DAPI (blue, DNA), anti-ARL13B (green, cilia), and anti-F4/80 antibody (red, macrophages). **(A)** Overview of separate and overlayed channels of the original image as well as the detailed zoomed-in image used for 3D reconstruction (right). Squares indicate the zoomed in area shown below. Scale bars: 50 μm, except for zoomed in image: 10 μm. **(B)** 3D reconstruction of the selected image area via 3D viewer ImageJ plugin. Multiple nuclei are on top of the vessel, some of which are ciliated.

3.8.2 Whole mount staining of pre-AT on postnatal day 5

Next, I used pre-AT at P5 as a model that contains all cell types within the AT but not too many lipid-filled adipocytes. First, I visualized mature adipocytes by staining with an anti-perilipin antibody. Perilipin coats lipid droplets and controls lipid metabolism by regulating access of cytosolic lipases to stored triacylglycerol in the lipid droplets (Brasaemle, 2007; Greenberg *et al.*, 1991; Sztalryd and Brasaemle, 2017). Anti-Perilipin staining confirmed the presence of differentiated adipocytes in various sizes throughout the tissue, verifying the presence of growing and fully matured adipocytes (Figure 41A). The distribution of the mature adipocytes displayed a rather patchy pattern, indicating that differentiation occurs locally in certain tissue niches. To identify proliferating cells, I stained P5 pre-AT with the anti-Ki-67 antibody (Figure 41B): Ki-67^{+} nuclei were highly abundant. In contrast to mature adipocytes labeled by perilipin, Ki-67^{+} cells displayed a rather equal distribution pattern. Lastly, I visualized vascularization by labeling endothelial cells via anti-PECAM-1 antibody (Figure 41C). My results showed a well-vascularized P5 pre-AT as at P4 (Figure 39C).
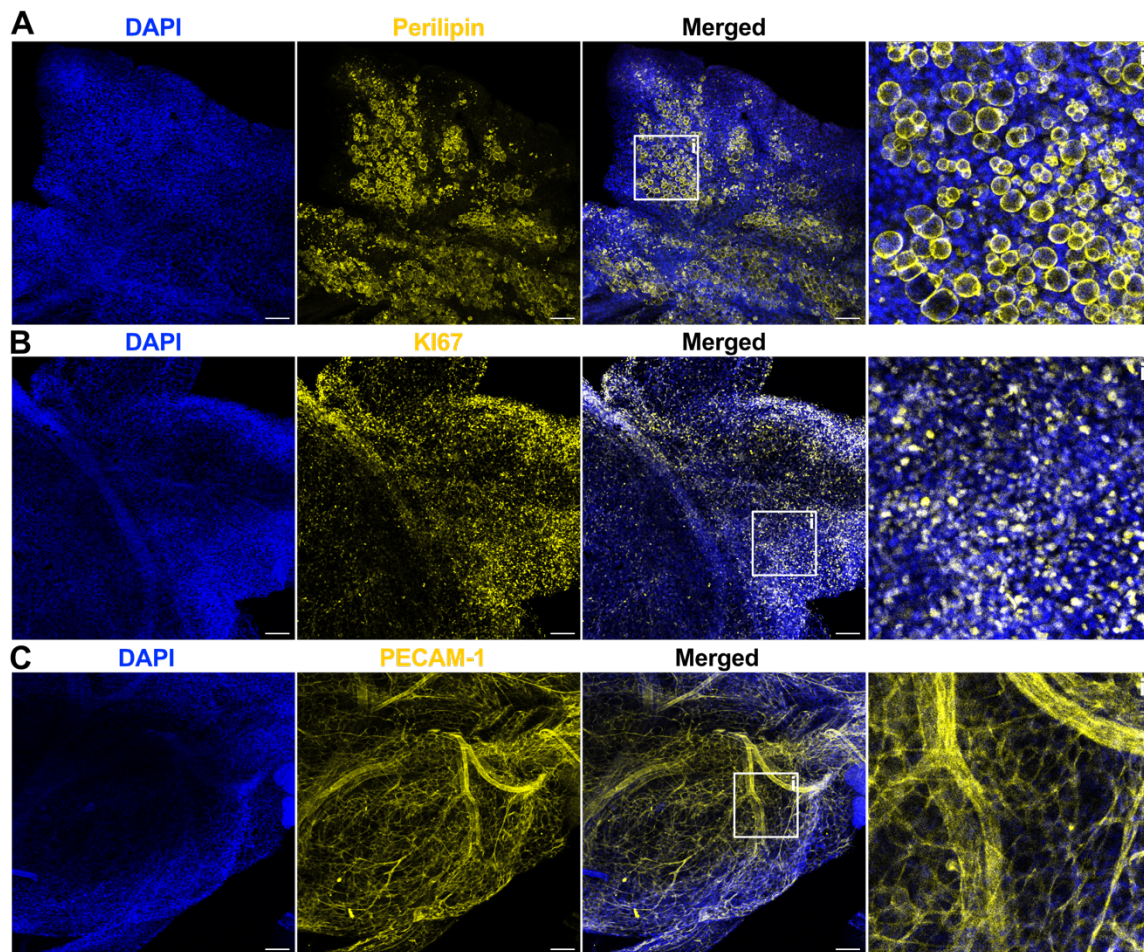
Figure 41: Maturating precursor gWAT tissue show good vascularization, high proliferation and first lipid-filled adipocytes. Precursor gWAT tissue was isolated at P5 from wildtype mice and fixed with 1% PFA for 30 mins before staining with DAPI (blue, DNA) and different antibodies. These overview images were acquired with 10x objective. Samples were stained with either anti-Perilipin **(A)**, -KI-67 **(B)**, or -PECAM-1 antibodies **(C)**, marking mature adipocytes, proliferation or vascularization, respectively (all, yellow). Squares indicate the zoomed in area shown on the right. Scale bars: 100 µm. Experiments were partly performed by Ernesto Picòn-Galindo.

Next, I investigated the complex cellular network in P5 pre-AT by combining the labeling for mature adipocytes (Perilipin), macrophages (F4/80), and primary cilia (ARL13B). Lipid-filled adipocytes occurred in different sizes: Whereas some displayed the typical unilocular, big lipid droplet, others displayed smaller and multiple lipid droplets (Figure 42,Figure 43A). Macrophages were present in an area with a low density of mature adipocytes, which was filled with ciliated cells (Figure 42, Figure 43A). Thus, macrophages might interact and communicate with the surrounding pre-adipocytes to regulate AT development. To investigate this further, I performed a 3D reconstruction (Figure 42B). It clearly showed a central nucleus engulfed in F4/80-positive signal that also extends to surrounding ciliated cells. Hence, macrophages interact with pre-adipocytes.
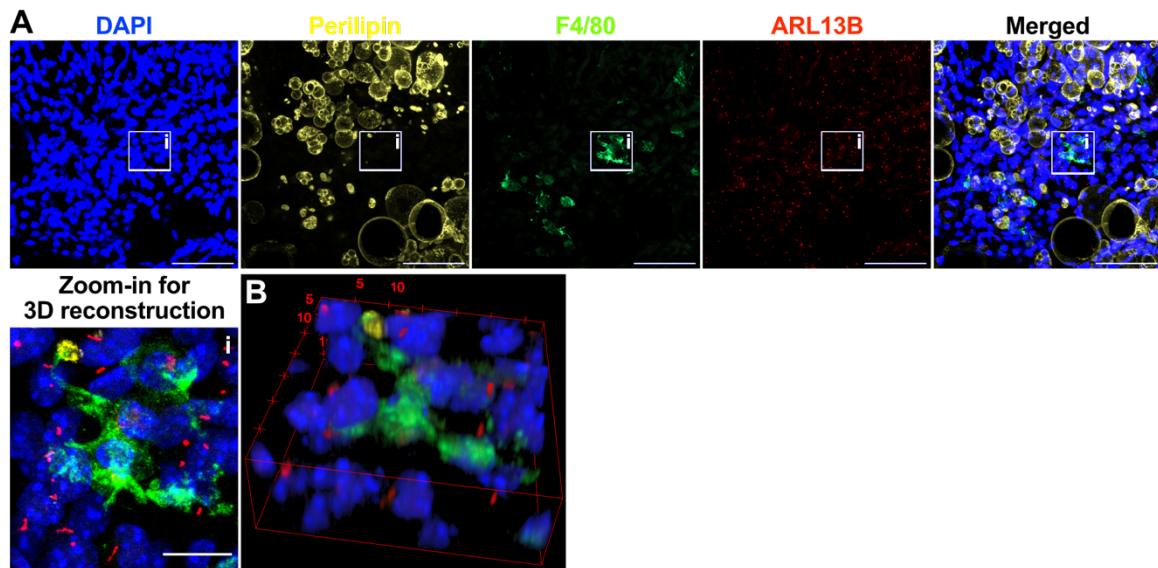
Figure 42: Macrophages interact with ciliated cells in maturating gonadal pre-adipose tissue. Precursor gWAT tissue was isolated at P5 from wildtype mice and fixed with 1% PFA for 30 mins before staining with DAPI (blue, DNA), anti-Perilipin (yellow, lipid droplets), anti-F4/80 (green, macrophages), and anti-ARl13B antibody (red, cilia). **(A)** Overview of separate and overlayed channels of the original image as well as the detailed zoomed-in image used for 3D reconstruction (below). Squares indicate the zoomed in area shown below. Scale bars: 50 µm, except for zoomed in image: 10 µm. **(B)** 3D reconstruction of the selected image area via 3D viewer ImageJ plugin. Multiple ciliated nuclei are in close proximity of the macrophage. Experiments were performed by Ernesto Picòn-Galindo.

Then, I co-stained primary cilia (ARL13B) and proliferating cells (KI-67) in P5 pre-AT. Proliferating cells were present throughout the tissue, as were primary cilia (Figure 43B). The precise assignment of a primary cilium to a specific cell, identified by a Ki67$^+$ nucleus, was rather complicated without additional information about cilia orientation, e.g., by labeling of the basal body, especially in a whole tissue context, where cells are on top of each other. Nevertheless, proliferating cells (KI-67$^+$) should not harbor a primary cilium and the presence of ciliated cells in close proximity of proliferating cells only indicates that proliferating cells are not triggering surrounding cells to also undergo proliferation. Future co-staining of mature adipocytes and proliferating cells might clarify if maturating adipocytes directly promote proliferation and differentiation of surrounding pre-adipocytes. Lastly, I stained primary cilia (ARL13B) and endothelial cells (PECAM-1) to identify the proposed progenitor niche: The vasculature formed a dense network, whereby most cells were in close proximity of vessels and many were also ciliated (Figure 43C). Since angiogenesis was reported to be an essential requirement for AT development (Han *et al.*, 2011), it is possible that adipogenesis happens first in close proximity to bigger vessels. In future experiments, this could be investigated by co-staining mature adipocytes.
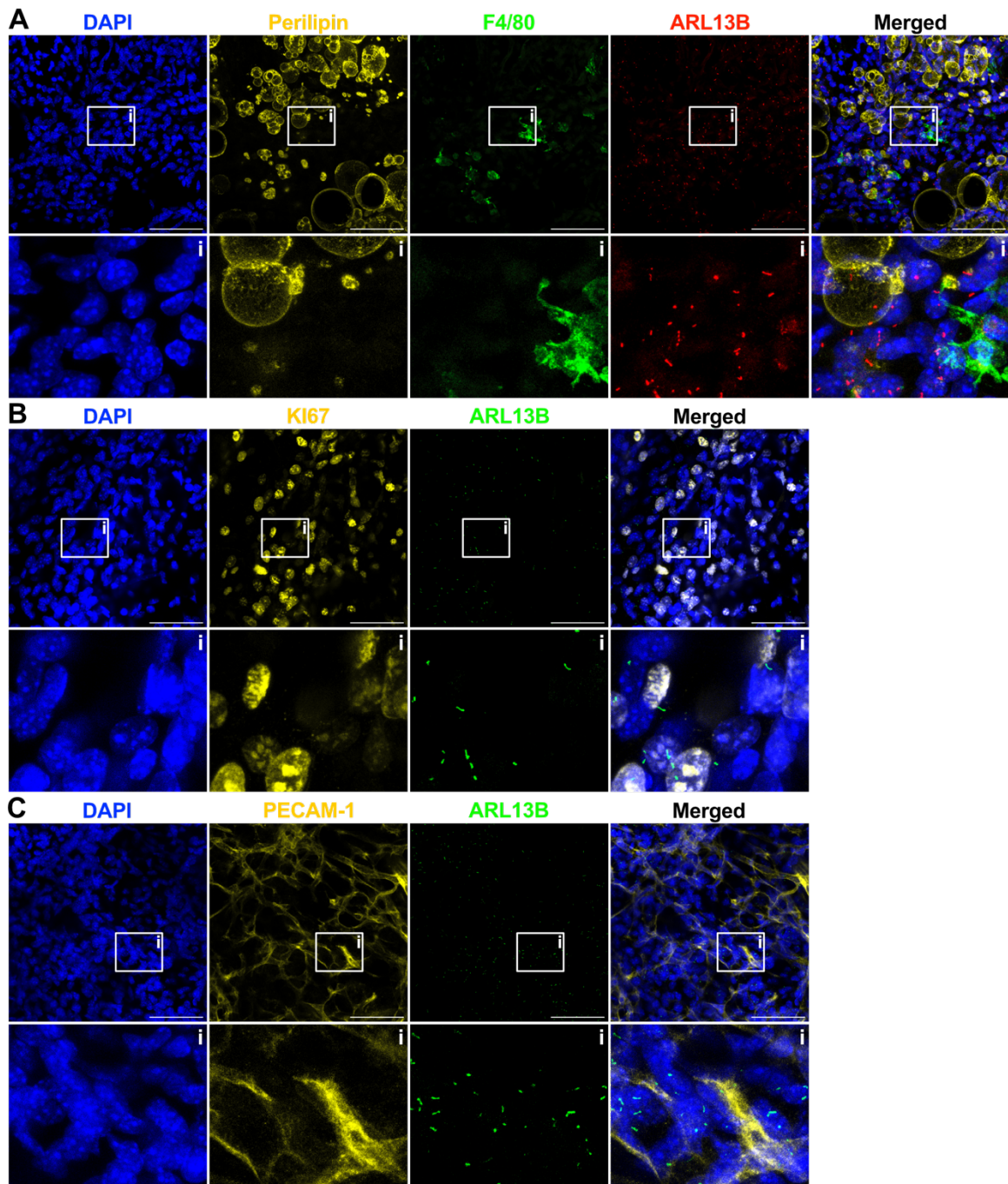
Figure 43: Detailed images of maturating precursor gWAT tissue show a high abundance of primary cilia, as well as good vascularization, high proliferation, lipid-filled adipocytes, and macrophages.
Precursor gWAT tissue was isolated at P5 from wildtype mice and fixed with 1% PFA for 30 mins before staining with DAPI (blue, DNA) and different antibodies. These detailed images were acquired with 63x objective. **(A)** Primary cilia were stained with anti-ARL13B antibody (red), while anti-Perilipin and anti-F4/80 antibodies marked mature adipocytes (yellow) and macrophages (green), respectively. **(B-C)** Primary cilia were stained with anti-ARL13B antibody (green), while anti-KI67 and anti-PECAM-1 antibodies marked proliferating cells **(B)** and endothelial cells **(C)**, respectively (all, yellow). Squares indicate the zoomed in area shown below. Scale bars: 50 µm. Experiments were partly performed by Ernesto Picòn-Galindo.

3.8.3 Whole mount staining of mature AT

When labeling primary cilia on pre-adipocytes in mature AT, I encountered several problems: 1) high autofluorescence, 2) high scattering of light, and 3) low penetrance

of the antibodies (Richardson and Lichtman, 2015; Willows *et al.*, 2021). In turn, it was difficult to identify primary cilia on pre-adipocytes with only one antibody, but I rather had to use multiple antibodies. Furthermore, different ciliary markers revealed different results: While the anti-ac. α-TUB antibody detected the highest number of primary cilia, not all of these cilia were positive for ARL13B or AC3 (Figure 44). This might reflect differences in cell type, stage of ciliary signaling, or growth. Ac. α-TUB is a structural component of the ciliary axoneme and might therefore be the most robust marker, which is present in all cell types independent of the state of ciliogenesis.
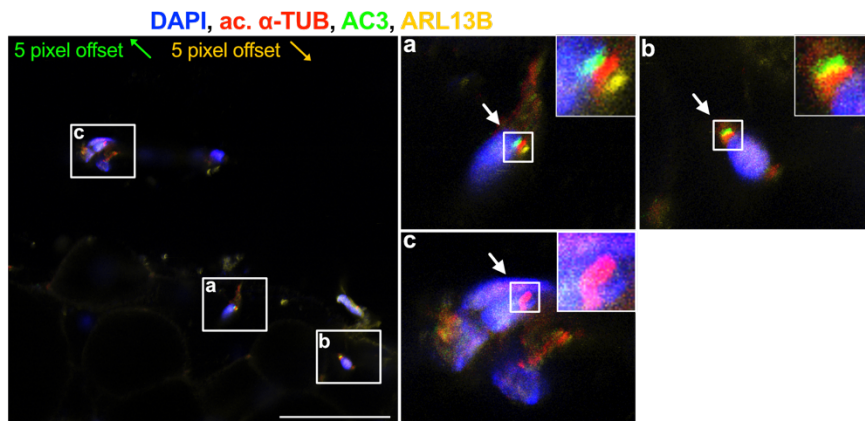
Figure 44: Staining of primary cilia with multiple antibodies in mature AT. AT isolated from wildtype mice was fixed with 1% PFA for 30 mins before staining with DAPI (blue, DNA) and different antibodies. Primary cilia were stained with an anti-ac. α-TUB (red), anti-AC3 (green), and anti-ARL13B (yellow) antibodies. Green and yellow channel are pixel-shifted by 5 pixels up or down as indicated by the arrows. Squares indicate the zoomed in areas shown on the right. Scale bars: 50 μm, 63x objective.

Most detected cilia were close to the surface of the tissue sample, indicating a possible problem with antibody penetration or in-depth imaging. Images also became fuzzier and were weaker labeled deeper in the tissue. To overcome these problems in future experiments, a tissue clearing method could be used (Richardson and Lichtman, 2015). Recently, a clearing method designed especially for AT, which includes a de-lipidation step, has been described (Chi *et al.*, 2018).

The only antibody that repeatedly worked on mature AT was the anti-PECAM-1 antibody, a marker for endothelial cells (Pusztaszeri *et al.*, 2006), visualizing vascularization. Antibody labeling revealed an intensive network of vasculature throughout the AT (Figure 45A). The signal became fainter in higher magnifications (63x), but could still be detected (Figure 45B). PECAM-1^{+} cells were intercalated between the lipid laden mature adipocytes (Figure 45). This staining reminded me of a pattern observed in the reporter mice (Pdgfra[cre/+] R26-mT/mG[tg/+]), where mG or mT labels *Pdgfra*-expressing and non-expressing cells, respectively. Co-staining with anti-PECAM-1 antibody clarified that the observed non-targeted mT^{+} cells are endothelial cells of the vasculature (Figure 45B).

Overall, co-staining of P4 and P5 pre-AT enables an intriguing insight in the localization and possible interplay between different cell types, regulating and maintaining AT tissue development and homeostasis. However, more markers need to be established

and characterized to define most suitable marker combinations to identify the variety of different cell types. Co-staining primary cilia with an additional pre-adipocyte and various combinations of other cell markers might elucidate the progenitor niche further. Also, imaging quality and analysis needs to be improved. In summary, whole mount staining of P4 and P5 pre-AT works fine, while mature AT is not suitable without further processing, such as a tissue clearing procedure (Chi *et al.*, 2018).
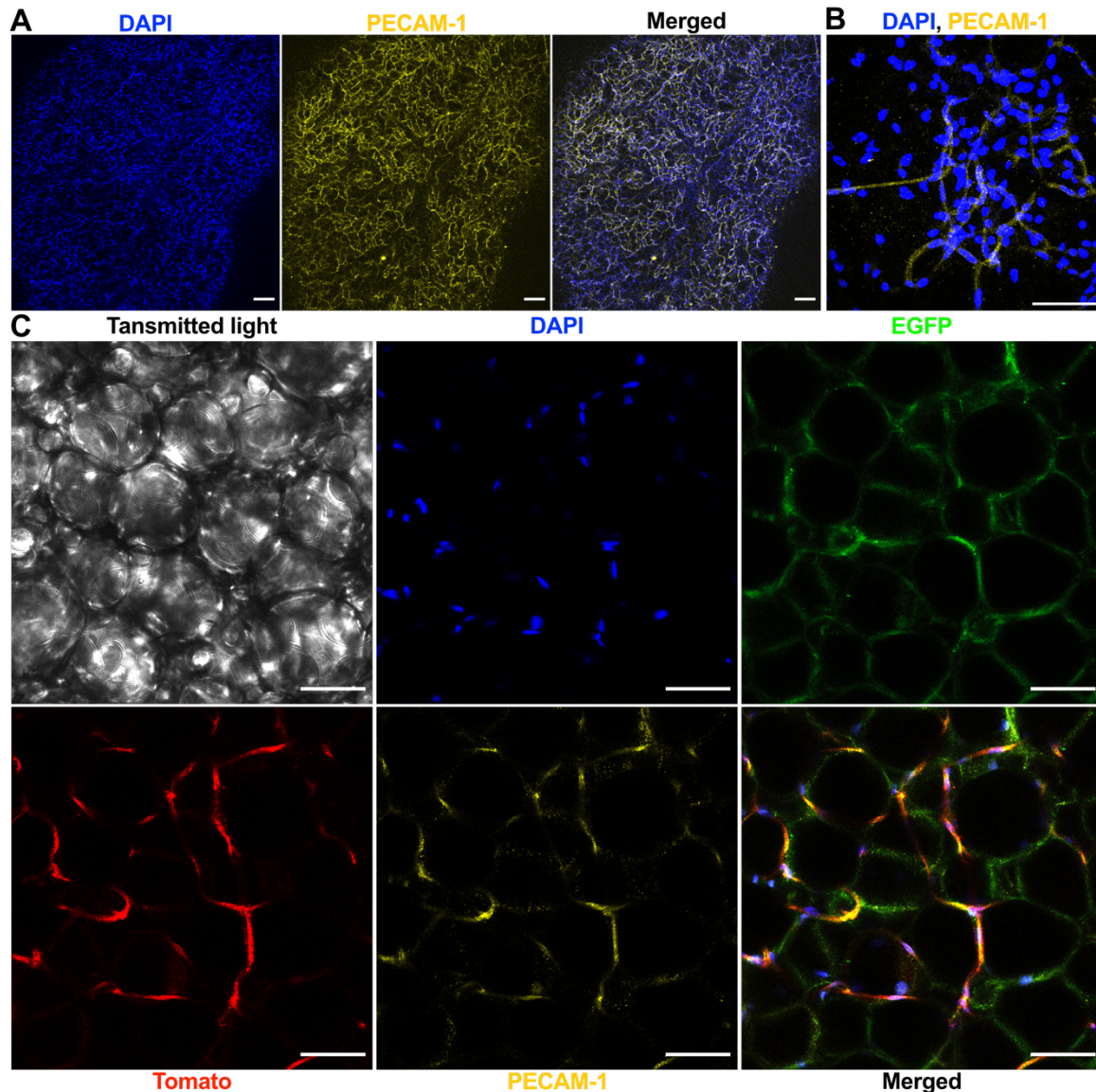
Figure 45: An endothelial marker robustly labels endothelial cells of the vasculature in mature AT. Mature gWAT tissue was isolated from wildtype or Pdgfra[cre/+] R26-mT/mG[tg/+] reporter mice and fixed with 1% PFA for 30 mins before staining with DAPI (blue, DNA) and anti-PECAM-1 antibody (yellow). **(A-B)** Anti-PECAM-1 antibody stained an extensive vasculature network in AT from 2 wks old wildtype mice. An overview image was acquired with 10x objective **(A)** and detailed image with 63x objective **(B)**. **(C)** In Pdgfra[cre/+] R26-mT/mG[tg/+] reporter mice, *Pdgfra* expressing cells are labeled by mG (green) and non-expressing cells by mT (red). Tomato[+] (red) cells are co-stained by anti-PECAM-1 antibody identifying these cells as endothelial cells. Scale bars: 50 μm, except for 10x objective images 100 μm.

3.9 Analysis of pre-adipocytes from white adipose tissue

To scrutinize the contribution of pre-adipocyte signaling pathways, in particular primary cilia signaling pathways, to AT remodeling, function and homeostasis, I established an *in vitro* culture using primary pre-adipocytes.

3.9.1 Characterization of the SVF primary culture

Pre-adipocytes can be isolated as part of the stromal vascular fraction (SVF) from WAT and cultured *in vitro* (Bourin *et al.*, 2013; Rodbell, 1964). To this end, WAT was enzymatically digested and lipid-filled mature adipocytes were separated from other cells by centrifugation. Furthermore, erythrocytes were lysed, whereby the remaining SVF cell suspension only contained pre-adipocytes, different immune cells, endothelial cells, fibroblasts, pericytes, and smooth muscle cells (Figure 46A) (Sárvári *et al.*, 2021). When cultivating this heterogenous cell population *in vitro*, not all cells adhered. Those cells that proliferated and grew to confluency were 60-80 % ciliated (Figure 46B,C). However, as not only pre-adipocytes but also other cells such as endothelial cells or fibroblasts are ciliated (Antal *et al.*, 2017; Van der Heiden *et al.*, 2008), I had to establish markers to identify pre-adipocytes in this heterogenous cell population.
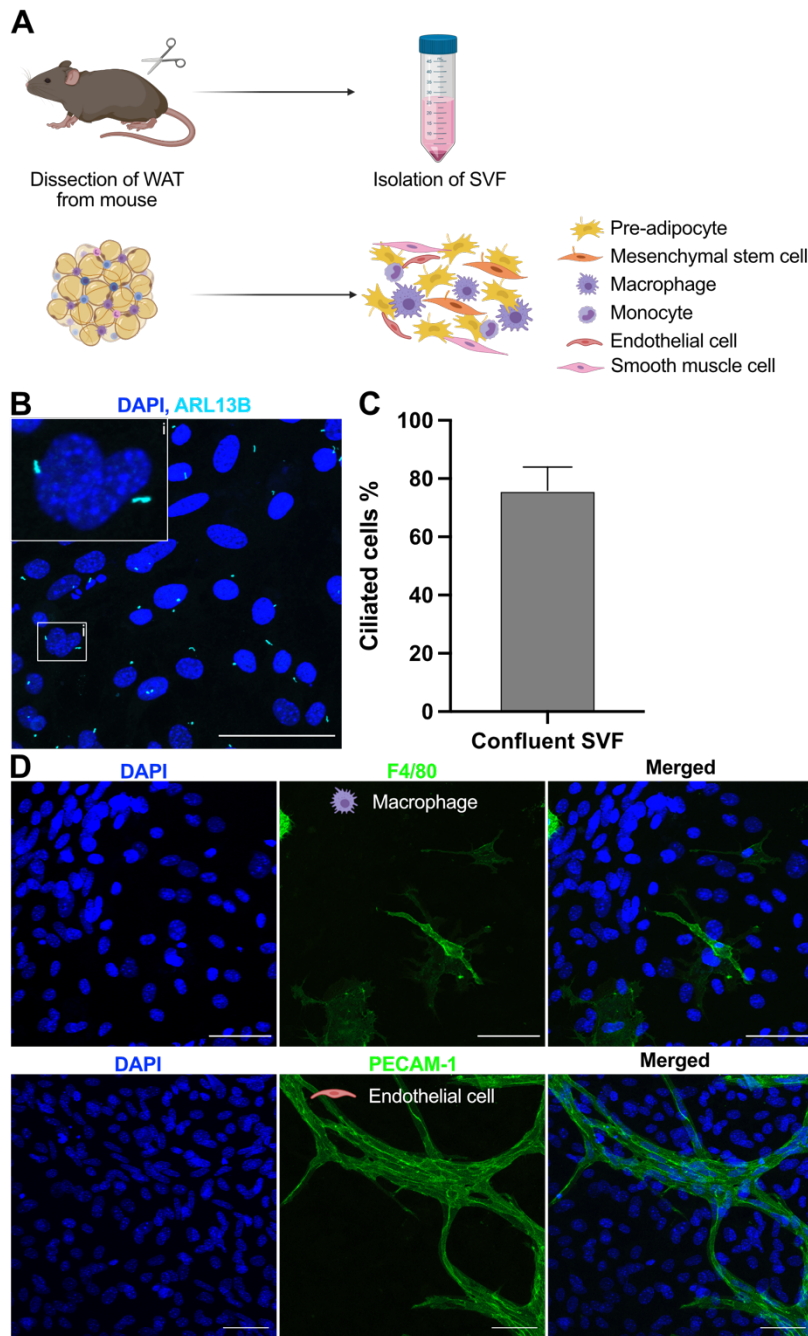
Figure 46: AT-derived stromal vascular fraction represents a hetero-genous cell population. (A) Schematic illustration of stromal vascular fraction (SVF) isolated from murine WAT. During the isolation, the lipid-laden adipocytes are separated and discarded, whereas all others cells, such as pre-adipocytes, macrophages, smooth muscle cells, endothelial cells, and fibroblasts are recovered. Erythrocytes are lysed before seeding. **(B)** The SVF was isolated from murine gWAT and cells were seeded, grown to confluency, and analyzed by immunocytochemistry using DAPI (blue, DNA) and an anti-ARL13B antibody (cyan, cilia). **(C)** Quantification of ciliated cells in confluent SVF, calculated as cilia count normalized to nuclei count. Data are shown as mean ± S.D., n = 4 **(D)** The SVF contains a variety of cells, including macrophages, stained with anti-F4/80 antibody (green) and endothelial cells, stained with anti-PECAM-1 antibody (green) (the latter has been performed by Dr. Mylene Huebecker). Scale bar: 50 µm.

3.9.2 Establishing pre-adipocyte markers

Different markers have been proposed to be present on pre-adipocytes. However, the markers differ between studies, AT depots, cellular pre-selection method, and the stage of commitment and differentiation. Additionally, these markers are often not exclusively expressed in pre-adipocytes and only a combination of different markers might allow to identify pre-adipocytes. Due to these drawbacks, no single specific surface marker has been identified yet (Berry *et al.*, 2015; Cawthorn *et al.*, 2012). I tested different potential pre-adipocyte markers, i.e., stem cell antigen 1 (SCA1), vascular adhesion protein 1 (VAP1), fatty acid binding-protein 4 (FABP4), and CCAAT/enhancer-binding protein β (CEBPβ) (Figure 47).

SCA1 (also known as Ly6a) has been consistently identified on pre-adipocytes and is an integral part of recent labeling strategies to characterize pre-adipocytes via flow cytometry or RNA sequencing (Rodeheffer *et al.*, 2008; Sarantopoulos *et al.*, 2018; Schwalie *et al.*, 2018; Steenhuis *et al.*, 2008). My analysis confirmed the presence of SCA1-labeled cells in my *in vitro* culture (Figure 47A). Although, I previously showed that other cell types are present in the SVF, the SCA1 antibody seemed to label rather all cells. This indicates that labeling was not restricted to pre-adipocytes and that SCA1 was therefore not suitable as a single pre-adipocyte marker. However, this marker cannot be dismissed until co-staining experiments with other cell markers clarify this supposed non-specificity.

Next, I tested an antibody against VAP1 (or amine oxidase copper containing 3), a recently described marker for committed pre-adipocytes (Merrick *et al.*, 2019; Schwalie *et al.*, 2018). VAP1 is a membrane protein, which displays both adhesion properties involved in leucocyte adhesion and migration and an amino oxidase activity (Salmi and Jalkanen, 2019; Smith *et al.*, 1998). I identified some ciliated VAP1$^+$ cells, but also a lot of highly fluorescent specks in the extracellular space in close proximity to VAP1$^+$ cells (Figure 47B). As VAP1 not only exists in a membrane-bound form, but also as a soluble form released by adipocytes (Abella *et al.*, 2004), these specks could represent aggregates of soluble VAP1 released from VAP1$^+$ pre-adipocytes. Thus, VAP1 serves as marker for a subset of pre-adipoctyes, but these extracellular specks complicate the image acquisition.

FABP4 (also known as adipocyte protein 2) has also been reported as a marker for committed pre-adipocytes (Merrick *et al.*, 2019; Schwalie *et al.*, 2018). So far, FABP4 has been used as a marker for adipocytes, as its expression is upregulated during terminal differentiation into mature adipocytes (Furuhashi *et al.*, 2014). Whether it is also expressed on pre-adipocytes remains controversial: While FABP4 expression could not be verified using a GFP reporter system (Tang *et al.*, 2008), more recent studies demonstrated FABP4 expression in at least a subset of pre-adipocytes using either a tdTomato reporter mouse line (Shan *et al.*, 2013) or single-cell RNA sequencing (Merrick *et al.*, 2019; Schwalie *et al.*, 2018). Finally, results from a FABP4 reporter mouse line demonstrated that FABP4 is not expressed in pre-adipocytes but rather in other cell types (Krueger *et al.*, 2014). My culture contained FABP4$^+$ cells, but only the minority carried a primary cilium (Figure 47C). Thus, FABP4 is not a good pre-adipocyte marker, as FABP4$^+$ cells are not all ciliated.

Next, I tested C/EBPβ, a transcription factor controlling adipocyte lineage commitment and early stages of adipogenesis (Cao *et al.*, 1991; Farmer, 2006). I observed many C/EBPβ$^+$ cells and most of them were ciliated (Figure 47D). Thus, C/EBPβ is the most promising pre-adipocyte marker. To verify its specificity, I used this marker in combination with two other markers: PECAM-1, a marker for endothelial cells (Pusztaszeri *et al.*, 2006) and FABP4. Co-staining with an antibody against PECAM-1 demonstrated that the anti-C/EBPβ antibody does not label endothelial cells (Figure 48A). Cells labeled with an anti-FABP4 and an anti-C/EBPβ antibody were distinct and the staining did not overlap, indicating that most FABP4$^+$ cells are not pre-adipocytes (Figure 48B). Interestingly, high intensity FABP4$^+$ cells morphologically

resemble PECAM-1$^+$ endothelial cells, which have been shown to also express FABP4 (Elmasri *et al.*, 2009). Altogether, C/EBPβ is expressed in ciliated cells, which are not endothelial cells, which is a first step towards identifying pre-adipocytes in my culture.
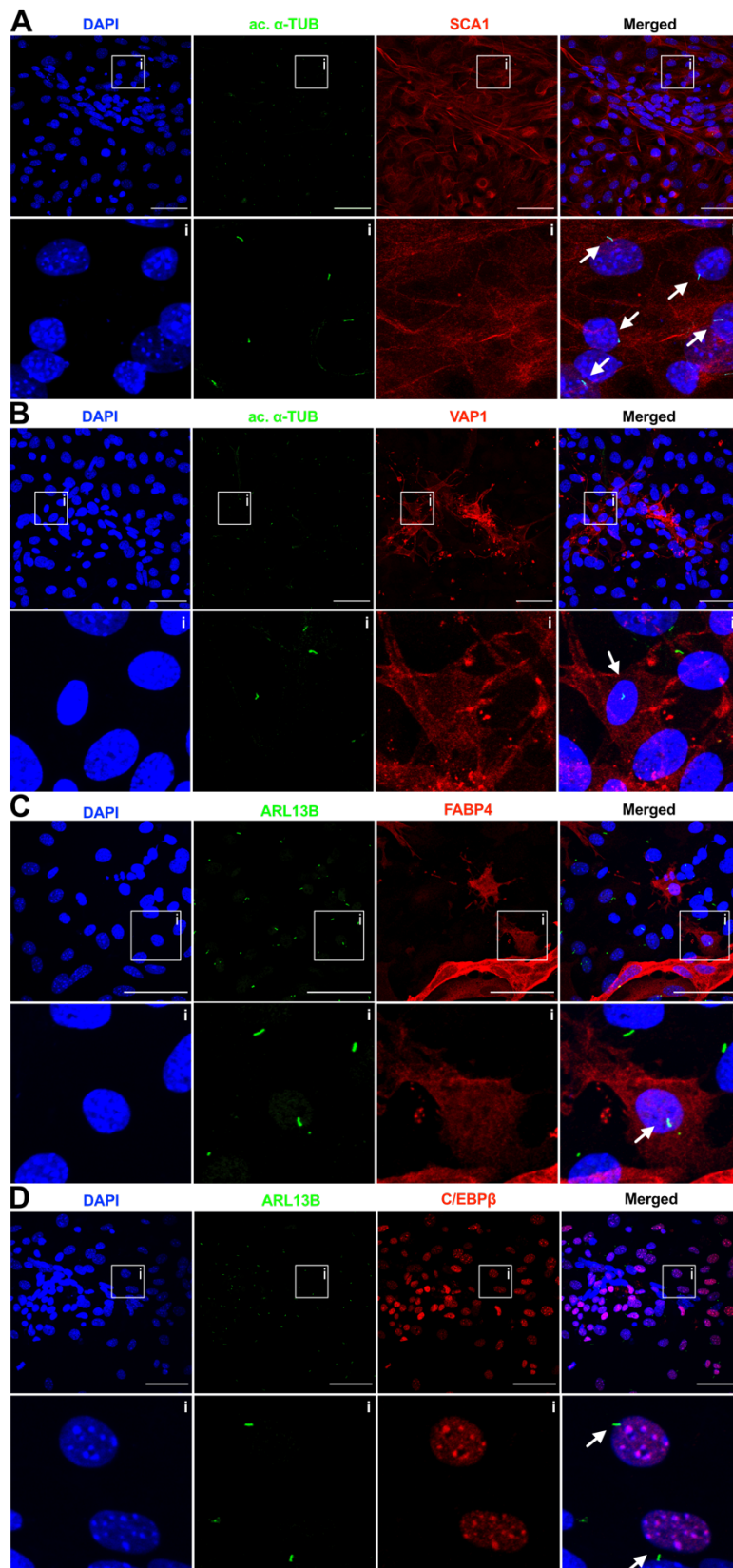
Figure 47: Identification of ciliated pre-adipocytes in SVF by different markers. SVF was isolated from murine gWAT, and cells were seeded, grown to confluency, and kept confluent for two days before performing immunochemistry. Nuclei were stained with DAPI (blue, DNA), primary cilia were stained with an anti-ARL13B antibody (green, **A-B**) or an anti-ac. α -TUB antibody (green, **C-D**), and antibodies against potential pre-adipocytes marker proteins, i.e., fatty-acid binding protein 4 (FABP4) **(A)**, CCAAT/enhancer-binding protein β (C/EBPβ) **(B)**, stem cell antigen 1 (SCA1) **(C)**, and vascular adhesion protein 1 (VAP1) antibody (**D**, all in red). Squares indicate the zoomed in area shown below and white arrows indicate marker positive cells with cilia. Scale bars: 50 μm.
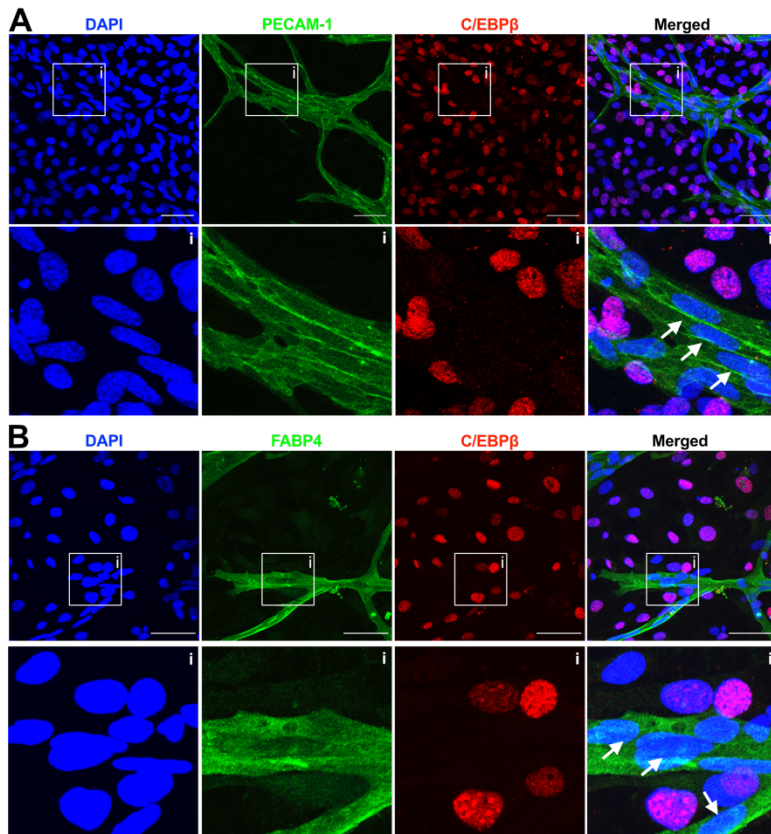
Figure 48: Potential pre-adipocyte marker C/EBPβ does not stain the same cells as PECAM-1 or FABP4. SVF was isolated from murine gWAT, and cells were seeded, grown to confluency, and kept confluent for two days before performing immunochemistry. Nuclei were stained with DAPI (blue, DNA) and pre-adipocytes were stained with anti-C/EBPβ antibody (red). Co-staining of either endothelial cells with anti-PECAM-1 (green, **A**) or of another potential pre-adipocyte marker with anti-FABP4 antibody (green, **B**). Squares indicate the zoomed in area shown below and white arrows indicate co-stain positive cells without C/EBPβ signal. Scale bars: 50 µm.

3.9.3 Differentiating primary pre-adipocytes *in vitro*

Differentiating pre-adipocytes replenish the pool of adipocytes, providing a metabolically healthy way of AT expansion by *de novo* generation of adipocytes (Gustafson *et al.*, 2009). The highly complex, orchestrated differentiation program has been termed adipogenesis (Cristancho and Lazar, 2011; Farmer, 2006). I hypothesize that primary cilia on pre-adipocytes sense extracellular signals to regulate pre-adipocyte commitment, fate, and differentiation, thereby maintaining tissue homeostasis. To analyze how ciliary signaling regulates pre-adipocyte differentiation, I established an assay to quantify adipogenesis *in vitro*. The key drivers of adipogenesis are the transcription factors peroxisome proliferator-activated receptor γ (PPARγ) (Koutnikova *et al.*, 2003) and C/EBPα/β/δ (Cao *et al.*, 1991), which can be activated by e.g., insulin, rosiglitazone, isobutylmethylxanthine (IBMX), and the glucocorticoid dexamethasone (Ding *et al.*, 2003; Farmer, 2006) (Figure 49A).

A read-out for adipogenesis is lipid droplet formation, which can be visualized and quantified by staining with the lysochrome oil-red-o (Kraus *et al.*, 2016; Ramírez-Zacarías *et al.*, 1992) or fluorescent labeling using the neutral-lipid dye LD540, an improved variant of Bodipy (Gocze and Freeman, 1994; Nishimura *et al.*, 2007; Spandl *et al.*, 2009) (Figure 49B). I isolated cells from wild-type mice, cultured them *in vitro*, induced adipogenesis when cells were confluent, and maintained the cells in differentiation medium for seven days (Figure 49C). I quantified the ciliation rate during differentiation using immunocytochemistry and analyzed lipid droplet formation using both, the lysochrome oil-red-o and LD540 (Figure 49D-F). At day 0-2 after induction, the percentage of ciliated cells was 70-80 %, but decreased to 60 % until day 6

(Figure 49D), underlining previous results (Hilgendorf *et al.*, 2019). I quantified lipid accumulation by measuring the absorbance of the lysochrome oil-red-o (Figure 49E) or by performing fluorescence microscopy of lipid droplets stained with LD540 (Figure 49F) and demonstrated that lipid droplet formation significantly increased during differentiation.
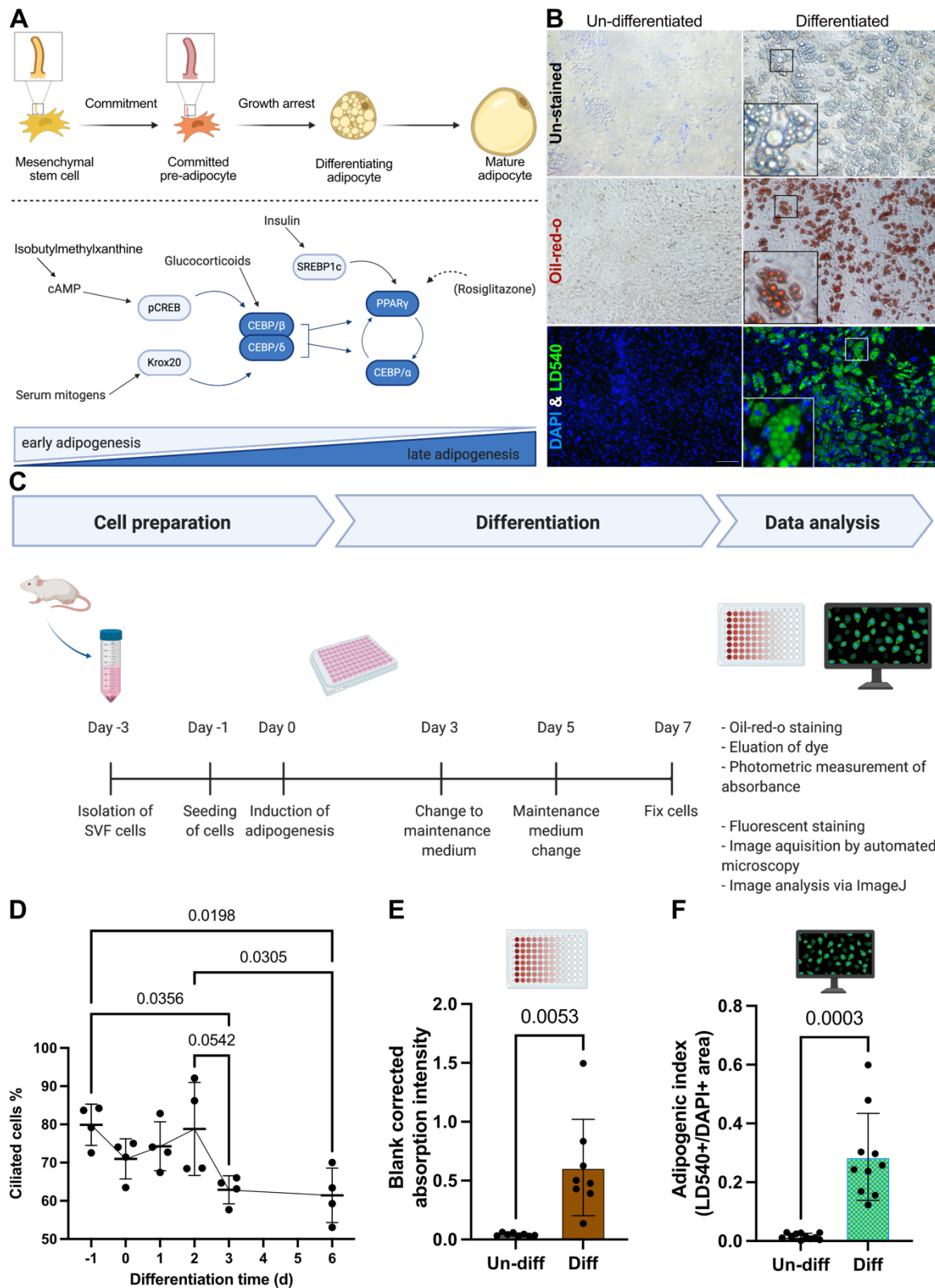
Figure 49: Differentiation of pre-adipocytes *in vitro*. (A) Schematic illustration of adipogenesis, resulting in the formation of mature adipocytes from ciliated pre-adipocytes (above). The key transcription factors peroxisome proliferator- activated receptor γ (PPARγ) and CCAAT/enhancer-binding protein α/β/δ (C/EBPα/β/δ) (dark blue) can be activated by various pharmacological stimuli, i.e., insulin, rosiglitazone, isobutylmethylxanthine (IBMX), and the glucocorticoid dexamethasone (bottom). **(B)** SVF was isolated from murine gWAT of wildtype mice and cells were seeded confluently before adipogenesis was induced for three days with an induction cocktail (5 µg/ml Insulin, 1 µM Dexamethasone, 100 µM IBMX, 1 µM Rosiglitazone). Adipogenesis was maintained by adding either 1 µM Rosiglitazone (oil-red-o quantification) or 1 µg/ml Insulin (fluorescent quantification) for another 4 days. Induced (differentiated)

94

and non-induced (un-differentiated) cells were fixed and either imaged directly (un-stained) or stained with either lysochrome oil-red-o (red) or with DAPI (blue, DNA) and the lipophilic dye LD540 (green, lipids). In contrast to the un-differentiated cells, differentiated cells contain lipid-laden adipocytes. **(C)** Experimental timeline. Adipogenesis can be quantified by either measuring the absorbance of eluted oil-red-o dye or by image-based analysis of fluorescent staining with LD540. **(D)** Percentage of ciliated cell in SVF during adipogenesis, calculated as cilia count normalized to nuclei. The number of ciliated cells decreases with differentiation. Data are shown as mean ± S.D. and with individual data points, p-values were calculated by one-way ANOVA, n = 4 analysed images per timepoint, n = 1 biological replicate. (E-F) Quantification of adipogenesis comparing induced and non-induced cells. **(E)** Cells were stained with oil-red-o and the dye was eluted with 100% isopropanol. The absorbance of the eluted dye was measured at 492 nm and blank corrected. **(F)** Cells were stained with fluorescent dyes (DAPI and LD540). After image acquisitions with an automated microscope plate-reader, images were analyzed via ImageJ. Area of lipid droplets (LD540) and area of nuclei (DAPI) were determined to calculate the adipogenic index, defined as lipid droplet area (LD540) divided by nuclei area (DAPI). Data are shown as mean ± S.D. and with individual data points, p-values were calculated by unpaired Student's t-test, n ≥ 8.

3.9.4 Signaling pathways regulating adipogenesis under physiological and pathological conditions

Next, I tested different signaling pathways, which have been reported to modulate adipogenesis in a primary cilia-dependent manner under physiological and pathological conditions. The Sonic Hedgehog (SHH) pathway is one of the best characterized signaling pathways in primary cilia (Gigante and Caspary, 2020) and has been shown to inhibit adipogenesis (Shi and Long, 2017; Suh *et al.*, 2006). The following model for SHH signaling has been proposed: In the absence of SHH, its receptor Patched1 (PTCH1) and the G protein-coupled receptor 161 (GPR161) localize to the cilium, while ciliary localization of the downstream mediator Smoothened (SMO) is prevented by PTCH1 (May *et al.*, 2021; Mukhopadhyay and Rohatgi, 2014; Mukhopadhyay *et al.*, 2013; Rohatgi *et al.*, 2007). GPR161 is targeted to the ciliary membrane by the protein kinase A regulatory subunit type I α (PKA-RIα) (Bachmann *et al.*, 2016; May *et al.*, 2021) and, as a constitutively active $G_{\alpha s}$-coupled GPCR, GPR161 activates transmembrane adenylyl cyclases (ACs), thereby, increasing cAMP levels (Mukhopadhyay and Rohatgi, 2014; Mukhopadhyay *et al.*, 2013; Rohatgi *et al.*, 2007). In turn, PKA is activated and its catalytical subunit (PKA-C) triggers the phosphorylation of the glioma-associated transcription factors (GLI), GLI2 and GLI3. This phosphorylation results in further proteolytic processing to form a C-terminally truncated GLI repressor (GLI-R), which inhibits SHH target-gene expression in the nucleus (Gigante and Caspary, 2020; Kotani, 2012). SHH activates the pathway by binding PTCH1, resulting in the removal of PTCH1 and GPR161 from the cilium, while SMO translocates into the cilium (Mukhopadhyay and Rohatgi, 2014; Mukhopadhyay *et al.*, 2013; Rohatgi *et al.*, 2007). Replacement of constitutively active $G_{\alpha s}$-coupled GPR 161 with SMO results in a drop of ciliary cAMP levels (Tschaikner *et al.*, 2020). Thereby, PKA is no longer activated and GLI proteins, in turn, remain as non-processed, full-length proteins. They accumulate at the ciliary tip, where they are converted into an activator form (GLI-A), promoting the expression of SHH target genes (May *et al.*, 2021; Mukhopadhyay and Rohatgi, 2014; Tuson *et al.*, 2011). The pathway can also be pharmacologically activated using SMO agonists, such as Purmorphamine (P) (Sinha and Chen, 2006) or N-Methyl-N′-(3-pyridinylbenzyl)-N′-(3-

chlorobenzo[b]thiophene-2-carbonyl)-1,4-diaminocyclohexane (SAG) (Chen *et al.*, 2002) (Figure 50A).

To test the effect of Hh signaling on adipogenesis, I supplemented the media with 2 µM P during differentiation and analyzed adipogenesis: lipid accumulation in the presence of P was reduced (Figure 50B-D), in particular when normalizing each replicate to the vehicle control with DMSO (Figure 50D). Thus, my approach verified the inhibitory effect of Hh signaling on adipogenesis.
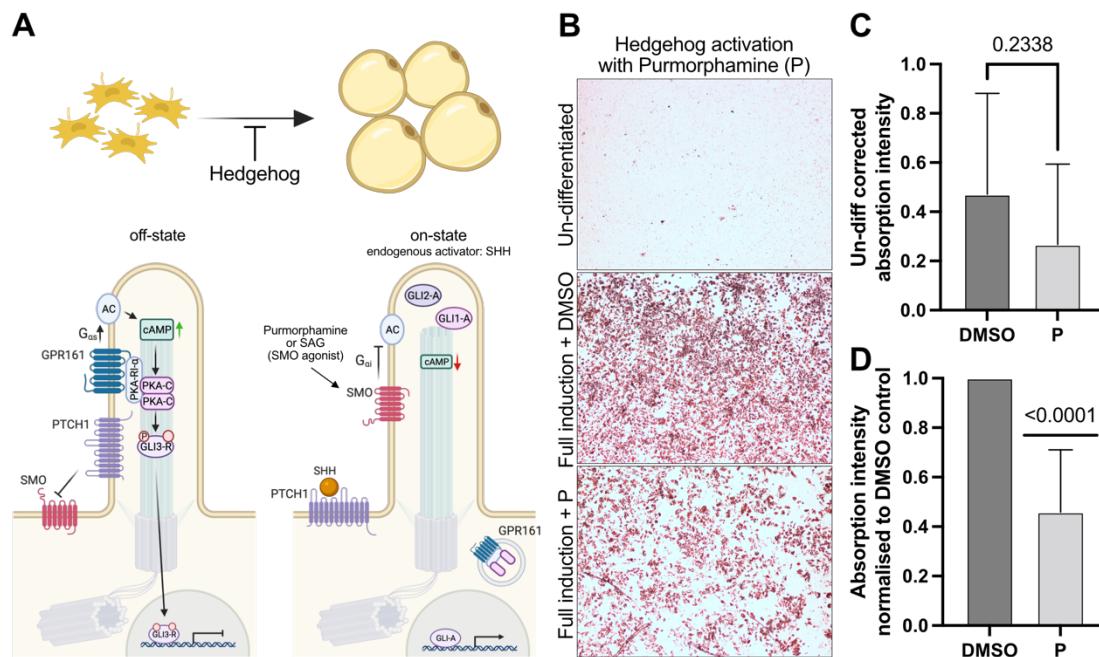
Figure 50: Hedgehog signaling reduces adipogenesis *in vitro*. (A) Canonical Hedgehog (Hh) signaling (bottom) inhibits adipogenesis (top). In the off-state, Patched 1 (PTCH1) and GPR161 reside in the ciliary membrane, while ciliary localization of Smoothened receptor (SMO) is inhibited. Cyclic AMP levels are high, activating PKA and triggering GLI processing into their repressor form. Hh signaling can be activated by Sonic hedgehog (Shh) binding to PTCH1 or by pharmacological activation of SMO using Purmorphamine (P) or SAG. Upon activation, PTCH1 and GPR161 are removed from the cilium, while SMO enters the cilium. Levels of cAMP decreases, whereby PKA is no longer activated and GLI processing is prevented. Thereby, they are kept in their active state, which reduces adipogenesis. **(B)** Representative images of oil-red-o stained SVF differentiated with and without Hh activation. SVF was isolated from murine gWAT of wildtype mice and cells were seeded confluently before adipogenesis was induced for three days with an induction cocktail (5 µg/ml Insulin, 1 µM Dexamethasone, 100 µM IBMX, 1 µM Rosiglitazone, and 2 µM Purmorphamine (P) or DMSO as vehicle control. Adipogenesis was maintained by 1 µM Rosiglitazone for another 4 days. Induced (with P or DMSO) and non-induced (un-differentiated) cells were fixed and stained with lysochrome oil-red-o (red). The number of lipid-laden adipocytes in differentiated cells was reduced upon Hh activation with P. **(C-D)** Quantification of adipogenesis comparing undifferentiated cells and differentiated cells with or without Hh activation. Cells were stained with oil-red-o, the dye was eluted with 100% isopropanol, and the absorbance of the eluted dye was measured at 492 nm. Values of induced DMSO and P conditions were corrected for blank- and un-differentiated (un-diff) values **(C)** or additionally normalized to DMSO **(D)**. Data are shown as mean ± S.D., p-values were calculated by unpaired Student's t-test **(C)** or by one sample t-test to theoretical mean of 1 **(D)**, n = 10.

SMO directly interacts with some BBSome proteins, e.g., Bbs1, and its retrograde transport depends on the BBSome/BBS chaperonin complex (Zhang *et al.*, 2012a). Indeed, different BBS models (*Bbs1 M390R/M390R* knock-in, *Bbs2*-, *Bbs3*-, *Bbs4*-KO) display an increase in ciliary SMO levels under basal conditions (Zhang *et al.*, 2012a)

(Zhang *et al.*, 2011), and previous work by my colleague Dr. Klausen showed a similar increase in ciliary SMO levels in mouse embryonic fibroblasts (MEFs) from *Bbs8*^{-/-} and *Bbs6*^{-/-} mice (Klausen, 2020). Therefore, I analyzed the ciliary SMO localization in cells from *Bbs8*^{-/-} and *Bbs8*^{+/+}. To this end, I isolated cells from the gWAT SVF of *Bbs8*^{-/-} and *Bbs8*^{+/+} mice, treated the cells with 1 µM SAG for 48 h, and analyzed the ciliary SMO localization using immunocytochemistry and CiliaQ analysis. As the background threshold intensity was subtracted to improve the analysis of the ciliary SMO localization, this led to negative intensities, when ciliary intensities were below background threshold. My results demonstrate that SMO was not localized in primary cilia of *Bbs8*^{+/+} cells under control conditions but resided in the cilium after simulation with SAG (Figure 51). The ciliary SMO localization after SAG stimulation was not different between *Bbs8*^{-/-} and *Bbs8*^{+/+} cells (*Bbs8*^{-/-}: 954.9 ± 98.4, *Bbs8*^{+/+}: 1050 ± 92) (Figure 51). However, under basal conditions, the ciliary SMO fluorescent intensities in *Bbs8*^{-/-} cells were significantly increased (102.5 ± 33.7) compared to *Bbs8*^{+/+} cells (-15.72 ± 10.57) (Figure 51), in line with previous findings in other cell lines (Zhang *et al.*, 2012a) (Klausen, 2020). My findings indicate that Bbs6 and Bbs8 both control SMO localization in the cilium. Based on these results, I hypothesized that the increase in basal ciliary SMO levels in pre-adipocytes already activates Hh signaling, which, in turn, reduces the adipogenic potential of pre-adipocytes and shifts AT expansion towards hypertrophy.
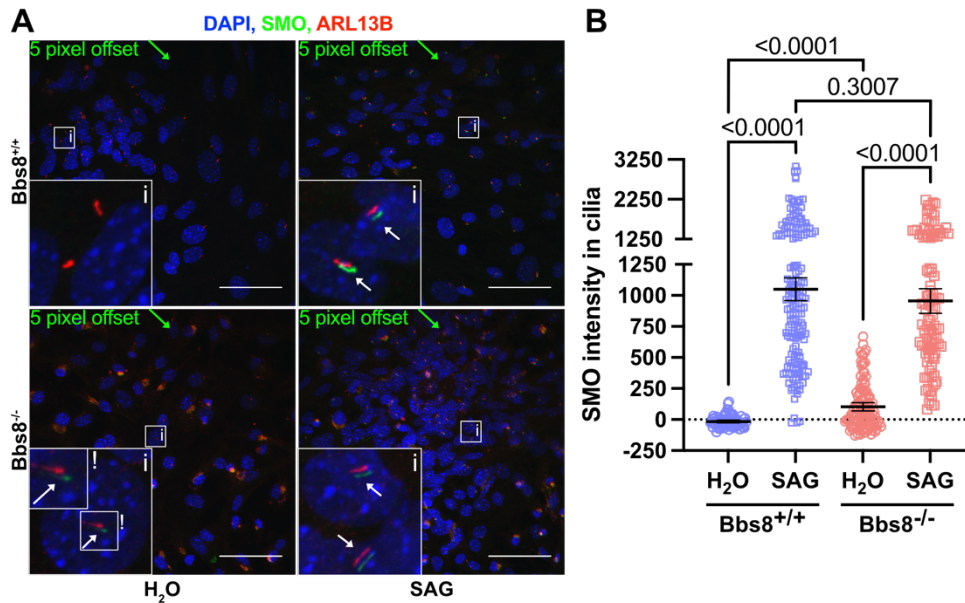
Figure 51: Loss of Bbs8 increased the ciliary SMO localization under basal conditions. (A) The SVF isolated from gWAT of Bbs8$^{-/-}$ and Bbs8$^{+/+}$ was cultured until confluency for at least 48 h before stimulation with 1 µM Smoothend Agonist (SAG) to activate Hh signaling. Two days later, cells were fixed and stained with DAPI (blue, DNA), an anti-SMO antibody (green), and an anti-ARL13B antibody (red, cilia). The green channel is shifted by 5 pixels. White arrows indicate SMO localized to cilia. Scale bars: 50 µm. **(B)** Quantification of Smo localization in the cilium. The fluorescence intensity in the cilium from the SVF of Bbs8$^{-/-}$ and Bbs8$^{+/+}$ mice was quantified using CiliaQ (Hansen *et al.*, 2021). Cilia were reconstructed in the cilia channel (red) by a Flood-Filler algorithm, detecting objects above an automated intensity threshold. For background correction, the background intensity threshold was subtracted from SMO cilia signal-intensities. The background intensity threshold was calculated as mean of 10% highest intensity voxels of background and was set as baseline for unspecific signals, represented as dotted line. Data are shown as mean ± 95 % confidence interval (CI) and with colored individual values, p-values were calculated by Mann-Whitney test, n = 1, including at least 79 cilia per condition.

To test this hypothesis, I analyzed adipogenesis after activating Hh signaling using P (Figure 52A,B). I first compared the basal adipogenic potential of WT and KO cells and observed no difference between WT and KO mice for both Bbs6 and Bbs8 mouse lines (Figure 52C,D), demonstrating that the adipogenic potential was generally not affected by mislocalized SMO under basal conditions. There might be a slight tendency towards reduced adipogenesis in the KOs, but this did not reach significance due to high variations between replicates. Next, I activated the pathway with 2 µM P (Figure 52E,F,G,H). Here, adipogenesis was significantly reduced after normalization to the vehicle control (DMSO) to 0.43 in *Bbs8$^{+/+}$* and 0.45 in *Bbs8$^{-/-}$* cells and to 0.52 and 0.40 in *Bbs6$^{+/+}$* and *Bbs6$^{-/-}$*, respectively (Figure 52G,H). However, there was no difference in the P response between WT and KO in both *Bbs* models (Figure 52G,H). Furthermore, they also reacted equally to SHH activation (Figure 52G,H).

In summary, my results demonstrate that the increased basal ciliary SMO localization does neither affect the adipogenic potential of pre-adipocytes nor their response to Hh signaling.

Of note, rosiglitazone, which is part of the pharmacological cocktail to induce adipogenesis, directly activates the key transcription factor PPARγ (Lehmann *et al.*, 1995; Tontonoz and Spiegelman, 2008) to promote adipogenesis. Thereby, it acts downstream of any possible ciliary signaling pathways and might cover subtle ciliary

signals. Hence, the use of rosiglitazone and generally high concentrations of the components in the induction cocktail have raised concerns as they might shortcut all regulatory pathways orchestrating adipogenesis (Hilgendorf *et al.*, 2019). Thus, it cannot be ruled out that impairment of adipogenesis due to pre-activation of Hh signaling is present in BBS mouse models, but is not detectable under these experimental conditions. To investigate this in more detail, rosiglitazone should be avoided or at least reduced.

Additionally, quantification of adipogenesis using oil-red-o requires a robust and strong signal. The lower the signal the higher the error due to high background and well-to-well variations. This method had to be performed in at least a 24-well format to produce detectable signals, which requires a lot of cells, which are limited due to the nature of isolated primary cells. Due to these major drawbacks, I switched to the other quantification method using fluorescence microscopy image analysis, which allowed a high throughput analysis in a 96-well plate format.
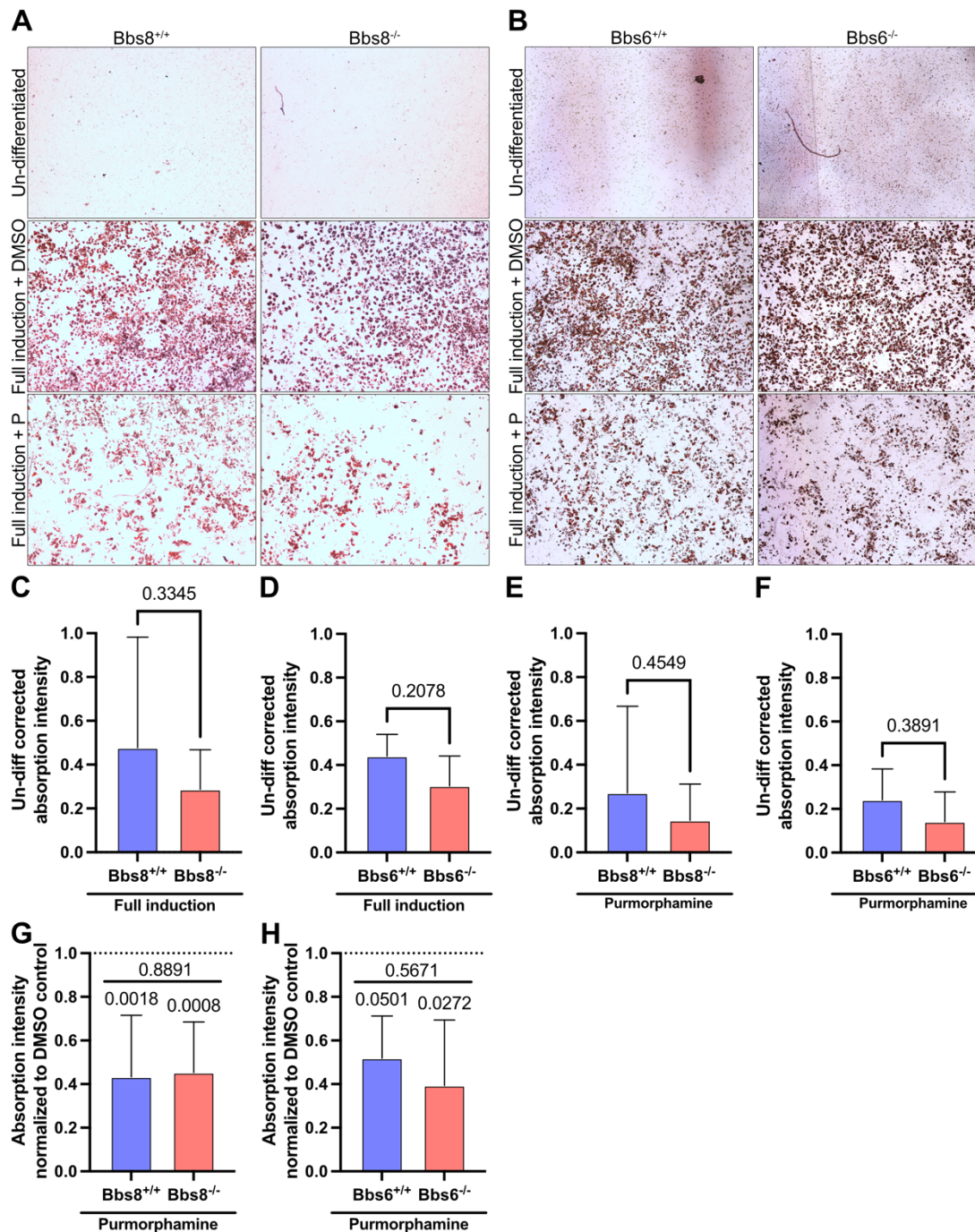
Figure 52: Hedgehog-dependent inhibition of adipogenesis remains unchanged in the absence of Bbs8 and Bbs6. (A-B) Representative images of the effect of Hh activation on adipogenesis from Bbs8 **(A)** and Bbs6 **(B)** WT and KO mice. SVF was isolated from murine gWAT of Bbs-WT and -KO mice and cells were seeded confluently before adipogenesis was induced for three days with an induction cocktail (5 µg/ml Insulin, 1 µM Dexamethasone, 100 µM IBMX, 1 µM Rosiglitazone and either 2 µM Purmorphamine (P) or DMSO as vehicle control. Adipogenesis was maintained by 1 µM Rosiglitazone for another 4 days. Induced (with P or DMSO) and non-induced (un-differentiated) cells were fixed and stained with lysochrome oil-red-o (red). The dye was eluted with 100% isopropanol, and the absorbance of the eluted dye was measured at 492 nm. Absorption intensities were corrected for blank- and un-differentiated (un-diff) values. **(C-D)** Quantification of basal adipogenesis without Hh activation comparing KO and WT SVF derived from Bbs8 **(C)** and Bbs6 **(D)**. **(E-F)** Quantification of adipogenesis after Hh activation comparing KO and WT SVF derived from Bbs8 **(E)** and Bbs6 **(F)**. Data are shown as mean ± S.D., p-values were calculated by unpaired Student's t-test, n ≥ 6 (Bbs8), n ≥ 3 (Bbs6). **(G-H)** Quantification of adipogenesis inhibited by Hh activation comparing KO and WT SVF derived from Bbs8 **(G)** and Bbs6 **(H)**. Absorption intensities were normalized to DMSO, indicated by dotted line. Data are

shown as mean ± S.D., p-values were calculated by unpaired Student's t-test (KO vs WT, indicated by line covering both bars) or by one sample t-test to theoretical mean of 1 (compared to DMSO normalization, p values directly above the respective bar), n ≥ 6 (Bbs8), n ≥ 3 (Bbs6).

Recently, a novel ciliary signaling pathway promoting adipogenesis has been proposed: the free fatty acid receptor 4 (FFAR4 also known as GPR120) has been shown to localize to primary cilia, where it is activated by the omega-3 fatty acid docosahexaenoic acid (DHA) and, in turn, increases ciliary cAMP levels. Downstream, this resulted in EPAC-dependent chromatin remodeling and promoted adipogenesis (Hilgendorf *et al.*, 2019) (Figure 57A). To detect this ciliary regulatory effect on adipogenesis, I removed rosiglitazone from the medium and changed to the reported control cocktail (reduced cocktail), in which the components that induce adipogenesis are titrated down to a threshold, at which the progenitors were just about to undergo adipogenesis. Furthermore, I maintained adipogenesis with 1 µg/ml insulin instead of 1 µM rosiglitazone (Hilgendorf *et al.*, 2019). Thereby, the system allows to detect the influence of ciliary signaling on adipogenesis. Adipogenesis war largely reduced using the control compared to full induction cocktail (Figure 53B-E). In line with previous results, addition of DHA or the FFAR4 agonist TUG891 did evoke a significant increase in adipogenesis (Figure 53B-E). Thus, I have established an *in vitro* system that allows to analyze the role of ciliary signaling in controlling adipogenesis.
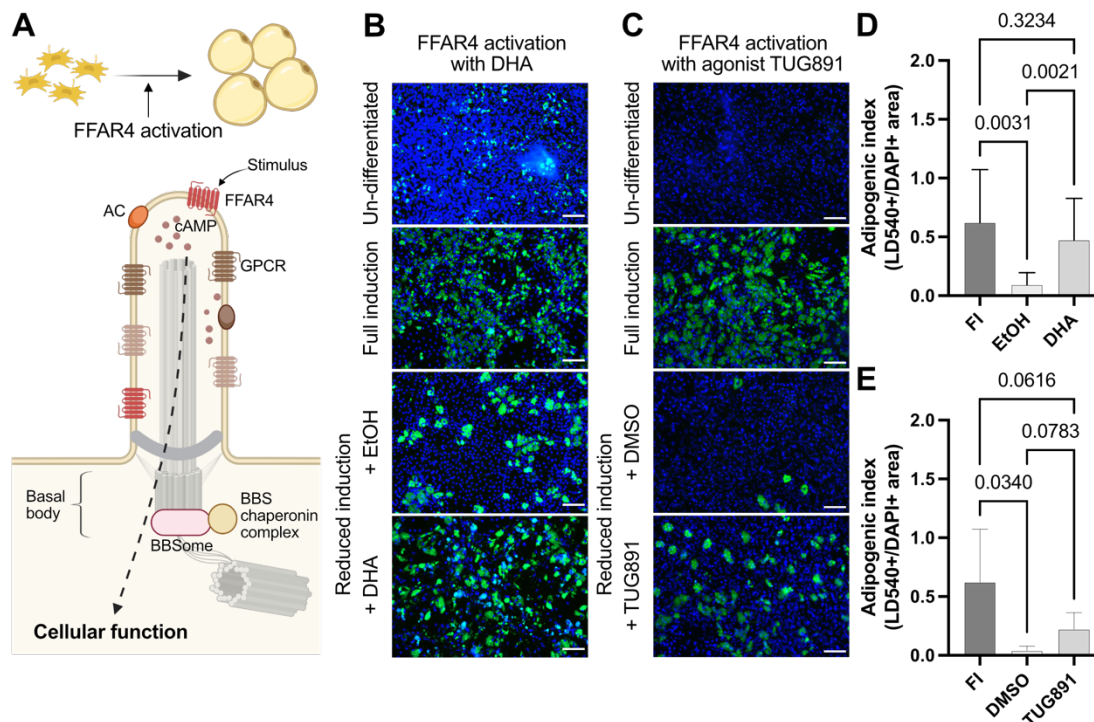
Figure 53: FFAR4 signaling induces adipogenesis *in vitro*. (A) Free fatty acid receptor 4 (FFAR4) signaling (bottom) induces adipogenesis (top). FFAR4 is a ciliary GPCR, which increases ciliary cAMP levels by activating adenylate cyclases (ACs). In turn, this leads to chromatin remodeling and subsequently to the expression of pro-adipogenic genes (Hilgendorf *et al.*, 2019). **(B-C)** To detect the effects of ciliary signaling on adipogenesis, the pharmacological cocktail that induces adipogenesis *in vitro* has been adjusted (reduced induction). **(B)** Omega-3 polyunsaturated fatty acids (PUFAs), such as docosahexaenoic acid (DHA), are natural FFAR4 ligands and activate the pathway. Differentiation was induced for three days either with the full induction cocktail (5 μg/ml Insulin, 1 μM Dexamethasone, 100 μM IBMX, 1 μM Rosiglitazone) or the reduced cocktail (0.4 μg/ml Insulin, 0.1 μM Dexamethasone, 20 μM IBMX), containing either 100 μM DHA or ethanol as vehicle control. Subsequently, differentiation was maintained by adding 1 μg/ml Insulin for another four days. Cells were fixed and stained with DAPI (blue) and LD540 (green). **(C)** Effect of the synthetic FFAR4 agonist TUG891 on adipogenesis. Conditions see (B) with 100 μM TUG891 and DMSO as vehicle control. **(D-E)** Images were analyzed via ImageJ. Area of lipid droplets (LD540) and area of nuclei (DAPI) were determined to calculate the adipogenic index, defined as lipid droplet area (LD540) divided by nuclei area (DAPI). Quantification of adipogenesis after full induction and upon FFAR4 activation with DHA **(D)** or TUG891 **(E)**. Data are shown as mean ± S.D., p-values were calculated by mixed-effects one-way ANOVA, $n \geq 13$ **(D)**, $n \geq 5$ **(E)**.

3.10 Analysis of the role of cAMP signaling for adipogenesis

The second messenger cAMP plays an important role for ciliary signaling (Johnson, Yan). In mammals, ACs synthesize cAMP mainly by transmembrane ACs that transduce signals from GPCRs (Kamenetsky *et al.*, 2006). Ciliary cAMP levels have been shown to increase upon FFAR4 activation. Therefore, it was hypothesized that FFAR4 signaling activates ACs in primary cilia, which in turn elevates cAMP levels, triggering a signaling cascade that leads to a pro-adipogenic cellular response (Hilgendorf *et al.*, 2019).

I aimed to scrutinize this link of GPCRs activating ACs in the cilium in more detail. To this end, I already showed that AC3 is localized to primary cilia in pre-adipocytes (Chapter 3.1).

To investigate the role of AC3 for the reported FFAR4 signaling pathway, I used the Pdgfra-Ac3 knock-out mouse line, in which *Adcy3* is conditionally knocked-out in

Pdgfra-expressing cells, such as pre-adipocytes. To this end, I isolated SVF from Pdgfra$^{cre/+}$Ac3$^{f/f}$ and Pdgfra$^{+/+}$Ac3$^{f/f}$ mice and performed adipogenesis assay in the presence of the natural ligand DHA and the pharmacological agonist TUG891, which both activate the FFAR4 signaling pathway. First, I assessed the general impact of AC3 loss on adipogenesis by comparing full induction, reduced induction, and insulin only: The adipogenic index was reduced under all three conditions in Pdgfra$^{cre/+}$Ac3$^{f/f}$ compared to Pdgfra$^{+/+}$Ac3$^{f/f}$ cells (Figure 54A-C). However, only after normalization to Pdgfra$^{+/+}$Ac3$^{f/f}$, values reached differences due to high variance between experiments (Figure 54C). These results highlight the key role of AC3 for adipogenesis: as only in the presence of AC3, cells can react to pharmacological, pro-adipogenic stimuli, AC3 seems to be key in controlling ciliary cAMP levels and, thereby, to promote adipogenesis in a cAMP-dependent manner. Even the strong inducer rosiglitazone in the full induction cocktail is not able to fully compensate for the loss of AC3 signaling.
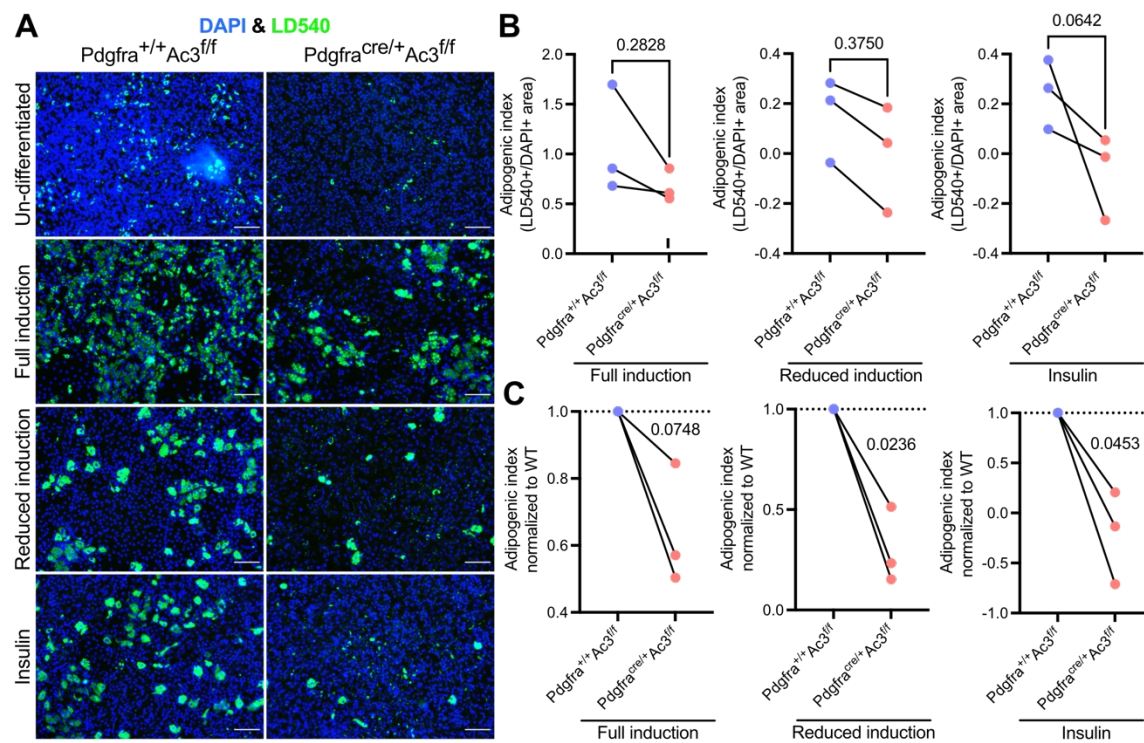
Figure 54: *Ac3* knockout in pre-adipocytes impairs adipogenesis *in vitro*. SVF was isolated from gWAT of Pdgfra$^{+/+}$Ac3$^{f/f}$ and Pdgfra$^{cre/+}$Ac3$^{f/f}$ mice and subjected to the adipogenesis assay. Adipogenesis was induced with either the full induction or the reduced induction cocktail, or with 0.4 µg/mL Insulin and maintained with 1 µg/ml Insulin. **(A)** Representative images of SVF stained with DAPI (DNA, blue) and LD540 (green, lipids). Differentiation of Pdgfra$^{cre/+}$Ac3$^{f/f}$ cells was reduced under all conditions compared to Pdgfra$^{+/+}$Ac3$^{f/f}$ cells. Scale bar: 100 µm. **(B-C)** Quantification of adipogenesis shown in **(A)**. **(B)** Adipogenic index, defined as lipid droplet area (LD540) divided by nuclei area (DAPI), was calculated and background corrected by subtraction of the un-differentiated condition. Data are shown as individual values, p-values were calculated by unpaired Student's t-test, n = 3. **(C)** To quantify the difference between Pdgfra$^{+/+}$Ac3$^{f/f}$ and Pdgfra$^{cre/+}$Ac3$^{f/f}$ cells, the adipogenic index was normalized to Pdgfra$^{+/+}$Ac3$^{f/f}$. Data are shown as individual values, p-values were calculated by one sample t-test to theoretical mean of 1 (indicated by dotted line representing normalization to Pdgfra$^{+/+}$Ac3$^{f/f}$), n = 3. Experiments were performed by Katharina Sieckmann.

Next, I compared the FFAR4-dependent adipogenic response by using either DHA or TUG891. I either used the reduced induction cocktail supplemented by DHA or vehicle

control (Figure 55A) or only insulin supplemented by TUG891 or vehicle control (Figure 55B). To compare the different conditions, I calculated the delta (Δ) in the response between vehicle control and FFAR4 activator. Additionally, I normalized the Δadipogenic index to the maximal response evoked by the full induction cocktail, thereby taking the general reduction in adipogenic capacity into account. My results revealed no significant difference in the DHA-dependent response, while the TUG891-dependent response was reduced in $Pdgfra^{cre/+}Ac3^{f/f}$ compared $Pdgfra^{+/+}Ac3^{f/f}$ cells (Figure 55C,D). These results could indicate a functional difference between DHA and TUG891.
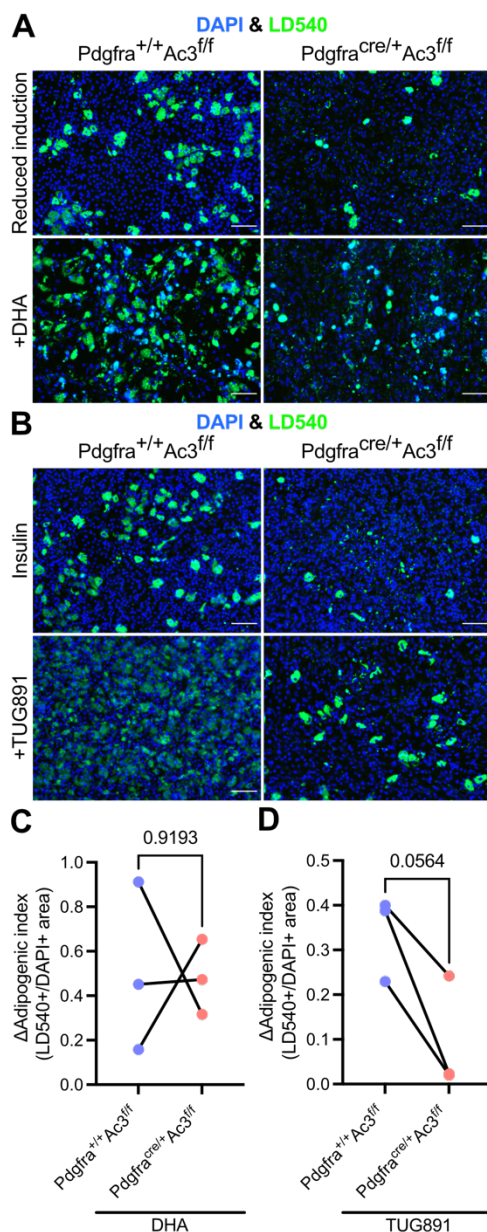
Figure 55: Loss of AC3 in pre-adipocytes impairs FFAR4-dependent promotion of adipogenesis *in vitro*. SVF from murine gWAT from $Pdgfra^{+/+}Ac3^{f/f}$ and $Pdgfra^{cre/+}Ac3^{f/f}$ was isolated and subjected to the adipogenesis assay. FFAR4 was activated with its natural ligand DHA **(A&C)** or the pharmacological agonist TUG891 **(B&D)**. **(A-B)** Representative images of SVF from $Pdgfra^{+/+}Ac3^{f/f}$ and $Pdgfra^{cre/+}Ac3^{f/f}$ stained with DAPI (DNA, blue) and LD540 (green, lipids). Adipogenesis was induced with reduced induction cocktail containing either 100 µM DHA or EtOH as vehicle control **(A)** or with 0.4 µg/mL Insulin containing either 100 µM TUG891 or DMSO as vehicle control **(B)** and maintained with 1 µg/ml Insulin. Scale bar: 100 µm. **(C-D)** To quantify the difference in FFAR4-dependent adipogenesis between $Pdgfra^{+/+}Ac3^{f/f}$ and $Pdgfra^{cre/+}Ac3^{f/f}$ cells, the difference between the adipogenic index of vehicle control and FFAR4 activator (DHA **(C)** or TUG891 **(D)**) was calculated and normalized to the maximal response achieved by the full induction cocktail. Data are shown as individual values, p-values were calculated by unpaired Student's t-test, n = 3. Experiments were performed by Katharina Sieckmann.

Of note, DHA addition often induced cytotoxic effects, leading to increased cell death identified by a loss of DAPI signal, which, in turn, artificially increased the adipogenic index (Figure 56). Additionally, I observed accumulations of weakly positive LD540 areas (turquoise-looking), which also appeared as morphological darker cells in the

brightfield image (Figure 56). Based on these observations, I dismissed the DHA results and only considered the TUG891 results to address my initial question. Since the TUG891-dependent response was reduced upon AC3 loss, my results strengthen the hypothesis that FFAR4 activates AC3 to increase ciliary cAMP levels, which, in turn, activates the pro-adipogenic signaling cascade. To further prove this missing link in the proposed ciliary pathway, ciliary cAMP levels need to be measured using a ciliary targeted cAMP biosensor and cAMP levels could be manipulated by optogenetic tools using a light-activated AC or phosphodiesterase (PDE) to induce or repress adipogenesis, respectively (Hansen *et al.*, 2020; Klausen *et al.*, 2019). This could also be used to rescue the reduced adipogenic capacity of Pdgfra$^{cre/+}$Ac3$^{f/f}$ cells.
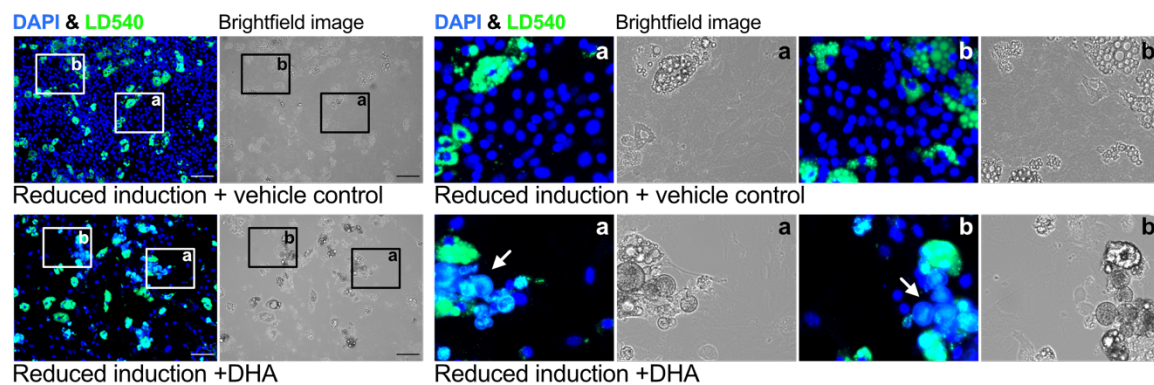
Figure 56: Cytotoxic effect of DHA addition *in vitro*. SVF from murine gWAT from wildtype was isolated and subjected to the adipogenesis assay with DHA supplementation. Exemplary images of SVF stained with DAPI (DNA, blue), LD540 (lipids, green), and corresponding brightfield images (left). Squares indicate zoomed in areas (a) & (b) shown on the right. Adipogenesis was induced with reduced induction cocktail containing either EtOH as vehicle control (top) or 100 µM DHA (bottom). White arrows indicate DHA-unique turquoise staining results. Scale bar: 100 µm.

3.10.1 The role of BBS proteins in controlling ciliary, adipogenic signaling

Loss of BBS proteins disturbs the ciliary protein composition and, thereby, ciliary signaling. Multiple GPCRs haven been shown to be absent or falsely present in primary cilia of BBS models, e.g., SSTR3, MCHR1, NPY2R, GPR161, and SMO (Berbari *et al.*, 2008; Datta *et al.*, 2015; Lechtreck *et al.*, 2013; Liu and Lechtreck, 2018; Loktev and Jackson, 2013; Xu *et al.*, 2015). Therefore, the ciliary localization of cAMP signaling components, such as G$_{\alpha s}$- or G$_{\alpha i}$-coupled GPCRs or ACs might be disturbed in BBS. Thus, I hypothesized that cAMP-dependent FFAR4 signaling pathway might be compromised in *Bbs*-mutants. First, I set out to analyze whether ciliary localization of FFAR4 is disturbed in *Bbs*-mutant, but so far, several commercially available antibodies against FFAR4 (also called GPR120) failed to produce a specific ciliary signal in cells from the SVF (Figure 57A) or 3T3-L1 cells, a pre-adipocyte cell culture cell line (Figure 57B). On the one hand, the anti-FFAR4 antibody from santa cruz (AB sc-390752) showed no signal and on the other hand, the antibody from thermofisher (AB PA5-50973) stained structures representing most likely nucleoli, cytoskeleton, and endoplasmatic reticulum or GOLGI apparatus, but not cilia. Hence, the analysis of ciliary FFAR4 localization was impossible.
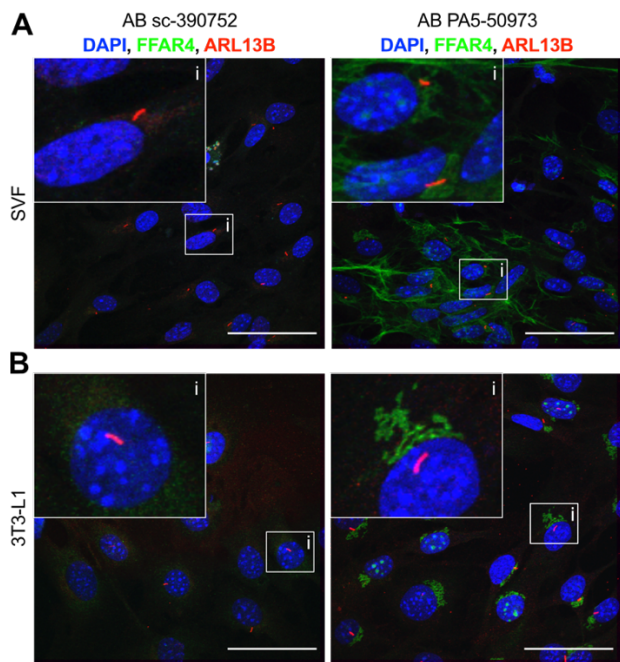
Figure 57: FFAR4 antibody testing fails to reproduce reported specific ciliary signal in SVF cells and 3T3-L1 preadipocytes. Testing of two commercially available antibodies against FFAR4 for immunocyto-chemistry. Staining protocol was adapted to the literature using 3 % BSA + 0.4 % Saponin (Hilgendorf *et al.*, 2019). Cilia were co-stained with anti-ARL13B (red) and nuclei with DAPI (blue). **(A-B)** Staining of two different antibodies against FFAR4 (green) using SVF cells isolated from wildtype mice **(A)** or 3T3-L1 pre-adipocyte cell culture line **(B)**. Left: santa cruz (sc-390752), right: thermofisher (PA5-50973). Scale bars: 50 µm. White squares indicate zoomed in areas.

So next, I analyzed ciliary localization of AC3 as the cAMP-signaling component downstream of FFAR4 in pre-adipocytes of *Bbs*-KO mice. To this end, I performed immunocytochemistry on SVF from *Bbs*-WT and -KO mice and stained for AC3 and a ciliary marker. AC3 was localized to primary cilia in WT cells, whereas the signal was reduced or fully lost in Bbs8$^{-/-}$ and Bbs6$^{-/-}$ cells (Figure 58A,D). I then used the ImageJ PlugIn CiliaQ for image-based analysis of ciliary AC3 intensity and colocalization (Hansen *et al.*, 2021). In this analysis, the ciliary structure was first separated from the background based on the ciliary marker signal and the background threshold was determined. Background threshold intensity was subtracted to highlight intensities due to ciliary accumulation of AC3 compared to background staining. This led to negative intensities when ciliary intensities were below background threshold. Colocalization described the percentage of pixel in the ciliary structure, which are also AC3 positive, defined as 1.5x standard deviations above background intensity threshold.

Both AC3 intensities and colocalization were significantly decreased in Bbs8$^{-/-}$ and Bbs6$^{-/-}$ cells compared to control cells (Figure 58B,C,E,F). Hence, ciliary AC3 localization seems to be impaired in *Bbs*-KO cells. This might alter the sensibility to FFAR4 signaling and, consequently, the response of pre-adipocytes to adipogenic signals, disturbing WAT remodeling, and contributing to pathogenesis.
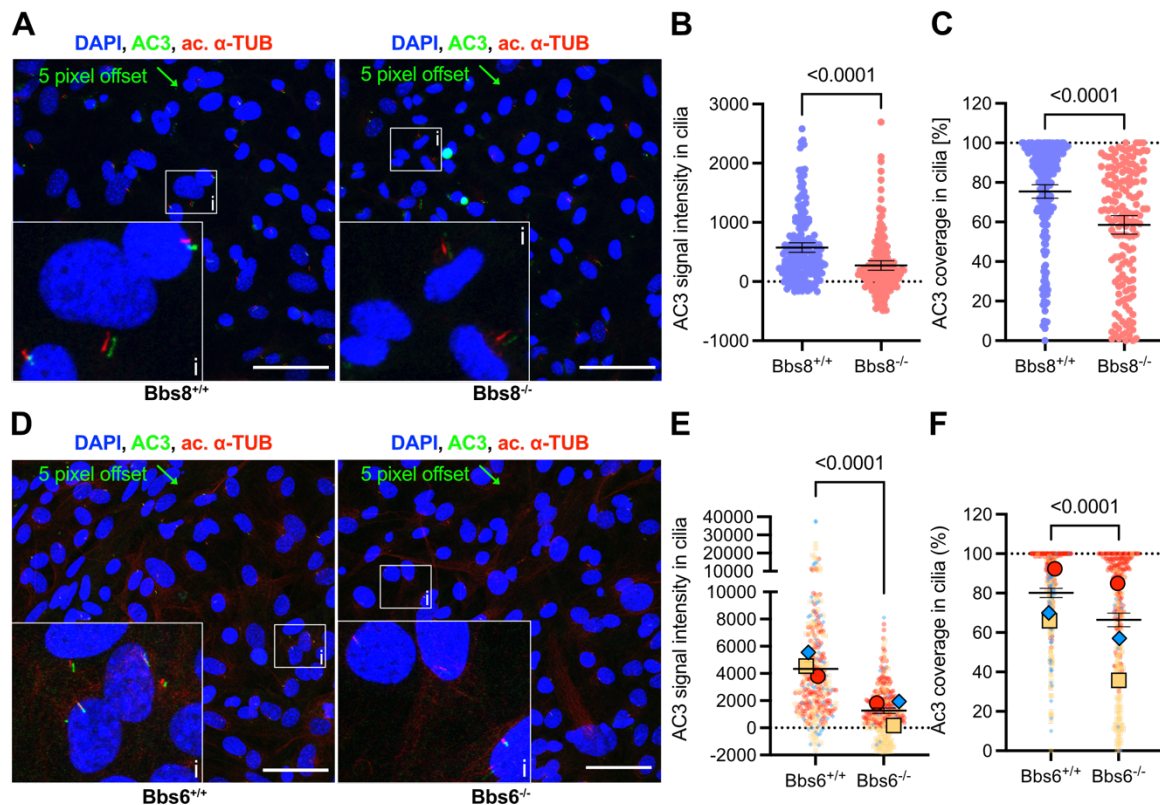
Figure 58: Loss of BBS proteins reduces the ciliary AC3 localization in pre-adipocytes. The pre-adipocyte-containing SVF was isolated from 15 weeks old mice and stained with DAPI (blue, DNA) as well as with an anti-acetylated α-tubulin (red, cilia) and an anti-AC3 (green) antibody. **(A)** Representative images of AC3 localization in primary cilia of SVF from $Bbs8^{+/+}$ and $Bbs8^{-/-}$ mice. White squares indicate zoomed in areas. The green channel has been shifted by 5 pixels. Scale bars: 50 µm. **(B)** To quantify the difference between $Bbs8^{+/+}$ and $Bbs8^{-/-}$ cells, AC3 fluorescence intensity in cilia was analyzed with CiliaQ. AC3 signal intensity was measured in cilia, which were reconstructed based on the ciliary marker channel (red). As background correction, the background intensity threshold was subtracted from AC3 cilia signal intensities. The background intensity threshold was set as baseline for unspecific signals, represented as dotted line. **(C)** Ciliary AC3 coverage was calculated as percentage of ciliary volume with AC3 signal intensities above the background threshold. Dotted line represents perfect coverage of 100%. Data are shown as mean ± 95 % confidence interval (CI) and with colored individual values, p-values were calculated by Mann-Whitney test, n = 1, including at least 159 cilia. **(D-F)** Same as B-C but with SVF isolated from Bbs6 mice. Data are shown as mean ± 95 % confidence interval (CI) and with colored individual values and means representing different n-number, p-values were calculated by Mann-Whitney test, n = 3, including 13 to 183 cilia per experiment. 2 n using alternative ciliary marker ARL13B.

To determine the functional impact of the reduced ciliary AC3 localization for adipogenesis, I performed an adipogenesis assay using the SVF isolated from Bbs8 and Bbs6 mice. First, I assessed the general impact of loss of BBS proteins on adipogenesis by comparing the full and reduced induction cocktail. There was no significant difference between WT and KO SVF, neither using full nor the reduced induction cocktail (Figure 59). There was also no consistent trend observable as indicated by normalization of the data to WT, where KO values were above and below WT values (Figure 59C,F). Analysis of adipogenesis displayed huge variations, including some cells failing to differentiate at all, indicated by the different indices of full induction, ranging from close to one down to nearly zero (Figure 59B,E). Low indices are a result of low to no adipogenesis. So, if full induction did not provoke a robust strong adipogenic response, then a reduction in pro-adipogenic signals will also

show no adipogenesis. Therefore, it might be beneficial to determine a threshold for cells/experiments responding, to only use those for further analysis, normalization, and comparison.
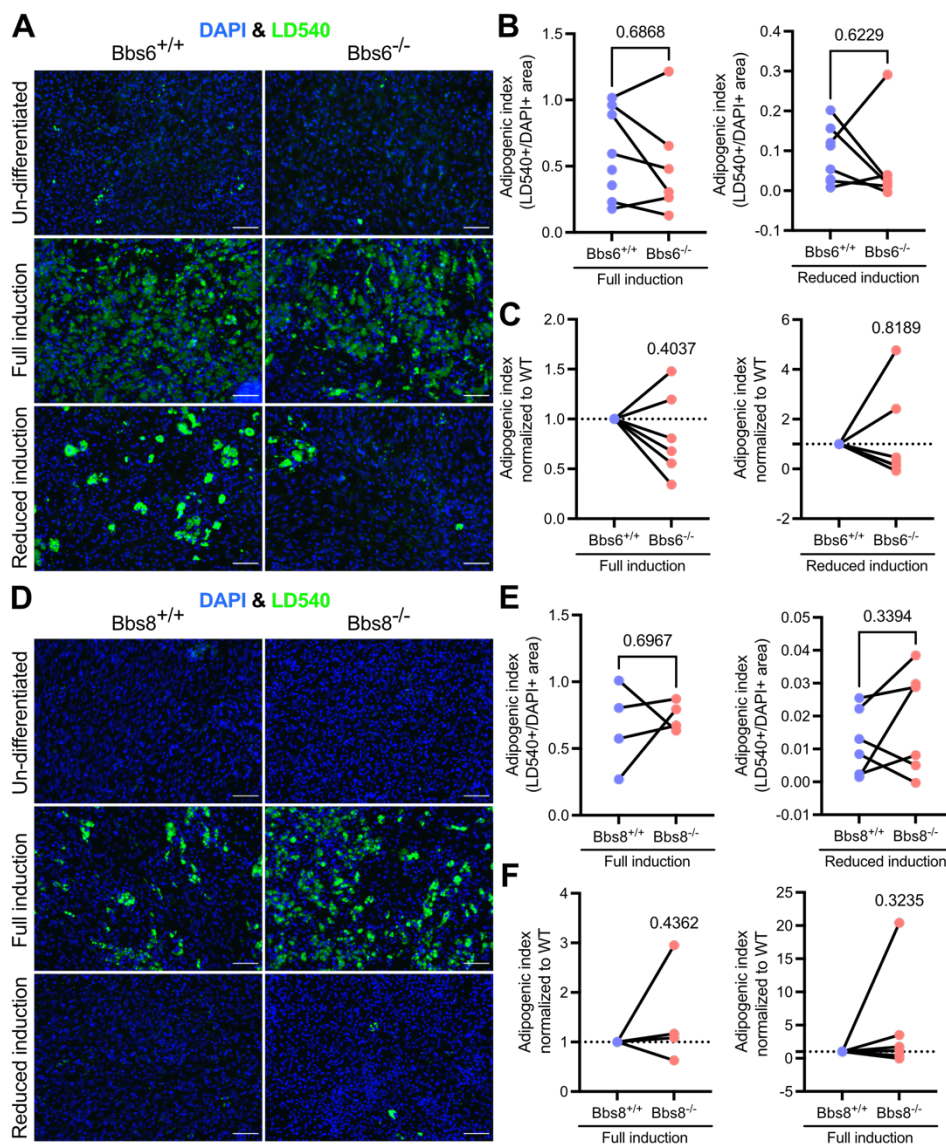
Figure 59: *Bbs6* and *Bbs8* knockout in pre-adipocytes still undergo adipogenesis *in vitro*. SVF was isolated from gWAT of *Bbs*-WT and *Bbs*-KO mice and subjected to the adipogenesis assay. Adipogenesis was induced with either the full induction-, the reduced induction cocktail, or 0.4 µg/mL Insulin and maintained with 1 µg/ml Insulin. **(A)** Representative images of SVF isolated from Bbs6 mice stained with DAPI (DNA, blue) and LD540 (green, lipids). Scale bar: 100 µm. **(B-C)** Quantification of adipogenesis shown in **(A)**. **(B)** Adipogenic index, defined as lipid droplet area (LD540) divided by nuclei area (DAPI), was calculated and background corrected by subtraction of the un-differentiated condition. Data are shown as individual values, p-values were calculated by unpaired Student's t-test, n = 3. **(C)** To quantify the difference between Bbs6$^{+/+}$ and Bbs6$^{-/-}$ cells, the adipogenic index was normalized to Bbs6$^{+/+}$. **(D-F)** Equivalent data from Bbs8 mice. Data are shown as individual values, p-values were calculated by paired one sample t-test or for normalized data by one sample t-test to theoretical mean of 1 (indicated by dotted line representing normalization to WT), n ≥ 4. Some experiments were performed by Katharina Sieckmann.

To assess the responsiveness to FFAR4 signaling, I used TUG891 in the reduced induction cocktail. The vehicle control (DMSO) showed a very low adipogenic index compared to the positive control (full induction), as expected (Figure 60). However, the

adipogenic index upon TUG891 stimulation even remained low in Bbs8$^{+/+}$ cells (Figure 60). In turn, the effect of TUG891 on Bbs8$^{-/-}$ cannot be examined. This might be due to experimental issues as TUG891 had been working previously on other WT cells. It is also possible that mouse line-specific differences in the susceptibility to adipogenic induction, e.g., by altered pre-adipocyte composition of total SVF, require to adjust the concentrations of pharmacological pro-adipogenic substances. Thus, the analysis of FFAR4 signaling in *Bbs*-models will have to be repeated by first establishing conditions that result in a detectable pro-adipogenic effect on WT cells. Nevertheless, the altered ciliary protein composition in BBS might impair the ability to react to adipogenic signals and is worth to be further explored.
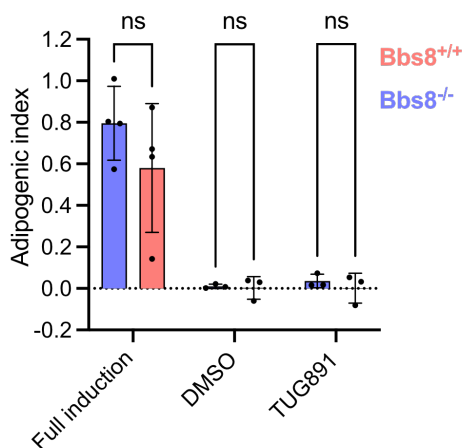
Figure 60: FFAR4 agonist fails to induce adipogenesis *in vitro* in Bbs8 mice. SVF from murine gWAT from Bbs8$^{+/+}$ and Bbs8$^{-/-}$ was isolated and subjected to the adipogenesis assay. Adipogenesis was induced with either the full- or the reduced induction cocktail, and maintained with 1 µg/ml Insulin. FFAR4 was activated with the pharmacological agonist TUG891 during induction with the reduced induction cocktail. Adipogenic index, defined as lipid droplet area (LD540) divided by nuclei area (DAPI), was calculated and background corrected by subtraction of the un-differentiated condition. Data are shown as individual values, p-values were calculated by Šídák's multiple comparisons test, n = 3. Some experiments were performed by Katharina Sieckmann.

3.11 Cilia knockout reduces WAT development *in vivo*

I could demonstrate that loss of *Adcy3* altered ciliary signaling in pre-adipocytes and the physiological response to adipogenic signals. To test the role of primary cilia *per se* in controlling WAT development, plasticity, and health, I created a mouse line lacking cilia in *Pdgfra*-expressing cells (Pdgfra-Ift20) (Chapter 3.1.1). First, I characterized the effect of cilia loss by analyzing the AT mouse phenotype. Pdgfra$^{cre/+}$ Ift20$^{f/f}$ mice were smaller, thinner, and weaker compared to control litter mates (Figure 61A). This severe phenotype caused a deteriorating health and mice had to be sacrifice after a few weeks. However, the phenotype did not show a full penetration of the phenotype with different levels of severity. Less severely affected mice were able to reach up to 8 wks of age, while the most severely affected mice only reached 2 wks of age before their strong phenotype prompted the necessity of euthanasia. Therefore, I analyzed body and different AT depot weights of Pdgfra$^{cre/+}$ Ift20$^{f/f}$ mice at 2-3 and 5-8 wks, representing mice with a severe and less severe phenotype, respectively (Figure 61B). Different AT-depots showed distinct phenotypes (Figure 61B,C). A reduction in gWAT was present independent of the severity of the phenotype, indicating a penetrant phenotype. In contrast, iWAT was affected depending on the severity of the overall phenotype and iBAT was not affected at all. This strongly indicates that WAT but not iBAT development is impaired due to cilia ablation.

I then focused on the most severely affected WAT depot, the gWAT. The testicular gWAT of 3 wks old Pdgfra$^{cre/+}$ Ift20$^{f/f}$ mice was much smaller and resembled an early

postnatal stage P4-5 compared to a fully developed gWAT in control mice (Figure 61D). Additionally, I performed HE staining on paraffin sections of gWAT from 3 wks old mice and whole mount staining labeling lipid droplets with an anti-Perilipin antibody (Figure 61E-F). HE-labeled tissue sections showed a striking difference in tissue morphology between genotypes with hardly any mature adipocytes being visually present in Pdgfra$^{cre/+}$ Ift20$^{f/f}$ mice (Figure 61E). However, Perilipin staining revealed that in fact, mature adipocytes were present, but the lipid droplet size was strongly reduced (Figure 61F), indicating that adipocytes in Pdgfra$^{cre/+}$ Ift20$^{f/f}$ mice display a defect in lipid uptake or energy homeostasis. Interestingly, a recent paper identified a similar phenotype in mice that lack resident macrophages (Cox *et al.*, 2021). Here, lipid storage was impaired and mechanistically, this relies on PDGFcc-dependent signaling from resident macrophages to adipocytes (Cox *et al.*, 2021). Based on these results, I hypothesize that ablation of cilia in pre-adipocytes impairs the responsiveness to PDGFcc in gWAT. In contrast to gWAT, the mass of iWAT was only decreased in the more severely affected mice. Interestingly, iWAT develops prenatal and Pdgfra$^{cre/+}$ Ift20$^{f/f}$ pups at P4 all showed developed iWAT. Therefore, cilia ablation in pre-adipocytes does not impair WAT development prenatally but only postnatally. Also, in less severely affected mice reaching 5-8 wks of age, Pdgfra$^{cre/+}$ Ift20$^{f/f}$ and Pdgfra$^{+/+}$ Ift20$^{f/f}$ mice displayed equal iWAT mass although the body weight was still different. Hence, the observed reduction in iWAT at 3 wks might be a consequence of the overall severe physical state. Alternatively, the reduction in iWAT in severely affected mice might also be a consequence of ciliary dysfunction in iBAT. It was shown that blockage of PDGFcc increased thermogenesis in iBAT (Cox *et al.*, 2021). So, if iBAT cannot react to PDGFcc in Pdgfra$^{cre/+}$ Ift20$^{f/f}$ mice this might result in an increased energy expenditure via dysregulated thermogenesis, which depletes prenatal normally developed iWAT over time in severely affected mice. This could be examined via infrared imaging of the mice.

In summary, cilia ablation in *Pdgfra*-expressing cells resulted in a reduction in WAT mimicking the reported phenotype of mice lacking resident macrophages, in which a concomitant loss of PDGFcc, normally produced by resident macrophages, was shown to be responsible for this phenotype. Since loss of cilia or resident macrophages lead to a similar phenotype, these might be the players communicating via PDGFcc. This thesis is supported by the fact that PDGFcc has a high binding affinity to PDGFRα (Gilbertson *et al.*, 2001; Li *et al.*, 2000), which has been shown to localize to primary cilia of different cell types, including mouse embryonic fibroblasts (MEFs), mouse osteoblast, human embryonic stem cells, rat astrocytes and neuroblasts (Schneider, Awan, Danilov, Noda, Vestergaard). Although, ciliary localization of PDGFRα in pre-adipocytes has not been investigated yet, I used and verified *Pdgfra*-promotor driven conditional gene knock-out mouse models to target pre-adipocytes. Therefore, I know that PDGFRα is present in pre-adipocytes and assume that it localizes to primary cilia and senses PDGFcc released by resident macrophages to promote homeostatic WAT remodeling.
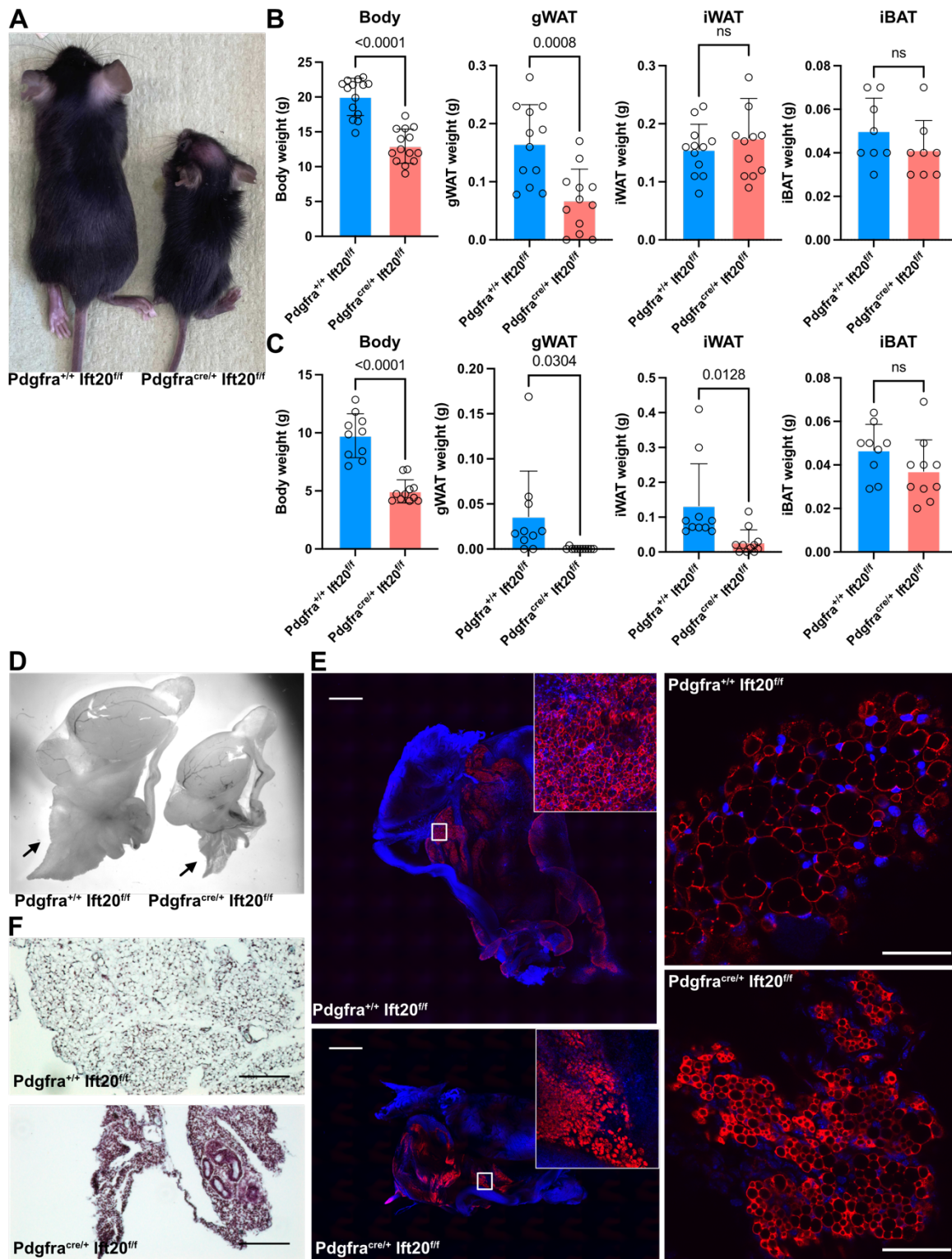
Figure 61: Loss of primary cilia in pre-adipocytes reduced gWAT development. (A) 3 wks old runted Pdgfra$^{cre/+}$ Ift20$^{f/f}$ vs healthy Pdgfra$^{+/+}$ Ift20$^{f/f}$ mouse. (B-C) Comparison of body, gWAT, iWAT, and iBAT weight between Pdgfra$^{cre/+}$ Ift20$^{f/f}$ and Pdgfra$^{+/+}$ Ift20$^{f/f}$ mice aged 5-8 (less severe phenotype) **(B)** and 2-3 wks (more severe phenotype) **(C)**. Data are shown as mean ± S.D. and with individual data points, p-values were calculated by unpaired Student's t-test, n ≥ 8. **(D)** Testis and epididymis with gWAT from 3 wks old Pdgfra$^{+/+}$ Ift20$^{f/f}$ and Pdgfra$^{cre/+}$ Ift20$^{f/f}$ mice. **(E)** Tissues have been stained with DAPI (blue, DNA) and an anti-perilipin antibody (red). As an overview over the whole tissue (left), an image was generated using a 10x (double check in lab book) objective, stitching multiple images together and overlaying two different depths. Scale bar: 1 mm. A detailed single-plane image (right) was generated

using a 60x objective. Scale bar: 50 µm. **(F)** Hematoxylin- and eosin-stained paraffin sections of gWAT of 3 weeks old Pdgfra$^{+/+}$ Ift20$^{f/f}$ and Pdgfra$^{cre/+}$ Ift20$^{f/f}$. Scale bar: 100 µm.

3.11.1 Adipose tissue lacking primary cilia in pre-adipocytes differentiates normally *ex vivo*

My results demonstrate that cilia ablation in *Pdgfra*-expressing cells results in a severely reduced gWAT mass *in vivo*. To be able to perform more mechanistic studies, I cultivated WAT explants *ex vivo*. It was shown that postnatal development of gWAT starts after P4 until it is fully maturated at P14 (Figure 62A) (Han *et al.*, 2011). So, I isolated the testis with the pre-AT appendix of male Pdgfra-Ift20 pups at P4 and dissected the translucent pre-AT from the testis, epididymis, and vas deferens (Figure 62B). Then, I cultivated the tissue *ex vivo* over 14 days. It has been previously described that pre-AT differentiates and forms lipid filled mature adipocytes without addition of adipogenic stimuli *ex vivo* (Figure 62C) (Cox *et al.*, 2021). Pdgfra$^{cre/+}$ Ift20$^{f/f}$ and Pdgfra$^{+/+}$ Ift20$^{f/f}$ mice differentiated equally during *ex vivo* cultivation (Figure 62D): In contrast to the impaired gWAT mass development *in vivo*, cilia loss had no impact on the ability to form mature lipid filled adipocytes *ex vivo*. There might be different reasons for this discrepancy between *in vivo* and *ex vivo*: 1) primary cilia are not required for adipogenesis, but important to stimulate lipid up-take by mature adipocytes upon sensing PDGFcc, and a defect in lipid uptake in the absence of primary cilia might not be detectable at this early developmental stage *ex vivo*, 2) adipogenesis is not exclusively regulated by primary cilia and alternative pathways might be activated (e.g., due to addition of 10 % FCS) during *ex vivo* cultivation, which under physiological conditions would never be high enough to override ciliary loss, 3) primary cilia act not only as signal receiver but subsequently also as signal transmitter: in response to PDGFcc, an autocrine signal is secreted by ciliated pre-adipocytes triggering a cilia-independent pro-adipogenic pathway and this secreted signal is present in the medium of the *ex vivo* culture and, therefore, rescues the phenotype of cilia loss. Alternatively, the secreted signal could also act in a paracrine manner to induce lipid uptake in mature adipocytes upon detection of PDGFcc.

To further investigate these possibilities, alternatives to FCS supplementation should be tested, such as serum-free or chemically defined media. While serum-free media still contain undefined factors, such as serum albumin, growth factors, and hormones, chemically defined media are completely free of such ingredients and the concentration of each component is listed (Dessels *et al.*, 2016; Usta *et al.*, 2014). Factors that need to be analyzed could then be added in defined concentrations. Another alternative would be supplementation with serum or plasma (Dessels *et al.*, 2016; Kocaoemer *et al.*, 2007). Serum collected from Pdgfra$^{cre/+}$ Ift20$^{f/f}$ mice should replicate the extracellular *in vivo* situation, which would allow to test possibility 3 compared to the effect of serum collected from Pdgfra$^{+/+}$ Ift20$^{f/f}$ mice. For *ex vivo* explant cultivation, which does not require a large volume of medium, serum derived from mice could be feasible although the collected amount is limited. One way to test possibility 1 would be the addition of PDGFcc to the *ex vivo* explant. If this factor is triggering rapid lipid uptake in a cilia-dependent manner, then explant from Pdgfra$^{cre/+}$

Ift20$^{f/f}$ mice should not be able to react in comparison to explants from Pdgfra$^{+/+}$ Ift20$^{f/f}$ mice.
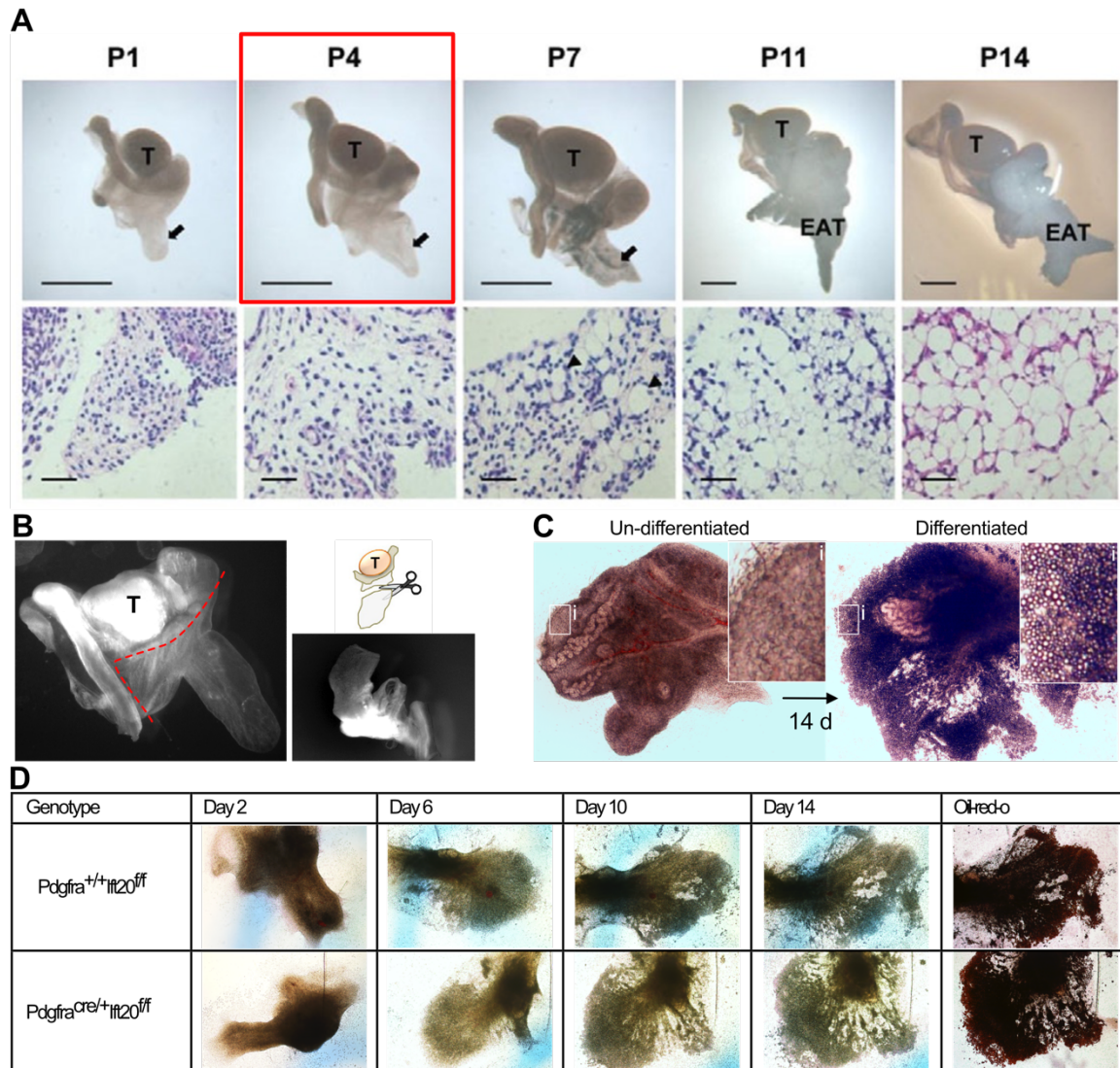
Figure 62: gWAT precursor tissue lacking primary cilia in pre-adipocytes differentiates into lipid-filled adipose tissue *ex vivo*. (A) Development of gWAT precursor tissue into mature adipose tissue over 14 days *in vivo* (image adopted from Han 2014 (Han *et al.*, 2011)). Testes (T) with tissue developing into gWAT were isolated at postnatal days 1-14. Hematoxylin and eosin (HE)-stained cryo sections of these tissues are shown below. Arrowheads at P7 indicate first detectable mature adipocytes. Arrows in the upper row indicate pre-adipose tissue. Scale bar: 100 μm top and 1 mm bottom. **(B)** Testis (T) with gWAT precursor tissue, isolated at P4 from wildtype mice (left); red-dotted line indicates where the gWAT has been cut off from the testis, as schematically shown on the right. **(C)** Over a period of 14 days, isolated precursor tissue differentiates *ex vivo* into tissue with lipid-filled adipocytes. **(D)** Images from time course of gWAT differentiation *ex vivo* from Pdgfra$^{+/+}$ Ift20$^{f/f}$ and Pdgfra$^{cre/+}$ Ift20$^{f/f}$: tissue at day 14 has been fixed 10% PFA and stained with oil-red-o to label neutral lipids (red); n = 4.

3.11.2 Pre-adipocytes lacking primary cilia differentiate into adipocytes *in vitro*

To elucidate the consequence of ciliary loss on pre-adipocytes further, I analyzed adipogenesis also *in vitro.* To this end, I isolated SVF from iWAT instead of gWAT, because gWAT mass was too small for SVF isolation from 3 wks old Pdgfra$^{cre/+}$ Ift20$^{f/f}$ mice. I performed the adipogenesis assay, as described earlier (Chapter 3.10) and could demonstrate that cilia ablation did not impair adipogenesis (Figure 63).

Furthermore, pre-adipocytes isolated from Pdgfra$^{cre/+}$ Ift20$^{f/f}$ mice were still reactive to pro-adipogenic signaling induced by FFAR4 agonist TUG891 (Figure 63). This result contradicts not only the *in vivo* phenotype, but also the reported concept of FFAR4 signaling as a ciliary pathway (Hilgendorf *et al.*, 2019). However, FFAR4 can also localize to the plasma membrane as shown for non-ciliated mature adipocytes (Oh *et al.*, 2010). This might explain the responsiveness to FFAR4 activation despite cilia loss. Of note, I used iWAT and not gWAT, which might function differently. Nevertheless, these results challenge the concept that primary cilia are required for adipogenesis.

In summary, cilia ablation in *Pdgfra*-expressing cells produced conflicting results comparing *in vivo*, *ex vivo*, and *in vitro* experiments. Cilia ablation *in vivo* revealed a severe phenotype with a severely reduced body and gWAT weight, which is partially due to contribution of other *Pdgfra*-expressing cells, e.g., in the brain (Chapter 3.3, Figure 21). *Ex vivo* and *in vitro* experiments to specifically investigate the effect of cilia loss for WAT showed surprisingly no defect in Pdgfra$^{cre/+}$ Ift20$^{f/f}$ mice. As cilia generally play an important role in controlling cell fate, differentiation, and signaling, it is unlikely that the function in pre-adipocytes is different and also recent publications underline this (Hilgendorf, 2021). Thus, the experimental conditions need to be optimized to reveal the molecular and cellular phenotype.
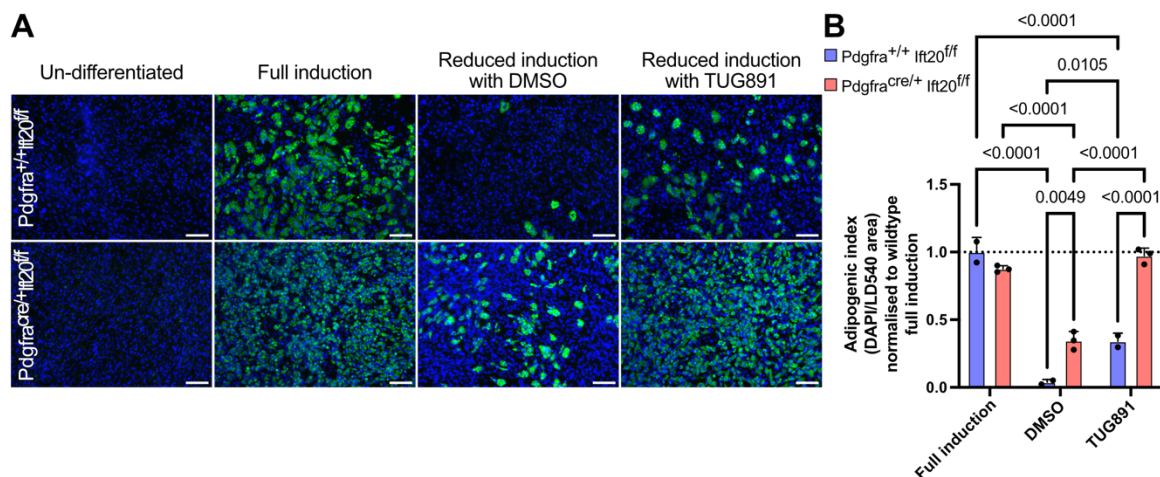
Figure 63: Loss of primary cilia in pre-adipocytes does not impair adipocytes differentiation and rather improves adipogenesis upon pharmacological activation of FFAR4. (A) SVF cells were isolated from iWAT of Pdgfra$^{cre/+}$ Ift20$^{f/f}$ and Pdgfra$^{+/+}$ Ift20$^{f/f}$ mice. Differentiation was induced for three days with either full induction cocktail (5 µg/ml Insulin, 1 µM Dexamethasone, 100 µM IBMX, 1 µM Rosiglitazone) or reduced induction cocktail (0.4 µg/ml Insulin, 0.1 µM Dexamethasone, 20 µM IBMX) containing 100 µM TUG891 or DMSO as vehicle control. Adipogenesis was maintained by adding 1 µg/ml Insulin for another 4 days. Cells were fixed and stained with DAPI (blue, DNA) and with the lipophilic dye LD540 (green, lipids). Scale bar: 100 µm. **(B)** Quantification of adipogenesis normalized to full induction in wildtype cells by calculating the adipogenic index, defined as lipid droplet area (LD540) divided by nuclei area (DAPI). Data are shown as mean ± S.D. with individual data points per technical replicate, p-values were calculated by two-way ANOVA, p = ns not shown, n = 2-3 (technical replicates), n =1 (biological replicates).

3.12 Characterizing pre-adipocyte subpopulations via flow cytometry

The differentiation capacity of pre-adipocytes into mature adipocytes shapes WAT plasticity and critically determines WAT health. Consequently, a detailed

understanding of precursor cells fate and function is needed. Extensive single-cell transcriptomic analysis revealed a tremendous heterogeneity and the existence of multiple subpopulations (Burl *et al.*, 2018; Cho *et al.*, 2019; Hepler *et al.*, 2018; Merrick *et al.*, 2019; Nahmgoong *et al.*, 2022; Sárvári *et al.*, 2021; Schwalie *et al.*, 2018). Although a consistent definition of pre-adipocytes is still lacking, pre-adipocytes are mostly defined as CD31$^-$/CD45$^-$/Ter119$^-$/Sca1$^+$/CD29$^+$ (Cho *et al.*, 2019; Ferrero *et al.*, 2020; Schwalie *et al.*, 2018). Thus, I based my analysis on these markers to identify pre-adipocytes within the total SVF.

At least three subpopulations with distinct functions have been determined by several groups: An early, highly proliferative progenitor population with multi-lineage capacity ("P1"), a committed, highly adipogenic pre-adipocytes population ("P2"), and a regulatory pre-adipocyte population that shows the potential to inhibit adipogenesis of the other subpopulations in a paracrine manner ("P3") (Burl *et al.*, 2018; Cho *et al.*, 2019; Ferrero *et al.*, 2020; Hepler *et al.*, 2018; Merrick *et al.*, 2019; Sárvári *et al.*, 2021; Schwalie *et al.*, 2018) (Figure 64). Transplantation experiments with fluorescently labeled cells revealed that P1 can give rise to P2 and P3 subpopulations, while P2 and P3 are not able to turn into P1 cells. This underlines the unidirectionality of AT lineage-commitment (Merrick *et al.*, 2019) (Figure 64). The equilibrium between interconvertible P2 and P3 might be an important factor affecting WAT remodeling and health. I wondered whether ciliary dysfunction alters fate and function of the different subpopulations, e.g., commitment from P1 to mature adipocytes via P2 or the balance between P2 and P3 and their function.
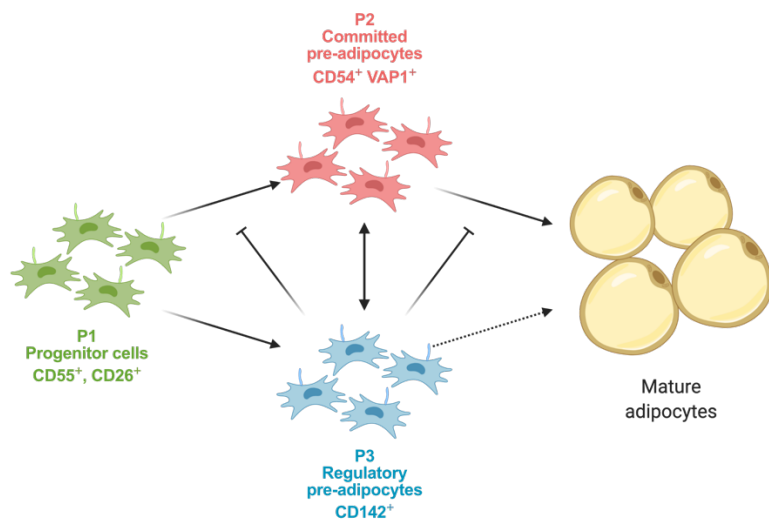
Figure 64: Proposed model of pre-adipocyte subpopulations and lineage hierarchy. Schematic model of pre-adipocyte subpopulations and their lineage hierarchy. Multiple papers defined three different pre-adipocyte subsets based on gene expression profiles and identified unique markers for each subpopulation. Trajectory analysis revealed lineage hierarchy (Merrick *et al.*, 2019), while functional assays indicated paracrine inhibitory function of P3 (Schwalie *et al.*, 2018).

3.12.1 Establishing a gating strategy to identify subpopulations

I investigated pre-adipocyte subpopulations in the SVF isolated from murine WAT by flow cytometry to examine the role of primary cilia in controlling precursor cell fate and function (Figure 65A). First, I established a panel of different markers to identify pre-adipocytes in the heterogenous SVF and to distinguish the three reported subpopulations based on the previously reported marker combinations: CD55 and CD26 (also known as DPP4) as P1 markers, CD54 (also known as ICAM1) and VAP1 as P2 markers, and CD142 as P3 marker (Merrick *et al.*, 2019; Schwalie *et al.*, 2018).

Pre-adipocytes were defined as Lin⁻ (Lin: TER118⁺, CD45⁺, and CD31⁺; marker for erythrocytes, immune-, and endothelial cells, respectively) CD29⁺ SCA1⁺ cells (Cho *et al.*, 2019; Ferrero *et al.*, 2020; Schwalie *et al.*, 2018)) (Figure 65B). For an unbiased approach to analyze pre-adipocyte heterogeneity, I combined the results of different samples to use a multi-dimensional reduction algorithm. To this end, I gated for single, live pre-adipocytes (Figure 65C) and then combined Lin⁻/CD29⁺/SCA1⁺ gate (pre-adipocytes: "SCA1⁺") from different samples into a concatenated file. I used this concatenated file to run a multi-dimensional reduction algorithm, such as uniform manifold approximation and projection (UMAP) (Figure 65D) (McInnes and Healy, 2018). UMAP visualizes clusters of data points, here cells, based on their similarity and their relative proximities. Thereby, this visualization helps to identify the number of distinct groups/clusters within the analyzed cell population, limited by the number of different markers.
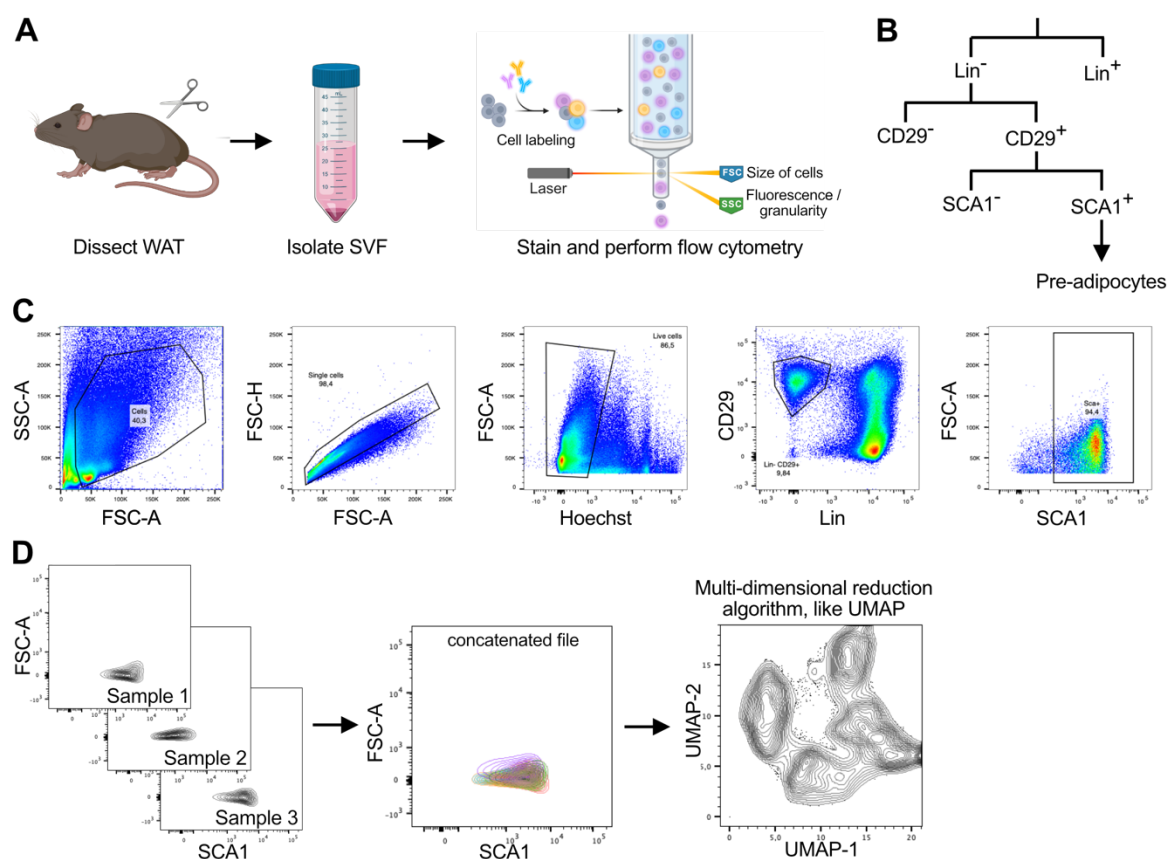
Figure 65: Workflow and preparation to use multi-dimensional reduction as an unbiased approach to analyze pre-adipocyte heterogeneity using flow cytometry. (A) Schematic workflow: SVF was isolated from murine WAT and stained with multiple antibodies against different markers before performing flow cytometry to detect characteristic marker expression of cell populations. **(B)** Schematic overview of gating strategy to select pre-adipocytes. **(C)** Gating strategy to identify single, live pre-adipocytes, defined as Lin⁻ CD29⁺ SCA1⁺ (Lin: TER118⁺, CD45⁺, and CD31⁺; marker for erythrocytes, immune-, and endothelial cells). **(D)** Schematic workflow to generate a multi-dimensional reduction plot, such as UMAP. SCA1⁺ gate, representing pre-adipocytes from different samples were down-sampled to 770 events, combined into one concatenated file, and used to run a multi-dimensional reduction algorithm via a custom-made R-script provided by the group of Elvira Mass. Multi-dimensional reduction algorithms allow to visualize high-dimensional data by clustering data points that favor the preservation of local distances over global distance.

To investigate the effect of Bbs8$^{-/-}$ and HFD-induced obesity, I combined samples from all five different conditions: Bbs8$^{+/+}$ CD/HFD, Bbs8$^{+/-}$ CD, and Bbs8$^{-/-}$ CD/HFD. Thereby, changes in subpopulation's identity in any condition will be detectable. To ensure equal contribution of each condition, I reduced the number of events in the SCA1^{+} gate of each sample to end up with a total of 3000 events per condition using the FlowJo PlugIn "Downsample" before the subsequent clustering and visualization. The cluster analysis was performed based on these down-sampled flow cytometry data files using a custom-made R-script kindly provided by the group of Elvira Mass. The intensities for each marker within the UMAP are visualized and represent the basis for the clustering (Figure 66A). First, I checked whether I could identify the three previously described subpopulations in my UMAP based on the corresponding cluster-heatmap, which visualizes the intensities of the different markers in each cluster and also attributes the frequency of data points to each cluster (Figure 66B,C). Of note, the values were scaled, which means that the values were shifted and rescaled so that they range between 0 and 1. After pre-selection of certain markers, like SCA1 and CD29, all cells should be positive for these markers, rescaling just visualizes slight existing differences. I decided to focus on the more relevant clusters and to ignore extremely small clusters (below 2%). I identified P1 as the only cluster clearly positive for both P1 markers (CD55 & CD26), whereas P2 and two P3 clusters displayed high similarities (Figure 66B,C). Both were negative for P1 markers, but were positive for P2 markers (VAP1 and CD54). I defined P2 as the cluster with low intensities for P3 marker and P3 as the clusters with higher P3 marker intensity. I also detected additional clusters, which all seemed to represent intermediate cell types. Then, I focused on the clusters present in the Bbs8$^{+/+}$ CD condition, which represents the condition most other reports have used to identify the P1-3 subpopulations (Figure 66D,E). Visualization of only this condition reduced the number of clusters, indicating that some of my other condition produce distinct cell clusters. However, all three subpopulations were present in the Bbs8$^{+/+}$ CD condition, although only very few events represented P3, in line with previously reported single cell transcriptomic data showing P3 to be a very small population under physiological conditions (Merrick *et al.*, 2019; Sárvári *et al.*, 2021; Schwalie *et al.*, 2018). Additionally, one intermediate subpopulations (dark blue) lacking the P1 marker CD55 could be identified. Nevertheless, this intermediate populations with 2.5% is a rather small populations compared to P1 with 20% (Figure 66E). I also observed that some of my other conditions displayed a shift in the identify of some clusters rather than displaying additional clusters, which I will analyze in more detail later (Chapter 3.12.3). The shift in those populations seemed to be characterized by VAP1 expression (Chapter 3.12.3,Figure 74). Thus, I decided to establish a gating strategy independent of this marker to still capture and separate the general three subpopulations to analyze and compare the frequencies between my different conditions.
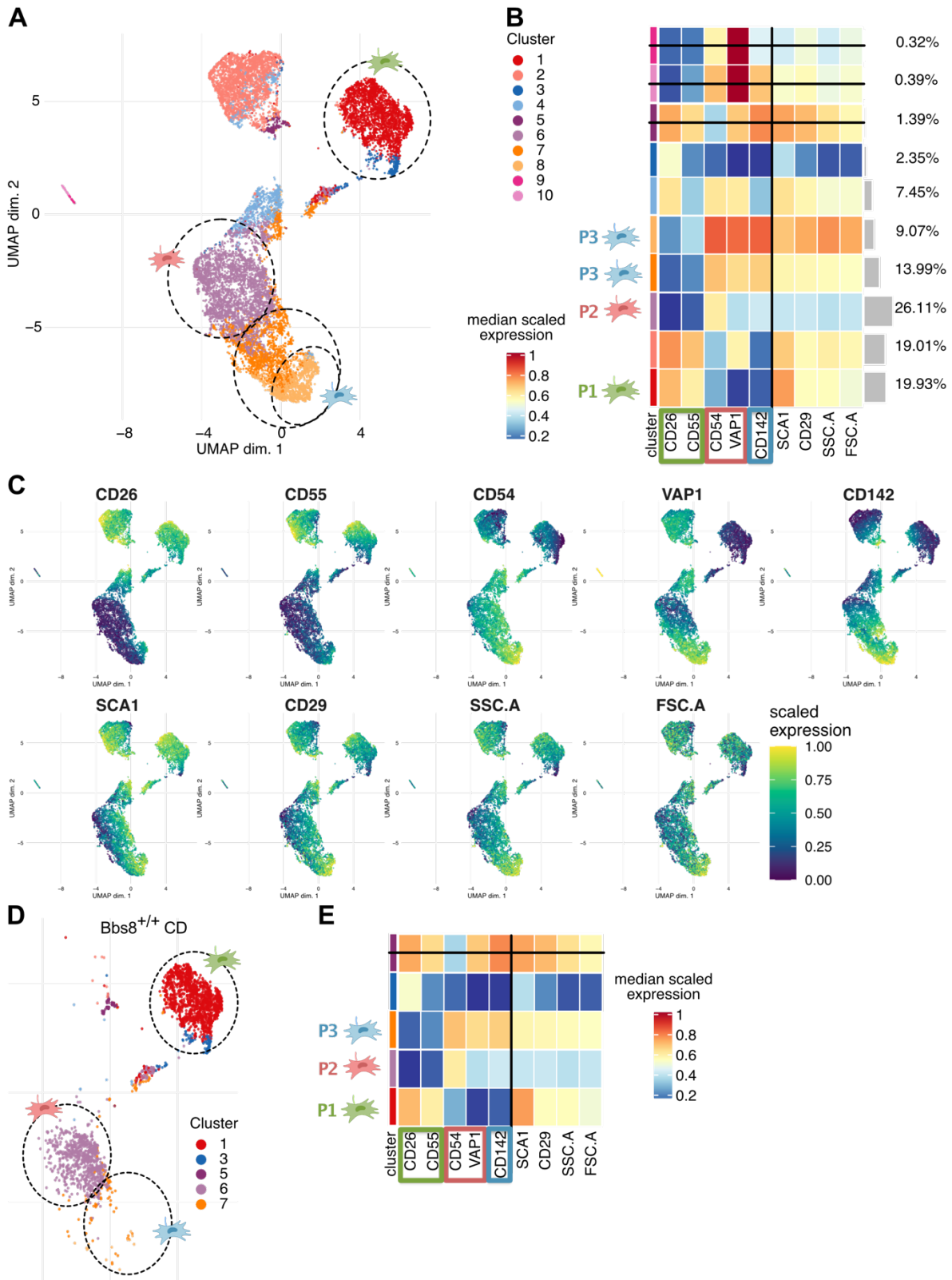
Figure 66: Multi-dimensional reduction reveal multiple subpopulations in the pre-adipocyte pool, including the reported three subpopulations present in the homeostatic control condition. Equal numbers of events for each condition, defined as a combination of diet and genotype, was used to visualize sub-groups within my pre-adipocyte population using a multi-dimensional reduction algorithm via a custom-made R-script provided by the group of Elvira Mass. UMAP and clustering was generated using 3000 events for each condition. Mice from two different experiments were included and batch-corrected on the condition Bbs8$^{+/+}$ HFD using CytoNorm plugin via FlowJo and R. **(A)** UMAP subdivided into 10 colored clusters and assigned P1-3. **(B)** Cluster heatmap corresponding to the cluster in the

UMAP in **(A)** with assigned P1-3. Values were scaled, which means that the values were shifted and rescaled so that they range between 0 and 1. After pre-selection of certain markers, like SCA1 and CD29, all cells should be positive for these markers, rescaling just visualizes slight existing differences. **(C)** Scale intensities for each marker overlayed to UMAP visualizing the basis for the clustering. **(D)** Extraction of the homeostatic condition (Bbs8$^{+/+}$ CD) from the previous UMAP reveals a reduction in the number of present clusters, but the presence of P1-3. **(E)** Cluster heatmap of the present cluster in the homeostatic condition UMAP.

To this end, I gated for pre-adipocytes (SCA1$^+$) and further differentiated by selecting the P1 population based on both P1 markers, and then separating the rest into P2 and P3 based on the CD142 marker (Figure 67A). I verified my gating selection by fluorescence minus one (FMO) controls, in which all but one marker antibody were used. Samples missing either the P1 markers CD26 or CD55 clearly displayed an expected shift of the recorded events, resulting in a location outside of the selected gate. I used the same procedure to verify my gating approach for P2 and P3 gating (Figure 67B). As P2 was weakly positive for the P3 marker CD142, and the CD142 intensity gradually increased within the P3 population, the position of the gate was much more difficult to determine and might be more prone to variations. To keep the gating as consistent as possible, I always re-applied the gating from a previous experiment and then used the sample with the highest CD142 signal in each experiment as orientation to slightly correct the gating.
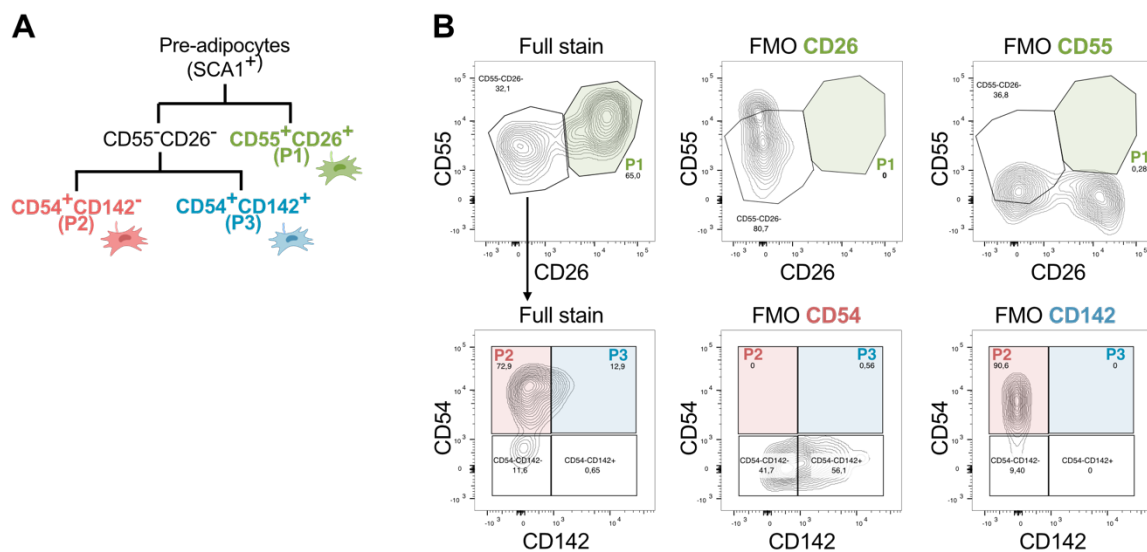
Figure 67: Gating strategy to separate the subpopulations P1, P2, and P3. (A) Schematic overview of the gating strategy to distinguish P1, P2, and P3 from total SCA1$^+$ pre-adipocytes. **(B)** Gating for P1 (green), P2 (red), and P3 (blue) using cells stained with all marker antibodies (full stain) and cells stained with all, but one marker antibody (fluorescence minus one (FMO)). The markers CD55, CD26, CD54, and CD142 are essential for the gating. Therefore, an FMO for each marker was performed to verify the gate selection. Indeed, all four FMOs resulted in empty gates. Black arrow indicates the gate that was used to further differentiate in the next gate.

Additionally, I analyzed the signal intensity of each population-specific marker in the three gated subpopulations to check if the gated subpopulations indeed showed the intended marker-specific signals (Figure 68). My results clearly verified signal specificity for both P1 markers (CD55 and CD26) as well as the P2 marker CD54. The second P2 marker (VAP1) displayed the correct trend, but the difference between

marker negative P1 and positive P2 and P3 population was only minor. While the P3 marker CD142 was clearly absent from P1, it showed the previously mentioned continuous increase in intensity from P2 to P3, making the separation difficult. Overall, all marker signal intensities recapitulated the characteristics of the three subpopulations and verified my selected gating strategy.
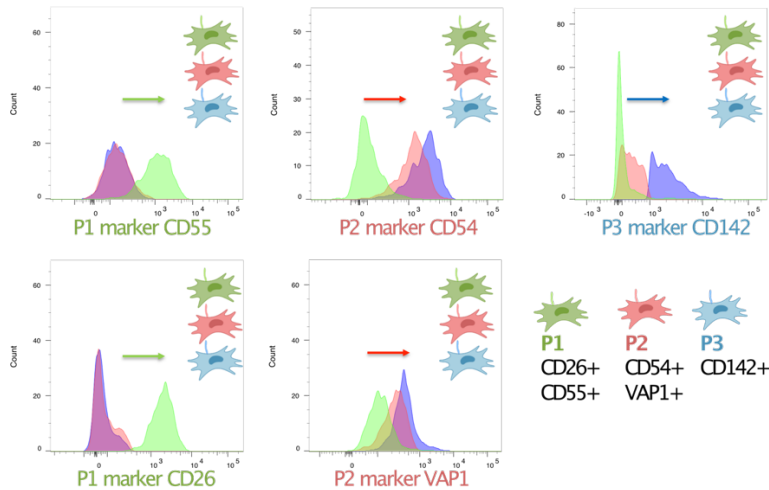
Figure 68: Marker intensities in the gated subpopulations verify the gating strategy. Representative histograms for the five subpopulations-specific markers of the gated P1 (green), P2 (red), and P3 (blue) subpopulations analyzed in WT mice on CD. Each gated subpopulation displays the intended population-specific signal for each marker, verifying the selected gating method.

I first established the staining and gating strategy on SVF from iWAT and then transferred the same gating strategy to SVF isolated from gWAT. I observed one major difference between the different WAT depots: The P2 marker CD54 was a specific marker for P2 and P3 in iWAT cells, but not in gWAT cells as all cells were positive for CD54 (Figure 69). Thus, I adapted my gating strategy to this gWAT-specific change in CD54 signal. Other studies verified this finding, although it has not been pointed out specifically (Merrick *et al.*, 2019; Stefkovich *et al.*, 2021). In these studies, the selected gating strategy resulted in a nearly absent P1 population in gWAT, as the cells moved into an intermediate gate. Others defined these intermediate cells as a separate cell population (Nahmgoong *et al.*, 2022). Generally, I was able to transfer my gating strategy also to gWAT cells and identified an overall CD54$^+$ signal as a gWAT-specific characteristic of pre-adipocytes. Whether this change in marker specificity also affects the function of this subpopulation in gWAT compared to iWAT cells by e.g., facilitating commitment or differentiation, remains to be clarified. Indeed, transplant experiments seem to indicate that this difference in WAT depots coincides with increased commitment to the adipocyte lineage (Nahmgoong *et al.*, 2022).
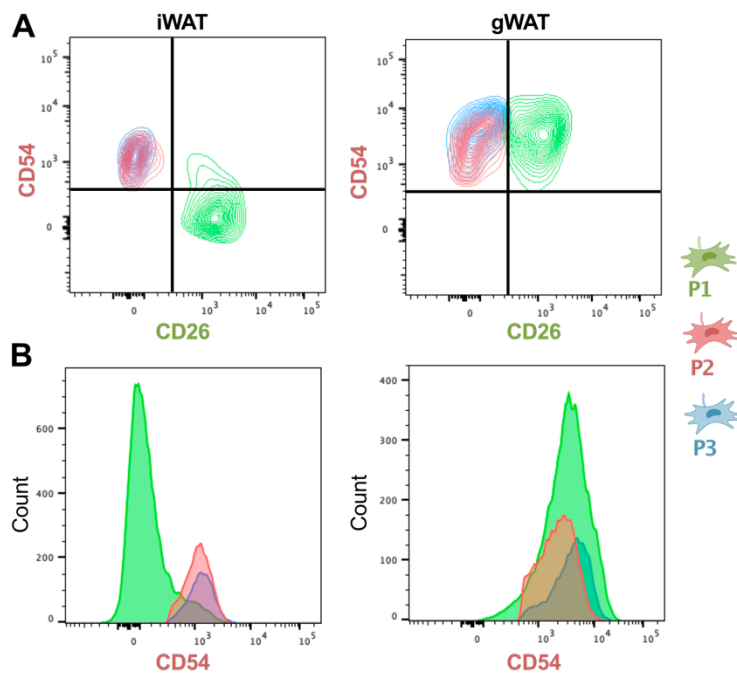
Figure 69: CD54+ signal is a gWAT-specific characteristic of pre-adipocytes. (A) Comparison of iWAT and gWAT by analyzing the CD54 and CD26 signal intensity of the gated P1 (green), P2 (red), and P3 (blue) subpopulations from WT mice on CD. Black grid indicates the separation between marker-positive and -negative cells for each axis. **(B)** CD54 histogram of P1-3 in iWAT and gWAT visualizes the difference in CD54$^+$ signal intensity.

Next, I compared the distribution of the three subpopulations in the SVF isolated from iWAT to gWAT. To this end, I investigated the P1-3 frequency of the total pre-adipocyte population (SCA1$^+$) and combined the data of all 18-20 wks old WT mice on CD, regardless of the strain background to reach sufficient animal numbers. In both iWAT and gWAT, the P1 subpopulation constitutes the largest pre-adipocytes subpopulation, while P3 represented the smallest subpopulation (Figure 70A,B). The relative distribution was similar in both WAT depots, but the absolute frequencies of P1 and P2 were significantly different (Figure 70C): While 70 % of total pre-adipocytes were P1 in iWAT, only 45 % were P1 in gWAT. Also, 15 % of the pre-adipocytes were P2 in iWAT in comparison to 25 % in gWAT. Thus, my results indicate intrinsic differences between the analyzed WAT-depots, which might contribute to the distinct metabolic outcomes. The increased presence of the P2 marker CD54 in gWAT pre-adipocytes might contribute to these changes in subpopulation proportions. The functional consequences of these differences for WAT remodeling and health need further investigation.

In summary, I was able to identify the reported three subpopulations and to develop a gating strategy that allowed me to analyze and compare the frequency of these three subpopulations in the total pre-adipocyte pool in iWAT and gWAT. Previous reports also demonstrated that P1 is the most and P3 the least abundant subpopulation in iWAT (Merrick *et al.*, 2019) and gWAT (Sárvári *et al.*, 2021). Another report also showed the same proportions after correction for the different definitions of subpopulations: here, S1+2 corresponds to my P1 and S3 corresponds to my P2+P3 (Nahmgoong *et al.*, 2022). In contrast to my results for gWAT, another report has demonstrated an opposite distribution with P3 being the most abundant subpopulations (Merrick *et al.*, 2019). This might be a consequence of the previously mentioned CD54$^+$ signal of all pre-adipocytes in gWAT and the gating strategy that

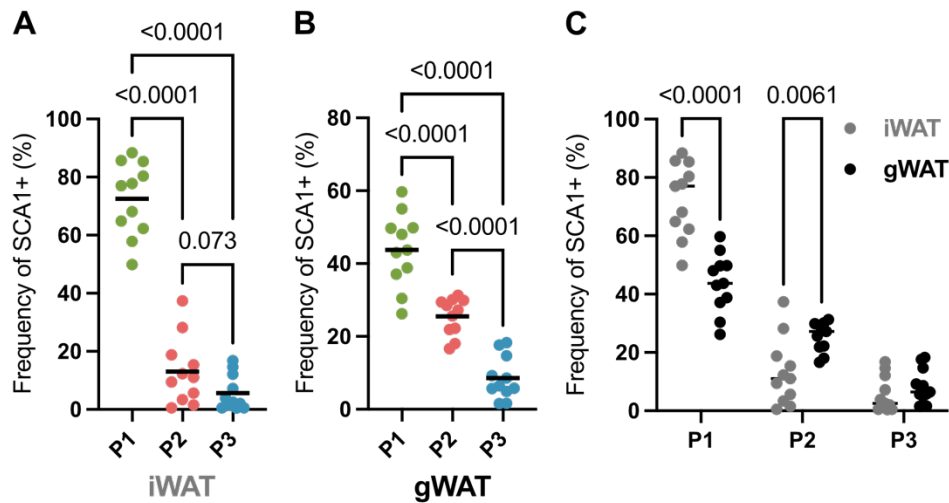they applied, whereby most cells were located in an intermediate gate and were not further investigated.

Figure 70: P1 is the most abundant subpopulation in iWAT and gWAT despite intrinsic differences in absolute frequencies. SVF isolated from iWAT and gWAT of 18-20 wks old WT mice on CD of different strain backgrounds were analyzed via flow cytometry. **(A-B)** Frequency of the total pre-adipocyte pool (SCA1$^+$) of the gated P1 (green), P2 (red), and P3 (blue) subpopulations in iWAT **(A)** and gWAT **(B)**. **(C)** Comparison of P1-3 frequencies in iWAT and gWAT. Data are shown as individual values, p-values were calculated by Šídák's multiple comparisons test, n = 11.

3.12.2 Characterization of obesity-dependent changes of subpopulations

To investigate the role of primary cilia for WAT remodeling and function, I used different models with ciliary dysfunction, which develop an obesity phenotype (Chapter 3.2). I first analyzed the general effect of obesity development on pre-adipocytes using HFD in WT mice. To this end, I combined the populations frequency data of all 18-20 wks old WT mice on CD or HFD to reach sufficient animal numbers. In iWAT, P1 was significantly reduced in obese mice, whereas P2 was unchanged, and P3 was slightly but not significantly increased (Figure 71A). Similar to iWAT, P1 was reduced and P3 was increased in gWAT from obese mice, although the differences were only close to being significant (Figure 71B). Additionally, P2 was slightly but not significantly decreased (Figure 71B). Since there were high variations in the degree of obesity due to individual and line-specific differences in weight-gain susceptibility (Chapter 3.2), I decided to correlate the frequency of the subpopulations with the total tissue weight. My analysis for iWAT revealed a tissue-weight dependent decrease in P1 (Figure 71C) and an increase in P3 (Figure 71E), while P2 seem to be independent of the tissue weight (Figure 71D). In gWAT, the correlations were less strong, but P1 also displayed a weight-dependent decrease (Figure 71F). In addition, P2 showed a weight-dependent decrease (Figure 71G) and P3 an increase, but the deviation of the data points in P3 was very high (Figure 71H). In summary, this confirmed the observed tendencies in the frequencies between lean and obese WT mice, demonstrating that obesity causes a decrease in the early progenitor cells P1 and, although to a lesser degree, an increase in regulatory P3 cell population, thought to counteract adipogenesis. My results are in line with the previous reported changes after HFD-

induced obesity in iWAT and gWAT (Merrick *et al.*, 2019), although another report indicated an increase in P2 instead of P3 in gWAT (Sárvári *et al.*, 2021).
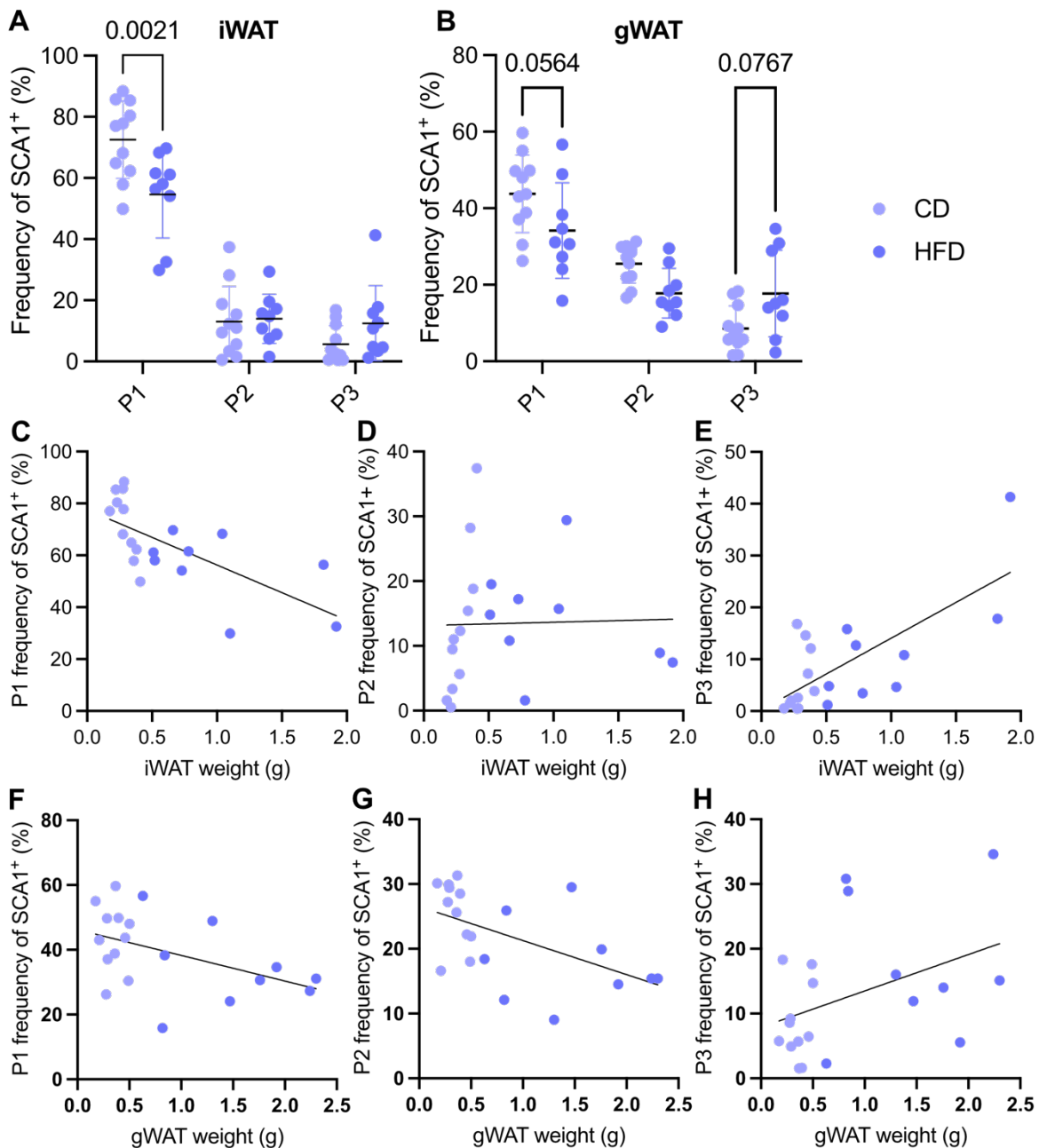
Figure 71: HFD induces a tissue weight-dependent increase in P1 and decrease in P3 in WAT. SVF from murine WAT was isolated from WT mice aged 18-20 weeks fed a HFD or CD and subjected to analysis via flow cytometry. **(A-B)** Comparison of the P1-3 frequency in iWAT **(A)** and gWAT**(B)** from HFD- and CD-fed mice. Data are shown as mean ± S.D., n ≥ 9, p-values were calculated by Šídák's multiple comparisons test. **(C-E)** Correlation of iWAT tissue weight and the frequency of P1 **(C)**, P2 **(D)**, or P3 **(E)**. **(F-H)** Correlation of gWAT tissue weight and the frequency of P1 **(F)**, P2 **(G)**, or P3 **(H)**. Data are shown as individual values, black line indicates simple linear regression line.

3.12.3 Characterization of genotype-specific changes in the different subpopulations

After I verified the diet-induced effect on pre-adipocyte subpopulations, I analyzed the effect of ciliopathy- versus diet-induced obesity. Here, the most severely obese model, Bbs8$^{-/-}$, also displayed the most striking changes in the frequency of P1-3

subpopulations (Figure 72A): In iWAT and gWAT, the frequency of P1 was significantly reduced in obese mice, i.e., $Bbs8^{+/+}$ on HFD as well as $Bbs8^{-/-}$ on CD and HFD. The reduction was similar between comparable obese $Bbs8^{+/+}$ on HFD and $Bbs8^{-/-}$ on CD, indicating that P1 cells from $Bbs8^{-/-}$ mice react to obesity as control mice to diet-induced obesity. Increasing the obesity in $Bbs8^{-/-}$ mice further by HFD feeding led to a stronger decrease, especially in gWAT, where the P1 population from $Bbs8^{-/-}$ on HFD was even significantly reduced compared to $Bbs8^{+/+}$ mice on HFD (Figure 72A). Similar to the effect of diet-induced obesity, the P2 population also remained unchanged in iWAT in obese $Bbs8^{-/-}$ mice on both CD and HFD, but were slightly but not significantly reduced in gWAT (Figure 72A). Furthermore, the increase in P3 was observed in obese $Bbs8^{-/-}$ mice on both CD and HFD (Figure 72A). In summary, the distribution of the P1-3 subpopulations indicated the same changes as evoked by diet-induced obesity. Also, the Bbs6 model displayed the similar tendencies as observed for diet-induced obesity in iWAT (Figure 72B), although only mice on HFD fed significantly gained weight (Chapter 3.2.2, Figure 17: Body- and AT depot weights of Bbs6 mouse lines at obese timepoints.). $Bbs6^{-/-}$ mice on CD already showed a slight reduction in P1 compared to $Bbs6^{+/+}$ mice on CD, although both were equally lean. Thus, there might be a genotype-specific and obesity-independent decrease in P1. In contrast, in gWAT, P1 showed the opposite effect in $Bbs6^{-/-}$ mice, but without reaching significance (Figure 72B), indicating a genotype-specific difference in gWAT. Alternatively, iWAT could be the first WAT-depot that reacts to excess energy in Bbs6 animals and as obesity development was generally mild, even in $Bbs6^{-/-}$ on HFD, gWAT might only react at a later time point. Surprisingly, Pdgfra-Ac3 mice showed hardly any differences (Figure 72C), although $Pdgfra^{+/+}Ac3^{f/f}$ mice on HFD and $Pdgfra^{cre/+}Ac3^{f/f}$ on CD and HFD developed obesity and glucose tolerance was severely impaired (Figure 72C). However, it highlights mouse line specific differences in the general response to obesity. Only for iWAT, P1 was significantly reduced in $Pdgfra^{cre/+}Ac3^{f/f}$ mice on HFD compared to the lean controls, indicating an obesity-related decrease in P1. In summary, ciliary dysfunction does not alter the frequency of the subpopulation's frequencies to obesity.
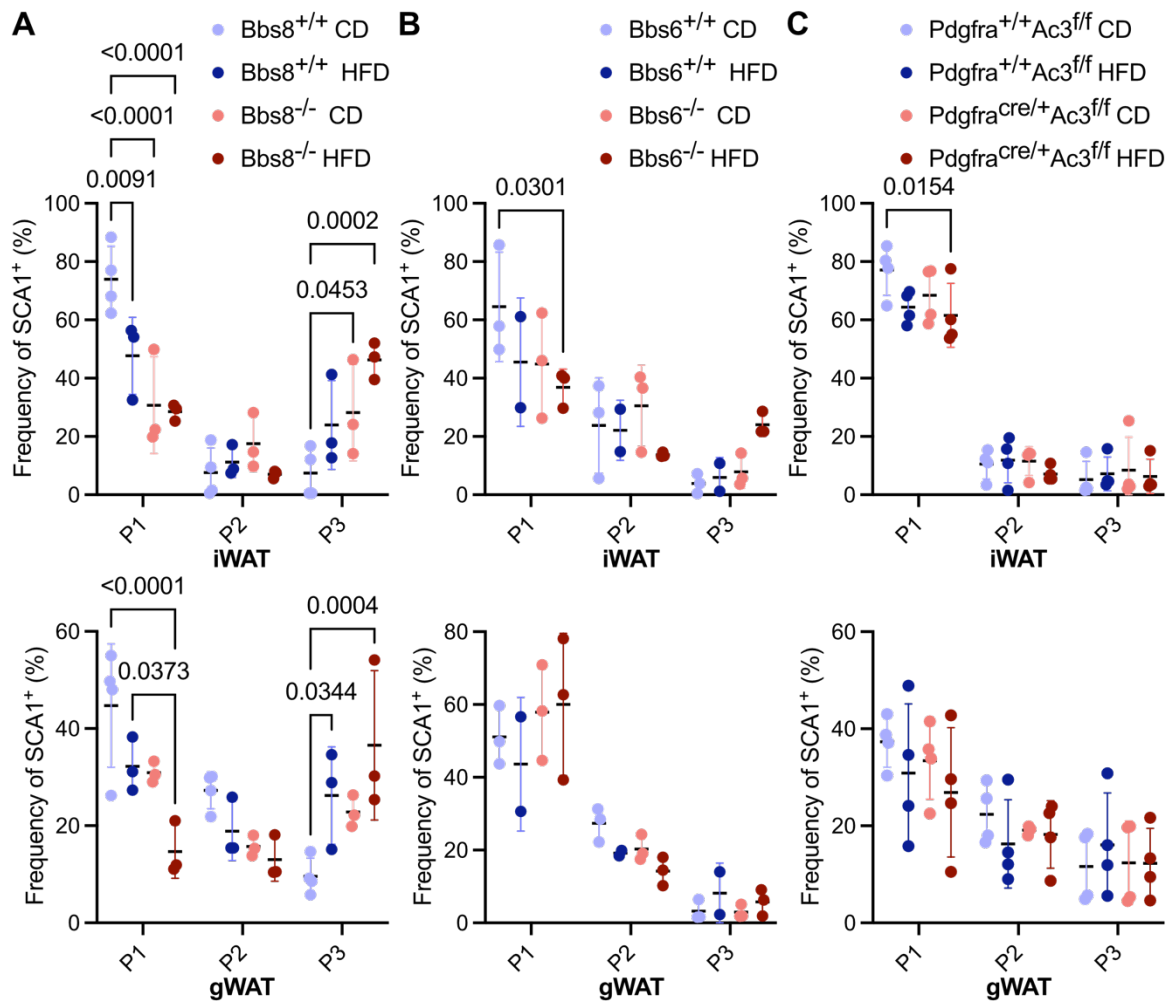
Figure 72: Ciliary dysfunction results in similar changes of P1 and P3 frequencies as observed in diet-induced obesity. SVF isolated from iWAT and gWAT of 18-20 wks old mice on HFD or CD were analyzed via flow cytometry. **(A-C)** Frequency of total pre-adipocyte pool (SCA1$^+$) of the gated P1 (green), P2 (red), and P3 (blue) subpopulations in iWAT (top) and gWAT (bottom) in Bbs8 **(A),** Bbs6 **(B)**, and Pdgfra-Ac3 **(C)** mice. Data are shown as individual values, p-values were calculated by Šídák's multiple comparisons test, n ≥ 3 (Bbs8), n ≥ 2 (Bbs6), n = 4 (Pdgfra-Ac3).

Primary cilia on pre-adipocytes might not only be necessary to regulate lineage commitment and differentiation upon obesity to enable healthy WAT expansion, but might also play a role in regulating the fate of pre- and mature adipocytes, thereby impacting WAT modeling and development independent of obesity. To investigate whether the ciliopathy models display any changes independent of obesity, I also analyzed the ciliopathy models before the onset of obesity. To this end, I analyzed Bbs8 and Pdgfra-Ac3 mice at the pre-obese age of 7-10 wks. I investigated iWAT, as this WAT-depot displayed the strongest effects so far. First, I compared WT mice from both mouse models and could verify that P1 represents the biggest and P3 the smallest subpopulation in both mouse models (Figure 73A). Also, there was no significant difference between both mouse models (Figure 73B). Comparison of Pdgfra$^{cre/+}$Ac3$^{f/f}$ with control littermates showed no difference in any subpopulation (Figure 73C). In contrast, in Bbs8$^{-/-}$ mice, P1 was significantly reduced and P2 significantly increased (Figure 73D). These *Bbs8*-loss induced changes were dose-dependent: Bbs8$^{+/-}$ mice

displayed an intermediate state between Bbs8$^{+/+}$ and Bbs8$^{-/-}$ mice (Figure 73D). The P3 remained unchanged in Bbs8$^{-/-}$ mice (Figure 73D), indicating that a P3 increase is a major feature of obesity. P3 is thought to inhibit adipogenesis and might thereby represent a regulatory feedback loop to limit WAT expansion. Interestingly, deletion of *Bbs8* increased the frequency of committed pre-adipocytes (P2), indicating an increased recruitment of new adipocytes. However, this did not result in a change in AT morphology, i.e., a decrease in hypertrophy (Chapter 3.6, Figure 29Figure 33), but this is in line with increased AT mass before obesity (Chapter 3.2.1, Figure 12). In summary, loss of *Bbs8* but not *Adcy3* already changed the frequency of the P1-3 subpopulations before the onset of obesity.
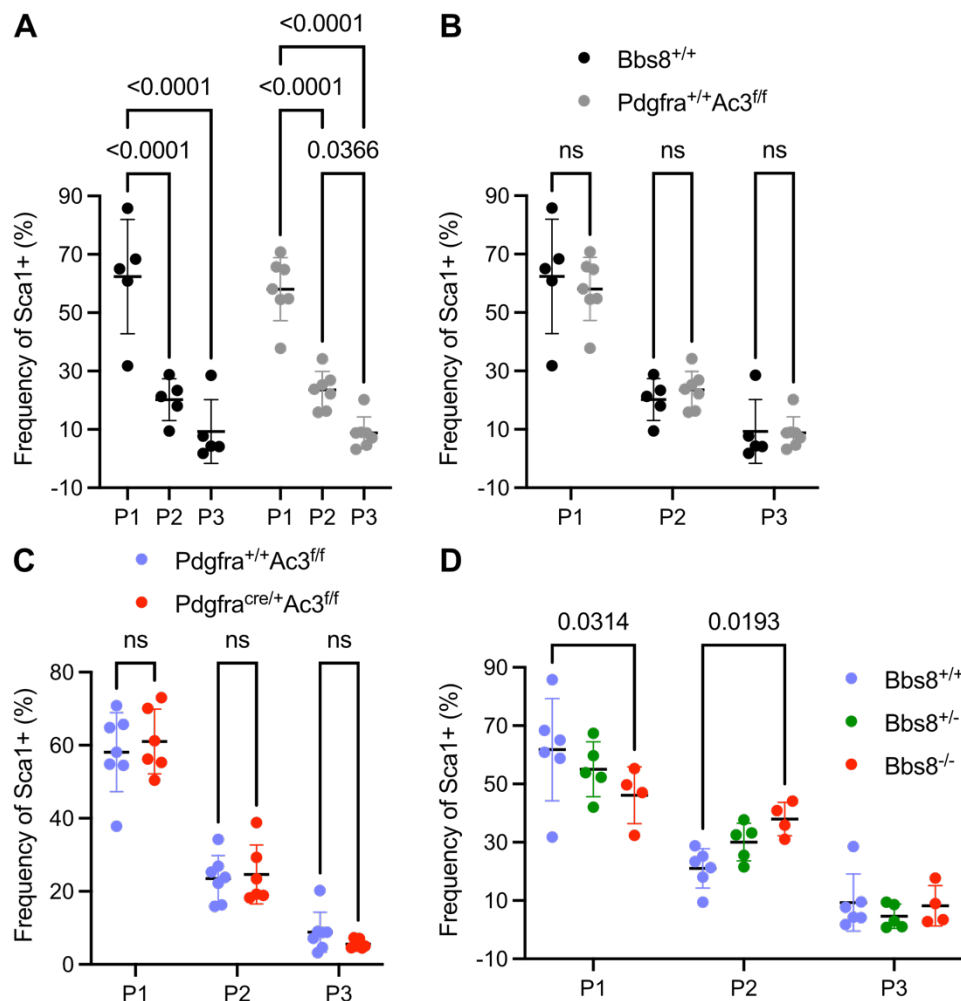
Figure 73: Loss of Bbs8 changes pre-adipocyte subpopulation distribution even before obesity onset. SVF from murine iWAT was isolated from mice aged 7-10 weeks, representing a lean timepoint in all analyzed mouse lines (Bbs8 and Pdgfra-Ac3). **(A)** P1 makes up most of all pre-adipocytes and P3 is representing the smallest subset in Bbs8 and Pdgfra-Ac3 wildtype cells. **(B)** Frequencies of P1, P2, and P3 of total SCA1$^+$ pre-adipocytes in wildtypes from different mouse lines are comparable. **(C)** Loss of AC3 has no effect on pre-adipocyte subpopulations. **(D)** Loss of BBS8 results in a decrease of P1 and an increase of P2 in a dose-dependent manner. Data are shown as mean ± S.D., n ≥ 4.

Next, I investigated the Bbs8-dependent changes in older mice in more detail via UMAP visualization. As mentioned previously the UMAP incorporating all conditions

(Figure 74A) displayed more cluster than the same UMAP corresponding to the control condition (Bbs8$^{+/+}$ on CD). So, I separated the UMAP according to the five different conditions, defined as combination of diet and genotype. The UMAP takes all markers into account simultaneously and this directly indicated a genotype-specific loss of the normal P1 subpopulation in Bbs8$^{+/-}$ and Bbs8$^{-/-}$ mice (Figure 74B). Instead, another cluster could be detected (pink cluster marked by an orange pre-adipocyte) independent of obesity (Figure 74B). The corresponding cluster-heatmap showed that this new cluster resembled P1, but was additionally positive for the P2 marker VAP1. I examined the P1 population for this VAP1 signal also from the other ciliopathy models, but I only observed this switch in P1 in Bbs8$^{-/-}$ (Figure 75A), but not in Bbs6$^{-/-}$ (Figure 75B) or Pdgfra$^{cre/+}$Ac3$^{f/f}$ mice.
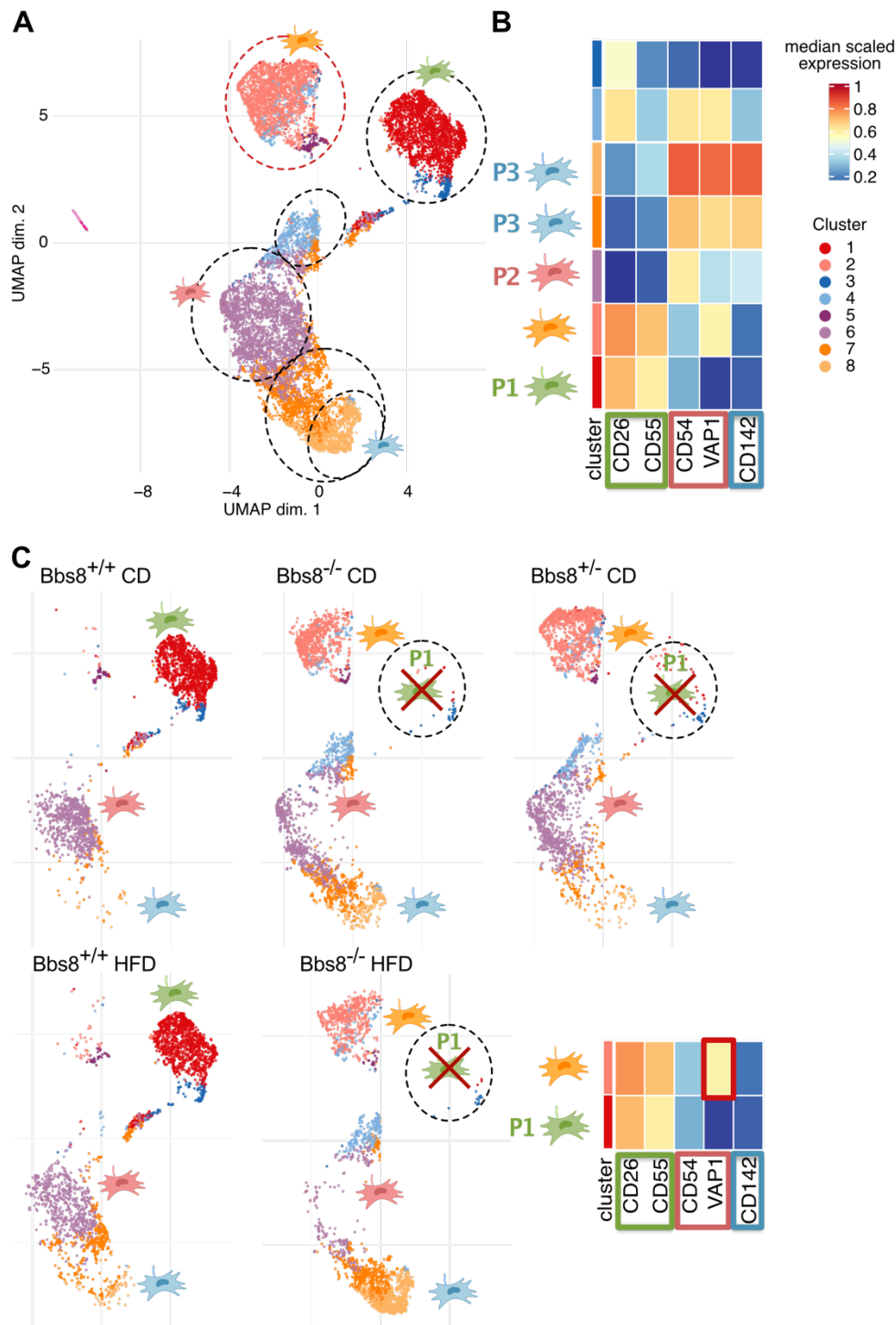
Figure 74: Loss of *Bbs8* abolishes P1 formation and results in an alternative P1 cluster with additionally high VAP1 intensity. SVF from murine WAT was isolated from WT mice aged 18-20 weeks fed a HFD or CD and subjected to analysis via flow cytometry. **(A)** UMAP generated with data from multiple conditions revealed multiple subpopulations marked by dotted circles. **(B)** Simplified cluster heatmap with only the five relevant markers to distinguish the subpopulations and only clusters incorporating more than 2% of all events. **(C)** UMAP separated by conditions, which each contribute with 3000 events. UMAP visualization indicates a genotype-dependent change in the detected clusters: loss of classical P1 and appearance of alterative cluster similar to P1 but with an additional VAP1 signal. This alternative P1 cluster was marked by an orange pre-adipocyte symbol. Obesity increases P3 and especially the light orange cluster, representing higher CD142 expression independent of the genotype.
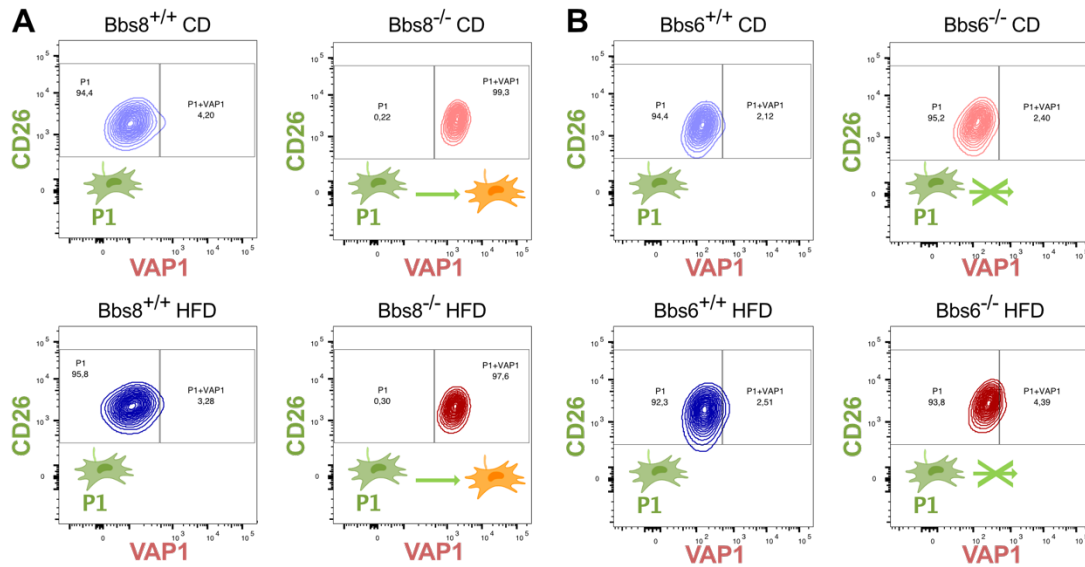
Figure 75: Only loss of *Bbs8* triggers a shift in the VAP1 signal of P1. SVF from murine WAT was isolated from WT mice aged 18-20 weeks fed a HFD or CD and subjected to analysis via flow cytometry to gate for P1 subpopulation. **(A-B)** Visualization of CD26 and VAP1 signal intensities of the gated P1 subpopulation (CD55⁺/CD26⁺) of Bbs8 **(A)** and Bbs6 **(B)**. In Bbs8⁻/⁻ P1 shifts towards higher VAP1 intensities representing cluster previously detected by the UMAP visualization and marked by the orange pre-adipocyte. In contrast, Bbs6⁻/⁻ mice do not display this shift.

However, a more detailed analysis revealed that this signal was independent of the VAP1 marker. The marker for VAP1 was coupled to the DyeLight488 fluorophore, which is measured in the FITC channel. This channel is known to be prone for autofluorescence due to e.g., flavins or lipofuscin (Aubin, 1979; Benson *et al.*, 1979; Çelik-Uzuner and O'Neill, 2021; Wagnières *et al.*, 1998). Therefore, I analyzed unstained samples, which were only treated with the live-dead stain, Hoechst, to exclude dead cells (Figure 76A). While Bbs6⁻/⁻ and Pdgfra^cre/+Ac3^f/f mice showed the same weak autofluoresent signal as their respective control mice, Bbs8 mice displayed a dose-dependent increase in the autofluorescent signal in the FITC channel (Figure 76B).
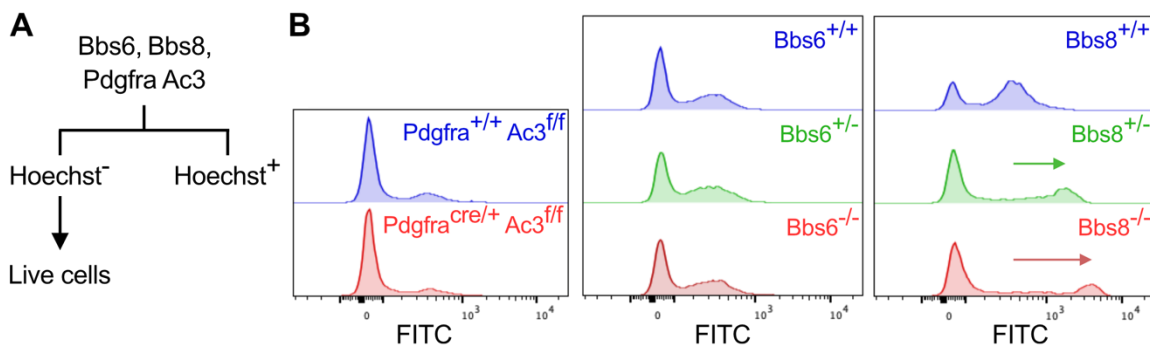
Figure 76: The Bbs8-dependent change in subpopulations is also observed for the autofluorescence. (A) SVF from murine iWAT was isolated from lean mice aged 7-10 weeks and stained only with Hoechst before acquiring flow cytometry data. **(B)** While loss of AC3 or BBS6 showed no difference, loss of BBS8 exhibited a strong shift in autofluorescence in a dose-dependent manner, visible in the FITC channel.

This strong autofluorescent signal upon loss of Bbs8 affected all SCA1$^+$ pre-adipocytes, but not other cells excluded by Lin$^+$ (Figure 77). This indicates that this autofluorescent signal is specific for the pre-adipocyte pool in Bbs8$^{+/-}$ and Bbs8$^{-/-}$ cells. Thus, although the autofluorescence masks the VAP1 specific signal, I can still use the FITC autofluorescence signal as a marker for a change in the precursor cells upon loss of BBS8. Autofluorescence has been used previously as a marker for specific cell types, such as glandular trichomes or breast cancer subpopulations (Bergau *et al.*, 2016; Shah *et al.*, 2017).

This finding shows that loss of Bbs8 has a strong effect on the autofluorescence of pre-adipocytes, indicating increased levels in natural fluorophores, e.g., flavins or lipopigments (Wagnières *et al.*, 1998). Loss of BBS6 or AC3 does not has this effect. The molecular mechanism underlying this increase in autofluorescence remains to be elucidated as well as the effect on the function of the three subpopulations.
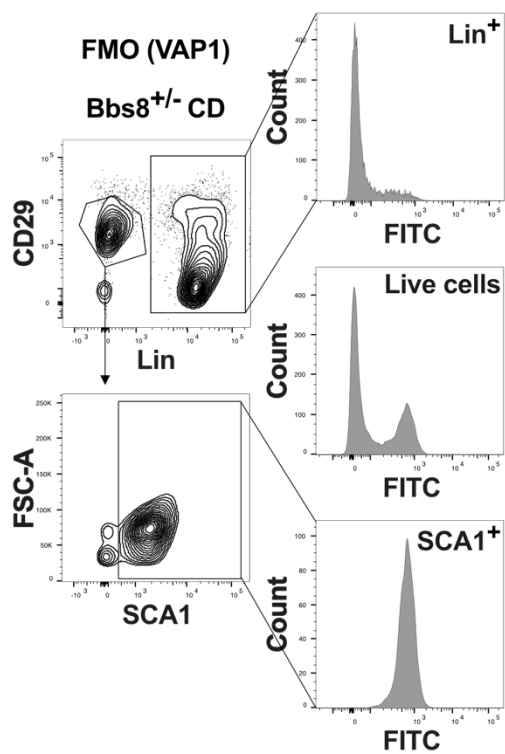
Figure 77: The increased autofluorescence in Bbs8$^{-/-}$ mice is specific for pre-adipocytes. SVF was isolated from a lean Bbs8$^{+/-}$ mouse aged 13 wks and stained with all marker antibodies except for VAP1 (FMO VAP1). The gates for the selection of all pre-adipocytes are shown on the left: Separation of Lin$^-$/CD29$^+$ and Lin$^+$ cells (top) and further distinguishing SCA1$^+$ cells from Lin$^-$/CD29$^+$ (below). The arrow indicates the gate selected for the next separation. The signal intensity measured in the FITC channel is shown as histograms on the right for different subsets of cells: All live cells are shown in the middle, Lin$^+$ cells are shown on the top, and SCA1+ pre-adipocytes are shown at the bottom. Lines indicate the gates used for the cell populations-specific signal histograms. Comparison of the histograms show that the autofluorescent signal is specific for pre-adipocytes, but not Lin$^+$ cells, such as endothelial and immune cells.

3.12.4 Functional characterization of different subpopulations *in vitro*

After my quantitative analysis of the pre-adipocyte precursor subpopulations, I wondered whether the function of these cells might be impaired in any ciliopathy model, especially in Bbs8$^{-/-}$ mice. To this end, I established a sorting strategy to separate the three subpopulations by fluorescence activated cell sorting (FACS) for subsequent RNA sequencing or functional assays (Figure 78).
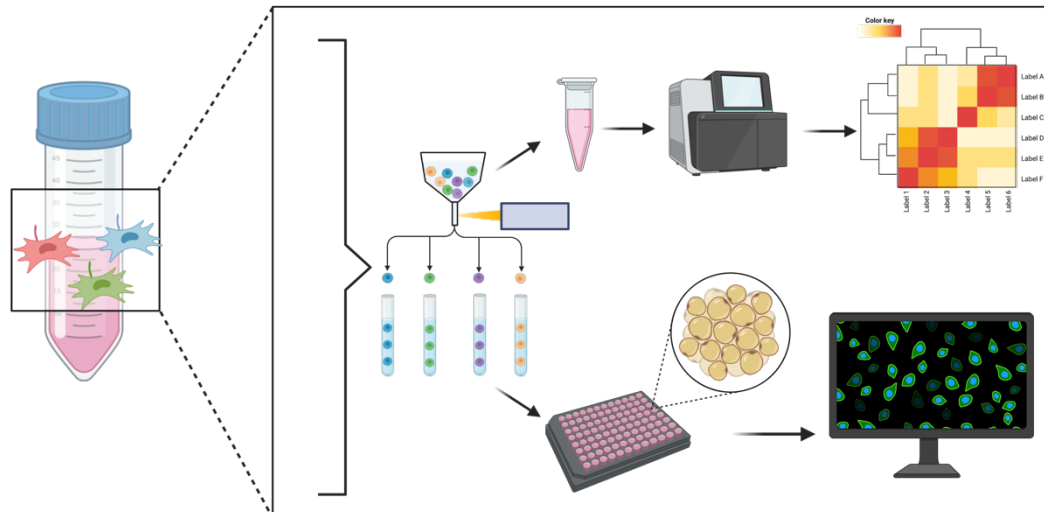
Figure 78: Workflow to separate the different subpopulations for subsequent transcriptomic or functional analyses. The SVF isolated from all three ciliopathy models was sorted to separate the three subpopulations, which were either used for population-specific transcriptomic analysis (top) or for functional adipogenesis assay (bottom).

First, I transferred my gating strategy to the cell sorter, then sorted P1-3, and afterwards verified the sorting by re-analyzing the sorted three subpopulations (Figure 79A). I compared the gates before (Figure 79B) and after sorting (Figure 79C). The re-analysis revealed that sorted P1 and P2 cells were exclusively localized in their respective gates, while P3 was clearly enriched in the respective gate but also displayed a tendency to be localized into the P2 gate (Figure 79C). This might be due to the close relationship with P2. Nevertheless, it verifies the sorting approach, but suggests that CD142 expression in P3 might get lost over time after removing the cells from their tissue context.
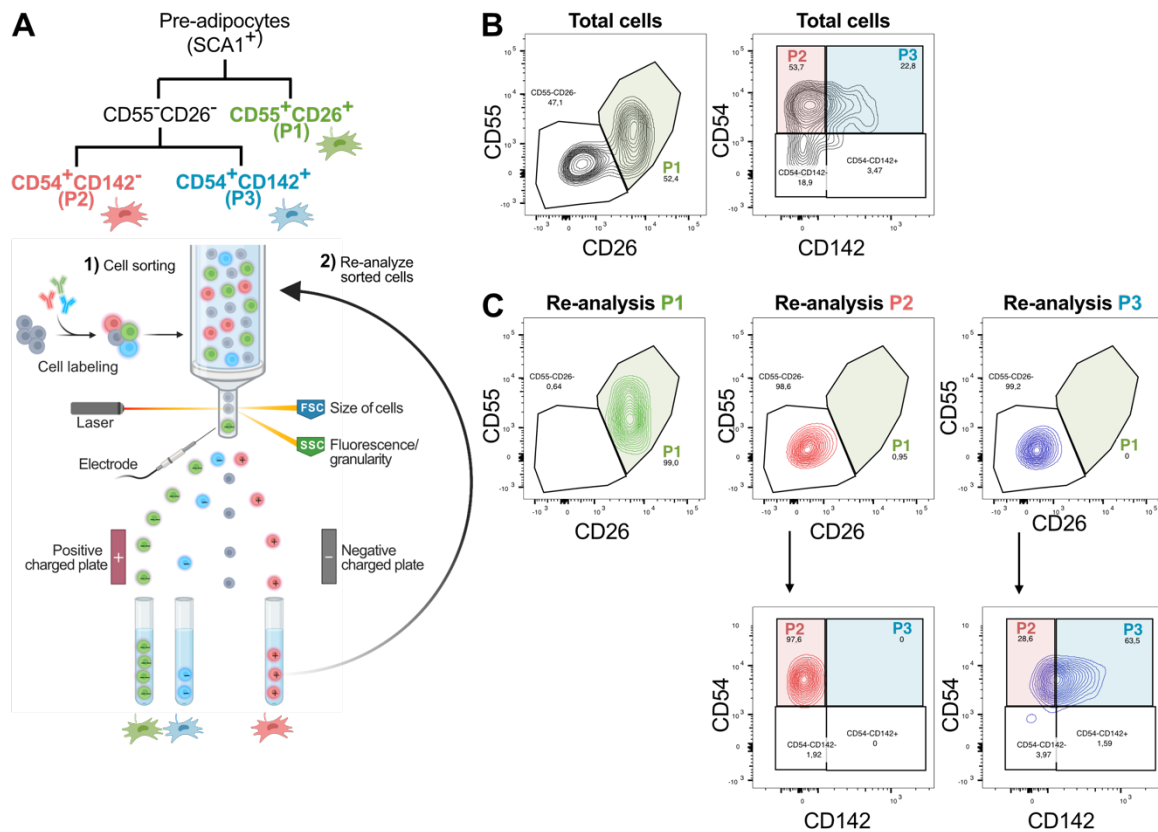
Figure 79: Sorting of P1, P2, and P3 and quality control. (A) Schematic overview of cell sorting and quality control via re-analyzing sorted subpopulations. Isolated SVF was stained with multiple marker antibodies and sorted via fluorescence activated cell sorting (FACS). Single cells are sorted by specific markers and separated into different tubes. **(B)** Input (SVF) gated for P1 (green), P2 (red), and P3 (blue). **(C)** Re-analysis of sorted subpopulations P1, P2, and P3 as quality control. Re-analysis of sorted P1 and P2 demonstrated that both are exclusively localized in their respective gates. P3 is strongly enriched in the respective gate, but also spills into the P2 gate.

I then cultured the isolated subpopulations to perform functional adipogenesis assays. I first tested the adipogenesis assay with isolated P1-3 cells from WT mice. Of note, due to limited cell numbers, a defined cell concentration could not be used for seeding. Instead, each cell population was equally distributed into different numbers of wells. P1 as the most abundant cell population was easily transferred to the *in vitro* culture and was highly proliferative, in line with previous reports (Cho *et al.*, 2019). Induction of adipogenesis with the full induction cocktail evoked a strong adipogenic response with nearly all cells differentiating (Figure 80A). Such a strong effect of full induction was not observed for the total SVF (Chapter 3.9.4, Figure 53), although a direct comparison on the same experimental day is missing. The initially strong adipogenic response of P1 cells seemed to decreased with time or passage number (Figure 80A). As induction was initiated by visual inspection of confluency, this might also contribute to increased variations in the density at induction between different timepoints.

Next, I analyzed the P1 population of Bbs8$^{+/+}$ and Bbs8$^{+/-}$ mice *in vitro* by comparing the adipogenic potential and responsiveness to the FFAR4 pro-adipogenic pathway. However, I could identify no obvious differences (Figure 80B): Both showed a strong differentiation rate upon full induction, but a rather low response to FFAR4 agonist

TUG891. This indicates that P1 might not be the most responsive subpopulation to FFAR4 signaling, but this needs further investigation and comparison with the other subpopulations.

The *in vitro* culture of the other two subpopulations proofed to be challenging, mainly due to the limited cell numbers. The cell viability after the sorting procedure seemed to be generally low, as many dead cells were observed. This further reduced the cell numbers in P2 and P3. Nevertheless, some P2 cells adhered and grew, but the proliferation rate was rather low and after a while, they stopped growing before even reaching a cell density for subsequent adipogenic analysis. This was even worse for P3. Here, the low yield of P3 cells in young, lean mice did not allow to culture the cells *in vitro* as the cells died and the few surviving cells did not proliferate.

In summary, the *in vitro* culture of isolated P1-3 subpopulations recapitulated previous findings of increased proliferation capacity of P1 compared to P2 and P3. The lower proliferative capacity of the P2 and P3 populations in combination with the low cell numbers limited the culture of the isolated subpopulations *in vitro*. Here, a high number of animals would be necessary to pool sorted subpopulations to increase initial cell numbers to overcome these limitations. Alternatively, the assay needs to be established for 384 wells.
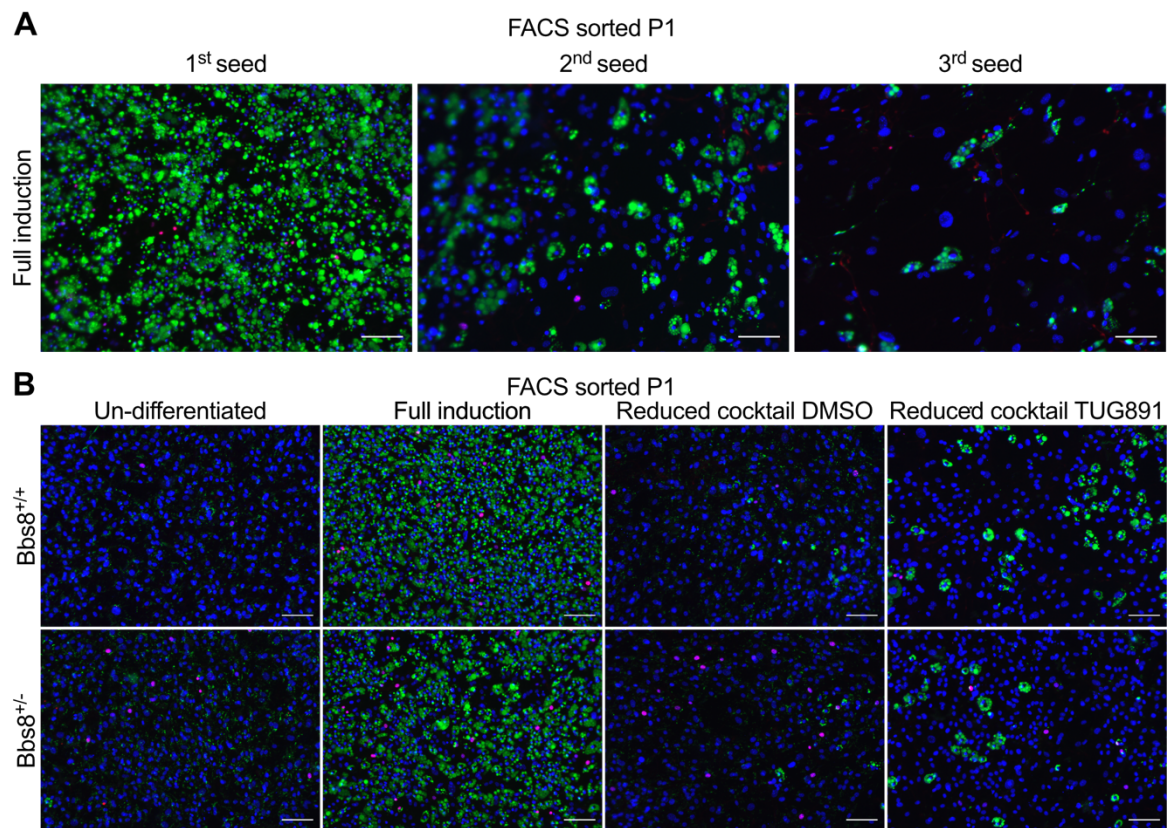
Figure 80: *In vitro* **culture and adipogenesis assay of isolated P1 cells.** SVF cells were isolated from iWAT of 19 wks old WT mice and sorted via fluorescence activated cell sorting (FACS). Isolated P1 cells were cultured *in vitro* and subjected to functional analysis via adipogenesis assay. Differentiation was induced for three days with either full induction cocktail (5 µg/ml Insulin, 1 µM Dexamethasone, 100 µM IBMX, 1 µM Rosiglitazone) or reduced induction cocktail (0.4 µg/ml Insulin, 0.1 µM Dexamethasone, 20 µM IBMX) containing 100 µM TUG891 or DMSO as vehicle control. Adipogenesis was maintained by adding 1 µg/ml Insulin for another 4 days. Cells were fixed and stained with DAPI (blue, DNA) and with the lipophilic dye LD540 (green, lipids). **(A)** Representative images of full induction cocktail on sorted P1 cells subjected to the assay after the first, second, and third passaging. Adipogenicity reduces over each passaging. **(B)** Representative images of sorted P1 cells from Bbs8$^{+/+}$ and Bbs8$^{+/-}$ mice show no difference. In adipogenic potential or FFAR4 pathway responsiveness. Scale bar: 100 µm.

To overcome these limitations, I tested an alternative approach to separate the three subpopulations via magnetic-activated cell sorting (MACS). I used streptavidin beads to separate the subpopulations of the total SVF via biotin-coupled antibodies. I first removed all Lin$^+$ cells by using the same biotin-coupled combinations of antibodies to select for immune-, endothelial cells, and any residual erythrocytes as for FACS. In a second step, I pulled out the P1 cells using biotin-labeled CD55 and CD26 antibodies. In turn, the flow through should contain P2 and P3 cells, while the cells isolated by MACS are P1 cells. A striking difference to FACS was the overall higher cell numbers and reduced cell death. However, the P2-3 population contained the highest cell numbers, indicating that other stromal cells were included in this fraction. Also, the depletion of Lin$^+$ and P1 cells might have been not a 100 %, whereby this population represents a fraction that contains a reduced P1 population but is not fully devoid of this cell type. In summary, MACS might be advantageous in terms of cell numbers that are needed to perform the adipogenesis assay with defined starting cell numbers, but

as a drawback might be less homogenous and still represents a mixture of cell types. However, P2-3 fraction after MACS negative selection of Lin[+] and P1 cells showed increased adipogenic potential, demonstrating that pre-adipocytes have been enrichted (Figure 81A). Even the un-differentiated condition showed spontaneous differentiation and the reduced induction cocktail evoked a complete differentiation response as did full induction (Figure 81A). As the reduced cocktail already resulted in full differentiation, activation of FFAR4 via the agonist TUG891 could not further enhance adipogenesis (Figure 81A). It has been previously reported that P2 shows increased adipogenic potential compared to P1 (Merrick *et al.*, 2019). My results show that the MACS approach enriches P2 cells, resulting in an extremely high differentiation rate even under low induction conditions. To analyze the responsiveness to FFAR4 signaling, it might be sufficient to add the agonist TUG891 without any other pre-adipogenic signals.

However, the strong adipogenic potential was lost over time during *in vitro* expansion (Figure 81B). I also observed some difficulties with the isolated P1 cells, because they were sticking to the metallic beads and it took a while until cells started to adhere to the cultivation dish. In an alternative approach to fish out P2 instead of P1, I observed that P2 cells that remained bound to the beads never adhered on the dish. I suppose that the isolated cells stick to the beads and only migrate to the dish via proliferation. This explains why this worked better with highly proliferative P1 cells but not with less proliferative P2 cells. One way to improve this would be to leave the beads in the culture for a longer period before washing. Nevertheless, also the P1 population isolated by MACS proliferated *in vitro*. Cells fully differentiated upon full induction and to a lesser extend using the reduced induction cocktail (Figure 81C). In addition, the adipogenesis increased in response to activation of FFAR4 (Figure 81C). Interestingly, the differentiation rate was identical to the second passage of P2-3 (Figure 81B). Since, P2-3 fraction was most likely not a 100 % depleted of P1 cells, it is possible that P1 cells still present in the P2-3 cell fraction had overgrown over time due to its higher proliferation rate and that this is explaining the identical differentiation behavior, rather than passaging itself. This could be investigated by flow cytometry. Anyway, it highlights that those cells should be used for functional assays as quickly as possible to avoid loss of adipogenic potential or identify of the cell fractions.

In summary, I established an experimental approach to isolate P1-3 by FACS sorting strategy and the isolated cells will be analyzed by RNA sequencing to identify the effect of ciliary dysfunctions on the identity and function of the pre-adipocyte subpopulations. This will also shed light on the nature of the observed autofluorescence signal in pre-adipocytes of Bbs8^{-/-} mice. I succeeded in culturing P1 cells *in vitro*, but the low cell numbers are limiting and prevented the analysis of less abundant P2 and P3 cells. The alternative separation method MACS seem to increase the cell yield, but has other drawbacks and the specificity of the enrichment or depletion of certain subpopulations needs to be validated. Nevertheless, MACS might be a good alternative for functional analysis if working with a cell pool depleted of certain cell types and quickly starting the functional assay to reduce any changes in cell type proportions due to proliferative differences. My first experiments with FACS and MACS sorted cells verified the

described functional characteristics of P1 and P2 cells, being highly proliferative and adipogenic, respectively. Further investigation will be needed to characterize the different subpopulations in more detail and to examine the consequence of ciliary dysfunction.
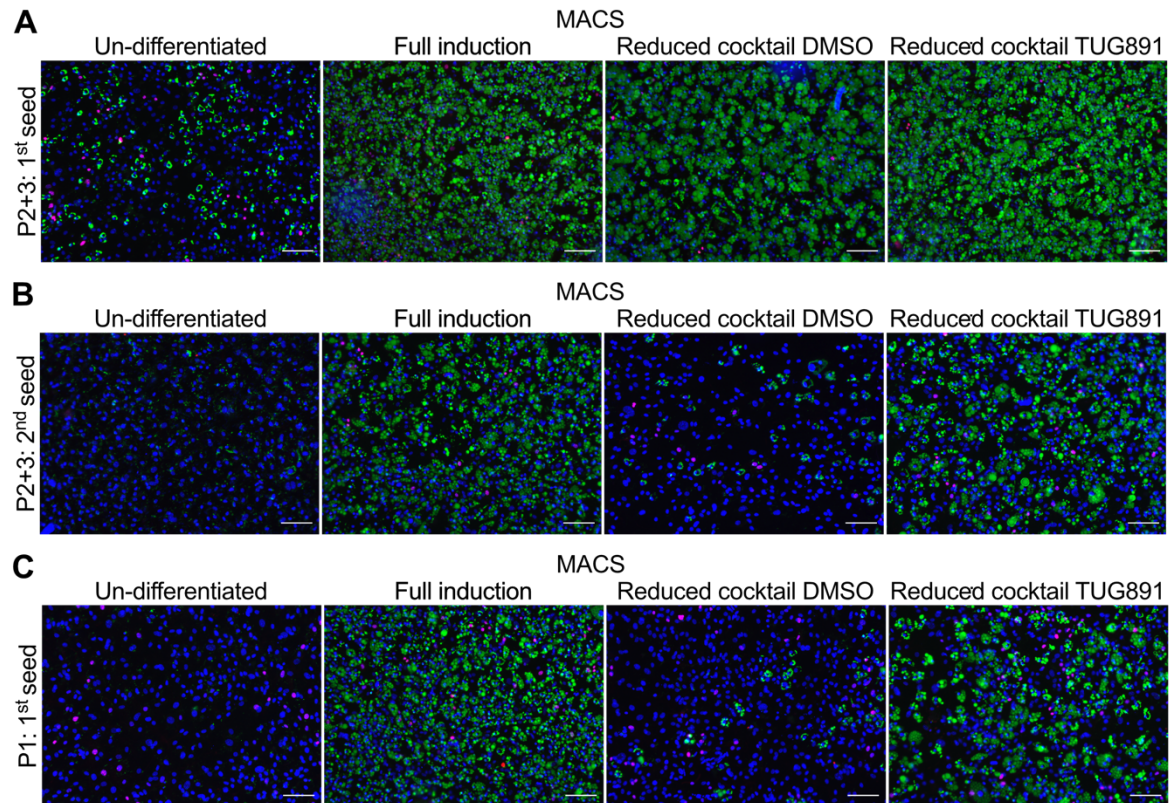
Figure 81: Cultivation and adipogenesis assay using P1 and P1 depleted cells (P2+3) isolated via MACS. SVF cells were isolated from iWAT of 19 wks old WT mice and sorted via magnetic activated cell sorting (MACS). First, Lin⁺ cells were removed from total SVF. Then P1-specific antibodies were used to separate P1 from the rest of the cells. Sorted P1 or P1 depleted cells (P2+3) were transferred to *in vitro* cultivation and subsequently subjected to functional analysis via adipogenesis assay. Differentiation was induced for three days with either full induction cocktail (5 µg/ml Insulin, 1 µM Dexamethasone, 100 µM IBMX, 1 µM Rosiglitazone) or reduced induction cocktail (0.4 µg/ml Insulin, 0.1 µM Dexamethasone, 20 µM IBMX) containing 100 µM TUG891 or DMSO as vehicle control. Adipogenesis was maintained by adding 1 µg/ml Insulin for another 4 days. Cells were fixed and stained with DAPI (blue, DNA) and with the lipophilic dye LD540 (green, lipids). **(A-C)** Representative images of sorted P2+3 after the first passaging **(A)**, the second passaging **(B)**, and of sorted P1 cells **(C)**.

4. Discussion

In my thesis, I demonstrated that loss of different BBS proteins results in distinct phenotypes. Loss of BBSome complex component, BBS8, induced severe obesity accompanied by hypertrophy, but was protected from metabolic deterioration, while loss of BBS chaperonin complex component, BBS6, induced mild obesity with a tendency towards increased hyperplasia, but with severe glucose intolerance. The WAT is prone to develop inflammation and thus promoting the metabolic consequences of obesity. Pre-adipocytes regulate WAT homeostasis as they control the response of the tissue to excess energy. Moreover, pre-adipocytes have a cilium,

which is implicated in controlling their function to undergo adipogenesis via ciliary cAMP signaling. This is supported by my finding that loss of AC3 abrogates the response to pro-adipogenic signals in pre-adipocytes, which *in vivo* resulted in strongly impaired glucose tolerance. Interestingly, I detected a reduction of ciliary AC3 localization in pre-adipocytes from both *Bbs*-models. Thus, loss of BBS proteins induces a disturbance in ciliary cAMP signaling in pre-adipocytes, which could affect either function or fate of pre-adipocytes. A detailed analysis of the reported three pre-adipocytes subpopulations revealed a change in the fate in Bbs8$^{-/-}$ mice, before the onset of obesity and an altered frequency of the different subpopulations, which was not detectable in the other mouse models. This change might result in the observed improved glucose tolerance in Bbs8$^{-/-}$ mice. To investigate the effect of this change in the pre-adipocyte subpopulation, I established a sorting strategy of the subpopulations. Transcriptomic analysis and further functional investigation into these changed cells will shed light on the underlying molecular mechanisms.

4.1 How do different BBS proteins affect cellular functions?

The important role of primary cilia in controlling WAT homeostasis is highlighted by severe obesity in the ciliopathies BBS and ALMS. Although both, BBS and ALMS present with hyperphagia and early onset obesity, the development of type II diabetes during childhood is very rare in BBS (2-6 %), but common in ALMS (75 %) (Beales *et al.*, 1999; Girard and Petrovsky, 2011; Lodh, 2019). In addition, WAT morphology shows a distinct shift from increased hyperplasia in BBS to increased hypertrophy in ALMS (Geberhiwot *et al.*, 2021; Marion *et al.*, 2012; Marion *et al.*, 2009), demonstrating that the genetic mutation that causes ciliary dysfunction determines the cellular and tissue-dependent outcome. While ALMS is a monogenetic disease, there are more than 20 genes known to be involved in BBS (Forsythe *et al.*, 2018). But so far, differences in BBS based on the genetic cause have not been investigated in detail, although some data indicate that the genetic alterations differentially affect the metabolic phenotype (Feuillan *et al.*, 2011; Imhoff *et al.*, 2011; Mujahid *et al.*, 2018). I could demonstrate that Bbs8$^{-/-}$ and Bbs6$^{-/-}$ mice display distinct phenotypes: under non-challenged conditions, hyperphagia was only present in Bbs8$^{-/-}$ mice, leading to obesity. In contrast, challenging Bbs6$^{-/-}$ mice with HFD induced hyperphagia and obesity development. My results also revealed distinct outcomes on glucose metabolism, i.e., glucose tolerance (Figure 82), indicating that the two BBS proteins control distinct cellular and metabolic functions.
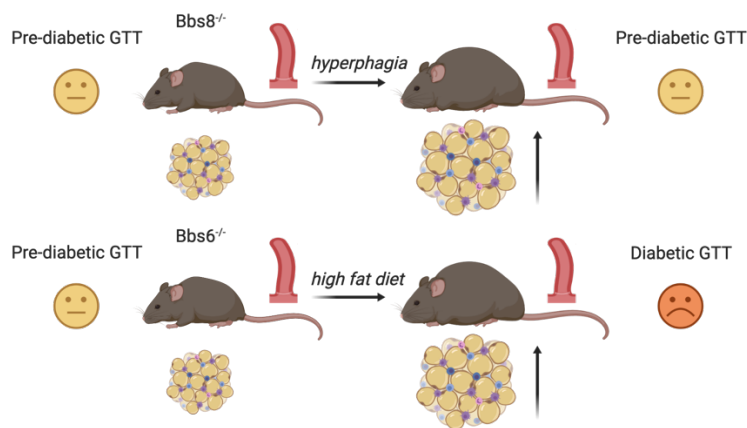
Figure 82: Obesity develop-ment differentially affected glucose tolerance impairment in *Bbs*-KO mouse models. Both, Bbs8^{-/-} and Bbs6^{-/-} mice, displayed impairments in glucose tolerance test (GTT) before obesity onset. Surprisingly, although obesity is known to induce glucose intolerance, GTT only aggravated in Bbs6^{-/-}, but not in Bbs8^{-/-} mice.

On the molecular levels, this might be due to 1) a difference in ciliary localization of the Bbs6 vs Bbs8, 2) differences in protein function, or 3) isoform-specific protein interactions.

BBS proteins have been assigned to different subcellular locations and protein complexes, correlating with different functions and, thereby, distinct disease phenotypes after loss-of-function. BBS13-16 have been associated with the basal body, whereas BBS19 and BBS20 have been associated with retrograde IFT (Aldahmesh *et al.*, 2014; Bujakowska *et al.*, 2015; Qin *et al.*, 2007; Wang *et al.*, 2018; Wang *et al.*, 2009a). BBS3 recruits the BBSome (Jin *et al.*, 2010), consisting of BBS1/2/4/5/7/8/9/18 (Nachury *et al.*, 2007), to the ciliary base, whereas BBS6/10/12 form the BBS chaperonin complex (Seo *et al.*, 2010; Zhang *et al.*, 2012b). A recent meta-analysis of phenotype-genotype correlations indicated a milder phenotype in patients with mutations in *Bbs3* compared to mutations in BBSome- or BBS chaperonin complex encoding genes (Niederlova *et al.*, 2019). Also, mutations in other *BBS* genes that do not encode for proteins forming the BBSome or chaperonin complex, presented with less cardinal features (Niederlova *et al.*, 2019). Interestingly, there was no significant difference among patients with mutations in any of the three genes encoding for BBS chaperonin-complex proteins (Niederlova *et al.*, 2019), indicating that their function is similar, but non-redundant. In contrast, mutations in genes encoding for different BBSome proteins showed high variability (Niederlova *et al.*, 2019). Between different affected BBSome-proteins, two features displayed strong phenotype-genotype association: i) the penetrance of polydactyly was higher in patients with mutations in *Bbs2* and lower in patients with mutations in *Bbs1,* and ii) renal anomalies were most frequent in mutated *Bbs2*, *Bbs7*, and *Bbs9*, but less frequent in mutated *Bbs1*, *Bbs4*, and *Bbs8* (Niederlova *et al.*, 2019). These data indicate that even different proteins within the same complex fulfill distinct functions and their dysfunction leads to a different cellular outcome. Of note, this meta-analysis for genotype-phenotype correlation only focusses on the presence or absence of pathological features, but does not take severity level within the same feature into account. For example, obesity is a feature with high penetrance in all causative mutated *BBS* genes, but the severity and obesity-associated outcome can be notably different (Feuillan *et al.*, 2011; Marion *et al.*, 2012; Mujahid *et al.*, 2018; Pomeroy *et al.*, 2021). This is underlined by my

results, demonstrating that Bbs8$^{-/-}$ mice displayed a much more pronounced obesity phenotype than Bbs6$^{-/-}$ mice.

Also, the type of mutation has been shown to contribute to the severity of symptoms: Loss-of-function mutations generally show a more severe phenotype (Niederlova *et al.*, 2019; Pomeroy *et al.*, 2021). For *BBS8*, nearly all of the described mutations so far are predicted to result in a complete loss of function: two different point mutations induce an early stop codon, resulting in a truncated protein, while nine other mutations affect splice sites and another four mutations induce frameshifts, which most likely lead to nonsense-mediated decay of the alternative transcripts and, thereby, complete loss of the functional protein (Ansley *et al.*, 2003; Sato *et al.*, 2019; Ullah *et al.*, 2017). Only one in-frame deletion was reported, affecting two amino acids, which have been found to be highly conserved (Ansley *et al.*, 2003; Sato *et al.*, 2019). For *BBS6*, even more mutations have been identified, but only six lead to loss of function (Stepanek, 2022). To understand why loss of different BBS proteins result in distinct disease phenotypes, it is crucial to understand the structure of the protein complexes and the role of the individual proteins within these complexes. The two BBS proteins that I analyzed in my thesis are components of the BBSome gatekeeper (BBS8) and the BBS chaperonin complex (BBS6). Cryo-electron microscopy (cryo-EM) with a resolution of down to 3.1-3.5 Å together with the prediction of structural domains and interaction studies has greatly enhanced our understanding of the structure of the BBSome (Chou *et al.*, 2019; Klink *et al.*, 2020; Klink *et al.*, 2017; Singh *et al.*, 2020; Yang *et al.*, 2020). The BBSome favors a closed, autoinhibited conformation involving BBS2 and BBS7, and undergoes a conformational change into an open form, which can be maintained by binding of ARL6^{GTP}/BBS3 to the β-propeller domain of BBS1 and BBS7 (Chou *et al.*, 2019; Singh *et al.*, 2020; Yang *et al.*, 2020). This open confirmation allows cargo binding to the C-terminal part of the β-propeller domain of BBS7 (Yang *et al.*, 2020). Arl6/BBS3 also recruits the BBSome to the cilium by association of its amphipathic N-terminal helices with the ciliary membrane in a guanosine-5'-triphosphate (GTP)-dependent manner (Jin *et al.*, 2010; Singh *et al.*, 2020). This membrane association of the BBSome/BBS3 is bolstered by the interaction of the two BBS5 pleckstrin homology (PH) domains, which bind preferably to multi-phosphorylated phosphatidylinositol-phosphates PIPs (especially phosphatidylinositol-3,4-bisphosphat PI(3,4)P$_2$) (Jin *et al.*, 2010; Klink *et al.*, 2020; Nachury *et al.*, 2007). However, it has been shown that BBS5 is not exclusively responsible for BBSome interaction with PIPs (Klink *et al.*, 2020). For BBS4, a localization to the pericentriolar satellites has been described, recruiting the BBSome to the base of the cilium (Nachury *et al.*, 2007). The other proteins, BBS8, BBS9, and BBS18, act as stabilizing and interacting proteins within the core of the BBSome (Chou *et al.*, 2019; Klink *et al.*, 2020; Klink *et al.*, 2017). Generally, the function of this protein complex seems to rely on the ability to undergo conformational changes. It is possible that dependent on the type of mutation, some structural proteins of the BBSome might only decrease the stability of the complex or the balance between open and closed conformation and, thereby, modulate but not completely abolish BBSome function. Although BBS8 is centrally located and interacts with BBS18 and BBS9 (Chou *et al.*, 2019; Klink *et al.*, 2020; Klink *et al.*, 2017; Seo *et al.*, 2011; Zhang

et al., 2012b), siRNA-dependent depletion had only a minor impact on BBSome formation (Seo *et al.*, 2011; Zhang *et al.*, 2012b). In contrast, systematic depletion of BBS1, BBS2, BBS7, or BBS9 showed that they are required for BBSome assembly, while depletion of BBS4 also had only a minor impact, and depletion of BBS5 had no effect on BBSome formation (Seo *et al.*, 2011; Zhang *et al.*, 2012b). This is in line with BBS5 and BBS4 representing peripheral subunits (Chou *et al.*, 2019; Klink *et al.*, 2020; Klink *et al.*, 2017; Seo *et al.*, 2011; Zhang *et al.*, 2012b). Additionally, recent data also identified BBSome complexes lacking BBS5 or BBS7 (Chou *et al.*, 2019; Singh *et al.*, 2020), indicating that some BBS proteins are dispensable for BBSome assembly and function. Therefore, it has been suggested that the conformation and/or composition of the BBSome might even be different dependent on the activation state (Klink *et al.*, 2020; Klink *et al.*, 2017) or be tissue-specific (Patnaik *et al.*, 2020)(Seo). Hence, the pathological outcome of an affected BBS protein might also depend on its tissue-specific function. Thus, further structural data from different cell types is needed to fully resolve the variety of the BBSome ultrastructure. Also, BBS8-specific interactions and functions besides the interaction with other BBSome proteins are ill-defined. BBS8 is almost entirely comprised of tetratricopeptide (TPR) repeats, which are important motifs for protein-protein interactions. Interestingly, these TPR motifs have functionally also been connected to the binding and transportation of proteins by the peroxisomal import receptor complex (Blatch and Lässle, 1999). So, still unidentified, direct interactions of BBS8 with cargo proteins might be possible, which would further corroborate functional distinct phenotypes in *BBS8* patients.

BBS6, on the other hand, has sequence homology to the CCT/TRiC family of group II chaperonins, similar to BBS10 and BBS12. Together, they form a complex, recruiting six other CCT chaperonins, and have been shown to interact with BBS7 to mediate BBSome assembly (Seo *et al.*, 2010; Zhang *et al.*, 2012b). The BBS chaperonin complex is thought to stabilize and prevent proteasomal degradation of an intermediate complex, BBS7-BBS2-BBS9, and, thereby, assists during the first steps of BBSome formation (Zhang *et al.*, 2012b). Dysfunction of BBS chaperonin complex might disturb the sequential order of BBSome assembly by failing to stabilize the correct intermediate protein complex. This could lead to the accumulation of incorrect complexes, which might result in partial or complete loss of function. Alternatively, failure to stabilize this intermediate complex might result in increased proteasomal degradation, leading to a reduction or total depletion of BBSome complexes. Possible, tissue-specific modulations in the composition of the BBSome would most likely be regulated by the BBS chaperonin complex by recruiting different CCT chaperonins and mediate an alternative assembly of the BBSome. So, it is possible that different BBS chaperonin complex proteins might also recruit or enable the association of distinct proteins to the BBSome complex, resulting in different phenotypes. Contradictory to that idea, pathological mutations affecting BBS6, BBS10, or BBS12 mostly interfere with the interaction among them, indicating that their function depends on their multimeric complex (Seo *et al.*, 2010), and that they rather present with similar phenotypes. This is in line with the before mentioned data of a meta-analysis of phenotype-genotype correlations, detecting no difference between those affected

genes (Niederlova *et al.*, 2019). Previous investigations in *Bbs12*-KO mouse model and *in vitro* ablation of either *Bbs10* or *Bbs12* have shown that loss of both, *Bbs10 or Bbs12*, increases adipogenesis (Marion *et al.*, 2012; Marion *et al.*, 2009). In line with these results, I could demonstrate that Bbs6$^{-/-}$ mice also show increased hyperplasia, whereas Bbs8$^{-/-}$ mice expanded mostly via hypertrophy similar as observed for diet-induced obesity. So, the function of a specific BBS protein depends on its localization and specific interaction with other proteins. However, the specific function of different BBS proteins and their individual contribution in regulating ciliary protein im- and export is still ill-defined, especially for those functioning in a complex with other BSB proteins. Therefore, the molecular function of BBS proteins needs future investigations to clarify and identify the cause of phenotype variability.

4.2 Disturbed ciliary cAMP signaling drives obesity

So far, the obesity phenotype in BBS has been mainly attributed to the increased energy uptake due to hyperphagia. Interestingly, global AC3 knock-out (Wang *et al.*, 2009b), or ablation of AC3 in the hypothalamus or specifically in the ventromedial hypothalamic (PVH) nucleus, also result in hyperphagia and obesity (Cao *et al.*, 2016). This indicates a role for cAMP signaling in the regulation of food intake, which is orchestrated by specific neuronal cell populations, AgRP and pro-opiomelanocortin (POMC) neurons, within the hypothalamus (Abdalla, 2017). Additionally, our group has demonstrated a higher weight gain in mice lacking AC3 specifically in AgRP neurons in the arcuate nucleus, which are upstream of PVH neurons (Klausen, 2020). Thus, loss of AC3-dependent cAMP signaling drives the hyperphagic phenotype. However, another report showed that increasing cAMP levels in AgRP neurons using a G$_{\alpha s}$-coupled G-protein-coupled designer receptors, exclusively activated by designer drugs (DREADDs) also resulted in increased food intake and weight gain (Nakajima *et al.*, 2016). Hence, an increase in cAMP by DREADD activation in the cell soma and loss of AC3-dependent cAMP signaling, which mainly affects ciliary cAMP signaling due to specific localization of AC3 to the cilium, have opposing effects on the regulation of food intake. Recently, our group showed that the ability to distinguish and selectively increase cAMP levels either in the soma or the cilium is crucial and, in fact, exerts opposing effects (Hansen *et al.*, 2020). Based on these results, hyperphagia could be induced by two means: an increase in cAMP levels in the soma or a decrease in ciliary cAMP levels. In BBS, ciliary protein localization is disturbed due to defects in proteins involved in selective ciliary protein transportation, resulting in loss of some ciliary proteins, in particular GPCRs (e.g., SSTR3, MCHR1, and NPY2R (Berbari *et al.*, 2008; Loktev and Jackson, 2013)) or accumulation of others (e.g., SMO, PTCH1, phospholipase D, or dopamine D1 receptor (Lechtreck *et al.*, 2013; Zhang *et al.*, 2013; Zhang *et al.*, 2012a)). Our group confirmed the loss of ciliary NPY2R localization in Bbs8$^{-/-}$ brain slices (Klausen, 2020). Hence, loss of GPCR-dependent ciliary cAMP signaling in neurons most likely produces the hyperphagic phenotype in BBS. It is likely that multiple neuronal cell populations are affected and collectively contribute to the severity of disrupted energy homeostasis. BBS is a pleiotropic syndrome, affecting multiple organ systems and cell types. Thus, ciliary dysfunction occurs in all tissues,

contributing to disease severity. I demonstrated that ciliated pre-adipocytes in the AT depend on AC3 to respond to pro-adipogenic signals. The second messenger cAMP generally has been established as pro-adipogenic (Petersen *et al.*, 2008; Siersbæk and Mandrup, 2011; Zhang *et al.*, 2004). Therefore, increasing cAMP levels by inhibiting PDE activity is an integral part of all adipogenic induction cocktails (Zebisch *et al.*, 2012). However, pharmacological substances do not provide any spatial precision and it remained ill-defined whether ciliary or somatic cAMP signaling drives adipogenesis. The role of ciliary cAMP signaling in driving adipogenesis has recently been shown for FFAR4 signaling (Hilgendorf *et al.*, 2019). My results demonstrate that loss of ciliary AC3 prevents the pro-adipogenic response to FFAR4 activation, confirming the role of ciliary cAMP for this pathway and identifying AC3 as the key downstream AC to regulate cAMP levels specifically in the primary cilium. Therefore, ciliary cAMP plays a crucial role in regulating WAT expansion. The deregulation of ciliary protein localization in BBS not only drives hyperphagia but also contributes to obesity development by altering adipogenesis. Some *Bbs*-KO models reportedly displayed increased adipogenesis (Marion *et al.*, 2012; Marion *et al.*, 2009), insinuating an increase in ciliary cAMP levels. In contrast, my results demonstrated a reduced ciliary AC3 localization in *Bbs*-KO cells, indicating either distinct roles of different BBS proteins or ciliary AC3 levels are downregulated in BBS to counteract the BBS-induced increase in ciliary cAMP levels. The latter would be a consequence of mislocalized GPCRs, either due to an accumulation of G_{as}- or a loss of G_{ai}- coupled GPCRs. (Hansen *et al.*, 2020)To investigate the role of ciliary cAMP in more detail, we aim to apply a ciliary targeted cAMP biosensors to determine ciliary cAMP levels in different *Bbs*-KO models in pre-adipocytes. Additionally, we will use optogenetic tools to specifically modulate ciliary cAMP levels upon light activation (Hansen *et al.*, 2020) to investigate whether increasing ciliary cAMP levels in pre-adipocytes is sufficient to induce adipogenesis. In parallel, the same tools will be used to investigate the role of cAMP in neurons and to control food intake by light. Thereby, this will enable us to disentangle the different contributions of cAMP signaling in different ciliated cell types in BBS.

Generally, primary cilia integrate multiple and possibly simultaneous signals (Hilgendorf *et al.*, 2016; Wachten and Mick, 2021) either by transforming the signals into a common downstream ciliary second messenger, like cAMP, or by nanodomains within the primary cilia established by ciliary PDEs neutralizing diffusing cAMP and, thereby, restricting high cAMP concentrations close to activated ACs. Nanodomains have already been shown to exists within motile cilia, i.e., sperm flagella (Mukherjee *et al.*, 2016; Raju *et al.*, 2019).This would allow the separation of different signaling pathways. Primary cilia on pre-adipocytes harbor multiple receptors that have been implicated in modulating adipogenesis (Ambele *et al.*, 2020; Hilgendorf, 2021). Hh, Wnt, and TGFβ signaling have been shown to exert anti-adipogenic effects, while IGF-1R and FFAR4 signaling have been shown to induce pro-adipogenic effects. Interestingly, some ciliary receptors have also been shown to localize to the plasma membrane, such as FFAR4 (Oh *et al.*, 2010) and IGF-1R (Dalbay *et al.*, 2015; Zhu *et al.*, 2009). Although the benefit of ciliary localization of these receptors might at first be

unclear, it was shown that ciliary localization of IGF-1R resulted in increased receptor sensitivity: Receptor activation happened faster and at lower concentrations of the ligand (Hilgendorf, 2021; Zhu *et al.*, 2009). Hence, the ciliary localization of distinct receptors, pro- or anti-adipogenic, might determine the adipogenic potential of pre-adipocytes. Ciliary receptor localization could be temporally adapted to push pre-adipocytes into full differentiation during commitment and differentiation. This is corroborated by a reported increase in primary cilia length upon adipogenic induction, accompanied by an increased recruitment of IGF-1R into the cilium (Dalbay *et al.*, 2015). Thus, the balance between pro-and anti-adipogenic receptors in the cilium might mediate the adipogenic potential of the different pre-adipocyte subpopulations. This effect could also cause WAT-depot specific differences in AT expansion. Strong adipogenic induction by pharmacology might be able to overwrite ciliary signaling defined by the repertoire of ciliary receptors and, thereby, activate even the less sensitive receptors localized to the plasma membrane. That would explain why all pre-adipocyte subpopulations displayed high adipogenic potential under a strong induction cocktail, while less strong inducer only evoked a high adipogenesis rate in *bona fine* committed pre-adipocytes (Merrick *et al.*, 2019). Therefore, the components of adipogenic induction cocktails have to be considered with care to avoid masking cilia specific effects. Also, the activation of specific signaling pathways should stay in physiological ranges and might need titration to separate the response of sensitive receptors localized to cilia from less sensitive receptors residing in the plasma membrane.

4.3 The role of primary cilia on precursor subpopulation for tissue development and homeostasis

Single-cell transcriptomics has improved our understanding of the molecular heterogeneity of tissues and cell types, enabled the detection of small or short-lived transitioning cell populations, and helped to identify specific cell markers (Kukurba and Montgomery, 2015; Wen and Tang, 2018). Analyzing the dynamics of different precursor subpopulations during development, differentiation, or disease progression will increase our understanding of tissue-specific remodeling, modulation, and adaptation, and hint towards possible targets to prevent pathophysiological changes or stimulate protective effects. Precursor subpopulations cover the full range from the early stem-cell like progenitor up to the stage where they are committed to a specific lineage.

Generally, adult stem cells are present among differentiated cells in the whole body after development and maintain tissue homeostasis by normal tissue turnover or in response to tissue damage enabling healing (Krishnan *et al.*, 2021). There are different types of adult stem cells, which are, in contrast to embryonic stem cells, restricted in their multi-lineage capacity. For example, hematopoietic stem cells (HSCs) give rise to different blood cells (Seita and Weissman, 2010), neuronal stem cells (NSCs) differentiate into neurons, astrocytes, or oligodendrocytes (Bonnamain *et al.*, 2012; Reynolds and Weiss, 1992), and MSCs can commit to adipogenic, osteogenic, and chondrogenic lineages (Krishnan *et al.*, 2021; Tonk *et al.*, 2020). Interestingly, primary

cilia have been identified on almost all stem cells (Liau *et al.*, 2020; Lyu and Zhou, 2017; Singh *et al.*, 2016; Vestergaard *et al.*, 2016; Yanardag and Pugacheva, 2021). Of note, their presence on HSCs is controversially discussed. Primary cilia signaling plays a crucial role in the maintenance and differentiation of stem cells (Yanardag and Pugacheva, 2021). The role of primary cilia during embryonic development has been extensively investigated. Here, and Hh signaling plays a crucial role in controlling differentiation and cell fate (Armas-López *et al.*, 2017). Hh signaling also plays a role in adult stem cells differentiation, e.g., it regulates neurogenesis (Breunig *et al.*, 2008; Machold *et al.*, 2003). Also, other ciliary signaling pathways have been shown to regulate differentiation, proliferation, and commitment (Yanardag and Pugacheva, 2021). For example, canonical Wnt signaling acts as a molecular switch to determine the commitment of MSCs into osteogenic or adipogenic lineage (Christodoulides *et al.*, 2009; Ross *et al.*, 2000; Yanardag and Pugacheva, 2021) and drives proliferation of NSCs and promotes neurogenesis (Krishnan *et al.*, 2021; Kriska *et al.*, 2016; Wei *et al.*, 2012). Therefore, primary cilia dysfunction on stem cells might interfere with stem cell function and contribute to disease progression. In BBS, cilia dysfunction on hypothalamic neurons impairs food regulation. NSCs have been shown to exist in the hypothalamus (Li *et al.*, 2012; Zhang *et al.*, 2017; Zhou *et al.*, 2020). Their distinct roles under homeostatic conditions are largely unknown, but it was shown that NSCs fulfil endocrine functions (Zhang *et al.*, 2017) and are stimulated by feeding or hunger to undergo neurogenesis (Paul *et al.*, 2017). Hence, NSCs subpopulation might contribute to the remodeling of the neuronal network to adapt the neuronal responsiveness. But whether their impaired ciliary signaling contributes to the phenotype in BBS is not clear. What is known, though, is that chronic HFD feeding impaired NSC survival, proliferation, and differentiation into neurons, including POMC neurons. This effect was attributed to inflammatory triggers in the micro-environment by activation of NF-κB (Li *et al.*, 2012). This loss of neuronal structure might possibly interfere with the regulation of satiety and hunger. Indeed, it was shown that partial loss of hypothalamic NSCs induced glucose intolerance and weight gain (Li *et al.*, 2014). Additionally, obesity and glucose intolerance were counteracted in HFD-fed mice by implanting NSCs expressing a negative regulator of NF-κB to ensure survival despite the HFD-induced hostile micro-environment in the hypothalamus (Li *et al.*, 2014). Thus, in BBS, loss of neuronal structure due to impaired NSCs might aggravate the phenotype either directly via disturbance of ciliary signaling, inhibiting neurogenesis, or indirectly as a secondary effect of hyperphagia-induced obesity, which alters the inflammatory environment. MSCs within the AT have been shown to contribute to the remodeling during WAT expansion (Caputo *et al.*, 2021; Hilgendorf, 2021; Jeffery *et al.*, 2015; Kulenkampff and Wolfrum, 2019; Vishvanath and Gupta, 2019). To understand the role of MSCs and more committed progenitor cells in obesity and specifically in BBS, I analyzed pre-adipocyte subpopulations via flow cytometry. My results showed that under homeostatic conditions, the main precursor pool is comprised of MSCs (P1), while the more committed subpopulations are much smaller. Obesity increases the demand for the recruitment of new cells to maintain healthy tissue homeostasis, leading to an intensive commitment and differentiation of P1 cells

to meet this high demand. Consequently, I detected a decrease in P1 during obesity, in line with previous reports (Merrick *et al.*, 2019; Sárvári *et al.*, 2021). Additionally, I observed an obesity-dependent increase in the anti-adipogenic P3 population, which might represent a natural brake to WAT expansion to maintain a critical level of P1. This is in line with the "limited expandability" hypothesis (Vidal-Puig, 2013; Virtue and Vidal-Puig, 2010). Interestingly, my results revealed that loss of BBS8 also caused a reduction in P1 even before the onset of obesity. In contrast to the obesity-dependent changes, the BBS8-dependent effect seemed to be a result of an increased commitment of P1 to P2, as committed P2 accumulated. This indicates that ciliary dysfunction facilitates pre-commitment of MSCs into the adipocyte lineage in Bbs8$^{-/-}$ mice. It was previously shown that loss of BBS12 in WAT displayed increased adipogenesis, which resulted in improved inflammatory and metabolic state (Marion *et al.*, 2012). However, the increased commitment observed in Bbs8$^{-/-}$ mice did not result in hyperplasia and at a later stage, when obesity reached steady-state levels, the frequency of P1, P2, and P3 remained unchanged. Since hyperplasia was not detected, other functions of these precursor cells might be altered and prevent worsening of glucose tolerance in Bbs8$^{-/-}$ mice.

Interestingly, MSCs also display immunomodulatory properties via immunosuppressive factors, cytokines, growth factors, and differentiation factors. This immunomodulatory effect of MSCs relies on local environmental stimuli, such as interferon-γ (IFNγ) together with other pro-inflammatory cytokines, including TNF, IL-1α, or IL-1β (Ren *et al.*, 2008; Wang *et al.*, 2014). In response to the combination of IFNγ with another proinflammatory cytokine, MSCs produce large amounts of chemokines, such as CXCL-9, CXCL-10, CXCR3, and CCR5, some of which potently attract T cells, and nitric oxide, which inhibits T cell responses, leading to the suppression of T cell proliferation (Ren *et al.*, 2008; Wang *et al.*, 2014), while TGF-β1 secretion facilitates Treg formation from conventional T cells (Melief *et al.*, 2013; Weiss and Dahlke, 2019). Furthermore, MSCs also have an effect on B cell function: Co-cultivation of B cells with MSCs demonstrated that IFNγ treatment of MSCs inhibits B cell proliferation (Luk) and via their secretion of IL-1 receptor antagonist (IL1RA) inhibits B cell differentiation toward plasmablasts (Luz-Crawford *et al.*, 2016; Weiss and Dahlke, 2019). Additionally, MSCs secretion of IL1RA has been shown to induce a functional shift to anti-inflammatory phenotypes in macrophages ((Luz-Crawford *et al.*, 2016; Weiss and Dahlke, 2019). Many more effector molecules have been described to be induced by MSCs, such as TSG6, prostaglandin E2, IL-10, an antagonistic variant of the chemokine CCL2, and iNOS (Nemeth *et al.*, 2010; Németh *et al.*, 2009; Ortiz *et al.*, 2007; Rafei *et al.*, 2009; Ren *et al.*, 2008; Wang *et al.*, 2014). In a sepsis model, MSCs injection led to a significant reduction in pro-inflammatory IL-6 and TNFα and an increase in IL-10 serum concentrations (Németh *et al.*, 2009). So overall, MSCs promote a phenotypic switch towards regulatory immune cells, inhibit the proliferation of natural killer, B and T cells, and reprogram monocytes and macrophages into an anti-inflammatory phenotype expressing IL-10 (Weiss and Dahlke, 2019). Interestingly, IL-10 expression in WAT was markedly increased in BBS patients and in Bbs12$^{-/-}$ mice (Marion *et al.*, 2012). So, it is possible that MSCs shift

the balance towards a rather anti-inflammatory state of the AT in BBS. The inflammatory state of AT is also tightly coupled to the development of metabolic syndrome (Hotamisligil, 2006). Therefore, an anti-inflammatory effect of BBS might also contribute to improved metabolic states. Bbs12$^{-/-}$ and Bbs8$^{-/-}$ mice both displayed improved glucose tolerance, however, only in Bbs12$^{-/-}$ mice displayed increased adipogenesis. Intriguingly, the pro-inflammatory cytokine IL-1, which in concert with INFγ stimulates MSCs, has been shown to induce elongation of primary cilia and secretion of nitric oxide and prostaglandin E2 in chondrocytes (Wann and Knight, 2012). Upon cilia loss due to *Ift88*-KO, the secretion of those effector molecules was abolished (Wann and Knight, 2012). Also, INFγ modulates ciliary beat frequency in respiratory epithelial cells in a concentration dependent manner (Grosse-Onnebrink *et al.*, 2016). These data indicate a role of cilia in response to those cytokines. So, ciliary function on precursor cells possibly not only regulate new cell recruitment via differentiation but also balance the immune response to tissue damage or inflammation. In that case, it would be possible that BBS-dependent mislocalization of ciliary proteins either prevents, increases, or decreases the response of MSC's cilia to inflammatory signals, which might result in different metabolic outcomes, as seen as differentially affected glucose tolerance between Bbs8$^{-/-}$ and Bbs6$^{-/-}$ mice. In this regard the Bbs8$^{-/-}$-dependent ciliary dysfunction on AT-MSCs might have a beneficial effect in delaying the negative effects of obesity by reducing tissue inflammation and, thereby, metabolic deterioration. As such, it would counteract the ciliary dysfunction on neurons. We will explore this possibility further not only in mouse models, but also by analyzing the immune cell phenotype of BBS patients.

5. References

Abdalla, M.M. 2017. Central and peripheral control of food intake. *Endocr Regul*. 51:52-70.

Abella, A., S. García-Vicente, N. Viguerie, A. Ros-Baró, M. Camps, M. Palacín, A. Zorzano, and L. Marti. 2004. Adipocytes release a soluble form of VAP-1/SSAO by a metalloprotease-dependent process and in a regulated manner. *Diabetologia*. 47:429-438.

Ahmad, B., C.J. Serpell, I.L. Fong, and E.H. Wong. 2020. Molecular Mechanisms of Adipogenesis: The Anti-adipogenic Role of AMP-Activated Protein Kinase. *Front Mol Biosci*. 7:76.

Aldahmesh, M.A., Y. Li, A. Alhashem, S. Anazi, H. Alkuraya, M. Hashem, A.A. Awaji, S. Sogaty, A. Alkharashi, S. Alzahrani, S.A. Al Hazzaa, Y. Xiong, S. Kong, Z. Sun, and F.S. Alkuraya. 2014. IFT27, encoding a small GTPase component of IFT particles, is mutated in a consanguineous family with Bardet-Biedl syndrome. *Hum Mol Genet*. 23:3307-3315.

Ambele, M.A., P. Dhanraj, R. Giles, and M.S. Pepper. 2020. Adipogenesis: A Complex Interplay of Multiple Molecular Determinants and Pathways. *Int J Mol Sci*. 21.

Amitani, M., A. Asakawa, H. Amitani, and A. Inui. 2013. The role of leptin in the control of insulin-glucose axis. *Front Neurosci*. 7:51.

Anderson, R.G. 1972. The three-dimensional structure of the basal body from the rhesus monkey oviduct. *J Cell Biol*. 54:246-265.

Andrikopoulos, S., A.R. Blair, N. Deluca, B.C. Fam, and J. Proietto. 2008. Evaluating the glucose tolerance test in mice. *Am J Physiol Endocrinol Metab*. 295:E1323-1332.

Angulo, P. 2007. GI epidemiology: nonalcoholic fatty liver disease. *Aliment Pharmacol Ther*. 25:883-889.

Ansley, S.J., J.L. Badano, O.E. Blacque, J. Hill, B.E. Hoskins, C.C. Leitch, J.C. Kim, A.J. Ross, E.R. Eichers, T.M. Teslovich, A.K. Mah, R.C. Johnsen, J.C. Cavender, R.A. Lewis, M.R. Leroux, P.L. Beales, and N. Katsanis. 2003. Basal body dysfunction is a likely cause of pleiotropic Bardet-Biedl syndrome. *Nature*. 425:628-633.

Antal, M.C., K. Bénardais, B. Samama, C. Auger, V. Schini-Kerth, S. Ghandour, and N. Boehm. 2017. Adenylate Cyclase Type III Is Not a Ubiquitous Marker for All Primary Cilia during Development. *PLoS One*. 12:e0170756.

Armas-López, L., J. Zúñiga, O. Arrieta, and F. Ávila-Moreno. 2017. The Hedgehog-GLI pathway in embryonic development and cancer: implications for pulmonary oncology therapy. *Oncotarget*. 8:60684-60703.

Arner, E., P.O. Westermark, K.L. Spalding, T. Britton, M. Rydén, J. Frisén, S. Bernard, and P. Arner. 2010. Adipocyte turnover: relevance to human adipose tissue morphology. *Diabetes*. 59:105-109.

Assimacopoulos-Jeannet, F., S. Brichard, F. Rencurel, I. Cusin, and B. Jeanrenaud. 1995. In vivo effects of hyperinsulinemia on lipogenic enzymes and glucose transporter expression in rat liver and adipose tissues. *Metabolism*. 44:228-233.

Aubin, J.E. 1979. Autofluorescence of viable cultured mammalian cells. *J Histochem Cytochem*. 27:36-43.

Bachmann, V.A., J.E. Mayrhofer, R. Ilouz, P. Tschaikner, P. Raffeiner, R. Röck, M. Courcelles, F. Apelt, T.W. Lu, G.S. Baillie, P. Thibault, P. Aanstad, U. Stelzl, S.S. Taylor, and E. Stefan. 2016. Gpr161 anchoring of PKA consolidates GPCR and cAMP signaling. *Proc Natl Acad Sci U S A*. 113:7786-7791.

Baer, P.C., and H. Geiger. 2012. Adipose-Derived Mesenchymal Stromal/Stem Cells: Tissue Localization, Characterization, and Heterogeneity. *Stem Cells International*. 2012:812693.

Bagchi, D.P., and O.A. MacDougald. 2019. Identification and Dissection of Diverse Mouse Adipose Depots. *J Vis Exp*.

Bapat, S.P., Y. Liang, and Y. Zheng. 2019. Characterization of Immune Cells from Adipose Tissue. *Curr Protoc Immunol*. 126:e86.

Beales, P.L., N. Elcioglu, A.S. Woolf, D. Parker, and F.A. Flinter. 1999. New criteria for improved diagnosis of Bardet-Biedl syndrome: results of a population survey. *J Med Genet*. 36:437-446.

Bedossa, P., C. Poitou, N. Veyrie, J.L. Bouillot, A. Basdevant, V. Paradis, J. Tordjman, and K. Clement. 2012. Histopathological algorithm and scoring system for evaluation of liver lesions in morbidly obese patients. *Hepatology*. 56:1751-1759.

Benedé-Ubieto, R., O. Estévez-Vázquez, P. Ramadori, F.J. Cubero, and Y.A. Nevzorova. 2020. Guidelines and Considerations for Metabolic Tolerance Tests in Mice. *Diabetes Metab Syndr Obes*. 13:439-450.

Benson, R.C., R.A. Meyer, M.E. Zaruba, and G.M. McKhann. 1979. Cellular autofluorescence--is it due to flavins? *J Histochem Cytochem*. 27:44-48.

Berbari, N.F., G.A. Bishop, C.C. Askwith, J.S. Lewis, and K. Mykytyn. 2007. Hippocampal neurons possess primary cilia in culture. *J Neurosci Res*. 85:1095-1100.

Berbari, N.F., J.S. Lewis, G.A. Bishop, C.C. Askwith, and K. Mykytyn. 2008. Bardet–Biedl syndrome proteins are required for the localization of G protein-coupled receptors to primary cilia. *Proceedings of the National Academy of Sciences*. 105:4242-4246.

Bergau, N., A. Navarette Santos, A. Henning, G.U. Balcke, and A. Tissier. 2016. Autofluorescence as a Signal to Sort Developing Glandular Trichomes by Flow Cytometry. *Front Plant Sci*. 7:949.

Bergmann, P., K. Militzer, P. Schmidt, and D. Büttner. 1995. Sex differences in age development of a mouse inbred strain: body composition, adipocyte size and organ weights of liver, heart and muscles. *Lab Anim*. 29:102-109.

Berry, D.C., D. Stenesen, D. Zeve, and J.M. Graff. 2013. The developmental origins of adipose tissue. *Development*. 140:3939-3949.

Berry, R., C.D. Church, M.T. Gericke, E. Jeffery, L. Colman, and M.S. Rodeheffer. 2014. Imaging of adipose tissue. *Methods Enzymol*. 537:47-73.

Berry, R., and M.S. Rodeheffer. 2013. Characterization of the adipocyte cellular lineage in vivo. *Nat Cell Biol*. 15:302-308.

Berry, R., M.S. Rodeheffer, C.J. Rosen, and M.C. Horowitz. 2015. Adipose Tissue Residing Progenitors (Adipocyte Lineage Progenitors and Adipose Derived Stem Cells (ADSC). *Curr Mol Biol Rep*. 1:101-109.

Bilal, M., A. Nawaz, T. Kado, M.R. Aslam, Y. Igarashi, A. Nishimura, Y. Watanabe, T. Kuwano, J. Liu, H. Miwa, T. Era, K. Ikuta, J. Imura, K. Yagi, T. Nakagawa, S. Fujisaka, and K. Tobe. 2021. Fate of adipocyte progenitors during adipogenesis in mice fed a high-fat diet. *Mol Metab*. 54:101328.

Bishop, G.A., N.F. Berbari, J. Lewis, and K. Mykytyn. 2007. Type III adenylyl cyclase localizes to primary cilia throughout the adult mouse brain. *J Comp Neurol*. 505:562-571.

Blatch, G.L., and M. Lässle. 1999. The tetratricopeptide repeat: a structural motif mediating protein-protein interactions. *Bioessays*. 21:932-939.

Bonnamain, V., I. Neveu, and P. Naveilhan. 2012. Neural stem/progenitor cells as a promising candidate for regenerative therapy of the central nervous system. *Front Cell Neurosci*. 6:17.

Booth, A., A. Magnuson, J. Fouts, and M.T. Foster. 2016. Adipose tissue: an endocrine organ playing a role in metabolic regulation. *Horm Mol Biol Clin Investig*. 26:25-42.

Bourin, P., B.A. Bunnell, L. Casteilla, M. Dominici, A.J. Katz, K.L. March, H. Redl, J.P. Rubin, K. Yoshimura, and J.M. Gimble. 2013. Stromal cells from the adipose tissue-derived stromal vascular fraction and culture expanded adipose tissue-derived stromal/stem cells: a joint statement of the International Federation for Adipose Therapeutics and Science (IFATS) and the International Society for Cellular Therapy (ISCT). *Cytotherapy*. 15:641-648.

Brasaemle, D.L. 2007. Thematic review series: adipocyte biology. The perilipin family of structural lipid droplet proteins: stabilization of lipid droplets and control of lipolysis. *J Lipid Res*. 48:2547-2559.

Breunig, J.J., M.R. Sarkisian, J.I. Arellano, Y.M. Morozov, A.E. Ayoub, S. Sojitra, B. Wang, R.A. Flavell, P. Rakic, and T. Town. 2008. Primary cilia regulate hippocampal neurogenesis by mediating sonic hedgehog signaling. *Proc Natl Acad Sci U S A*. 105:13127-13132.

Bruder-Nascimento, T., O.J. Ekeledo, R. Anderson, H.B. Le, and E.J. Belin de Chantemèle. 2017. Long Term High Fat Diet Treatment: An Appropriate Approach to Study the Sex-Specificity of the Autonomic and Cardiovascular Responses to Obesity in Mice. *Front Physiol*. 8:32.

Bujakowska, K.M., Q. Zhang, A.M. Siemiatkowska, Q. Liu, E. Place, M.J. Falk, M. Consugar, M.E. Lancelot, A. Antonio, C. Lonjou, W. Carpentier, S. Mohand-Saïd, A.I. den Hollander, F.P. Cremers, B.P. Leroy, X. Gai, J.A. Sahel, L.I. van den Born, R.W. Collin, C. Zeitz, I. Audo, and E.A. Pierce. 2015. Mutations in IFT172 cause isolated retinal degeneration and Bardet-Biedl syndrome. *Hum Mol Genet*. 24:230-242.

Burl, R.B., V.D. Ramseyer, E.A. Rondini, R. Pique-Regi, Y.H. Lee, and J.G. Granneman. 2018. Deconstructing Adipogenesis Induced by β3-Adrenergic Receptor Activation with Single-Cell Expression Profiling. *Cell Metab*. 28:300-309.e304.

Cai, X., Y. Lin, P.V. Hauschka, and B.E. Grottkau. 2011. Adipose stem cells originate from perivascular cells. *Biol Cell*. 103:435-447.

Cao, H., X. Chen, Y. Yang, and D.R. Storm. 2016. Disruption of type 3 adenylyl cyclase expression in the hypothalamus leads to obesity. *Integr Obes Diabetes*. 2:225-228.

Cao, Z., R.M. Umek, and S.L. McKnight. 1991. Regulated expression of three C/EBP isoforms during adipose conversion of 3T3-L1 cells. *Genes Dev*. 5:1538-1552.

Caputo, T., F. Gilardi, and B. Desvergne. 2017. From chronic overnutrition to metaflammation and insulin resistance: adipose tissue and liver contributions. *FEBS Lett*. 591:3061-3088.

Caputo, T., V.D.T. Tran, N. Bararpour, C. Winkler, G. Aguileta, K.B. Trang, G.M.P. Giordano Attianese, A. Wilson, A. Thomas, M. Pagni, N. Guex, B. Desvergne, and F. Gilardi. 2021. Anti-adipogenic signals at the onset of obesity-related inflammation in white adipose tissue. *Cell Mol Life Sci*. 78:227-247.

Caspary, T., C.E. Larkins, and K.V. Anderson. 2007. The graded response to Sonic Hedgehog depends on cilia architecture. *Dev Cell*. 12:767-778.

Cawthorn, W.P., E.L. Scheller, and O.A. MacDougald. 2012. Adipose tissue stem cells meet preadipocyte commitment: going back to the future. *J Lipid Res*. 53:227-246.

Çelik-Uzuner, S., and C. O'Neill. 2021. Cellular Autofluorescence in Mouse Embryonic Fibroblasts Interferes with Antigen Detection Using Flow Cytometry. *J Fluoresc*. 31:873-879.

Chang, E., M. Varghese, and K. Singer. 2018. Gender and Sex Differences in Adipose Tissue. *Curr Diab Rep*. 18:69.

Chen, H., X. Gu, Y. Liu, J. Wang, S.E. Wirt, R. Bottino, H. Schorle, J. Sage, and S.K. Kim. 2011. PDGF signalling controls age-dependent proliferation in pancreatic β-cells. *Nature*. 478:349-355.

Chen, J.K., J. Taipale, K.E. Young, T. Maiti, and P.A. Beachy. 2002. Small molecule modulation of Smoothened activity. *Proc Natl Acad Sci U S A*. 99:14071-14076.

Chen, Q., S.M. Lai, S. Xu, Y. Tan, K. Leong, D. Liu, J.C. Tan, R.R. Naik, A.M. Barron, S.S. Adav, J. Chen, S.Z. Chong, L.G. Ng, and C. Ruedl. 2021a. Resident macrophages restrain pathological adipose tissue remodeling and protect vascular integrity in obese mice. *EMBO Rep*. 22:e52835.

Chen, X., E. Maldonado, R.A. DeFronzo, and D. Tripathy. 2021b. Impaired Suppression of Glucagon in Obese Subjects Parallels Decline in Insulin Sensitivity and Beta-Cell Function. *J Clin Endocrinol Metab*. 106:1398-1409.

Chen, Z., J.I. Torrens, A. Anand, B.M. Spiegelman, and J.M. Friedman. 2005. Krox20 stimulates adipogenesis via C/EBPbeta-dependent and -independent mechanisms. *Cell Metab*. 1:93-106.

Chi, J., A. Crane, Z. Wu, and P. Cohen. 2018. Adipo-Clear: A Tissue Clearing Method for Three-Dimensional Imaging of Adipose Tissue. *J Vis Exp*.

Cho, D.S., B. Lee, and J.D. Doles. 2019. Refining the adipose progenitor cell landscape in healthy and obese visceral adipose tissue using single-cell gene expression profiling. *Life Sci Alliance*. 2.

Chou, H.T., L. Apelt, D.P. Farrell, S.R. White, J. Woodsmith, V. Svetlov, J.S. Goldstein, A.R. Nager, Z. Li, J. Muller, H. Dollfus, E. Nudler, U. Stelzl, F. DiMaio, M.V. Nachury, and T. Walz. 2019. The Molecular Architecture of Native BBSome Obtained by an Integrated Structural Approach. *Structure*. 27:1384-1394.e1384.

Christ, A., M. Lauterbach, and E. Latz. 2019. Western Diet and the Immune System: An Inflammatory Connection. *Immunity*. 51:794-811.

Christodoulides, C., C. Lagathu, J.K. Sethi, and A. Vidal-Puig. 2009. Adipogenesis and WNT signalling. *Trends Endocrinol Metab*. 20:16-24.

Coelho, M., T. Oliveira, and R. Fernandes. 2013. Biochemistry of adipose tissue: an endocrine organ. *Arch Med Sci*. 9:191-200.

Cottam, D.R., S.G. Mattar, E. Barinas-Mitchell, G. Eid, L. Kuller, D.E. Kelley, and P.R. Schauer. 2004. The chronic inflammatory hypothesis for the morbidity associated with morbid obesity: implications and effects of weight loss. *Obes Surg*. 14:589-600.

Cotter, T.G., and M. Rinella. 2020. Nonalcoholic Fatty Liver Disease 2020: The State of the Disease. *Gastroenterology*. 158:1851-1864.

Cousin, W., C. Fontaine, C. Dani, and P. Peraldi. 2007. Hedgehog and adipogenesis: fat and fiction. *Biochimie*. 89:1447-1453.

Cox, N., L. Crozet, I.R. Holtman, P.L. Loyher, T. Lazarov, J.B. White, E. Mass, E.R. Stanley, O. Elemento, C.K. Glass, and F. Geissmann. 2021. Diet-regulated production of PDGFcc by macrophages controls energy storage. *Science*. 373.

Crisan, M., S. Yap, L. Casteilla, C.W. Chen, M. Corselli, T.S. Park, G. Andriolo, B. Sun, B. Zheng, L. Zhang, C. Norotte, P.N. Teng, J. Traas, R. Schugar, B.M. Deasy, S. Badylak, H.J. Buhring, J.P. Giacobino, L. Lazzari, J. Huard, and B. Péault. 2008. A perivascular origin for mesenchymal stem cells in multiple human organs. *Cell Stem Cell*. 3:301-313.

Cristancho, A.G., and M.A. Lazar. 2011. Forming functional fat: a growing understanding of adipocyte differentiation. *Nat Rev Mol Cell Biol*. 12:722-734.

Dalbay, M.T., S.D. Thorpe, J.T. Connelly, J.P. Chapple, and M.M. Knight. 2015. Adipogenic Differentiation of hMSCs is Mediated by Recruitment of IGF-1r Onto the Primary Cilium Associated With Cilia Elongation. *Stem Cells*. 33:1952-1961.

Datta, P., C. Allamargot, J.S. Hudson, E.K. Andersen, S. Bhattarai, A.V. Drack, V.C. Sheffield, and S. Seo. 2015. Accumulation of non-outer segment proteins in the outer segment underlies photoreceptor degeneration in Bardet–Biedl syndrome. *Proceedings of the National Academy of Sciences*. 112:E4400-E4409.

Dent, P., A. Lavoinne, S. Nakielny, F.B. Caudwell, P. Watt, and P. Cohen. 1990. The molecular mechanism by which insulin stimulates glycogen synthesis in mammalian skeletal muscle. *Nature*. 348:302-308.

Dessels, C., M. Potgieter, and M.S. Pepper. 2016. Making the Switch: Alternatives to Fetal Bovine Serum for Adipose-Derived Stromal Cell Expansion. *Front Cell Dev Biol*. 4:115.

Ding, J., K. Nagai, and J.-T. Woo. 2003. Insulin-Dependent Adipogenesis in Stromal ST2 Cells Derived from Murine Bone Marrow. *Bioscience, Biotechnology, and Biochemistry*. 67:314-321.

Eckel, R.H., S.M. Grundy, and P.Z. Zimmet. 2005. The metabolic syndrome. *Lancet*. 365:1415-1428.

Eguether, T., J.T. San Agustin, B.T. Keady, J.A. Jonassen, Y. Liang, R. Francis, K. Tobita, C.A. Johnson, Z.A. Abdelhamed, C.W. Lo, and G.J. Pazour. 2014. IFT27 links the BBSome to IFT for maintenance of the ciliary signaling compartment. *Dev Cell*. 31:279-290.

Elgeti, J., and G. Gompper. 2013. Emergence of metachronal waves in cilia arrays. *Proc Natl Acad Sci U S A*. 110:4470-4475.

Elmasri, H., C. Karaaslan, Y. Teper, E. Ghelfi, M. Weng, T.A. Ince, H. Kozakewich, J. Bischoff, and S. Cataltepe. 2009. Fatty acid binding protein 4 is a target of VEGF and a regulator of cell proliferation in endothelial cells. *FASEB J*. 23:3865-3873.

Ezratty, E.J., N. Stokes, S. Chai, A.S. Shah, S.E. Williams, and E. Fuchs. 2011. A role for the primary cilium in Notch signaling and epidermal differentiation during skin development. *Cell*. 145:1129-1141.

Fain, J.N., A.K. Madan, M.L. Hiler, P. Cheema, and S.W. Bahouth. 2004. Comparison of the release of adipokines by adipose tissue, adipose tissue matrix, and adipocytes from visceral and subcutaneous abdominal adipose tissues of obese humans. *Endocrinology*. 145:2273-2282.

Farag, T.I., and A.S. Teebi. 1989. High incidence of Bardet Biedl syndrome among the Bedouin. *Clin Genet*. 36:463-464.

Farmer, S.R. 2006. Transcriptional control of adipocyte formation. *Cell Metabolism*. 4:263-273.

Fath, M.A., R.F. Mullins, C. Searby, D.Y. Nishimura, J. Wei, K. Rahmouni, R.E. Davis, M.K. Tayeh, M. Andrews, B. Yang, C.D. Sigmund, E.M. Stone, and V.C. Sheffield. 2005. Mkks-null mice have a phenotype resembling Bardet-Biedl syndrome. *Hum Mol Genet*. 14:1109-1118.

Félix, I., H. Jokela, J. Karhula, N. Kotaja, E. Savontaus, M. Salmi, and P. Rantakari. 2021. Single-Cell Proteomics Reveals the Defined Heterogeneity of Resident Macrophages in White Adipose Tissue. *Front Immunol*. 12:719979.

Ferrero, R., P. Rainer, and B. Deplancke. 2020. Toward a Consensus View of Mammalian Adipocyte Stem and Progenitor Cell Heterogeneity. *Trends in Cell Biology*. 30:937-950.

Feuillan, P.P., D. Ng, J.C. Han, J.C. Sapp, K. Wetsch, E. Spaulding, Y.C. Zheng, R.C. Caruso, B.P. Brooks, J.J. Johnston, J.A. Yanovski, and L.G. Biesecker. 2011. Patients with Bardet-Biedl syndrome have hyperleptinemia suggestive of leptin resistance. *J Clin Endocrinol Metab*. 96:E528-535.

Fisch, C., and P. Dupuis-Williams. 2011. Ultrastructure of cilia and flagella - back to the future! *Biol Cell*. 103:249-270.

Flood, P.R., and G.K. Totland. 1977. Substructure of solitary cilia in mouse kidney. *Cell Tissue Res*. 183:281-290.

Forsythe, E., J. Kenny, C. Bacchelli, and P.L. Beales. 2018. Managing Bardet-Biedl Syndrome-Now and in the Future. *Front Pediatr*. 6:23.

Fryk, E., J. Olausson, K. Mossberg, L. Strindberg, M. Schmelz, H. Brogren, L.M. Gan, S. Piazza, A. Provenzani, B. Becattini, L. Lind, G. Solinas, and P.A. Jansson. 2021. Hyperinsulinemia and insulin resistance in the obese may develop as part of a homeostatic response to elevated free fatty acids: A mechanistic case-control and a population-based cohort study. *EBioMedicine*. 65:103264.

Furuhashi, M., S. Saitoh, K. Shimamoto, and T. Miura. 2014. Fatty Acid-Binding Protein 4 (FABP4): Pathophysiological Insights and Potent Clinical Biomarker of Metabolic and Cardiovascular Diseases. *Clinical Medicine Insights: Cardiology*. 8s3:CMC.S17067.

Garcia, G., 3rd, D.R. Raleigh, and J.F. Reiter. 2018. How the Ciliary Membrane Is Organized Inside-Out to Communicate Outside-In. *Curr Biol*. 28:R421-r434.

Gealekman, O., K. Gurav, M. Chouinard, J. Straubhaar, M. Thompson, S. Malkani, C. Hartigan, and S. Corvera. 2014. Control of adipose tissue expandability in response to high fat diet by the insulin-like growth factor-binding protein-4. *J Biol Chem*. 289:18327-18338.

Geberhiwot, T., S. Baig, C. Obringer, D. Girard, C. Dawson, K. Manolopoulos, N. Messaddeq, P. Bel Lassen, K. Clement, J.W. Tomlinson, R.P. Steeds, H. Dollfus, N. Petrovsky, and V. Marion. 2021. Relative Adipose Tissue Failure in Alström Syndrome Drives Obesity-Induced Insulin Resistance. *Diabetes*. 70:364-376.

Gerdes, J., H. Lemke, H. Baisch, H.H. Wacker, U. Schwab, and H. Stein. 1984. Cell cycle analysis of a cell proliferation-associated human nuclear antigen defined by the monoclonal antibody Ki-67. *J Immunol*. 133:1710-1715.

Gerdes, J.M., S. Christou-Savina, Y. Xiong, T. Moede, N. Moruzzi, P. Karlsson-Edlund, B. Leibiger, I.B. Leibiger, C.G. Östenson, P.L. Beales, and P.O. Berggren. 2014. Ciliary dysfunction impairs beta-cell insulin secretion and promotes development of type 2 diabetes in rodents. *Nat Commun*. 5:5308.

Gerdes, J.M., E.E. Davis, and N. Katsanis. 2009. The vertebrate primary cilium in development, homeostasis, and disease. *Cell*. 137:32-45.

Ghaben, A.L., and P.E. Scherer. 2019. Adipogenesis and metabolic health. *Nat Rev Mol Cell Biol*. 20:242-258.

Gigante, E.D., and T. Caspary. 2020. Signaling in the primary cilium through the lens of the Hedgehog pathway. *WIREs Developmental Biology*. 9:e377.

Gilbertson, D.G., M.E. Duff, J.W. West, J.D. Kelly, P.O. Sheppard, P.D. Hofstrand, Z. Gao, K. Shoemaker, T.R. Bukowski, M. Moore, A.L. Feldhaus, J.M. Humes, T.E. Palmer, and C.E. Hart. 2001. Platelet-derived growth factor C (PDGF-C), a novel growth factor that binds to PDGF alpha and beta receptor. *J Biol Chem*. 276:27406-27414.

Gilpin, W., M.S. Bull, and M. Prakash. 2020. The multiscale physics of cilia and flagella. *Nature Reviews Physics*. 2:74-88.

Gilula, N.B., and P. Satir. 1972. The ciliary necklace. A ciliary membrane specialization. *J Cell Biol*. 53:494-509.

Giordano, A., I. Murano, E. Mondini, J. Perugini, A. Smorlesi, I. Severi, R. Barazzoni, P.E. Scherer, and S. Cinti. 2013. Obese adipocytes show ultrastructural features of stressed cells and die of pyroptosis. *J Lipid Res*. 54:2423-2436.

Girard, D., and N. Petrovsky. 2011. Alström syndrome: insights into the pathogenesis of metabolic disorders. *Nat Rev Endocrinol*. 7:77-88.

Gocze, P.M., and D.A. Freeman. 1994. Factors underlying the variability of lipid droplet fluorescence in MA-10 Leydig tumor cells. *Cytometry*. 17:151-158.

Goetz, S.C., and K.V. Anderson. 2010. The primary cilium: a signalling centre during vertebrate development. *Nat Rev Genet*. 11:331-344.

Gomez Perdiguero, E., K. Klapproth, C. Schulz, K. Busch, E. Azzoni, L. Crozet, H. Garner, C. Trouillet, M.F. de Bruijn, F. Geissmann, and H.R. Rodewald. 2015. Tissue-resident macrophages originate from yolk-sac-derived erythro-myeloid progenitors. *Nature*. 518:547-551.

Gonçalves, J., and L. Pelletier. 2017. The Ciliary Transition Zone: Finding the Pieces and Assembling the Gate. *Mol Cells*. 40:243-253.

Grarup, N., I. Moltke, M.K. Andersen, M. Dalby, K. Vitting-Seerup, T. Kern, Y. Mahendran, E. Jørsboe, C.V.L. Larsen, I.K. Dahl-Petersen, A. Gilly, D. Suveges, G. Dedoussis, E. Zeggini, O. Pedersen, R. Andersson, P. Bjerregaard, M.E. Jørgensen, A. Albrechtsen, and T. Hansen. 2018. Loss-of-

function variants in ADCY3 increase risk of obesity and type 2 diabetes. *Nat Genet*. 50:172-174.

Gray, S.L., and A.J. Vidal-Puig. 2007. Adipose tissue expandability in the maintenance of metabolic homeostasis. *Nutr Rev*. 65:S7-12.

Greenberg, A.S., J.J. Egan, S.A. Wek, N.B. Garty, E.J. Blanchette-Mackie, and C. Londos. 1991. Perilipin, a major hormonally regulated adipocyte-specific phosphoprotein associated with the periphery of lipid storage droplets. *J Biol Chem*. 266:11341-11346.

Grosse-Onnebrink, J., C. Werner, N.T. Loges, K. Hörmann, A. Blum, R. Schmidt, H. Olbrich, and H. Omran. 2016. Effect of TH2 cytokines and interferon gamma on beat frequency of human respiratory cilia. *Pediatr Res*. 79:731-735.

Gusel'nikova, V.V., and D.E. Korzhevskiy. 2015. NeuN As a Neuronal Nuclear Antigen and Neuron Differentiation Marker. *Acta Naturae*. 7:42-47.

Gustafson, B., S. Gogg, S. Hedjazifar, L. Jenndahl, A. Hammarstedt, and U. Smith. 2009. Inflammation and impaired adipogenesis in hypertrophic obesity in man. *Am J Physiol Endocrinol Metab*. 297:E999-e1003.

Haczeyni, F., K.S. Bell-Anderson, and G.C. Farrell. 2018. Causes and mechanisms of adipocyte enlargement and adipose expansion. *Obes Rev*. 19:406-420.

Hallakou, S., L. Doaré, F. Foufelle, M. Kergoat, M. Guerre-Millo, M.F. Berthault, I. Dugail, J. Morin, J. Auwerx, and P. Ferré. 1997. Pioglitazone induces in vivo adipocyte differentiation in the obese Zucker fa/fa rat. *Diabetes*. 46:1393-1399.

Han, J., J.E. Lee, J. Jin, J.S. Lim, N. Oh, K. Kim, S.I. Chang, M. Shibuya, H. Kim, and G.Y. Koh. 2011. The spatiotemporal development of adipose tissue. *Development*. 138:5027-5037.

Hansen, J.N., F. Kaiser, C. Klausen, B. Stüven, R. Chong, W. Bönigk, D.U. Mick, A. Möglich, N. Jurisch-Yaksi, F.I. Schmidt, and D. Wachten. 2020. Nanobody-directed targeting of optogenetic tools to study signaling in the primary cilium. *Elife*. 9.

Hansen, J.N., S. Rassmann, B. Stüven, N. Jurisch-Yaksi, and D. Wachten. 2021. CiliaQ: a simple, open-source software for automated quantification of ciliary morphology and fluorescence in 2D, 3D, and 4D images. *Eur Phys J E Soft Matter*. 44:18.

Hauke, S., K. Keutler, P. Phapale, D.A. Yushchenko, and C. Schultz. 2018. Endogenous Fatty Acids Are Essential Signaling Factors of Pancreatic β-Cells and Insulin Secretion. *Diabetes*. 67:1986-1998.

Hepler, C., B. Shan, Q. Zhang, G.H. Henry, M. Shao, L. Vishvanath, A.L. Ghaben, A.B. Mobley, D. Strand, G.C. Hon, and R.K. Gupta. 2018. Identification of functionally distinct fibro-inflammatory and adipogenic stromal subpopulations in visceral adipose tissue of adult mice. *Elife*. 7.

Hildebrandt, F., T. Benzing, and N. Katsanis. 2011. Ciliopathies. *N Engl J Med*. 364:1533-1543.

Hilgendorf, K.I. 2021. Primary Cilia Are Critical Regulators of White Adipose Tissue Expansion. *Front Physiol*. 12:769367.

Hilgendorf, K.I., C.T. Johnson, and P.K. Jackson. 2016. The primary cilium as a cellular receiver: organizing ciliary GPCR signaling. *Current Opinion in Cell Biology*. 39:84-92.

Hilgendorf, K.I., C.T. Johnson, A. Mezger, S.L. Rice, A.M. Norris, J. Demeter, W.J. Greenleaf, J.F. Reiter, D. Kopinke, and P.K. Jackson. 2019. Omega-3 Fatty Acids Activate Ciliary FFAR4 to Control Adipogenesis. *Cell*. 179:1289-1305.e1221.

Hill, J.O., H.R. Wyatt, and J.C. Peters. 2012. Energy balance and obesity. *Circulation*. 126:126-132.

Hoffstedt, J., E. Arner, H. Wahrenberg, D.P. Andersson, V. Qvisth, P. Löfgren, M. Rydén, A. Thörne, M. Wirén, M. Palmér, A. Thorell, E. Toft, and P. Arner. 2010. Regional impact of adipose tissue morphology on the metabolic profile in morbid obesity. *Diabetologia*. 53:2496-2503.

Holman, G.D., I.J. Kozka, A.E. Clark, C.J. Flower, J. Saltis, A.D. Habberfield, I.A. Simpson, and S.W. Cushman. 1990. Cell surface labeling of glucose transporter isoform GLUT4 by bis-mannose photolabel. Correlation with stimulation of glucose transport in rat adipose cells by insulin and phorbol ester. *J Biol Chem*. 265:18172-18179.

Hong, J., R.E. Stubbins, R.R. Smith, A.E. Harvey, and N.P. Núñez. 2009. Differential susceptibility to obesity between male, female and ovariectomized female mice. *Nutr J*. 8:11.

Hosogai, N., A. Fukuhara, K. Oshima, Y. Miyata, S. Tanaka, K. Segawa, S. Furukawa, Y. Tochino, R. Komuro, M. Matsuda, and I. Shimomura. 2007. Adipose tissue hypoxia in obesity and its impact on adipocytokine dysregulation. *Diabetes*. 56:901-911.

Hotamisligil, G.S. 2006. Inflammation and metabolic disorders. *Nature*. 444:860-867.

Hotamisligil, G.S., N.S. Shargill, and B.M. Spiegelman. 1993. Adipose expression of tumor necrosis factor-alpha: direct role in obesity-linked insulin resistance. *Science*. 259:87-91.

Huang, H., T.J. Song, X. Li, L. Hu, Q. He, M. Liu, M.D. Lane, and Q.Q. Tang. 2009. BMP signaling pathway is required for commitment of C3H10T1/2 pluripotent stem cells to the adipocyte lineage. *Proc Natl Acad Sci U S A*. 106:12670-12675.

Huang, P.L. 2009. A comprehensive definition for metabolic syndrome. *Dis Model Mech*. 2:231-237.

Imhoff, O., V. Marion, C. Stoetzel, M. Durand, M. Holder, S. Sigaudy, P. Sarda, C.P. Hamel, C. Brandt, H. Dollfus, and B. Moulin. 2011. Bardet-Biedl syndrome: a study of the renal and cardiovascular phenotypes in a French cohort. *Clin J Am Soc Nephrol*. 6:22-29.

Ishikawa, T. 2017. Axoneme Structure from Motile Cilia. *Cold Spring Harb Perspect Biol*. 9.

Item, F., and D. Konrad. 2012. Visceral fat and metabolic inflammation: the portal theory revisited. *Obes Rev*. 13 Suppl 2:30-39.

Jeffery, E., C.D. Church, B. Holtrup, L. Colman, and M.S. Rodeheffer. 2015. Rapid depot-specific activation of adipocyte precursor cells at the onset of obesity. *Nat Cell Biol*. 17:376-385.

Jeong, J.Y., D.H. Lee, and S.S. Kang. 2013. Effects of chronic restraint stress on body weight, food intake, and hypothalamic gene expressions in mice. *Endocrinol Metab (Seoul)*. 28:288-296.

Jin, H., S.R. White, T. Shida, S. Schulz, M. Aguiar, S.P. Gygi, J.F. Bazan, and M.V. Nachury. 2010. The conserved Bardet-Biedl syndrome proteins assemble a coat that traffics membrane proteins to cilia. *Cell*. 141:1208-1219.

Jo, J., O. Gavrilova, S. Pack, W. Jou, S. Mullen, A.E. Sumner, S.W. Cushman, and V. Periwal. 2009. Hypertrophy and/or Hyperplasia: Dynamics of Adipose Tissue Growth. *PLoS Comput Biol*. 5:e1000324.

Jonassen, J.A., J. San Agustin, J.A. Follit, and G.J. Pazour. 2008. Deletion of IFT20 in the mouse kidney causes misorientation of the mitotic spindle and cystic kidney disease. *J Cell Biol*. 183:377-384.

Kahn, B.B., and J.S. Flier. 2000. Obesity and insulin resistance. *J Clin Invest*. 106:473-481.

Kamenetsky, M., S. Middelhaufe, E.M. Bank, L.R. Levin, J. Buck, and C. Steegborn. 2006. Molecular details of cAMP generation in mammalian cells: a tale of two systems. *J Mol Biol*. 362:623-639.

Kanda, H., S. Tateya, Y. Tamori, K. Kotani, K. Hiasa, R. Kitazawa, S. Kitazawa, H. Miyachi, S. Maeda, K. Egashira, and M. Kasuga. 2006. MCP-1 contributes to macrophage infiltration into adipose tissue, insulin resistance, and hepatic steatosis in obesity. *J Clin Invest*. 116:1494-1505.

Karpe, F., and K.E. Pinnick. 2015. Biology of upper-body and lower-body adipose tissue--link to whole-body phenotypes. *Nat Rev Endocrinol*. 11:90-100.

Kellard, J.A., N.J.G. Rorsman, T.G. Hill, S.L. Armour, M. van de Bunt, P. Rorsman, J.G. Knudsen, and L.J.B. Briant. 2020. Reduced somatostatin signalling leads to hypersecretion of glucagon in mice fed a high-fat diet. *Mol Metab*. 40:101021.

Kersten, S. 2001. Mechanisms of nutritional and hormonal regulation of lipogenesis. *EMBO Rep*. 2:282-286.

Khan, R.M.M., Z.J.Y. Chua, J.C. Tan, Y. Yang, Z. Liao, and Y. Zhao. 2019. From Pre-Diabetes to Diabetes: Diagnosis, Treatments and Translational Research. *Medicina (Kaunas)*. 55.

Kim, J.B., and B.M. Spiegelman. 1996. ADD1/SREBP1 promotes adipocyte differentiation and gene expression linked to fatty acid metabolism. *Genes Dev*. 10:1096-1107.

Klausen, C. 2020. Analyzing the role of ciliary cAMP signaling in neurons. PhD Thesis.

Klausen, C., F. Kaiser, B. Stüven, J.N. Hansen, and D. Wachten. 2019. Elucidating cyclic AMP signaling in subcellular domains with optogenetic tools and fluorescent biosensors. *Biochem Soc Trans*. 47:1733-1747.

Kleemann, R., M. van Erk, L. Verschuren, A.M. van den Hoek, M. Koek, P.Y. Wielinga, A. Jie, L. Pellis, I. Bobeldijk-Pastorova, T. Kelder, K. Toet, S. Wopereis, N. Cnubben, C. Evelo, B. van Ommen, and T. Kooistra. 2010. Time-resolved and tissue-specific systems analysis of the pathogenesis of insulin resistance. *PLoS One*. 5:e8817.

Klein, D., and F. Ammann. 1969. The syndrome of Laurence-Moon-Bardet-Biedl and allied diseases in Switzerland. Clinical, genetic and epidemiological studies. *J Neurol Sci*. 9:479-513.

Klink, B.U., C. Gatsogiannis, O. Hofnagel, A. Wittinghofer, and S. Raunser. 2020. Structure of the human BBSome core complex. *Elife*. 9.

Klink, B.U., E. Zent, P. Juneja, A. Kuhlee, S. Raunser, and A. Wittinghofer. 2017. A recombinant BBSome core complex and how it interacts with ciliary cargo. *Elife*. 6.

Klip, A., and M.R. Pâquet. 1990. Glucose transport and glucose transporters in muscle and their metabolic regulation. *Diabetes Care*. 13:228-243.

Klymkowsky, M.W., and J. Hanken. 1991. Whole-mount staining of Xenopus and other vertebrates. *Methods Cell Biol*. 36:419-441.

Kocaoemer, A., S. Kern, H. Klüter, and K. Bieback. 2007. Human AB serum and thrombin-activated platelet-rich plasma are suitable alternatives to fetal calf serum for the expansion of mesenchymal stem cells from adipose tissue. *Stem Cells*. 25:1270-1278.

Kopinke, D., A.M. Norris, and S. Mukhopadhyay. 2021. Developmental and regenerative paradigms of cilia regulated hedgehog signaling. *Semin Cell Dev Biol*. 110:89-103.

Kotani, T. 2012. Protein kinase A activity and Hedgehog signaling pathway. *Vitam Horm*. 88:273-291.

Koutnikova, H., T.A. Cock, M. Watanabe, S.M. Houten, M.F. Champy, A. Dierich, and J. Auwerx. 2003. Compensation by the muscle limits the metabolic consequences of lipodystrophy in PPAR gamma hypomorphic mice. *Proc Natl Acad Sci U S A*. 100:14457-14462.

Kozminski, K.G., K.A. Johnson, P. Forscher, and J.L. Rosenbaum. 1993. A motility in the eukaryotic flagellum unrelated to flagellar beating. *Proc Natl Acad Sci U S A*. 90:5519-5523.

Kraus, N.A., F. Ehebauer, B. Zapp, B. Rudolphi, B.J. Kraus, and D. Kraus. 2016. Quantitative assessment of adipocyte differentiation in cell culture. *Adipocyte*. 5:351-358.

Krishnan, M., S. Kumar, L.J. Kangale, E. Ghigo, and P. Abnave. 2021. The Act of Controlling Adult Stem Cell Dynamics: Insights from Animal Models. *Biomolecules*. 11.

Kriska, J., P. Honsa, D. Dzamba, O. Butenko, D. Kolenicova, L. Janeckova, Z. Nahacka, L. Andera, Z. Kozmik, M.M. Taketo, V. Korinek, and M. Anderova. 2016. Manipulating Wnt signaling at different subcellular levels affects the fate of neonatal neural stem/progenitor cells. *Brain Res*. 1651:73-87.

Krueger, K.C., M.J. Costa, H. Du, and B.J. Feldman. 2014. Characterization of Cre recombinase activity for in vivo targeting of adipocyte precursor cells. *Stem Cell Reports*. 3:1147-1158.

Kukurba, K.R., and S.B. Montgomery. 2015. RNA Sequencing and Analysis. *Cold Spring Harb Protoc*. 2015:951-969.

Kulenkampff, E., and C. Wolfrum. 2019. Proliferation of nutrition sensing preadipocytes upon short term HFD feeding. *Adipocyte*. 8:16-25.

Kuroda, M., and H. Sakaue. 2017. Adipocyte Death and Chronic Inflammation in Obesity. *J Med Invest*. 64:193-196.

Lancaster, M.A., J. Schroth, and J.G. Gleeson. 2011. Subcellular spatial regulation of canonical Wnt signalling at the primary cilium. *Nat Cell Biol*. 13:700-707.

Lechtreck, K.F., J.M. Brown, J.L. Sampaio, J.M. Craft, A. Shevchenko, J.E. Evans, and G.B. Witman. 2013. Cycling of the signaling protein phospholipase D through cilia requires the BBSome only for the export phase. *J Cell Biol*. 201:249-261.

Lechtreck, K.F., E.C. Johnson, T. Sakai, D. Cochran, B.A. Ballif, J. Rush, G.J. Pazour, M. Ikebe, and G.B. Witman. 2009. The Chlamydomonas reinhardtii BBSome is an IFT cargo required for export of specific signaling proteins from flagella. *J Cell Biol*. 187:1117-1132.

LeDizet, M., and G. Piperno. 1991. Detection of acetylated alpha-tubulin by specific antibodies. *Methods Enzymol*. 196:264-274.

Lee, M.-J., and S.K. Fried. 2010. Depot-Specific Biology of Adipose Tissues: Links to Fat Distribution and Metabolic Risk. *In* Adipose Tissue in Health and Disease. 283-306.

Lee, M.J., Y. Wu, and S.K. Fried. 2013. Adipose tissue heterogeneity: implication of depot differences in adipose tissue for obesity complications. *Mol Aspects Med*. 34:1-11.

Lee, Y.S., J.W. Kim, O. Osborne, D.Y. Oh, R. Sasik, S. Schenk, A. Chen, H. Chung, A. Murphy, S.M. Watkins, O. Quehenberger, R.S. Johnson, and J.M. Olefsky. 2014. Increased adipocyte O2 consumption triggers HIF-1α, causing inflammation and insulin resistance in obesity. *Cell*. 157:1339-1352.

Lee, Y.S., and J. Olefsky. 2021. Chronic tissue inflammation and metabolic disease. *Genes Dev*. 35:307-328.

Lefterova, M.I., Y. Zhang, D.J. Steger, M. Schupp, J. Schug, A. Cristancho, D. Feng, D. Zhuo, C.J. Stoeckert, Jr., X.S. Liu, and M.A. Lazar. 2008. PPARgamma and C/EBP factors orchestrate adipocyte biology via adjacent binding on a genome-wide scale. *Genes Dev*. 22:2941-2952.

Lehmann, J.M., L.B. Moore, T.A. Smith-Oliver, W.O. Wilkison, T.M. Willson, and S.A. Kliewer. 1995. An Antidiabetic Thiazolidinedione Is a High Affinity Ligand for Peroxisome Proliferator-activated Receptor γ (PPARγ) &#x2217. *Journal of Biological Chemistry*. 270:12953-12956.

Li, J., Y. Tang, and D. Cai. 2012. IKKβ/NF-κB disrupts adult hypothalamic neural stem cells to mediate a neurodegenerative mechanism of dietary obesity and pre-diabetes. *Nat Cell Biol*. 14:999-1012.

Li, J., Y. Tang, S. Purkayastha, J. Yan, and D. Cai. 2014. Control of obesity and glucose intolerance via building neural stem cells in the hypothalamus. *Mol Metab*. 3:313-324.

Li, X., A. Pontén, K. Aase, L. Karlsson, A. Abramsson, M. Uutela, G. Bäckström, M. Hellström, H. Boström, H. Li, P. Soriano, C. Betsholtz, C.H. Heldin, K. Alitalo, A. Ostman, and U. Eriksson. 2000. PDGF-C is a new protease-activated ligand for the PDGF alpha-receptor. *Nat Cell Biol*. 2:302-309.

Liau, L.L., B.H.I. Ruszymah, M.H. Ng, and J.X. Law. 2020. Characteristics and clinical applications of Wharton's jelly-derived mesenchymal stromal cells. *Curr Res Transl Med*. 68:5-16.

Liew, G.M., F. Ye, A.R. Nager, J.P. Murphy, J.S. Lee, M. Aguiar, D.K. Breslow, S.P. Gygi, and M.V. Nachury. 2014. The intraflagellar transport protein IFT27 promotes BBSome exit from cilia through the GTPase ARL6/BBS3. *Dev Cell*. 31:265-278.

Lindstrand, A., E.E. Davis, C.M. Carvalho, D. Pehlivan, J.R. Willer, I.C. Tsai, S. Ramanathan, C. Zuppan, A. Sabo, D. Muzny, R. Gibbs, P. Liu, R.A. Lewis, E. Banin, J.R. Lupski, R. Clark, and N. Katsanis. 2014. Recurrent CNVs and SNVs at the NPHP1 locus contribute pathogenic alleles to Bardet-Biedl syndrome. *Am J Hum Genet*. 94:745-754.

Liu, P., and K.F. Lechtreck. 2018. The Bardet–Biedl syndrome protein complex is an adapter expanding the cargo range of intraflagellar transport trains for ciliary export. *Proceedings of the National Academy of Sciences*. 115:E934-E943.

Lodh, S. 2019. Primary Cilium, An Unsung Hero in Maintaining Functional β-cell Population. *Yale J Biol Med*. 92:471-480.

Loktev, A.V., and P.K. Jackson. 2013. Neuropeptide Y family receptors traffic via the Bardet-Biedl syndrome pathway to signal in neuronal primary cilia. *Cell Rep*. 5:1316-1329.

Lumeng, C.N., J.B. DelProposto, D.J. Westcott, and A.R. Saltiel. 2008. Phenotypic switching of adipose tissue macrophages with obesity is generated by spatiotemporal differences in macrophage subtypes. *Diabetes*. 57:3239-3246.

Luz-Crawford, P., F. Djouad, K. Toupet, C. Bony, M. Franquesa, M.J. Hoogduijn, C. Jorgensen, and D. Noël. 2016. Mesenchymal Stem Cell-Derived Interleukin 1 Receptor Antagonist Promotes Macrophage Polarization and Inhibits B Cell Differentiation. *Stem Cells*. 34:483-492.

Lyu, R., and J. Zhou. 2017. The Multifaceted Roles of Primary Cilia in the Regulation of Stem Cell Properties and Functions. *J Cell Physiol*. 232:935-938.

Machold, R., S. Hayashi, M. Rutlin, M.D. Muzumdar, S. Nery, J.G. Corbin, A. Gritli-Linde, T. Dellovade, J.A. Porter, L.L. Rubin, H. Dudek, A.P. McMahon, and G. Fishell. 2003. Sonic hedgehog is required for progenitor cell maintenance in telencephalic stem cell niches. *Neuron*. 39:937-950.

Madisen, L., T.A. Zwingman, S.M. Sunkin, S.W. Oh, H.A. Zariwala, H. Gu, L.L. Ng, R.D. Palmiter, M.J. Hawrylycz, A.R. Jones, E.S. Lein, and H. Zeng. 2010. A robust and high-throughput Cre reporting and characterization system for the whole mouse brain. *Nat Neurosci*. 13:133-140.

Malicki, J.J., and C.A. Johnson. 2017. The Cilium: Cellular Antenna and Central Processing Unit. *Trends Cell Biol*. 27:126-140.

Marcelin, G., and S. Chua, Jr. 2010. Contributions of adipocyte lipid metabolism to body fat content and implications for the treatment of obesity. *Curr Opin Pharmacol*. 10:588-593.

Marion, V., A. Mockel, C. De Melo, C. Obringer, A. Claussmann, A. Simon, N. Messaddeq, M. Durand, L. Dupuis, J.P. Loeffler, P. King, C. Mutter-Schmidt, N. Petrovsky, C. Stoetzel, and H. Dollfus. 2012. BBS-induced ciliary defect enhances adipogenesis, causing paradoxical higher-insulin sensitivity, glucose usage, and decreased inflammatory response. *Cell Metab*. 16:363-377.

Marion, V., C. Stoetzel, D. Schlicht, N. Messaddeq, M. Koch, E. Flori, J.M. Danse, J.-L. Mandel, and H. Dollfus. 2009. Transient ciliogenesis involving Bardet-Biedl syndrome proteins is a fundamental characteristic of adipogenic differentiation. *Proceedings of the National Academy of Sciences*. 106:1820-1825.

Marshall, J.D., R.T. Bronson, G.B. Collin, A.D. Nordstrom, P. Maffei, R.B. Paisey, C. Carey, S. Macdermott, I. Russell-Eggitt, S.E. Shea, J. Davis, S. Beck, G. Shatirishvili, C.M. Mihai, M. Hoeltzenbein, G.B. Pozzan, I. Hopkinson, N. Sicolo, J.K. Naggert, and P.M. Nishina. 2005. New Alström syndrome phenotypes based on the evaluation of 182 cases. *Arch Intern Med*. 165:675-683.

Marshall, J.D., P. Maffei, G.B. Collin, and J.K. Naggert. 2011. Alström syndrome: genetics and clinical overview. *Curr Genomics*. 12:225-235.

Marszalek, J.R., P. Ruiz-Lozano, E. Roberts, K.R. Chien, and L.S. Goldstein. 1999. Situs inversus and embryonic ciliary morphogenesis defects in mouse mutants lacking the KIF3A subunit of kinesin-II. *Proc Natl Acad Sci U S A*. 96:5043-5048.

Martínez-Uña, M., Y. López-Mancheño, C. Diéguez, M.A. Fernández-Rojo, and M.G. Novelle. 2020. Unraveling the Role of Leptin in Liver Function and Its Relationship with Liver Diseases. *Int J Mol Sci*. 21.

Martyn, J.A., M. Kaneki, and S. Yasuhara. 2008. Obesity-induced insulin resistance and hyperglycemia: etiologic factors and molecular mechanisms. *Anesthesiology*. 109:137-148.

May, E.A., M. Kalocsay, I.G. D'Auriac, P.S. Schuster, S.P. Gygi, M.V. Nachury, and D.U. Mick. 2021. Time-resolved proteomics profiling of the ciliary Hedgehog response. *J Cell Biol*. 220.

McInnes, L., and J. Healy. 2018. UMAP: Uniform Manifold Approximation and Projection for Dimension Reduction.

Melief, S.M., E. Schrama, M.H. Brugman, M.M. Tiemessen, M.J. Hoogduijn, W.E. Fibbe, and H. Roelofs. 2013. Multipotent stromal cells induce human regulatory T cells through a novel pathway involving skewing of monocytes toward anti-inflammatory macrophages. *Stem Cells*. 31:1980-1991.

Merrick, D., A. Sakers, Z. Irgebay, C. Okada, C. Calvert, M.P. Morley, I. Percec, and P. Seale. 2019. Identification of a mesenchymal progenitor cell hierarchy in adipose tissue. *Science*. 364.

Mick, D.U., R.B. Rodrigues, R.D. Leib, C.M. Adams, A.S. Chien, S.P. Gygi, and M.V. Nachury. 2015. Proteomics of Primary Cilia by Proximity Labeling. *Dev Cell*. 35:497-512.

Mitchison, H.M., and E.M. Valente. 2017. Motile and non-motile cilia in human pathology: from function to phenotypes. *J Pathol*. 241:294-309.

Miyazaki, Y., A. Mahankali, M. Matsuda, S. Mahankali, J. Hardies, K. Cusi, L.J. Mandarino, and R.A. DeFronzo. 2002. Effect of pioglitazone on abdominal fat distribution and insulin sensitivity in type 2 diabetic patients. *J Clin Endocrinol Metab*. 87:2784-2791.

Moore, S.J., J.S. Green, Y. Fan, A.K. Bhogal, E. Dicks, B.A. Fernandez, M. Stefanelli, C. Murphy, B.C. Cramer, J.C. Dean, P.L. Beales, N. Katsanis, A.S. Bassett, W.S. Davidson, and P.S. Parfrey. 2005. Clinical and genetic epidemiology of Bardet-Biedl syndrome in Newfoundland: a 22-year prospective, population-based, cohort study. *Am J Med Genet A*. 132a:352-360.

Mori, T., H. Sakaue, H. Iguchi, H. Gomi, Y. Okada, Y. Takashima, K. Nakamura, T. Nakamura, T. Yamauchi, N. Kubota, T. Kadowaki, Y. Matsuki, W. Ogawa, R. Hiramatsu, and M. Kasuga. 2005. Role of Krüppel-like factor 15 (KLF15) in transcriptional regulation of adipogenesis. *J Biol Chem*. 280:12867-12875.

Moseti, D., A. Regassa, and W.K. Kim. 2016. Molecular Regulation of Adipogenesis and Potential Anti-Adipogenic Bioactive Molecules. *Int J Mol Sci*. 17.

Mujahid, S., K.F. Hunt, Y.S. Cheah, E. Forsythe, J.M. Hazlehurst, K. Sparks, S. Mohammed, J.W. Tomlinson, S.A. Amiel, P.V. Carroll, P.L. Beales, M.S.B. Huda, and B.M. McGowan. 2018. The Endocrine and Metabolic Characteristics of a Large Bardet-Biedl Syndrome Clinic Population. *J Clin Endocrinol Metab*. 103:1834-1841.

Mukherjee, S., V. Jansen, J.F. Jikeli, H. Hamzeh, L. Alvarez, M. Dombrowski, M. Balbach, T. Strünker, R. Seifert, U.B. Kaupp, and D. Wachten. 2016. A novel biosensor to study cAMP dynamics in cilia and flagella. *Elife*. 5.

Mukhopadhyay, S., and R. Rohatgi. 2014. G-protein-coupled receptors, Hedgehog signaling and primary cilia. *Semin Cell Dev Biol*. 33:63-72.

Mukhopadhyay, S., X. Wen, B. Chih, C.D. Nelson, W.S. Lane, S.J. Scales, and P.K. Jackson. 2010. TULP3 bridges the IFT-A complex and membrane phosphoinositides to promote trafficking of G protein-coupled receptors into primary cilia. *Genes Dev*. 24:2180-2193.

Mukhopadhyay, S., X. Wen, N. Ratti, A. Loktev, L. Rangell, S.J. Scales, and P.K. Jackson. 2013. The ciliary G-protein-coupled receptor Gpr161 negatively regulates the Sonic hedgehog pathway via cAMP signaling. *Cell*. 152:210-223.

Murcia, N.S., W.G. Richards, B.K. Yoder, M.L. Mucenski, J.R. Dunlap, and R.P. Woychik. 2000. The Oak Ridge Polycystic Kidney (orpk) disease gene is required for left-right axis determination. *Development*. 127:2347-2355.

Muzumdar, M.D., B. Tasic, K. Miyamichi, L. Li, and L. Luo. 2007. A global double-fluorescent Cre reporter mouse. *Genesis*. 45:593-605.

Nachury, M.V., A.V. Loktev, Q. Zhang, C.J. Westlake, J. Peränen, A. Merdes, D.C. Slusarski, R.H. Scheller, J.F. Bazan, V.C. Sheffield, and P.K. Jackson. 2007. A core complex of BBS proteins cooperates with the GTPase Rab8 to promote ciliary membrane biogenesis. *Cell*. 129:1201-1213.

Nachury, M.V., and D.U. Mick. 2019. Establishing and regulating the composition of cilia for signal transduction. *Nat Rev Mol Cell Biol*. 20:389-405.

Nagy, A. 2000. Cre recombinase: the universal reagent for genome tailoring. *Genesis*. 26:99-109.

Nahmgoong, H., Y.G. Jeon, E.S. Park, Y.H. Choi, S.M. Han, J. Park, Y. Ji, J.H. Sohn, J.S. Han, Y.Y. Kim, I. Hwang, Y.K. Lee, J.Y. Huh, S.S. Choe, T.J. Oh, S.H. Choi, J.K. Kim, and J.B. Kim. 2022. Distinct properties of adipose stem cell subpopulations determine fat depot-specific characteristics. *Cell Metab*.

Nakajima, K., Z. Cui, C. Li, J. Meister, Y. Cui, O. Fu, A.S. Smith, S. Jain, B.B. Lowell, M.J. Krashes, and J. Wess. 2016. Gs-coupled GPCR signalling in AgRP neurons triggers sustained increase in food intake. *Nat Commun*. 7:10268.

Nakamura, A., and Y. Terauchi. 2013. Lessons from mouse models of high-fat diet-induced NAFLD. *Int J Mol Sci*. 14:21240-21257.

Nakayama, K., and Y. Katoh. 2018. Ciliary protein trafficking mediated by IFT and BBSome complexes with the aid of kinesin-2 and dynein-2 motors. *J Biochem*. 163:155-164.

Nauli, S.M., F.J. Alenghat, Y. Luo, E. Williams, P. Vassilev, X. Li, A.E. Elia, W. Lu, E.M. Brown, S.J. Quinn, D.E. Ingber, and J. Zhou. 2003. Polycystins 1 and 2 mediate mechanosensation in the primary cilium of kidney cells. *Nat Genet*. 33:129-137.

Nemeth, K., A. Keane-Myers, J.M. Brown, D.D. Metcalfe, J.D. Gorham, V.G. Bundoc, M.G. Hodges, I. Jelinek, S. Madala, S. Karpati, and E. Mezey. 2010. Bone marrow stromal cells use TGF-beta to suppress allergic responses in a mouse model of ragweed-induced asthma. *Proc Natl Acad Sci U S A*. 107:5652-5657.

Németh, K., A. Leelahavanichkul, P.S. Yuen, B. Mayer, A. Parmelee, K. Doi, P.G. Robey, K. Leelahavanichkul, B.H. Koller, J.M. Brown, X. Hu, I. Jelinek, R.A. Star, and E. Mezey. 2009. Bone marrow stromal cells attenuate sepsis via prostaglandin E(2)-dependent reprogramming of host macrophages to increase their interleukin-10 production. *Nat Med*. 15:42-49.

Niederlova, V., M. Modrak, O. Tsyklauri, M. Huranova, and O. Stepanek. 2019. Meta-analysis of genotype-phenotype associations in Bardet-Biedl syndrome uncovers differences among causative genes. *Hum Mutat*. 40:2068-2087.

Nishimura, S., I. Manabe, M. Nagasaki, Y. Hosoya, H. Yamashita, H. Fujita, M. Ohsugi, K. Tobe, T. Kadowaki, R. Nagai, and S. Sugiura. 2007. Adipogenesis in Obesity Requires Close Interplay Between Differentiating Adipocytes, Stromal Cells, and Blood Vessels. *Diabetes*. 56:1517.

Oh, D.Y., S. Talukdar, E.J. Bae, T. Imamura, H. Morinaga, W. Fan, P. Li, W.J. Lu, S.M. Watkins, and J.M. Olefsky. 2010. GPR120 is an omega-3 fatty acid receptor mediating potent anti-inflammatory and insulin-sensitizing effects. *Cell*. 142:687-698.

Okuno, A., H. Tamemoto, K. Tobe, K. Ueki, Y. Mori, K. Iwamoto, K. Umesono, Y. Akanuma, T. Fujiwara, H. Horikoshi, Y. Yazaki, and T. Kadowaki. 1998. Troglitazone increases the number of small adipocytes without the change of white adipose tissue mass in obese Zucker rats. *J Clin Invest*. 101:1354-1361.

Ortiz, L.A., M. Dutreil, C. Fattman, A.C. Pandey, G. Torres, K. Go, and D.G. Phinney. 2007. Interleukin 1 receptor antagonist mediates the antiinflammatory and antifibrotic effect of mesenchymal stem cells during lung injury. *Proc Natl Acad Sci U S A*. 104:11002-11007.

Palmer, B.F., and D.J. Clegg. 2015. The sexual dimorphism of obesity. *Mol Cell Endocrinol*. 402:113-119.

Parfrey, P.S., W.S. Davidson, and J.S. Green. 2002. Clinical and genetic epidemiology of inherited renal disease in Newfoundland. *Kidney Int*. 61:1925-1934.

Park, H.K., and R.S. Ahima. 2015. Physiology of leptin: energy homeostasis, neuroendocrine function and metabolism. *Metabolism*. 64:24-34.

Parlee, S.D., S.I. Lentz, H. Mori, and O.A. MacDougald. 2014. Quantifying size and number of adipocytes in adipose tissue. *Methods Enzymol*. 537:93-122.

Patnaik, S.R., A. Farag, L. Brücker, A.K. Volz, S. Schneider, V. Kretschmer, and H.L. May-Simera. 2020. Tissue-dependent differences in Bardet-Biedl syndrome gene expression. *Biol Cell*. 112:39-52.

Paul, A., Z. Chaker, and F. Doetsch. 2017. Hypothalamic regulation of regionally distinct adult neural stem cells and neurogenesis. *Science*. 356:1383-1386.

Pazour, G.J., B.L. Dickert, Y. Vucica, E.S. Seeley, J.L. Rosenbaum, G.B. Witman, and D.G. Cole. 2000. Chlamydomonas IFT88 and its mouse homologue, polycystic kidney disease gene tg737, are required for assembly of cilia and flagella. *J Cell Biol*. 151:709-718.

Petersen, R.K., L. Madsen, L.M. Pedersen, P. Hallenborg, H. Hagland, K. Viste, S.O. Døskeland, and K. Kristiansen. 2008. Cyclic AMP (cAMP)-mediated stimulation of adipocyte differentiation requires the synergistic action of Epac- and cAMP-dependent protein kinase-dependent processes. *Mol Cell Biol*. 28:3804-3816.

Pomeroy, J., A.D. Krentz, J.G. Richardson, R.L. Berg, J.J. VanWormer, and R.M. Haws. 2021. Bardet-Biedl syndrome: Weight patterns and genetics in a rare obesity syndrome. *Pediatr Obes*. 16:e12703.

Pusztaszeri, M.P., W. Seelentag, and F.T. Bosman. 2006. Immunohistochemical expression of endothelial markers CD31, CD34, von Willebrand factor, and Fli-1 in normal human tissues. *J Histochem Cytochem*. 54:385-395.

Qin, H., Z. Wang, D. Diener, and J. Rosenbaum. 2007. Intraflagellar transport protein 27 is a small G protein involved in cell-cycle control. *Curr Biol*. 17:193-202.

Quarmby, L.M., and J.D. Parker. 2005. Cilia and the cell cycle? *J Cell Biol*. 169:707-710.

Rafei, M., P.M. Campeau, A. Aguilar-Mahecha, M. Buchanan, P. Williams, E. Birman, S. Yuan, Y.K. Young, M.N. Boivin, K. Forner, M. Basik, and J. Galipeau. 2009. Mesenchymal stromal cells ameliorate experimental autoimmune encephalomyelitis by inhibiting CD4 Th17 T cells in a CC chemokine ligand 2-dependent manner. *J Immunol*. 182:5994-6002.

Rahmouni, K., M.A. Fath, S. Seo, D.R. Thedens, C.J. Berry, R. Weiss, D.Y. Nishimura, and V.C. Sheffield. 2008. Leptin resistance contributes to obesity and hypertension in mouse models of Bardet-Biedl syndrome. *J Clin Invest*. 118:1458-1467.

Raju, D.N., J.N. Hansen, S. Rassmann, B. Stüven, J.F. Jikeli, T. Strünker, H.G. Körschen, A. Möglich, and D. Wachten. 2019. Cyclic Nucleotide-Specific Optogenetics Highlights Compartmentalization of the Sperm Flagellum into cAMP Microdomains. *Cells*. 8.

Ramirez, N., L. Marrero, S. Carlo, and A.S. Cornier. 2004. Orthopaedic manifestations of Bardet-Biedl syndrome. *J Pediatr Orthop*. 24:92-96.

Ramírez-Zacarías, J.L., F. Castro-Muñozledo, and W. Kuri-Harcuch. 1992. Quantitation of adipose conversion and triglycerides by staining intracytoplasmic lipids with Oil red O. *Histochemistry*. 97:493-497.

Reiter, J.F., O.E. Blacque, and M.R. Leroux. 2012. The base of the cilium: roles for transition fibres and the transition zone in ciliary formation, maintenance and compartmentalization. *EMBO Rep*. 13:608-618.

Reiter, J.F., and M.R. Leroux. 2017. Genes and molecular pathways underpinning ciliopathies. *Nat Rev Mol Cell Biol*. 18:533-547.

Ren, G., L. Zhang, X. Zhao, G. Xu, Y. Zhang, A.I. Roberts, R.C. Zhao, and Y. Shi. 2008. Mesenchymal stem cell-mediated immunosuppression occurs via concerted action of chemokines and nitric oxide. *Cell Stem Cell*. 2:141-150.

Reynolds, B.A., and S. Weiss. 1992. Generation of neurons and astrocytes from isolated cells of the adult mammalian central nervous system. *Science*. 255:1707-1710.

Richardson, D.S., and J.W. Lichtman. 2015. Clarifying Tissue Clearing. *Cell*. 162:246-257.

Rodbell, M. 1964. Metabolism of Isolated Fat Cells. I. Effects of Hormones on Glucose Metabolism and Lipolysis. *J Biol Chem*. 239:375-380.

Rodeheffer, M.S., K. Birsoy, and J.M. Friedman. 2008. Identification of white adipocyte progenitor cells in vivo. *Cell*. 135:240-249.

Rohatgi, R., L. Milenkovic, and M.P. Scott. 2007. Patched1 regulates hedgehog signaling at the primary cilium. *Science*. 317:372-376.

Rohatgi, R., and W.J. Snell. 2010. The ciliary membrane. *Curr Opin Cell Biol*. 22:541-546.

Rosen, E.D., C.H. Hsu, X. Wang, S. Sakai, M.W. Freeman, F.J. Gonzalez, and B.M. Spiegelman. 2002. C/EBPalpha induces adipogenesis through PPARgamma: a unified pathway. *Genes Dev*. 16:22-26.

Rosen, E.D., and B.M. Spiegelman. 2006. Adipocytes as regulators of energy balance and glucose homeostasis. *Nature*. 444:847-853.

Rosenbaum, J.L., and G.B. Witman. 2002. Intraflagellar transport. *Nat Rev Mol Cell Biol*. 3:813-825.

Ross, A.J., H. May-Simera, E.R. Eichers, M. Kai, J. Hill, D.J. Jagger, C.C. Leitch, J.P. Chapple, P.M. Munro, S. Fisher, P.L. Tan, H.M. Phillips, M.R. Leroux, D.J. Henderson, J.N. Murdoch, A.J. Copp, M.M. Eliot, J.R. Lupski, D.T. Kemp, H. Dollfus, M. Tada, N. Katsanis, A. Forge, and P.L. Beales. 2005. Disruption of Bardet-Biedl syndrome ciliary proteins perturbs planar cell polarity in vertebrates. *Nat Genet*. 37:1135-1140.

Ross, S.E., R.L. Erickson, I. Gerin, P.M. DeRose, L. Bajnok, K.A. Longo, D.E. Misek, R. Kuick, S.M. Hanash, K.B. Atkins, S.M. Andresen, H.I. Nebb, L. Madsen, K. Kristiansen, and O.A. MacDougald. 2002. Microarray analyses during adipogenesis: understanding the effects of Wnt signaling on adipogenesis and the roles of liver X receptor alpha in adipocyte metabolism. *Mol Cell Biol*. 22:5989-5999.

Ross, S.E., N. Hemati, K.A. Longo, C.N. Bennett, P.C. Lucas, R.L. Erickson, and O.A. MacDougald. 2000. Inhibition of adipogenesis by Wnt signaling. *Science*. 289:950-953.

Rother, K.I. 2007. Diabetes treatment--bridging the divide. *N Engl J Med*. 356:1499-1501.

Saeed, S., A. Bonnefond, F. Tamanini, M.U. Mirza, J. Manzoor, Q.M. Janjua, S.M. Din, J. Gaitan, A. Milochau, E. Durand, E. Vaillant, A. Haseeb, F. De Graeve, I. Rabearivelo, O. Sand, G. Queniat, R. Boutry, D.A. Schott, H. Ayesha, M. Ali, W.I. Khan, T.A. Butt, T. Rinne, C. Stumpel, A. Abderrahmani, J. Lang, M. Arslan, and P. Froguel. 2018. Loss-of-function mutations in ADCY3 cause monogenic severe obesity. *Nat Genet*. 50:175-179.

Salma, N., H. Xiao, E. Mueller, and A.N. Imbalzano. 2004. Temporal recruitment of transcription factors and SWI/SNF chromatin-remodeling enzymes during adipogenic induction of the peroxisome proliferator-activated receptor gamma nuclear hormone receptor. *Mol Cell Biol*. 24:4651-4663.

Salmi, M., and S. Jalkanen. 2019. Vascular Adhesion Protein-1: A Cell Surface Amine Oxidase in Translation. *Antioxid Redox Signal*. 30:314-332.

Saltiel, A.R., and J.M. Olefsky. 2017. Inflammatory mechanisms linking obesity and metabolic disease. *J Clin Invest*. 127:1-4.

Sarantopoulos, C.N., D.A. Banyard, M.E. Ziegler, B. Sun, A. Shaterian, and A.D. Widgerow. 2018. Elucidating the Preadipocyte and Its Role in Adipocyte Formation: a Comprehensive Review. *Stem Cell Rev Rep*. 14:27-42.

Sárvári, A.K., E.L. Van Hauwaert, L.K. Markussen, E. Gammelmark, A.B. Marcher, M.F. Ebbesen, R. Nielsen, J.R. Brewer, J.G.S. Madsen, and S. Mandrup. 2021.

Plasticity of Epididymal Adipose Tissue in Response to Diet-Induced Obesity at Single-Nucleus Resolution. *Cell Metab*. 33:437-453.e435.

Satir, P., and S.T. Christensen. 2007. Overview of structure and function of mammalian cilia. *Annu Rev Physiol*. 69:377-400.

Satir, P., L.B. Pedersen, and S.T. Christensen. 2010. The primary cilium at a glance. *J Cell Sci*. 123:499-503.

Sato, S., T. Morimoto, K. Hotta, T. Fujikado, and K. Nishida. 2019. A novel compound heterozygous mutation in TTC8 identified in a Japanese patient. *Hum Genome Var*. 6:14.

Sauer, B. 1987. Functional expression of the cre-lox site-specific recombination system in the yeast Saccharomyces cerevisiae. *Mol Cell Biol*. 7:2087-2096.

Scholzen, T., and J. Gerdes. 2000. The Ki-67 protein: from the known and the unknown. *J Cell Physiol*. 182:311-322.

Schwalie, P.C., H. Dong, M. Zachara, J. Russeil, D. Alpern, N. Akchiche, C. Caprara, W. Sun, K.-U. Schlaudraff, G. Soldati, C. Wolfrum, and B. Deplancke. 2018. A stromal cell population that inhibits adipogenesis in mammalian fat depots. *Nature*. 559:103-108.

Seita, J., and I.L. Weissman. 2010. Hematopoietic stem cell: self-renewal versus differentiation. *Wiley Interdiscip Rev Syst Biol Med*. 2:640-653.

Seo, S., L.M. Baye, N.P. Schulz, J.S. Beck, Q. Zhang, D.C. Slusarski, and V.C. Sheffield. 2010. BBS6, BBS10, and BBS12 form a complex with CCT/TRiC family chaperonins and mediate BBSome assembly. *Proc Natl Acad Sci U S A*. 107:1488-1493.

Seo, S., D.F. Guo, K. Bugge, D.A. Morgan, K. Rahmouni, and V.C. Sheffield. 2009. Requirement of Bardet-Biedl syndrome proteins for leptin receptor signaling. *Hum Mol Genet*. 18:1323-1331.

Seo, S., Q. Zhang, K. Bugge, D.K. Breslow, C.C. Searby, M.V. Nachury, and V.C. Sheffield. 2011. A novel protein LZTFL1 regulates ciliary trafficking of the BBSome and Smoothened. *PLoS Genet*. 7:e1002358.

Shah, A.T., T.M. Cannon, J.N. Higginbotham, R.J. Coffey, and M.C. Skala. 2017. Autofluorescence flow sorting of breast cancer cell metabolism. *J Biophotonics*. 10:1026-1033.

Shan, T., W. Liu, and S. Kuang. 2013. Fatty acid binding protein 4 expression marks a population of adipocyte progenitors in white and brown adipose tissues. *FASEB J*. 27:277-287.

Shao, M., L. Vishvanath, N.C. Busbuso, C. Hepler, B. Shan, A.X. Sharma, S. Chen, X. Yu, Y.A. An, Y. Zhu, W.L. Holland, and R.K. Gupta. 2018. De novo adipocyte differentiation from Pdgfrβ(+) preadipocytes protects against pathologic visceral adipose expansion in obesity. *Nat Commun*. 9:890.

Shi, Y., and F. Long. 2017. Hedgehog signaling via Gli2 prevents obesity induced by high-fat diet in adult mice. *Elife*. 6.

Shinde, S.R., A.R. Nager, and M.V. Nachury. 2020. Ubiquitin chains earmark GPCRs for BBSome-mediated removal from cilia. *J Cell Biol*. 219.

Shulman, G.I., D.L. Rothman, T. Jue, P. Stein, R.A. DeFronzo, and R.G. Shulman. 1990. Quantitation of muscle glycogen synthesis in normal subjects and subjects with non-insulin-dependent diabetes by 13C nuclear magnetic resonance spectroscopy. *N Engl J Med*. 322:223-228.

Sieckmann, K., N. Winnerling, M. Huebecker, P. Leyendecker, D. Juliana Silva Ribeiro, T. Gnad, A. Pfeifer, D. Wachten, and J.N. Hansen. 2022. AdipoQ-a simple, open-source software to quantify adipocyte morphology and function in tissues and *in vitro*. *Mol Biol Cell*. 33:br22.

Siersbæk, R., and S. Mandrup. 2011. Transcriptional networks controlling adipocyte differentiation. *Cold Spring Harb Symp Quant Biol*. 76:247-255.

Silverman, M.A., and M.R. Leroux. 2009. Intraflagellar transport and the generation of dynamic, structurally and functionally diverse cilia. *Trends Cell Biol*. 19:306-316.

Singh, M., P. Chaudhry, and A.A. Merchant. 2016. Primary cilia are present on human blood and bone marrow cells and mediate Hedgehog signaling. *Exp Hematol*. 44:1181-1187.e1182.

Singh, S.K., M. Gui, F. Koh, M.C. Yip, and A. Brown. 2020. Structure and activation mechanism of the BBSome membrane protein trafficking complex. *Elife*. 9.

Sinha, S., and J.K. Chen. 2006. Purmorphamine activates the Hedgehog pathway by targeting Smoothened. *Nat Chem Biol*. 2:29-30.

Smith, D.J., M. Salmi, P. Bono, J. Hellman, T. Leu, and S. Jalkanen. 1998. Cloning of vascular adhesion protein 1 reveals a novel multifunctional adhesion molecule. *J Exp Med*. 188:17-27.

Sorokin, S. 1962. Centrioles and the formation of rudimentary cilia by fibroblasts and smooth muscle cells. *J Cell Biol*. 15:363-377.

Spalding, K.L., E. Arner, P.O. Westermark, S. Bernard, B.A. Buchholz, O. Bergmann, L. Blomqvist, J. Hoffstedt, E. Näslund, T. Britton, H. Concha, M. Hassan, M. Rydén, J. Frisén, and P. Arner. 2008. Dynamics of fat cell turnover in humans. *Nature*. 453:783-787.

Spandl, J., D.J. White, J. Peychl, and C. Thiele. 2009. Live cell multicolor imaging of lipid droplets with a new dye, LD540. *Traffic*. 10:1579-1584.

Steenhuis, P., G.J. Pettway, and M.A. Ignelzi, Jr. 2008. Cell surface expression of stem cell antigen-1 (Sca-1) distinguishes osteo-, chondro-, and adipoprogenitors in fetal mouse calvaria. *Calcif Tissue Int*. 82:44-56.

Stefkovich, M., S. Traynor, L. Cheng, D. Merrick, and P. Seale. 2021. Dpp4+ interstitial progenitor cells contribute to basal and high fat diet-induced adipogenesis. *Mol Metab*. 54:101357.

Stepanek, L., and G. Pigino. 2016. Microtubule doublets are double-track railways for intraflagellar transport trains. *Science*. 352:721-724.

Stepanek, O. 2022. dataBBaSe.

Stoetzel, C., J. Muller, V. Laurier, E.E. Davis, N.A. Zaghloul, S. Vicaire, C. Jacquelin, F. Plewniak, C.C. Leitch, P. Sarda, C. Hamel, T.J. de Ravel, R.A. Lewis, E. Friederich, C. Thibault, J.M. Danse, A. Verloes, D. Bonneau, N. Katsanis, O. Poch, J.L. Mandel, and H. Dollfus. 2007. Identification of a novel BBS gene (BBS12) highlights the major role of a vertebrate-specific branch of chaperonin-related proteins in Bardet-Biedl syndrome. *Am J Hum Genet*. 80:1-11.

Suh, J.M., X. Gao, J. McKay, R. McKay, Z. Salo, and J.M. Graff. 2006. Hedgehog signaling plays a conserved role in inhibiting fat formation. *Cell Metab*. 3:25-34.

Sun, X., J. Haley, O.V. Bulgakov, X. Cai, J. McGinnis, and T. Li. 2012. Tubby is required for trafficking G protein-coupled receptors to neuronal cilia. *Cilia*. 1:21.

Sztalryd, C., and D.L. Brasaemle. 2017. The perilipin family of lipid droplet proteins: Gatekeepers of intracellular lipolysis. *Biochim Biophys Acta Mol Cell Biol Lipids*. 1862:1221-1232.

Tadenev, A.L., H.M. Kulaga, H.L. May-Simera, M.W. Kelley, N. Katsanis, and R.R. Reed. 2011. Loss of Bardet-Biedl syndrome protein-8 (BBS8) perturbs olfactory function, protein localization, and axon targeting. *Proc Natl Acad Sci U S A*. 108:10320-10325.

Tang, H.N., C.Y. Tang, X.F. Man, S.W. Tan, Y. Guo, J. Tang, C.L. Zhou, and H.D. Zhou. 2017. Plasticity of adipose tissue in response to fasting and refeeding in male mice. *Nutr Metab (Lond)*. 14:3.

Tang, W., D. Zeve, J.M. Suh, D. Bosnakovski, M. Kyba, R.E. Hammer, M.D. Tallquist, and J.M. Graff. 2008. White fat progenitor cells reside in the adipose vasculature. *Science*. 322:583-586.

Tonk, C.H., M. Witzler, M. Schulze, and E. Tobiasch. 2020. Mesenchymal Stem Cells. *In* Essential Current Concepts in Stem Cell Biology. B. Brand-Saberi, editor. Springer International Publishing, Cham. 21-39.

Tontonoz, P., and B.M. Spiegelman. 2008. Fat and beyond: the diverse biology of PPARgamma. *Annu Rev Biochem*. 77:289-312.

Tschaikner, P., F. Enzler, O. Torres-Quesada, P. Aanstad, and E. Stefan. 2020. Hedgehog and Gpr161: Regulating cAMP Signaling in the Primary Cilium. *Cells*. 9.

Tuson, M., M. He, and K.V. Anderson. 2011. Protein kinase A acts at the basal body of the primary cilium to prevent Gli2 activation and ventralization of the mouse neural tube. *Development*. 138:4921-4930.

Ullah, A., M. Umair, M. Yousaf, S.A. Khan, M. Nazim-Ud-Din, K. Shah, F. Ahmad, Z. Azeem, G. Ali, B. Alhaddad, A. Rafique, A. Jan, T.B. Haack, T.M. Strom, T. Meitinger, T. Ghous, and W. Ahmad. 2017. Sequence variants in four genes underlying Bardet-Biedl syndrome in consanguineous families. *Mol Vis*. 23:482-494.

Usta, S.N., C.D. Scharer, J. Xu, T.K. Frey, and R.J. Nash. 2014. Chemically defined serum-free and xeno-free media for multiple cell lineages. *Ann Transl Med*. 2:97.

Vaanholt, L.M., I. Jonas, M. Doornbos, K.A. Schubert, C. Nyakas, T. Garland, Jr., G.H. Visser, and G. van Dijk. 2008. Metabolic and behavioral responses to high-fat feeding in mice selectively bred for high wheel-running activity. *Int J Obes (Lond)*. 32:1566-1575.

Van der Heiden, K., B.P. Hierck, R. Krams, R. de Crom, C. Cheng, M. Baiker, M.J. Pourquie, F.E. Alkemade, M.C. DeRuiter, A.C. Gittenberger-de Groot, and R.E. Poelmann. 2008. Endothelial primary cilia in areas of disturbed flow are at the base of atherosclerosis. *Atherosclerosis*. 196:542-550.

VanSaun, M.N., I.K. Lee, M.K. Washington, L. Matrisian, and D.L. Gorden. 2009. High fat diet induced hepatic steatosis establishes a permissive microenvironment for colorectal metastases and promotes primary dysplasia in a murine model. *Am J Pathol*. 175:355-364.

Varghese, J., J.V. James, R. Anand, M. Narayanasamy, G. Rebekah, B. Ramakrishna, A.J. Nellickal, and M. Jacob. 2020. Development of insulin resistance preceded major changes in iron homeostasis in mice fed a high-fat diet. *J Nutr Biochem*. 84:108441.

Vegiopoulos, A., M. Rohm, and S. Herzig. 2017. Adipose tissue: between the extremes. *Embo j*. 36:1999-2017.

Vestergaard, M.L., A. Awan, C.B. Warzecha, S.T. Christensen, and C.Y. Andersen. 2016. Immunofluorescence Microscopy and mRNA Analysis of Human Embryonic Stem Cells (hESCs) Including Primary Cilia Associated Signaling Pathways. *Methods Mol Biol*. 1307:123-140.

Vidal-Puig, A. 2013. Adipose tissue expandability, lipotoxicity and the metabolic syndrome. *Endocrinol Nutr*. 60 Suppl 1:39-43.

Virtue, S., and A. Vidal-Puig. 2010. Adipose tissue expandability, lipotoxicity and the Metabolic Syndrome--an allostatic perspective. *Biochim Biophys Acta*. 1801:338-349.

Virtue, S., and A. Vidal-Puig. 2021. GTTs and ITTs in mice: simple tests, complex answers. *Nat Metab*. 3:883-886.

Vishvanath, L., and R.K. Gupta. 2019. Contribution of adipogenesis to healthy adipose tissue expansion in obesity. *J Clin Invest*. 129:4022-4031.

Vishvanath, L., K.A. MacPherson, C. Hepler, Q.A. Wang, M. Shao, S.B. Spurgin, M.Y. Wang, C.M. Kusminski, T.S. Morley, and R.K. Gupta. 2016. Pdgfrβ+ Mural Preadipocytes Contribute to Adipocyte Hyperplasia Induced by High-Fat-Diet Feeding and Prolonged Cold Exposure in Adult Mice. *Cell Metab*. 23:350-359.

Wachten, D., and D.U. Mick. 2021. Signal transduction in primary cilia - analyzing and manipulating GPCR and second messenger signaling. *Pharmacol Ther*. 224:107836.

Wagner, R., L.H. Hakaste, E. Ahlqvist, M. Heni, J. Machann, F. Schick, E. Van Obberghen, N. Stefan, B. Gallwitz, T. Tuomi, H.U. Häring, L. Groop, and A. Fritsche. 2017. Nonsuppressed Glucagon After Glucose Challenge as a Potential Predictor for Glucose Tolerance. *Diabetes*. 66:1373-1379.

Wagnières, G.A., W.M. Star, and B.C. Wilson. 1998. In vivo fluorescence spectroscopy and imaging for oncological applications. *Photochem Photobiol*. 68:603-632.

Wang, J., and M.M. Barr. 2018. Cell-cell communication via ciliary extracellular vesicles: clues from model systems. *Essays Biochem*. 62:205-213.

Wang, Q., M. Taschner, K.A. Ganzinger, C. Kelley, A. Villasenor, M. Heymann, P. Schwille, E. Lorentzen, and N. Mizuno. 2018. Membrane association and remodeling by intraflagellar transport protein IFT172. *Nat Commun*. 9:4684.

Wang, Y., X. Chen, W. Cao, and Y. Shi. 2014. Plasticity of mesenchymal stem cells in immunomodulation: pathological and therapeutic implications. *Nat Immunol*. 15:1009-1016.

Wang, Y., A. Garraoui, L. Zeng, M. Lai, F. He, H. Wang, C. Jiang, Y. Chen, L. Dai, N. Fan, H. Yang, J. Zhang, and X. Liu. 2017. FBN3 gene involved in pathogenesis of a Chinese family with Bardet-Biedl syndrome. *Oncotarget*. 8:86718-86725.

Wang, Z., Z.C. Fan, S.M. Williamson, and H. Qin. 2009a. Intraflagellar transport (IFT) protein IFT25 is a phosphoprotein component of IFT complex B and physically interacts with IFT27 in Chlamydomonas. *PLoS One*. 4:e5384.

Wang, Z., V. Li, G.C. Chan, T. Phan, A.S. Nudelman, Z. Xia, and D.R. Storm. 2009b. Adult type 3 adenylyl cyclase-deficient mice are obese. *PLoS One*. 4:e6979.

Wann, A.K., and M.M. Knight. 2012. Primary cilia elongation in response to interleukin-1 mediates the inflammatory response. *Cell Mol Life Sci*. 69:2967-2977.

Waters, A.M., and P.L. Beales. 2011. Ciliopathies: an expanding disease spectrum. *Pediatr Nephrol*. 26:1039-1056.

Wei, L.C., Y.X. Ding, Y.H. Liu, L. Duan, Y. Bai, M. Shi, and L.W. Chen. 2012. Low-dose radiation stimulates Wnt/β-catenin signaling, neural stem cell proliferation and neurogenesis of the mouse hippocampus in vitro and in vivo. *Curr Alzheimer Res*. 9:278-289.

Weisberg, S.P., D. Hunter, R. Huber, J. Lemieux, S. Slaymaker, K. Vaddi, I. Charo, R.L. Leibel, and A.W. Ferrante, Jr. 2006. CCR2 modulates inflammatory and metabolic effects of high-fat feeding. *J Clin Invest*. 116:115-124.

Weisberg, S.P., D. McCann, M. Desai, M. Rosenbaum, R.L. Leibel, and A.W. Ferrante, Jr. 2003. Obesity is associated with macrophage accumulation in adipose tissue. *J Clin Invest*. 112:1796-1808.

Weiss, A.R.R., and M.H. Dahlke. 2019. Immunomodulation by Mesenchymal Stem Cells (MSCs): Mechanisms of Action of Living, Apoptotic, and Dead MSCs. *Front Immunol*. 10:1191.

Wen, L., and F. Tang. 2018. Boosting the power of single-cell analysis. *Nat Biotechnol*. 36:408-409.

Wheway, G., and H.M. Mitchison. 2019. Opportunities and Challenges for Molecular Understanding of Ciliopathies-The 100,000 Genomes Project. *Front Genet*. 10:127.

Wheway, G., L. Nazlamova, and J.T. Hancock. 2018. Signaling through the Primary Cilium. *Frontiers in Cell and Developmental Biology*. 6.

WHO. 2021. Obesity and overweight.

Wilcox, G. 2005. Insulin and insulin resistance. *Clin Biochem Rev*. 26:19-39.

Williams, C.L., C. Li, K. Kida, P.N. Inglis, S. Mohan, L. Semenec, N.J. Bialas, R.M. Stupay, N. Chen, O.E. Blacque, B.K. Yoder, and M.R. Leroux. 2011. MKS and NPHP modules cooperate to establish basal body/transition zone membrane associations and ciliary gate function during ciliogenesis. *J Cell Biol*. 192:1023-1041.

Willows, J.W., M. Blaszkiewicz, A. Lamore, S. Borer, A.L. Dubois, E. Garner, W.P. Breeding, K.B. Tilbury, A. Khalil, and K.L. Townsend. 2021. Visualization and analysis of whole depot adipose tissue neural innervation. *iScience*. 24:103127.

Wu, Y., and K.K. Hirschi. 2020. Tissue-Resident Macrophage Development and Function. *Front Cell Dev Biol*. 8:617879.

Xu, Q., Y. Zhang, Q. Wei, Y. Huang, Y. Li, K. Ling, and J. Hu. 2015. BBS4 and BBS5 show functional redundancy in the BBSome to regulate the degradative sorting of ciliary sensory receptors. *Sci Rep*. 5:11855.

Yanardag, S., and E.N. Pugacheva. 2021. Primary Cilium Is Involved in Stem Cell Differentiation and Renewal through the Regulation of Multiple Signaling Pathways. *Cells*. 10.

Yang, D.J., J. Hong, and K.W. Kim. 2021. Hypothalamic primary cilium: A hub for metabolic homeostasis. *Exp Mol Med*. 53:1109-1115.

Yang, S., K. Bahl, H.T. Chou, J. Woodsmith, U. Stelzl, T. Walz, and M.V. Nachury. 2020. Near-atomic structures of the BBSome reveal the basis for BBSome activation and binding to GPCR cargoes. *Elife*. 9.

Ye, F., A.R. Nager, and M.V. Nachury. 2018. BBSome trains remove activated GPCRs from cilia by enabling passage through the transition zone. *J Cell Biol*. 217:1847-1868.

Ye, R.Z., G. Richard, N. Gévry, A. Tchernof, and A.C. Carpentier. 2021. Fat Cell Size: Measurement Methods, Pathophysiological Origins, and Relationships with Metabolic Dysregulations. *Endocr Rev*.

Yıldız Bölükbaşı, E., S. Mumtaz, M. Afzal, U. Woehlbier, S. Malik, and A. Tolun. 2018. Homozygous mutation in CEP19, a gene mutated in morbid obesity, in Bardet-Biedl syndrome with predominant postaxial polydactyly. *J Med Genet*. 55:189-197.

Zebisch, K., V. Voigt, M. Wabitsch, and M. Brandsch. 2012. Protocol for effective differentiation of 3T3-L1 cells to adipocytes. *Analytical Biochemistry*. 425:88-90.

Zhang, J.W., D.J. Klemm, C. Vinson, and M.D. Lane. 2004. Role of CREB in transcriptional regulation of CCAAT/enhancer-binding protein beta gene during adipogenesis. *J Biol Chem*. 279:4471-4478.

Zhang, Q., D. Nishimura, S. Seo, T. Vogel, D.A. Morgan, C. Searby, K. Bugge, E.M. Stone, K. Rahmouni, and V.C. Sheffield. 2011. Bardet-Biedl syndrome 3 (Bbs3) knockout mouse model reveals common BBS-associated phenotypes and Bbs3 unique phenotypes. *Proc Natl Acad Sci U S A*. 108:20678-20683.

Zhang, Q., D. Nishimura, T. Vogel, J. Shao, R. Swiderski, T. Yin, C. Searby, C.S. Carter, G. Kim, K. Bugge, E.M. Stone, and V.C. Sheffield. 2013. BBS7 is required for BBSome formation and its absence in mice results in Bardet-Biedl

syndrome phenotypes and selective abnormalities in membrane protein trafficking. *J Cell Sci*. 126:2372-2380.

Zhang, Q., S. Seo, K. Bugge, E.M. Stone, and V.C. Sheffield. 2012a. BBS proteins interact genetically with the IFT pathway to influence SHH-related phenotypes. *Hum Mol Genet*. 21:1945-1953.

Zhang, Q., D. Yu, S. Seo, E.M. Stone, and V.C. Sheffield. 2012b. Intrinsic protein-protein interaction-mediated and chaperonin-assisted sequential assembly of stable bardet-biedl syndrome protein complex, the BBSome. *J Biol Chem*. 287:20625-20635.

Zhang, Y., M.S. Kim, B. Jia, J. Yan, J.P. Zuniga-Hertz, C. Han, and D. Cai. 2017. Hypothalamic stem cells control ageing speed partly through exosomal miRNAs. *Nature*. 548:52-57.

Zhou, X., S. Zhong, H. Peng, J. Liu, W. Ding, L. Sun, Q. Ma, Z. Liu, R. Chen, Q. Wu, and X. Wang. 2020. Cellular and molecular properties of neural progenitors in the developing mammalian hypothalamus. *Nat Commun*. 11:4063.

Zhu, D., S. Shi, H. Wang, and K. Liao. 2009. Growth arrest induces primary-cilium formation and sensitizes IGF-1-receptor signaling during differentiation induction of 3T3-L1 preadipocytes. *J Cell Sci*. 122:2760-2768.

Zimmermann, K.W. 1898. Beiträge zur Kenntniss einiger drüsen und epithelien. *Archiv für mikroskopische Anatomie*. 52:552-706.

Zúñiga, L.A., W.J. Shen, B. Joyce-Shaikh, E.A. Pyatnova, A.G. Richards, C. Thom, S.M. Andrade, D.J. Cua, F.B. Kraemer, and E.C. Butcher. 2010. IL-17 regulates adipogenesis, glucose homeostasis, and obesity. *J Immunol*. 185:6947-6959.

6. Danksagung